

Nucleate pool boiling on microstructured surfaces

zur Erlangung des akademischen Grades eines
DOKTORS DER INGENIEURWISSENSCHAFTEN (Dr.-Ing.)
der Fakultät für Maschinenbau
der Universität Paderborn

genehmigte
DISSERTATION

Von
Magister der Physik Alexander Ustinov
aus Moskau

Date of colloquium: 31.10.2008
Reviewer: Prof. Dr.-Ing. habil J. Mitrovic
Co-reviewer: Prof. Dr.-Ing. habil S. aus der Wiesche

ACKNOWLEDGEMENTS

I would like to express my gratitude to people, without whom this manuscript would never be possible. First of all, I would like to thank my wife, Daria Ustinova, for her love and support. She is my number one in everything, including listening to my scientific ideas. I also thank rest of my family, my father Dr. Alexander Konstantinovich Ustinov, mother Olga Victorovna Ustinova, and two younger brothers, Victor and Dimitriy. Without their support, love and fun that they bring into my life I would be unable to go any further.

With the greatest respect I do appreciate my scientific supervisor, Professor Dr.-Ing. Jovan Mitrovic. I am grateful to his wise guidance, valuable advices, and comprehensive help in work as well as in everyday life. I am delighted his ability to work hard and extensive knowledge. This self made man deserves to be an example of a Scientist, with the capital letter "S", for all young people seeking scientific career.

I would like to thank Prof. aus der Wiesche for his support as a co-referee of my work, and for his valuable advices.

I also would like to thank several people whose contribution was although indirect, but essentially influential. First of them is Engineer Gerrit Barthau who has recently passed away. He was a wise and kind "grandfather" to all of us, young co-workers in Stuttgart. His knowledge of thermal sciences was practically unbounded, and he gladly shared them with anyone. I will never forget hours of discussions with him.

Professor Yuri Alfredovich Kuzma-Kichta, who introduced me once to scientific work. He helps me with an advice up to now.

And last, but not least, Professor Hans Müller-Steinhagen, who invited me one day to Germany, what has determined my life for many following years.

With the highest respect I bow to all these people.

Alexander Ustinov

Paderborn, November 2008.

Content

NOMENCLATURE	7
1. INTRODUCTION.....	8
2. STATE-OF-THE-ART	9
2.1. PHYSICAL BASIS OF THE BOILING HEAT TRANSFER.....	9
<i>Initial nucleation.....</i>	9
<i>Growing vapor bubble.....</i>	12
<i>Second order effects.....</i>	14
2.2. CLASSIFICATION SYSTEM OF ENHANCED SURFACES.....	17
<i>Attached surface layers.....</i>	19
Thick layers	19
Thin layers	24
Super thin layers	26
<i>Direct surface modifications.....</i>	29
Roughness.....	29
Machined Microstructures	34
Etching	40
Laser drilling.....	42
<i>Combined methods.....</i>	43
2.3. TASK FOR INVESTIGATION	44
3. EXPERIMENTAL	46
3.1. EXPERIMENTAL APPARATUS	46
<i>Experimental installation.....</i>	46
<i>Test Tube.....</i>	48
<i>Creation and properties of microstructures</i>	49
3.2. MEASURING PROCEDURE	53
3.3. ESTIMATION OF MEASURING UNCERTAINTIES	53
3.4. EXPERIMENTAL PROGRAM	55

4.	RESULTS AND DISCUSSION	60
4.1.	EXPERIMENTS WITH SINGLE TUBES	60
	<i>Refrigerant R141b</i>	<i>60</i>
	Microstructure A418.....	60
	Microstructure A428.....	62
	<i>Refrigerant R134a</i>	<i>65</i>
	Microstructure A428.....	65
	Microstructure A419.....	73
	Microstructure A401.....	77
	Microstructure A437.....	81
	Microstructure A435.....	84
	Microstructure A431.....	87
	Microstructure A432.....	89
	Microstructure A425.....	91
	Microstructure A426.....	93
	Microstructure A427.....	95
	<i>Electronic liquid FC-3284</i>	<i>97</i>
	Microstructure A428.....	97
	Microstructure A437.....	99
	Microstructure A435.....	100
	Microstructure A431.....	101
	Microstructure A432.....	102
	Microstructure A425.....	103
	Microstructure A426.....	105
4.2.	SPECIAL BOILING EFFECTS ON MICROSTRUCTURED SURFACE.....	106
	<i>Constancy of the wall superheat.....</i>	<i>106</i>
	<i>Boiling inception as a front</i>	<i>110</i>
	<i>Boiling crisis.....</i>	<i>117</i>
	<i>Boiling hysteresis.....</i>	<i>120</i>
4.3.	SUMMARY ON THE SINGLE TUBES EXPERIMENTS.....	122
	<i>Effect of microstructure geometry on heat transfer.....</i>	<i>122</i>
	<i>Pressure effect on heat transfer.....</i>	<i>123</i>

<i>Liquid effect on heat transfer</i>	124
<i>Conclusion on the single tube experiments</i>	126
4.4. EXPERIMENTS WITH TANDEM TUBES.....	128
<i>Refrigerant R134a</i>	128
Tandem A428 + A425	128
Tandem A437 + A425	132
<i>Electronic fluid FC-3284</i>	134
Tandem A428 + A425	134
Tandem A437 + A425	137
<i>Conclusion on the tandem tube experiments</i>	139
5. STATISTICAL MODEL OF HEAT TRANSFER FROM ENHANCED SURFACE	140
5.1. SUGGESTIONS AND LIMITATIONS OF THE MODEL	140
5.2. MODEL EQUATIONS	140
5.3. CALCULATION RESULTS.....	145
5.4. PREDICTIONS AND EXTRAPOLATION OF THE MODEL	148
6. CONCLUSIONS	151
7. REFERENCES	155
APPENDICES	160

Nomenclature

d	[m]	nucleus or cavity diameter
f	[J/kg]	specific Gibbs energy
h	[W/(m ² K)]	heat transfer coefficient
l	[m]	distance between nucleation sites
N	[m ⁻²]	micro pins density
p	[Pa]	pressure
q	[W/m ²]	heat flux
S	[m ²]	surface area
T	[°C]	temperature
ΔT	[K]	wall superheat, T _w - T _s
TPL		three phase line
V	[m ³]	volume
ΔΦ	[J]	nucleus energy barrier
ρ	[kg/m ³]	density
σ	[N/m]	surface tension
θ	[°]	contact (wetting) angle
D		fractal dimension
L	[m]	length or distance
n*		number of active nucleation sites
n		number of potential nucleation sites
Σ		dispersion of cavities diameters
A		weight coefficient
r	[J/kg]	latent heat of evaporation

Subscripts

S	smooth, saturation
L	liquid
V	vapour
W	wall
cr	critical
conv	convective
boil	boiling

1. INTRODUCTION

Creation of a highly effective surface for boiling has been a continuous task for engineers and researchers over the last several decades. Many successful steps were undertaken in the past in this direction, providing a great number of choices in production of boiling surfaces. Main requirements for a boiling surface can be formulated as follows [1-6]:

- high heat transfer coefficient, compared with technically smooth surfaces
- low boiling inception superheat
- high critical heat flux
- independency of the surface superheat on the heat flux
- long-time performance stability
- no/weak fouling.

All those advantages are seldom met simultaneously with a single surface; therefore the search for an efficient boiling surface still remains an important task.

New enhancement techniques require some universal ordering, which would provide a better understanding of the physical source of enhancement for existing surfaces, and which, on the other hand, would be flexible enough for adding unknown yet future technologies. To propose a universal classification system for boiling surfaces one has to understand the mechanisms affecting the bubble nucleation. Although extensively studied, these mechanisms remain not completely understood and many questions are still opened. In the literature there are several ways aiming at an explanation of the very first steps of bubble nucleation.

2. STATE-OF-THE-ART

2.1. Physical basis of the boiling heat transfer

Initial nucleation

The very first stage of a vapor bubble life is the appearance of a vapor nucleus. It is agreed that first nuclei are created in liquid that starts to boil due to fluctuations of the liquid density. As a fluctuation process, it is characterized by a probability. Minimal diameter of a spherical nucleus that is able to form a viable bubble in the bulk liquid is given by equation (2.1.1) (see, for example, Labuntsov [7]):

$$d_{cr} = \frac{4\sigma}{\rho_V(f_V - f_L)} \quad (2.1.1)$$

When a nucleus is created near the surface, the surface energy must be taken into account. The energy barrier to be surmounted by a fluctuation is given by Labuntsov [7] as:

$$\Delta\Phi = (f_V - f_L)V\rho_V + \sigma S - \sigma S_W(1 - \cos\theta) \quad (2.1.2)$$

Equation (2.1.2) involves the concept of a wetting (contact) angle into consideration. It immediately divides all surfaces into two groups with different wetting properties: hydrophobic and hydrophilic. They have lower or higher values of the energy barrier (2.1.2) correspondingly, which is always lower in comparison with the nucleation inside the bulk liquid,

$$\Delta\Phi = (f_V - f_L)V\rho_V + \sigma S \quad (2.1.3)$$

Therefore one may expect lower inception superheats required for nucleation from hydrophobic surfaces, what has been confirmed by numerous experiments, Labuntsov [7].

Another way to decrease the energy barrier (2.1.2) is to provide a larger contact area between the nucleus and the wall (larger values of S_W in eq. 2.1.2). This leads to suggestion that rough surfaces must result in lower inception superheats; another widely confirmed experimental fact.

One must distinguish the difference between the local contact angle θ , appearing in (2.1.2), and the average contact angle, observed in experiments. Local contact angle is the result of energetic interaction of the molecules of liquid, solid and vapor and it is a physicochemical property of the system. The apparent contact angle (θ_0) is a more complex property, taking into account also microstructure of the surface. According to Deriagin [8], θ and θ_0 are connected by the following equation:

$$\cos\theta = \xi \cos\theta_0 \quad (2.1.4)$$

Equation (2.1.4) is also known as the Wenzel expression [42]; its thermodynamic bases were provided by Deriagin [8]. The quantity ξ is the ratio of the projected surface area on the actual (wetted) surface area. It is reverse to the roughness coefficient. As $\xi \leq 1$ for all real surfaces, $\theta > \theta_0$ for $\theta < \pi/2$ and $\theta < \theta_0$ for $\theta > \pi/2$. At present, the local contact angle remains unknown, while the apparent contact angle is poorly studied.

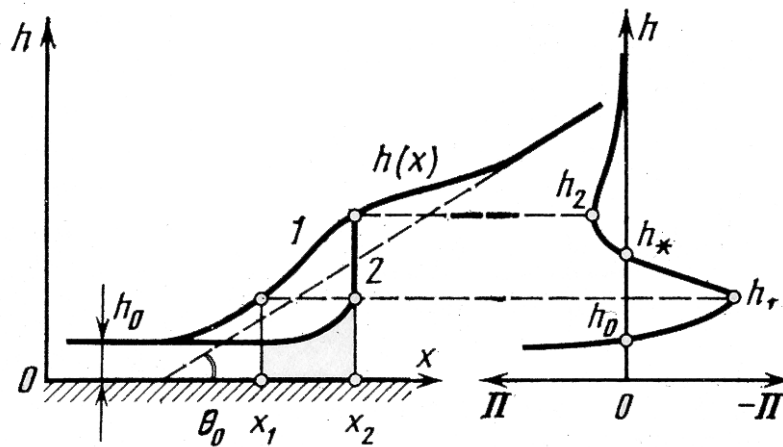


Figure 2.1.1: Possible interface profile $h(x)$, 1 and 2, for a given disjoining pressure isotherm (on the right) [9].

Contact angle has a sense only when a linear scale of the process under consideration is given. For very small scales, which include a nucleus, the Young-Neumann law, used in the development of (2.1.2), must be modified to add the linear tension, appearing in the system. As it was shown by Deriagin [9], the profile of a liquid between liquid and vapor in equilibrium state is not

unique for a given disjoining pressure. Figure 2.1.1 illustrates the possibility of two different interface profiles (1 and 2) and the disjoining pressure isotherm.

One may note that the very first stages of bubble life are still hidden, however important conclusion from the approach (2.1.1) – (2.1.2) is that only the surface cavities with size of about d , deduced from equation (2.1.2), can affect the initial nucleation. For larger cavities, the energy barrier (2.1.2) reaches its values equal to the bulk liquid.

For different liquids and pressures equation (2.1.1) gives the critical vapor bubble radius in the range of $1 \cdot 10^{-6}$ m to $1 \cdot 10^{-5}$ m. Therefore, cavities of such sizes are preferable for initial nucleation in general. Experimental validation of this result can be found in literature, for example Nelson [24] and Gorenflo [25]. Figure 2.1.2 illustrates dependence of number of surface cavities available for nucleation in dependence on their sizes.

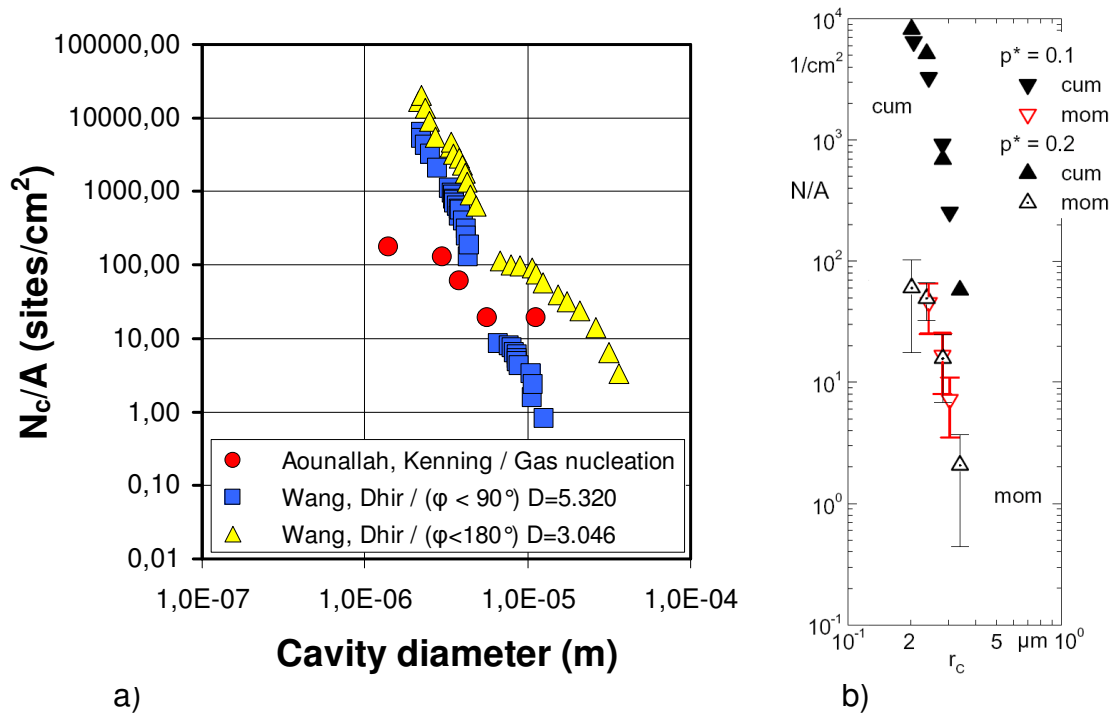


Figure 2.1.2: Active nucleation sites density in dependence on the cavity size.
 a) – Water and gas nucleation data [24]
 b) – Boiling of propane on a copper sandblasted tube [25].

Modified surfaces obtained with plasma or flame sprayed/backed particles have a great number of cavities with a wide range of sizes, providing low inception superheats and high heat transfer coefficients. A novel microstructure, developed by Mitrovic et al. [4-6, 26], allows obtaining even smaller cavities.

Growing vapor bubble

After the boiling inception further capability of a surface to produce vapor bubbles is determined by its number of nucleation sites. Enhanced surfaces serve a greater number of nucleation sites in comparison with a technically smooth surface, subsequently having higher heat transfer coefficients. A developed micro geometry of an enhanced surface acts as a vapor trapper as well, allowing bubbles to be created from the vapor rests inside the structure. However thicker structures have complex vapor – liquid counter flows inside of it, decreasing the performance (especially at high heat fluxes) and the critical heat flux significantly.

It is known that evaporation into the growing vapor bubble occurs mainly at its bottom in the three-phase line (TPL) region, projected as point A in Figure 2.1.3. Evaporation at the TPL depends strongly on the conditions of the surface, see Mitrovic [4], Labuntsov [10].

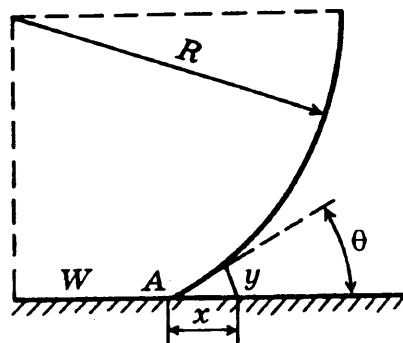


Figure 2.1.3: On determination of the local heat flux [10].

One of the first works, introduced the concept of the micro layer underlying a growing vapor bubble, was published by Labutsov [10]. It was suggested that the local heat flux, being received by a single vapor bubble, could be found as:

$$q \approx \lambda \Delta T / y \quad (2.1.5)$$

where y is the distance from the wall, which is:

$$y = y_A + 2 \sin(\theta/2) \quad (2.1.6)$$

In eq. (2.1.6) the quantity y_A denotes the minimal thickness of a liquid layer near the TPL, at which equation (2.1.5) still has sense and θ_0 is the average contact angle. Labuntsov [10] further suggested that the order of magnitude of y_A must be about intermolecular distances in a liquid, i.e. $y_A = (10^{-7}$ to $10^{-8})$ cm.

Physically, this means that there is always a layer of molecules of a liquid under a growing vapor bubble, which is unable to evaporate. Potential of the energy field, created by the surface forces, must be high enough to lock the liquid molecules in this layer. It seems that adsorption properties of the surface play the major role in this case as well as the microstructure of the surface with the characteristic linear scale about 1 nm. Some modern technologies considered below allow creation of surface layers with the thickness of several nanometers. Such surfaces seem to have great influence on the processes occurring along the TPL and in the micro layer.

As it was shown by Mitrovic [4] a longer TPL allows higher evaporation rates and subsequently higher heat transfer coefficients. Ideal would be to have a TPL with infinite length. For a bubble on the plain surface the TPL length is limited, while for modified surfaces with micro pins described by Mitrovic et al. [4-6, 26], the TPL length depends upon the number of structural elements (pins) per unit of area, and for a bubble with 1 cm^2 contact area it can be up to 6 m.

Considering the saturated nucleate boiling, one must not neglect simultaneous condensation of a growing vapor bubble at its interface contacting the liquid. As it was shown by Ustinov et al. [11] in the case of saturated water

boiling, condensation can consume up to 25% of the applied heat flux. Great number of vapor bubbles cools down the surface effectively, making the surface spatial-temporal temperature gradient to be noticeable. Some measurements (Auracher et al. [12], Kenning et al. [13]) give its values in dependence on the wall material and applied heat flux to be from 2 K for copper to 10 K for stainless steel, both values are for moderate heat fluxes.

Simultaneous evaporation and condensation of a single growing vapor bubble cause a complex temperature field of the surface, and determines the work of active nucleation sites. It can only be described basing on the local spatial-temporal characteristics of the process, while the averaged values are used in most of the present models. From the point of view of the interfacial evaporation-condensation it seems possible to take into account the reverse heat fluxes, occurring from the liquid to the heated wall and from the liquid to growing vapor bubble. Experimentally reverse heat fluxes were detected for the very first time by Ilyin et al. [14] and then later theoretically described by Mitrovic [15] and Ustinov et al. [11]. The surface temperature field seems to be even more complex for the subcooled boiling and boiling upon modified surface with a developed micro geometry.

It is known that the surface temperature undergoes oscillations. This process explained by some authors Shoji [16], Mosdorf [17] from the positions of chaos dynamics. It was shown that at higher heat fluxes when number of bubbles is large, the amplitude of the surface temperature oscillations rises. Experimental data on complete temperature field of enhanced surfaces are limited in literature, but one may expect even more complex behavior in comparison with a plain surface.

Second order effects

The above-mentioned processes affect the heat transfer from the surface to the boiling liquid directly. However, one may recognize so called “second order” effects, which also drive the system away from ideal behavior. This term was first introduced by Barthau et al. [27] showing that on a short time scale

(hours) the boiling heat transfer coefficient is very stable, but on a longer time scale (days, weeks) it continuously drifts. The direction of this drift depends on the “heat flux history” of the boiling surface. The drift effects are reversible and should not be confused with “common fouling”. Therefore, in experimental boiling studies, the history, i.e. the relevant time intervals of the experiments, seem to play an important role and must be better documented.

Macro convection seems to play influential role in the study of Barthau et al. [27]. Even in precisely temperature-controlled saturated nucleate boiling experiments ($\Delta T=0.02K$), the pool liquid may be superheated due to large-spaced recirculation flow in the boiling vessel. The degree of superheat will depend on the size and shape of the boiling vessel and it depends on system pressure and heat flux.

Those second order effects should be extended and probably taken into account in future investigations. Among them Marangoni convection and micro convection take place. Their influence is especially strong for mixtures, when there are two or more liquid components involved with different physical properties. For example in a binary mixture one of components can have hydrophobic behavior to the surface while the second one can be hydrophilic, giving selective adsorption. Binary mixtures can be negative respectively positive, in dependence on the surface tensions of components. Different kind of mixtures may have different directions of liquid micro flows between bubbles due to Marangoni convection, enhancing or decreasing the heat transfer during boiling, Figure 2.1.4.

Same hydrodynamic behavior is observed for one component liquids although in a lower degree, when vapor bubbles coalesce or disjoin from each other. Experimental measurements of this phenomenon are very limited in the literature due to its complexity.

Other poorly studied effect influencing the heat transfer during boiling is the thermal interaction of the nucleation sites. It seems possible to consider this interaction when new approach mentioned earlier is developed basing the surface temperature field.

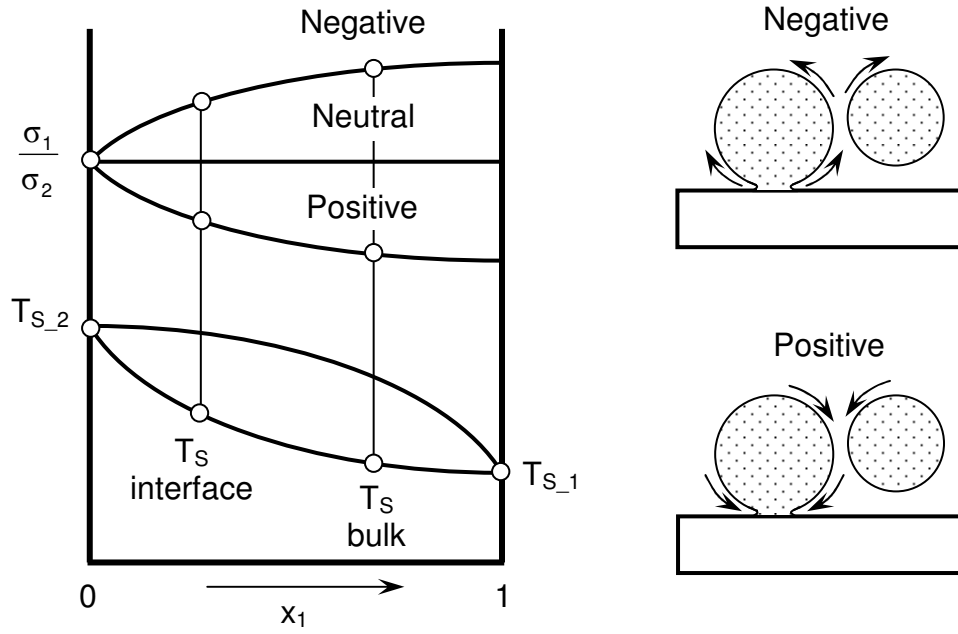


Figure 2.1.4: Surface tension distribution over the composition of a binary mixture (top) and scheme of Marangoni flows between vapor bubbles (bottom) [28].

2.2. Classification system of enhanced surfaces

Upon the above presented brief basic analysis of processes, underlying the nucleation and influencing the boiling heat transfer, a new classification system for enhanced surfaces is proposed, Figure 2.2.1. All modifications are divided into three groups, which will be discussed with examples in more details later. Those groups are:

- **attached layers**, when a new layer of any kind is attached to the base surface;
- **direct modifications**, obtained by a direct change of the surface and
- **combinations** of these two.

This grouping is determined by the production technology resulting in some common properties of those surfaces. Any attached layer and the base material have binding forces between them, what causes such effects as dislocation, detachment and subsequent performance drop after multiple cycles of warming up and cooling down. As the material of an attached layer often differs from the base surface material, they have different heat expansion coefficients. As temperature field of a modified surface has noticeable gradients during boiling, attached layers usually detach from the base wall after a certain period of time.

From this point of view the second group, direct modification of the base surface, is preferable. However, majority of surface modification technologies that can be attributed to this group are in general more complex and expensive in production. The question of stability of those modifications also remains open; as such data are practically absent in literature.

Both of those directions in the enhanced surfaces production are subjects of research for long time usability in industrial scale and fouling characteristics.

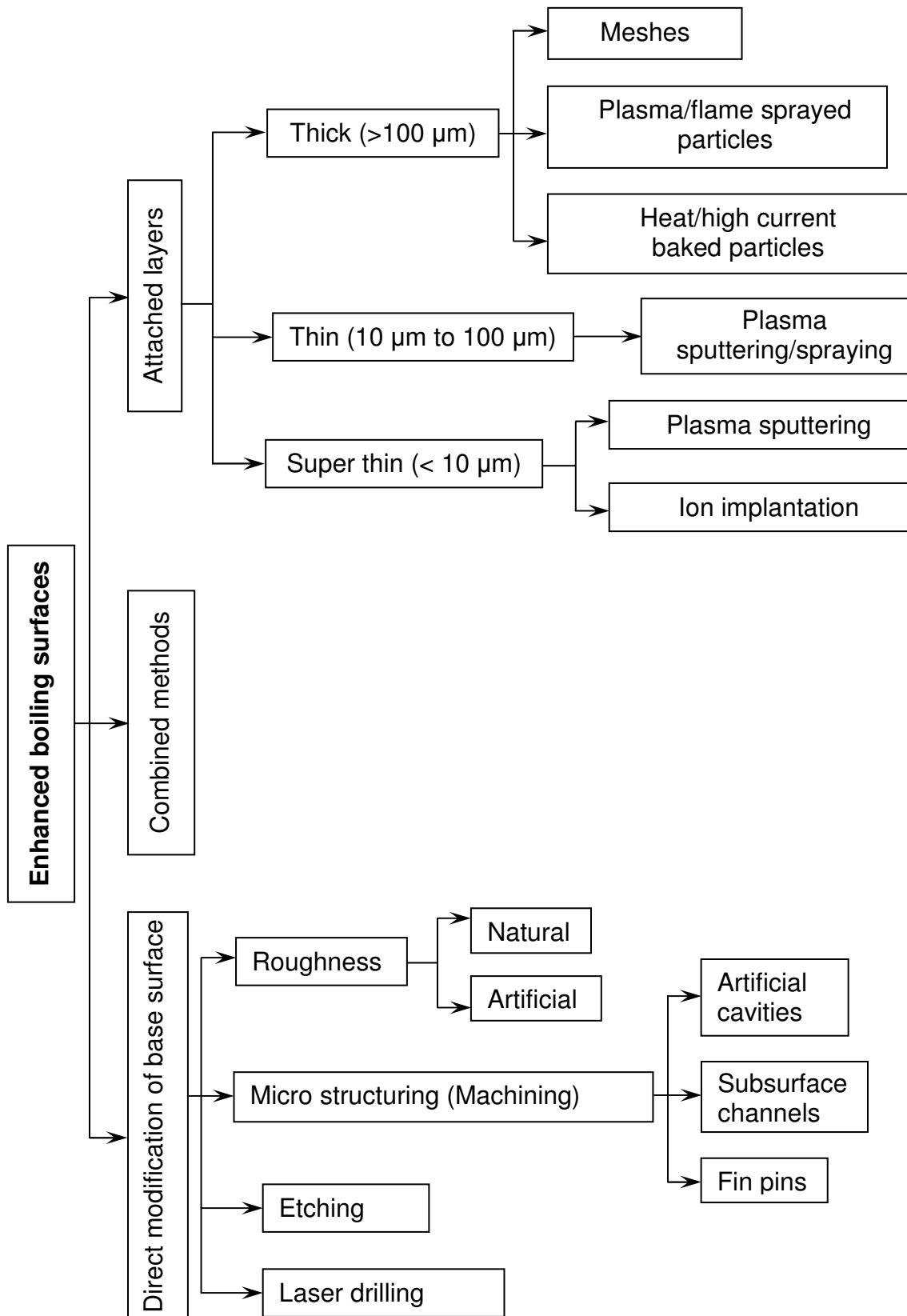


Figure 2.2.1: Classification system of modified surfaces for boiling.

Attached surface layers

Depending on the thickness of the layer, attached layers providing the heat transfer enhancement could be divided in three subgroups, Figure 2.2.1. Different thicknesses of the layer enhance the heat transfer at different stages of vapor bubble growth through different physical mechanisms. As mentioned above the size of a cavity which supports the initial nucleation is about 10^{-6} m. One may accept this value as a lower border for “super thin” layers, and its 10-fold value as a lower border of “thick” layers. All the layers with thicknesses in between would belong to thin layers group.

Taking such grouping, one can see that super thin layers affect the energy barrier (2.1.2) for creation of a nucleus through the surface wettability, but ***have no influence on the surface roughness***, that could result in a preferable geometrical place for nucleation. Thin layers ***affect both the wettability and the roughness*** of the surface. They can support growth of vapor bubbles only during the first stages of growth. Thick layers form a complex three dimensional porous matrix, where nucleation can occur at any place.

Thick layers

Thick layers are easy to obtain on a surface, as their production does not require sophisticated technologies. However, thick layers having porous structure, suffer such negative phenomena as vapor lock-up and the boiling crisis inside of them at high heat fluxes. This happens due to the complex two phase counter flows in a thick porous layer. Vapor cannot leave the layer quickly, especially at high heat fluxes, so liquid cannot penetrate the structure and wet its base. For such structures the critical heat flux sometimes decreases appreciably and the heat transfer coefficients are lower.

Layers of Meshes

Meshes are one of the easiest created surface enhancers on flat boiling surfaces and tubes. Such enhancement technique was used by Yagov et al. [18]. The porous coating has been obtained with the superposition of several layers of wire nets on a circular heat transfer surface. The grids were pressed on the heater surface. The structure shown in Figure 2.2.2a is commonly used in the filtering technique and is available in a wide range of geometrical parameters and materials. As materials for the metallic wire mesh stainless steel (AISI 304), aluminum, copper and brass were used. The effect of the height of the wire mesh structure has been tested by changing the number of net layers.

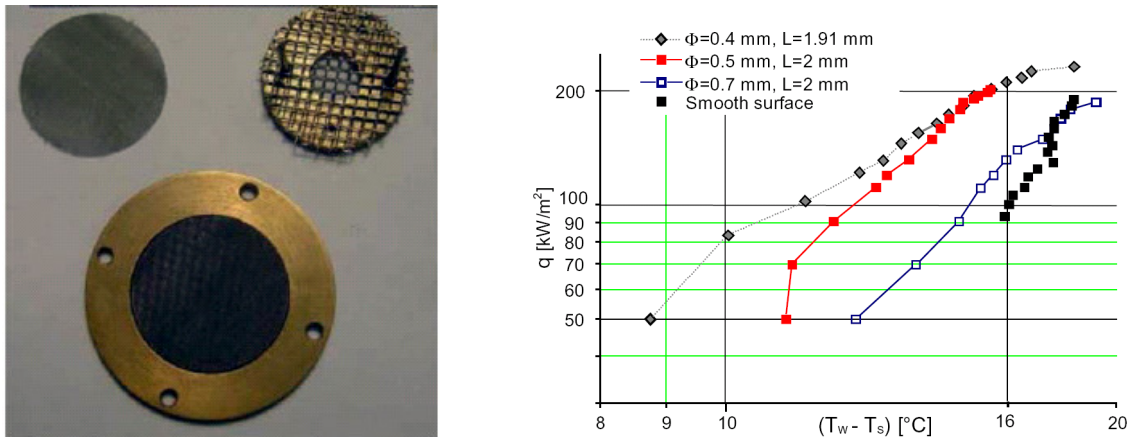


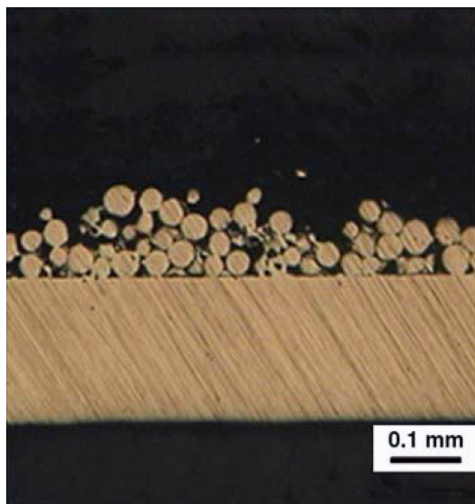
Figure 2.2.2: Mesh structures (a) and their boiling curves with R141b at 1 bar (b) [18].

The best performance was found for nets containing 3 to 7 layers of wires with diameters between 0.25 mm and 0.40 mm and mesh aperture of approximately 2 mm. A possibility to separate vapor and liquid flows and to increase the critical heat flux (CHF) by means of a finer wire net placed on the heated surface and larger wire nets on the upper levels has been confirmed. An increase in CHF up to 40% has been experimentally obtained. Greater number of mesh layers (despite the increased heat transfer surface) sometimes caused an earlier boiling crisis due to the complex two-phase flows inside the structure. Therefore, enhancement capability for such a meshed surface decreases with increasing heat flux.

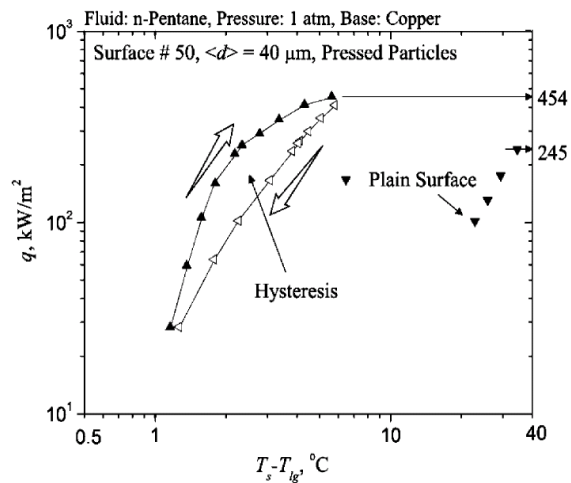
In an earlier work of Labuntsov and Yagov [19], meshes made of fluorocarbon polymer were used to stabilize and enhance the boiling of water at pressures of 36 mbar and 200 mbar. This has allowed decreasing the wall temperature at boiling inception from 25 K for a plain surface to 3.5 K for a surface with hydrophobic meshes; at the same time the critical heat flux was decreased drastically.

Plasma/flame sprayed particles

Another mean of boiling improvement is plasma or flame sprayed layer of metallic particles on the base substrate. Hwang and Kaviany [20] report experimental data on boiling of n-pentane at atmospheric pressure upon enhanced surfaces with loosely packed, shaken, or pressed copper particles with diameters between 40 μm to 80 μm , plasma sprayed on the base copper surface. The layer thickness was between 3 to 5 diameters of a particle, and it was uniformly disposed on the base surface (Figure 2.2.3a).



a)



b)

Figure 2.2.3: Micrograph (a) of side cross section of porous-layer coating (#50) and its boiling curve (b) [20].

Enhancement of the boiling process by a porous layer of particles is mainly associated with the rise of the number of nucleation sites in comparison to a smooth surface. For all the coatings as it was found by Hwang and Kaviany

[20] the critical heat flux (CHF) is about 1.8 times higher than for a plain surface. Hysteresis for modified surfaces was experimentally detected (Figure 2.2.3b), what is typical for this subgroup of modified surfaces. Hwang and Kaviany [20] suggest that presence of uniform porous coating influences the hydrodynamic (macro scale) stabilities in a way that statistically the critical Rayleigh–Taylor wavelength decreases. It is also possible that the vapor fraction increases in a manner to statistically cause a decrease in the dominant interfacial wavelength.

Liter and Kaviany [21] extended the method of plasma or flame particles spraying to obtain modulated porous coatings. Figure 2.2.4 represents SEM-photographs of tested surfaces with single- and dual height modulated porous-layer coatings.

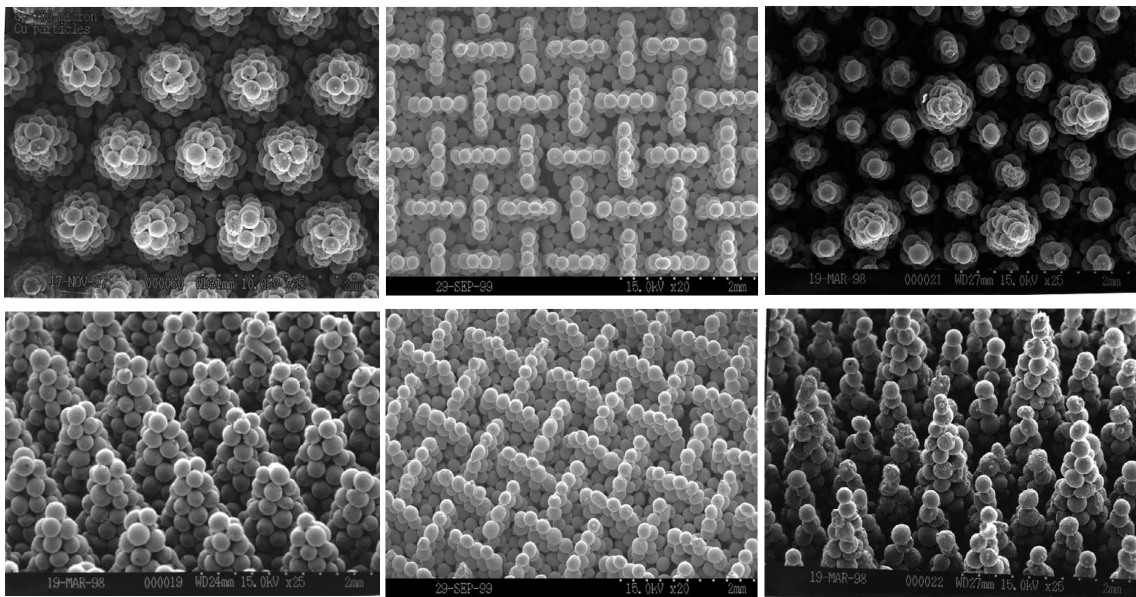


Figure 2.2.4: SEM photos of single-height (a, b) and dual height (c) modulated porous coating. Bottom – perspective view; top – top view of coatings [21].

The porous layers contain 200 μm spherical particles molded into conical stacks (Figures 2.2.4a and 2.2.4c) or tapered walls (Figure 2.2.4b). Experimental results were presented by Liter and Kaviany [21] showing the modulated porous coating with optimized size, shape and distribution provides a

three times increase in the critical heat flux, and decrease in the boiling inception superheat in comparison with a plain surface from 2 to 2.5 times.

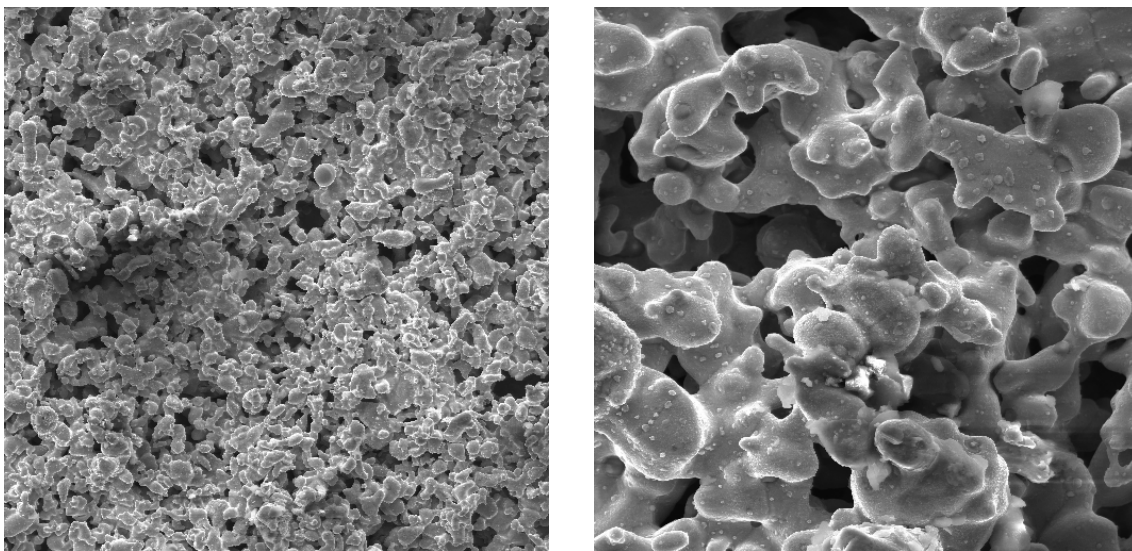
Along with metallic particles, other material can be sprayed with plasma or flame flow on the base surface. Chang and You [22] have produced several enhanced boiling surfaces on a square heater, combining silver flakes, epoxy, isopropyl alcohol, diamonds, copper, aluminum and methylethylketone. Aluminum particles in coatings were 1 μm to 20 μm , copper particles 1 μm to 50 μm , diamond 8 μm to 12 μm and randomly oriented layers of silver flakes 3 μm to 10 μm . All coatings were tested with FC-72 at atmospheric pressure. The micro porous enhanced surfaces showed about 80-90% reduction of incipience superheat, about 30% enhancement of the nucleate boiling heat transfer coefficient and about 100% enhancement in CHF over a plain surface. This enhancement was due to the creation of micro porous structures on the heater surface that significantly increased the number of active nucleation sites. It is obvious that the coated surfaces wettability was changes greatly as well. The great disadvantage of the specific coverings is the presence of volatile components in its composition, like alcohol and epoxies. Although some measures were presented by Chang and You [22] to ensure the stable operation during tests, one may expect a substantial performance decrease in time, already after a time span of 100 hours of work.

Heat/high current baked particles

Further development of technology of plasma/flame spraying of particles to the base surface is heat or high current baking of them. This can be done in a stove at temperatures about 80% of the melting values, or by passing high currents through the surface with particles. It provides a better attraction forces between particles themselves and particles with the wall. This technology allows **enhancing the inner tube surface and other hard accessible surfaces**. Typical microstructure obtained as result of this process is depicted at Figure 2.2.5.

Kuzma-Kichta et al. [23] report on the experiments on flow boiling of water on surfaces covered with high current backed particles. The sintered

porous coatings (Figure 2.2.5) of thickness 0.12 mm to 0.4 mm consisting of stainless steel and copper were tested at mass flow densities of $20\text{kg}/(\text{m}^2\text{s})$ to $10000\text{kg}/(\text{m}^2\text{s})$, pressures of 0.1 MPa to 6.0 MPa and thermodynamic steam qualities of **-0.3 up to 1.3**. The strong nonlinearity of performance was detected for all types of surface modifications of this subgroup (see Figure 2.2.1). The authors suggest optimization of such type of modified surfaces for every single application as the boiling crisis occurring inside the structure can decrease the overall heat transfer performance in some cases.



a)

b)

Figure 2.2.5: SEM photographs of surfaces with high current backed copper particles; a) top view, zoom 500x, b) top view, zoom 1000x [23].

Thin layers

Next subgroup of modified surface according to Figure 2.2.1 comprises thin layers attached to the base surface. It is proposed to account layers with thickness between $10\ \mu\text{m}$ and $100\ \mu\text{m}$ as thin. Physically thin layers could enhance the boiling heat transfer at the bubble origin, providing preferable physical and chemical conditions for initial nucleation, at the first stages of bubble growth, supporting the mass heat flux inside a vapor bubble in the TPL-region.

Such layers can be obtained only using several modern technologies developed over the last decades. There are at least two possibilities to create attached enhancing layers to the base surface, namely small particles plasma spraying process and plasma sputtering. During the plasma spraying the very fine particles are needed with the simultaneous layer thickness control. Plasma sputtering in its turn is relatively slow process and it takes tens of hours to produce enhancing layer of the pointed thickness.

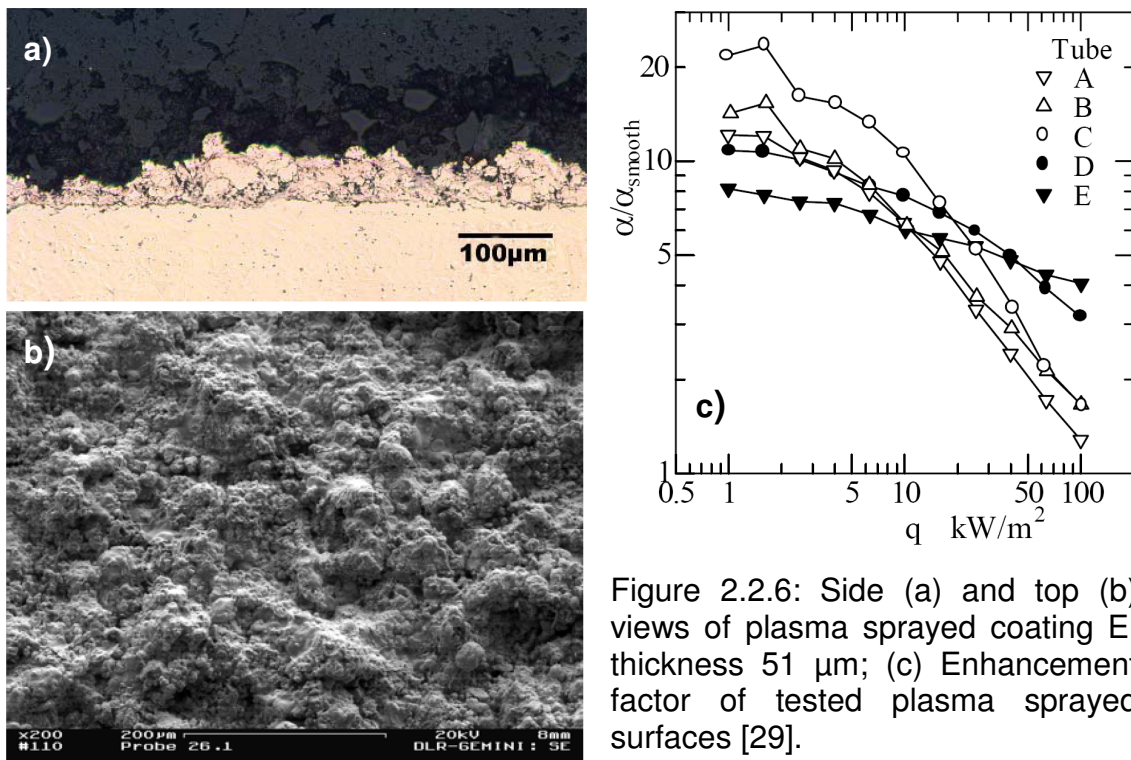


Figure 2.2.6: Side (a) and top (b) views of plasma sprayed coating E, thickness 51 μm; (c) Enhancement factor of tested plasma sprayed surfaces [29].

Plasma spraying

Asano et al. [29] investigated several plasma sprayed coatings with different properties and thicknesses. Example of such surface is presented in Figure 2.2.6; it is covered with the copper porous layer with thickness of 51 μm. All surfaces were tested with boiling R134a at saturation temperatures of -20°C, 0°C and 20°C. Enhancement ratio to the smooth tube as function of heat flux is presented in Figure 2.2.6c. It shows that the thinnest plasma sprayed coating (labeled with E in Figure 2.2.6c) has the most stable performance with the

increasing heat flux. As it was mentioned earlier, such behavior can be attributed to the complex counter flows of vapor and liquid inside the porous matrix at high heat fluxes, worsening supply of nucleation sites with liquid, what is practically absent for the thinner layer E.

Plasma sputtering

Another way to create a thin enhancing layer on the base surface is the plasma sputtering process. However, there are no experimental investigations in literature on boiling upon surfaces with plasma sputtered layers with thicknesses between 10 μm and 100 μm to the knowledge of the authors. The main reason for that seems to be the fact that plasma sputtering is a very time consuming process. It takes tens of hours to produce a sample with thickness even below 1 μm . Creation and testing of such surfaces could be the subject for future investigations as their advantage may be in a very precise adjustment of the boiling inception superheat through variation of the energy barrier (2.1.2).

Super thin layers

Plasma sputtering

As it was mentioned in the previous chapter, the plasma sputtering process serves some interesting possibilities in creation of surface enhancers. Layers with the thickness up to 10 μm are proposed to account as super thin in accordance with the classification system accepted in this work (see Figure 2.2.1). Super thin layers of just several nanometers thickness could be a strong enhancer of surface boiling heat transfer, especially in combinations with some other means of enhancement. For example, they could be used with microstructured or UV-irradiated surfaces.

Super thin layers can affect the initial nucleation through the surface force field, changing its potential in dependence on the material properties of the applied surface layer and its thickness. Therefore, there is a large field for studies in nucleate boiling heat transfer from surfaces with applied super thin enhancing layers.

Takata et al. [30] have prepared TiO_2 and $\text{TiO}_2+\text{SiO}_2$ sputtered surfaces and investigated the evaporation of a water droplet on them. The sputtered layers maximal thicknesses were 250 nm and 275 nm correspondingly. Obtained surfaces were disposed under the UV-irradiation, and the contact angles with water were decreased subsequently. This effect was called “photo-induced hydrophilicity” by Takata et al. [30]. After shielding the surfaces from the UV-radiation they recovered the properties back in few hours (see Figure 2.2.7). Super thin sputtered and UV-irradiated layers were found to decrease evaporation times greatly.

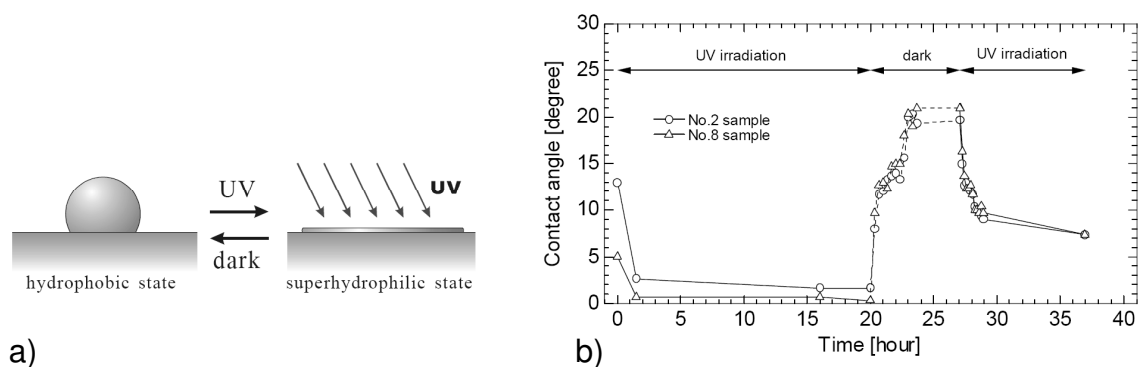


Figure 2.2.7: a). Photo-induced hydrophilicity;

b). Change in contact angle of TiO_2 -sputtered surface [30].

The enhancement method of Takata et al. [30] is a combined method of plasma sputtering and UV-radiation. It would be a promising topic for future investigations to measure boiling characteristics of a surface covered with a super thin enhancing layer.

Ion implantation

The last technology that will be considered in the group of attached enhancing layers is the ion implantation. This is a relatively new technology developed during the last several decades and lays on the border between attached enhancing layers and direct surface modifications (see Figure 2.2.1 for more details).

During the implantation process the base solid surface is bombarded by ions with energies within the range between keV and MeV. The ions penetrate the surface at depths between 10 nm and 1000 nm in dependence on their energy and the relation of their mass to the mass of the base surface atoms. As the implanted layer thickness is below 1 μm , its thermal resistance is negligible. This layer exist in the state of a solid solution, so there is no obvious interface between the base metal and the layer, therefore it is not easily removed, see Mueller-Steinhagen and Zhao [31].

No systematical studies of boiling heat transfer enhancement were done with the ion implanted surfaces. Mueller-Steinhagen and Zhao [31], however, have tested such surfaces for fouling during pool boiling of CaSO_4 water solutions. Figure 2.2.8 gives the basic ideas about low-fouling performance and long-time working stability of the ion implanted stainless steel surface.

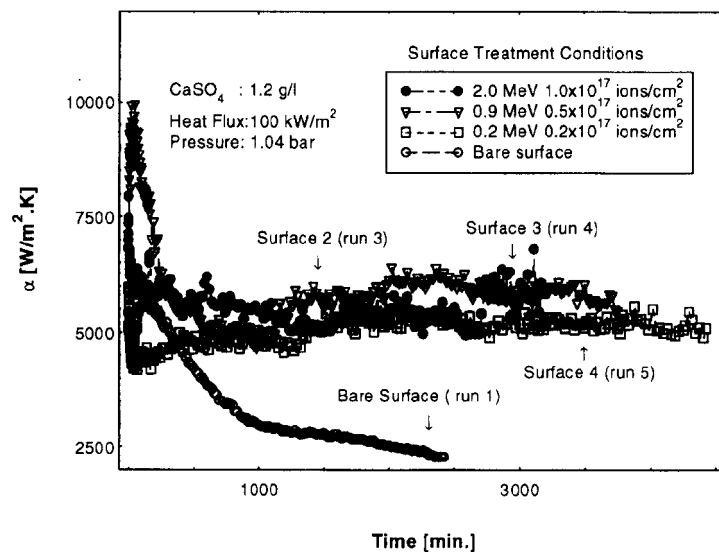


Figure 2.2.8: Effect of implantation conditions on heat transfer coefficient [31].

Some interesting results could be obtained in boiling experiments with the ion implanted surfaces, especially in combinations with some other enhancing techniques.

Direct surface modifications

As it was stated in above, the direct surface modifications are preferable versus the attached enhancing layers as there are no decrease of binding forces between the enhancer and the base surface. However, the surface force field could be essentially varied by the changed geometry and/or the chemical composition of the enhanced surface, correspondingly affecting the value of the energy barrier (2.1.2).

One must note that as a rule the directly modified surfaces have coarser structure than the surfaces with applied layers. Majority of direct modifications require contact methods of the surface treatment, such as cold machining for example. Therefore the linear scales of surface structure elements are limited to the size of treating tools.

Roughness

Historically, the very first enhancement during boiling was observed upon scratched and rough surfaces. At present, a relatively large information databank is accumulated for the boiling heat transfer upon rough surfaces. However, the main question remaining is the representation method of a real rough surface. Normally, the scalar parameter *roughness* is used for the complex three dimensional microstructure of a real surface representation. The roughness (R_z) is defined in accordance with DIN standard as average distance between the highest peak and lowest valley in each sampling length. It is obviously not adequate for the next generation models of the process of surface boiling. Some possible solutions of this fundamental problem will be considered in this chapter.

It is proposed to distinguish between natural and artificial roughness types. The natural roughness is the one of an untreated surface. Any kind of surface roughening changes its classification to the subgroup of artificial roughness (see Figure 2.2.1). It is known that the number of nucleation sites on a surface is directly proportional to its roughness.

Natural roughness

Using the fractal model of Mandelbrot, Solodov [32] has built up the realistic heat transfer boiling surface (Figure 2.2.9). This method is also used in computer modeling of surfaces.

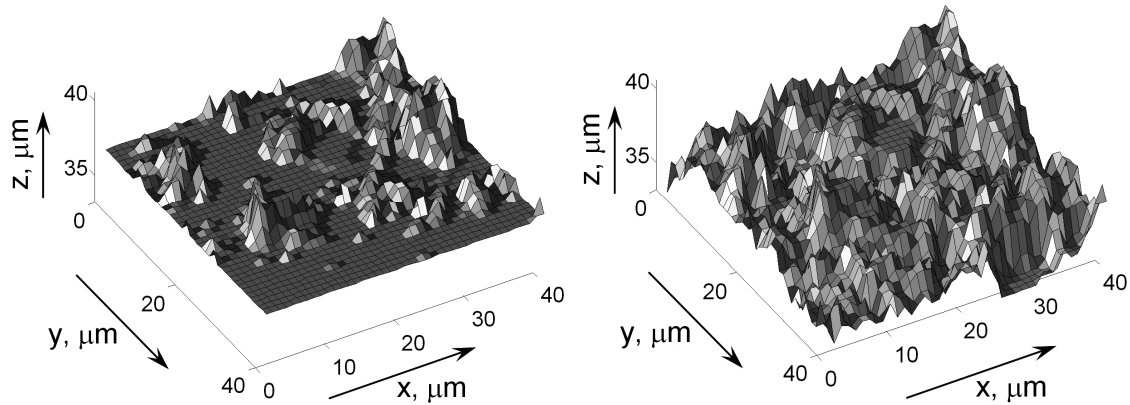


Figure 2.2.9: Realistic representation of an irregular surface [32].

Solodov [32] proposed a computer model of nucleate boiling heat transfer where a surface is characterized by the fractal dimension with the numerical value between 2 and 3. The linear distance between nucleation sites L is given by Solodov's model [32] as:

$$L = C \cdot \left(\frac{R_{cr}}{R_s} \right)^{(D-2)/2} \cdot R_{cr} \quad (2.2.1)$$

In equation (2.2.1) C is a fitting constant, R_s is a linear scale, R_{cr} is the critical vapor bubble diameter, $R_{cr} = d/2$, where d is given by eq. (2.1.1).

The constant C was fit in accordance with experimental data at pressure of 1 bar and then used for calculation at pressures up to 200 bars. The calculation results were compared with experimental data for boiling of water on silver tube, copper tube coated with nickel and chrome, and on stainless steel tube (Figure 2.2.10). Using the fractal dimension $D = 3$ (corresponding to a three dimensional object) allows obtaining results in agreement with experimental data.

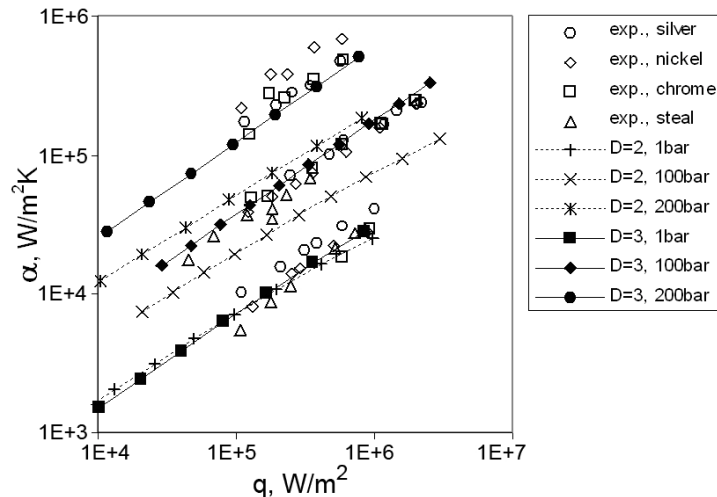


Figure 2.2.10: Comparison of fractal computer model with experimental data [32].

Solodov [32] concludes that introducing the fractal description of the heating surface simulates the distances decrease between active nucleation sites with increasing pressure correctly, improving calculation of the heat transfer coefficient with nucleate boiling.

Some other attempts to introduce the fractal dimension for a boiling surface representation are known. Cheng and Yu [33] have proposed another calculation model for boiling heat transfer from a real surface utilizing the concept of fractal dimension. A-posteriori analysis by Cheng and Yu [33] proposes to calculate the fractal dimensions from a photograph of a liquid boiling on a surface by the box-counting method. They found the fractal dimension between 1 and 2, i. e. as for a two dimensional object and consider the active cavities formed on the heated surfaces are analogous to pores in porous media. Based on this idea, Cheng and Yu [33] took advantages of developments on fractal theory of porous media. Using their model they succeeded to fit experimental data (Figure 2.2.11).

As it seems, the universal way of representation of a real surface as well as of a structured one, could be the above mentioned approach using the fractal dimension. However, no agreement exists among the researchers over the basic principles of the approach, so regular investigations are required.

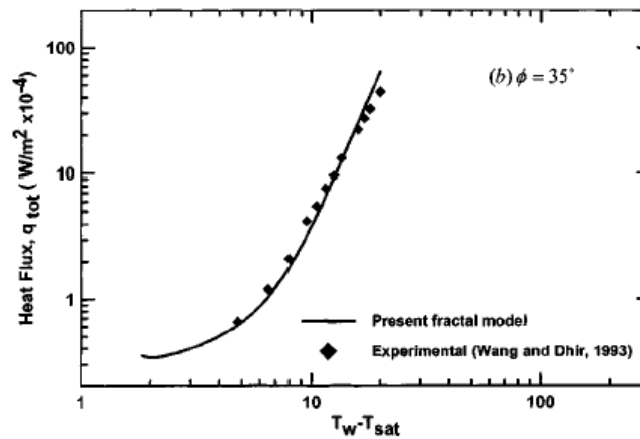


Figure 2.2.11: Comparison of the fractal model with experimental data [33].

Some non-metallic materials with natural structure are utilized as boiling heat sinks for needs of electronic devices cooling. El-Genk and Parker [35] report on experimental data on enhanced boiling of highly wetting HFE-7100 dielectric liquid on porous graphite at atmospheric pressure. The authors report this liquid as a substitute for FC-72.

The structure of porous graphite serves many interconnected pores and reentrant-like cavities, which enhance boiling it two ways. It is a preferable place for nucleation itself and secondly provides entrapped vapor. Figure 2.2.12a represents SEM photos of porous graphite and Figure 2.2.12b – boiling curves of HFE-7100 for saturated boiling at atmospheric pressure.

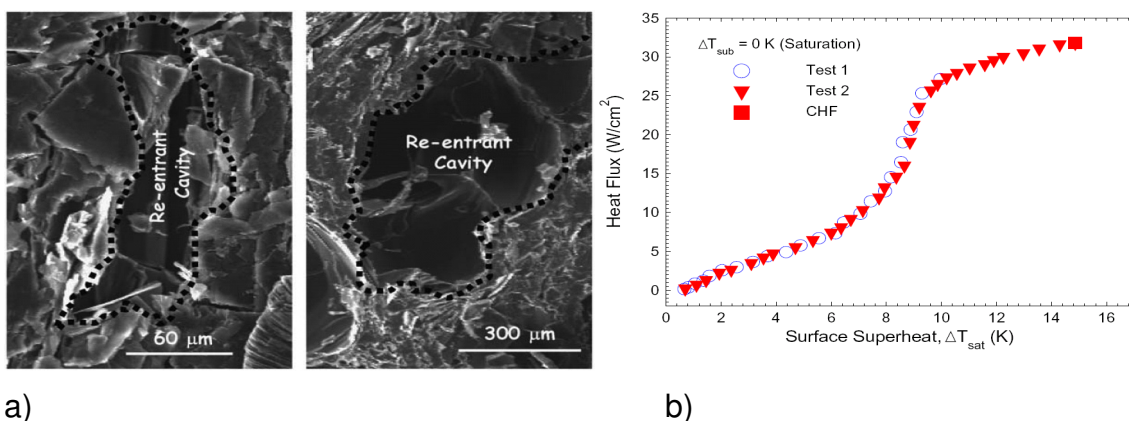


Figure 2.2.12: Heat transfer improvement by a graphite layer [35].

a) SEM images of the porous graphite (PG) surface

b) Boiling curves for saturation boiling of HFE-7100 on PG.

One may predict significant performance drop of the porous graphite structure after long time usage as the entrapped air is removed from it. This type of structure is not always applicable in industrial use, as the technology of the porous graphite application to a tube and other non-flat surface is not yet developed. Boiling curves for this structure are characterized by classical temperature rise with the increasing heat flux.

Artificial roughness

Artificially roughened surfaces are relatively good explored. The question of such surface representation remains opened, although the fractal approach mentioned above for a naturally rough surface seems to remain applicable here. Another way to represent a surface is the method developed by Gorenflo et al. [25]. A virtual ball of a certain diameter, rolling over a real surface, is supposed to provide smoothing curve for a two dimensional representation and a smoothing surface for a three dimensional (see Figure 2.2.13). The virtual ball procedure seems to be more complex in use and subsequently less universal for all enhancing surfaces. It is also not deprived of the subjective factors of using the “proper” ball radius, for more details see Gorenflo et al. [25].

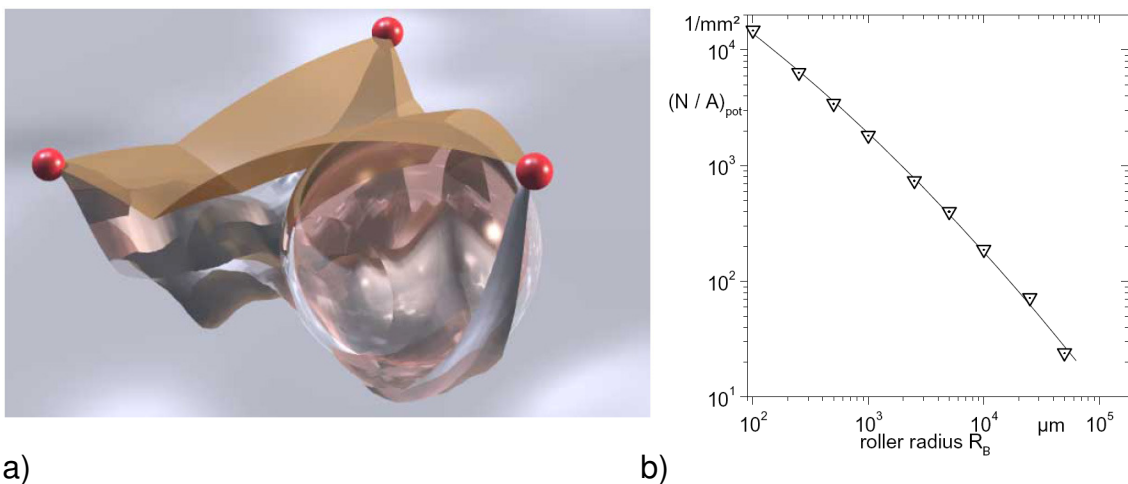


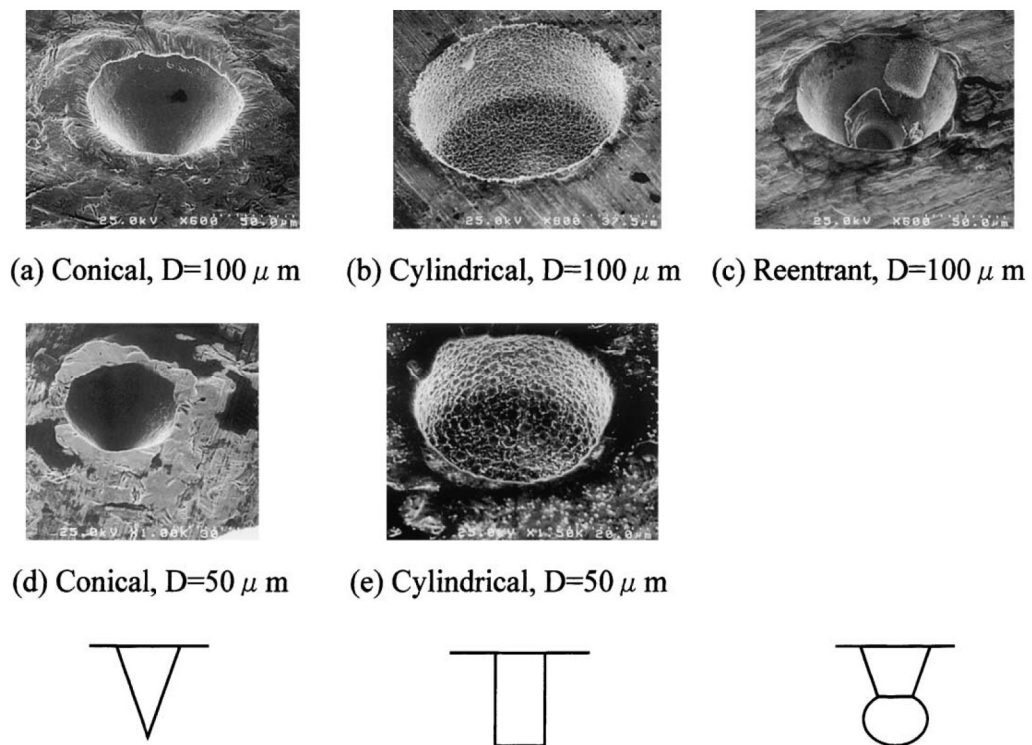
Figure 2.2.13: a) Definition of a cavity; b) Number of potential sites N/A_{pot} as function of the roller radius R_B [25].

Machined Microstructures

Technology development in machine treatment allows creating different kinds of subsurface structures with different characteristic sizes and complexity. Advantage of the machining is the relative cheapness and speed of the production process. However, the obtained structures are limited in linear scale to the size of the processing tool. For supporting the initial nucleation process and providing the largest possible amount of potential nucleation sites, machined surfaces must have the characteristic size of a structure element about the critical bubble radius, given by equation (2.1.1). Creation of such small microstructure is possible only with several new technologies, what will be considered later in the chapter.

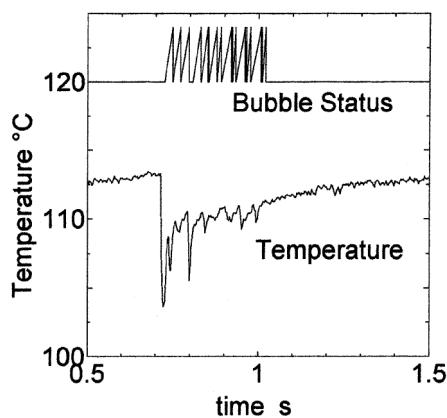
Artificial cavities

Artificial cavities are well known to intensify the heat transfer during surface boiling. Shoji and Takagi [34] have investigated bubbling features from a single artificial cavity of different micro geometries, Figure 2.2.14.



All cavities were manufactured on the surface of copper disk with 10 mm diameter and 0.1 mm thickness. Conical cavities were produced by pressing a diamond bit on the surface via a micro-hardness meter, and had diameters of 50 μm or 100 μm and depth of 30 μm or 50 μm correspondingly. Cylindrical cavities of same sizes were produced by the micro-electrical discharging machine. Reentrant cavities were produced by combination of those two means and had diameter of 100 μm and depth of 50 μm .

The apparatus of non-linear dynamics analysis was applied by Shoji and Takagi [34] to evaluate the experimental measurements of temperature under an artificial cavity. Using this type of analysis, Shoji and Takagi [34] have proved stable nucleation from cylindrical and reentrant cavities with low temperature oscillations. At the same time conical cavities demonstrated strong intermittence in bubbling phenomena and larger surface temperature fluctuations. Lowest superheats were required for boiling inception on surface with reentrant cavities. Conclusions of analytical results were confirmed by Shoji and Takagi [34] from visual observations, see Figure 2.2.15.



a)



b)

Figure 2.2.15: a). Temperature-time series for conical cavity $D=50 \mu\text{m}$, $P=1.7 \text{ W}$
 b). Bubbling from a conical cavity $D=100 \mu\text{m}$, $P=2.5 \text{ W}$ [34].

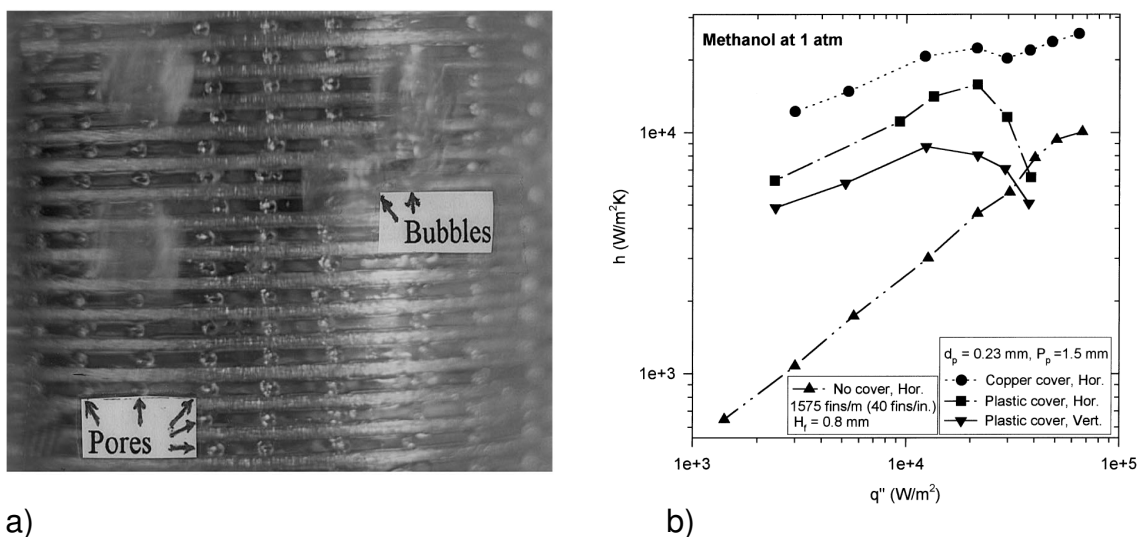
Although industrial use of enhanced surfaces with artificial cavities prepared with specific technologies described by Shoji and Takagi [34] seems to be questionable, some important insights are provided by them. In a case of

creation of a real enhancing heat transfer surface, cavities shapes and geometry optimization is required for every single application.

Subsurface channels

One of disadvantages of surfaces with artificial cavities, especially reentrant ones, is that they are hardly filled with liquid boiling at high heat fluxes. To overcome this problem the subsurface channels were proposed. They can act same way like reentrant cavities and at the same time supply neighboring cavities under the heat transfer surface with liquid.

Webb and Chien [36] have visualized the boiling process upon the enhanced surfaces with subsurface channels. They used a transparent cover to see what happens inside a subsurface tunnel. Photo of this process is presented in Figure 2.2.16a, some experimental data on heat transfer – in Figure 2.2.16b. For low heat fluxes ($q \leq 10 \text{ kW/m}^2$), the suction-evaporation mode of boiling occurs over 70-90% of the active tunnels. The remaining region has oscillating menisci. For higher heat fluxes evaporation on liquid menisci in the tunnel corners is the principal boiling mechanism for the surfaces with subsurface channels.



a) Saturated boiling on a vertical tube at 1 atm, $q = 5 \text{ kW/m}^2$;
 b) Boiling of methanol on the enhanced surface at 1 atm [36].

Several commercially available tubes with undersurface reentrant channels of different configurations were tested by Groll et al. [37], Figure 2.2.17:

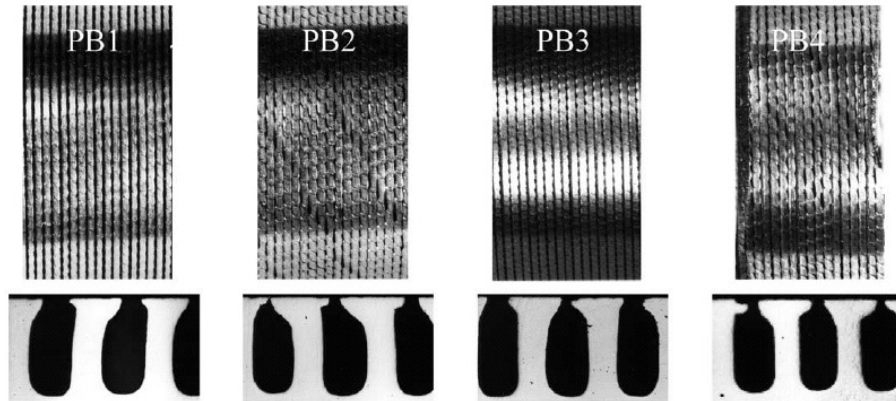


Figure 2.2.17: Surface topology of enhanced tubes (upper: structured surface; lower: corresponding sub-surface channels) [37].

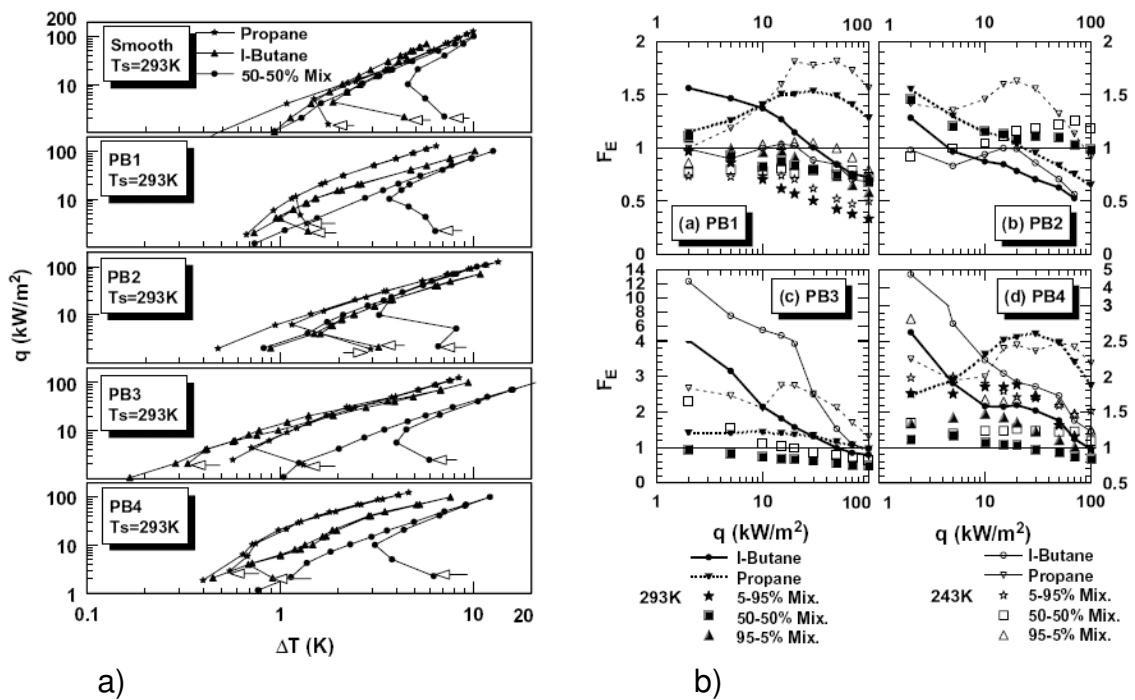


Figure 2.2.18: a) Boiling curves for increasing and decreasing heat fluxes; b) Improvement factor for four enhanced surfaces [37].

The experiments were conducted with propane, isobutane and their binary mixtures at saturation temperatures between 243 K and 293 K. Results of this investigation are presented in Figure 2.2.18.

Hysteresis was detected in all boiling regimes, as well as non-linearity in enhancement, compared with a smooth tube. In some boiling modes those enhanced surfaces exhibit even degradation of the boiling performance and have lower heat transfer coefficients than a smooth ones, Figure 2.2.18b. This effect is especially noticeable with boiling mixtures.

Fin pins

Pin finned surfaces make a new family of enhanced boiling surfaces. Guglielmini et al. [38] investigated boiling of saturated FC-72 on square cross-sectioned pin fin arrays with different configuration of the copper surface. Obtained by electro-discharging machine, pins were 3 mm or 6 mm long, 0.4 mm to 1.0 mm width, uniformly or non-uniformly spaced on the base copper surface, Figure 2.2.19.

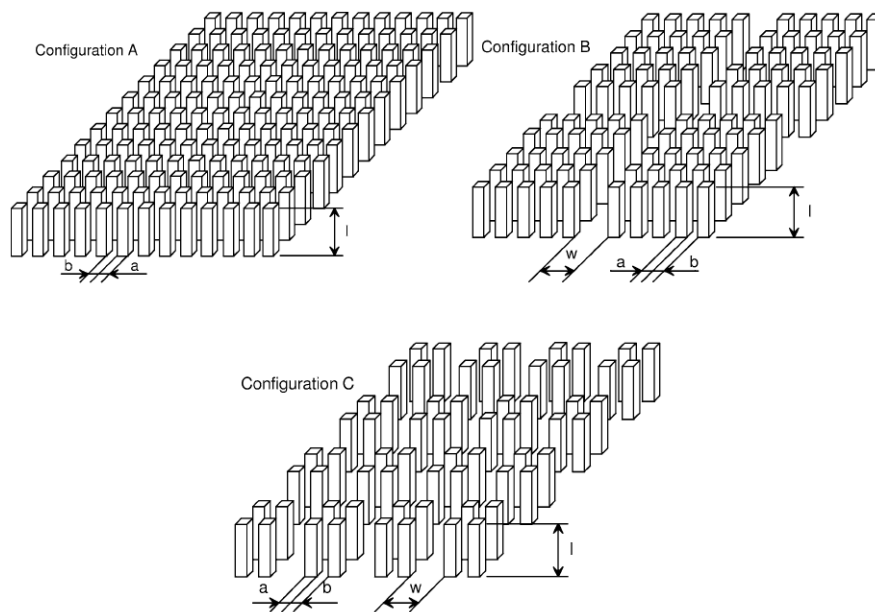


Figure 2.2.19: Configurations of extended surfaces [38]

It was found, that in the case of extended surfaces composed of uniformly spaced fins, longer fins appear to work slightly better, particularly in proximity to the maximum heat flux. When fin width and spacing decrease, the heat transfer rate increases, at high heat fluxes however the overall heat transfer coefficients reduce. At low heat fluxes, the finned surfaces show an appreciably higher overall heat transfer coefficient than a flat surface. All tested surfaces demonstrate strong non linear behavior in terms of heat transfer coefficients, Figure 2.2.20. This can be attributed to several factors, simultaneously affecting the bubbling phenomena. The large heat transfer surface generally leads to higher heat transfer coefficients. However reduction of the heat transfer area through decreasing the pins diameter and spacing leads to better wetting of the heat transfer surface.

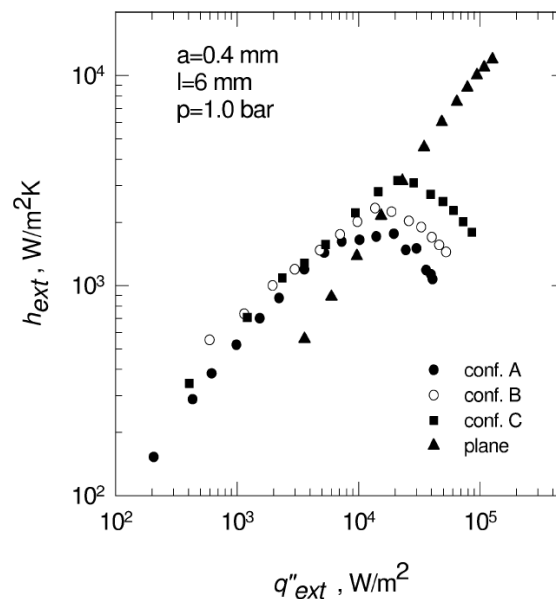


Figure 2.2.20: Effect of surface configuration on overall heat transfer coefficient, $p=1.0$ bar for fin pinned surfaces [38].

Surfaces, examined by Guglielmini et al. [38], had pins with spacing about 100 times larger as the critical vapor bubble diameter, obtained from equations (2.1.1) and (2.1.2). It means that the pins support the growing vapor bubbles rather than initial nucleation process. Non-linearity in performance makes a demand for geometry optimization for a certain application.

Etching

Mitrovic [4] has produced and tested the photo etched surfaces with the Refrigerant R11 (CF_2Cl_3) on a flat heater surface provided with artificial nucleation sites, Figure 2.2.21a. The surface cavities (diameter $180\ \mu\text{m}$, depth $120\ \mu\text{m}$, density $460\ \text{cm}^{-2}$, approximately) were arranged hexagonally. The walls of the cavities were not smooth but covered with a fine structure that largely governed the wall superheat.

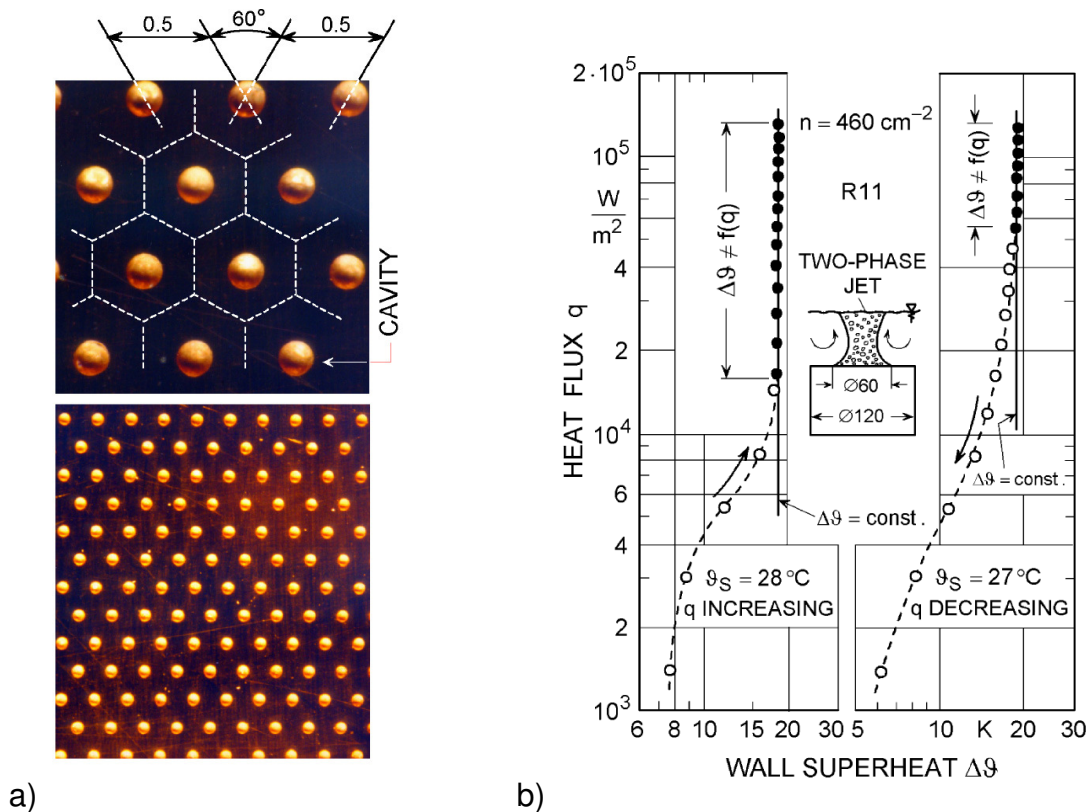


Figure 2.2.21: a) Cavity pattern on heating plate, tested with R11;
b) Boiling characteristic of the tested surface [4].

The constancy of the wall superheat has been observed at relatively high heat fluxes, Figure 2.2.21b. In the case of the increasing heat flux, the surface cavities were activated at nearly same heat flux. Bubbles detached almost simultaneously on the whole surface, resulting in a piston-like boiling oscillation. This boiling behavior was observed only in the horizontal orientation of the heating surface.

Honda et al. [39] have fabricated micro-pin-fins with the dimensions of several tens of microns on the surface of a square silicon chip ($10 \times 10 \times 0.5 \text{ mm}^3$) by using the dry etching technique. The surfaces were tested with nucleate pool boiling of degassed or gas-dissolved FC-72 at atmospheric pressure and subcoolings up to 45 K. Depending on etching conditions some pinned surfaces were additionally provided with the submicron scale roughness, Figure 2.2.22.

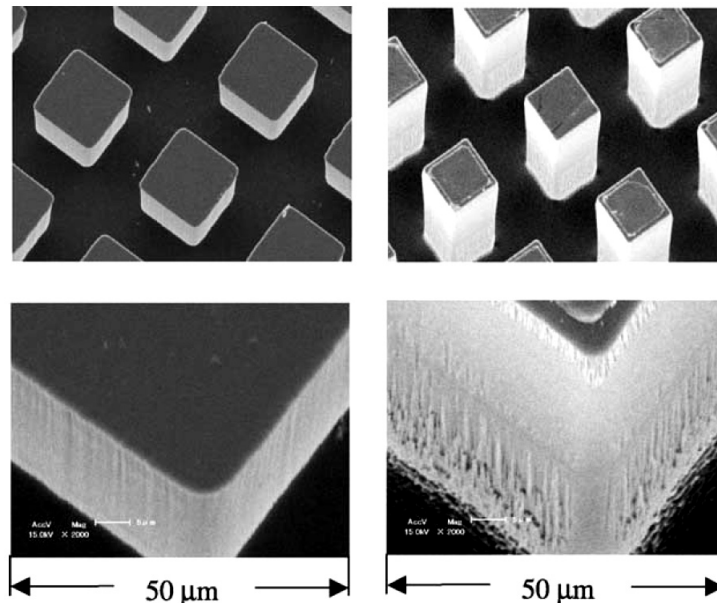


Figure 2.2.22: SEM view of silicon chips with micro-pin-fins [39].

The micro-pin-fins were effective in enhancing heat transfer in the nucleate boiling region and increasing critical heat flux. The boiling curve of the micro-pin-finned chip was characterized by a very sharp increase of the heat flux with increasing wall superheat. The slope of boiling curve was somewhat smaller for chip with the smallest fin height to fin pitch ratio, Figure 2.2.23. The wall superheat in the fully developed nucleate boiling region was lower for chips with larger surface roughness on the fin flank. For the chips with high fins, however, the boiling curve showed a bend in the high heat flux region and the slope decreased significantly. The wall temperature at the CHF point was always less than the upper limit ($\approx 85 \text{ }^\circ\text{C}$) for a reliable operation of LSI chips.

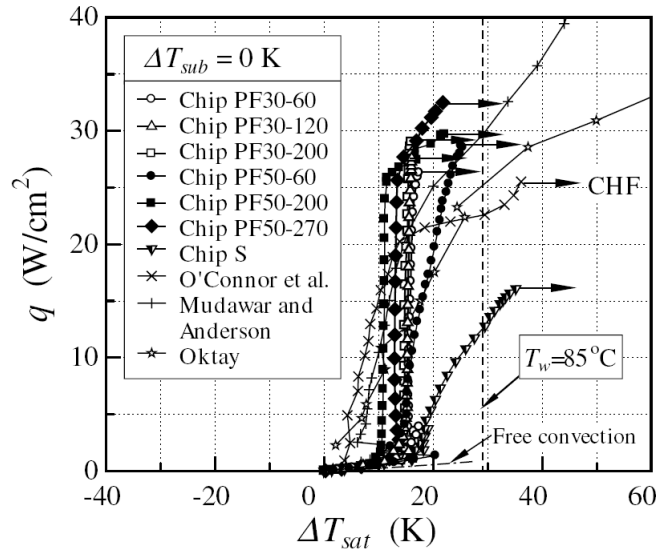


Figure 2.2.23: Comparison of boiling curves; $\Delta T_{sub} = 0$ K, degassed [39].

The enhancing etching technology of Honda et al. [39] although provides almost constant wall superheats in the nucleate boiling mode, is applicable only for silicon surfaces. The analogous technology exists, however, for metallic surfaces and will be considered further below in the article.

Laser drilling

The last direct surface treatment technique mentioned in this review is machining of mini- and microchannel boiling by laser drilling. Kandlikar et al. [40] generated by this technique micro cavities on the base copper surface, Figure 2.2.24. Investigation was aimed to study flow instabilities caused by nucleation in a channel so results were not presented in terms of the heat transfer. Therefore, it could be an interesting topic for future investigations. Although laser drilling was used for silicon surfaces (Hwang and Moran [41]), an industrially applicable technology is not available until recent. However, applying laser techniques results in a local melting of base material, so that the solidification of the melt usually leads to smooth surfaces on the micro-scale, which are less effective in nucleate boiling.

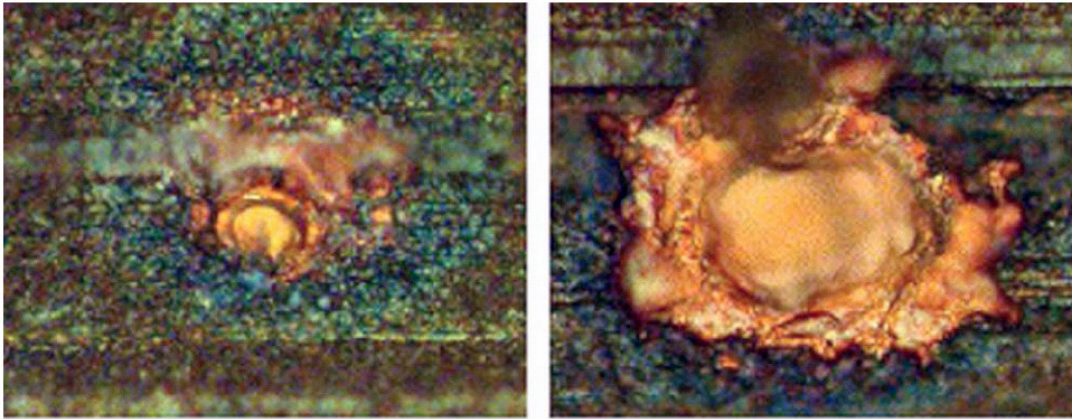


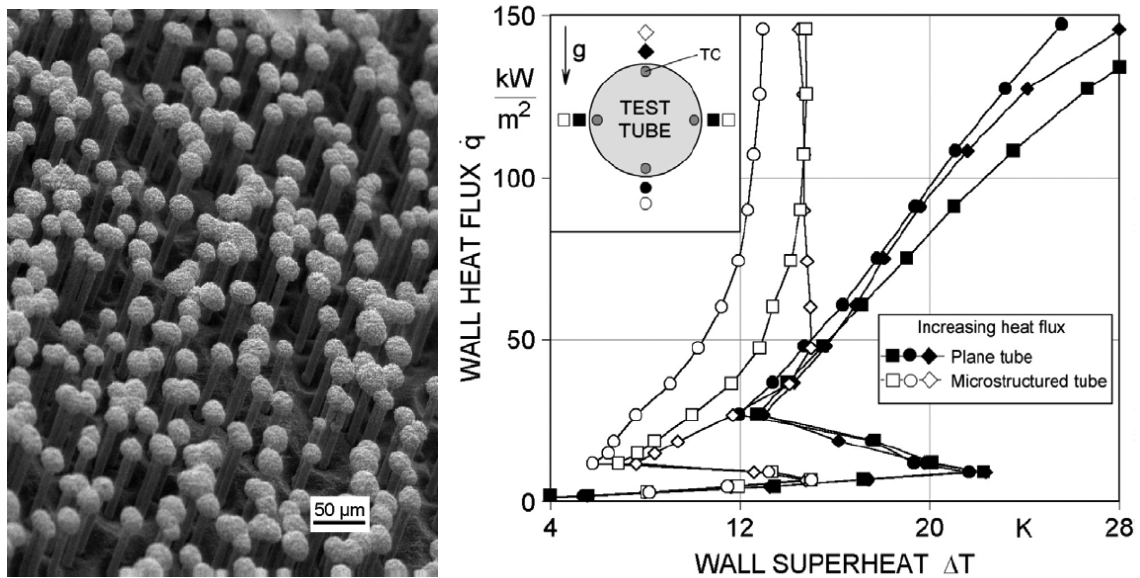
Figure 2.2.24: Laser drilled holes on microchannel surface [40].

- a) average diameter of 8 μm
- b) average diameter of 22 μm .

Combined methods

The last group of enhanced surfaces for boiling in accordance with the classification, illustrated in Figure 2.2.1 consists of surfaces, obtained with combined methods of treatment. Some methods mentioned above are the combined methods themselves, as almost every modern treatment technology is not simple and involve several different steps of fabrication.

An example of successful application of combined methods is the enhanced surface, described by Mitrovic et al. [26]. The microstructure production process involves ions bombardment, UV-irradiation combined with etching and galvanization steps. As this particular surface was investigated in the presented work, it will be described in more details below. However, some preliminary results can be obtained from Mitrovic et al. [26]. The structure consisting of cylindrical pins as basic elements is depicted in Figure 2.2.25a. To test the efficiency of the structure, the outer surface of a tube has been provided with such a structure and used in pool boiling experiments with the refrigerant R141b at atmospheric pressure. Obtained results show the heat flux to remain independent of the wall superheat in the fully developed boiling region, Figure 2.2.25b.



a)

b)

Figure 2.2.25: a) SEM-photo of the novel microstructured surface;
b) Boiling curves of plane and structured tube surfaces [26].

This microstructure, obtained with the combined enhancing method meets several requirements outlined in the introduction simultaneously and seems to be suitable for nucleate boiling in general, and especially for keeping the heating surface largely isothermal, despite the variation of the heat flux.

2.3. Task for investigation

The classification system for enhanced surfaces was proposed above basing upon common properties of different enhancement methods and consideration of basic physical principles governing the nucleation. Majority of existing surface enhancers for nucleate boiling were considered with pro and contra basing the proposed classification system.

Modified surfaces can enhance the boiling heat transfer either supporting the initial nucleation which is a probabilistic phenomenon, or by enlarging the length of TPL after a vapour bubble had been created and started to grow. To judge about certain way of enhancement for a real modified surface, a characteristic geometry scale of structure is proposed to calculate using the

fractal dimension. This quantity seems to be the universal one and applicable for different kind of microstructures, unlike the roughness parameter.

The new microstructures developed by Mitrovic et al. [4-6, 26] must be investigated in more details. It can meet simultaneously all requirements, show to enhanced surfaces, after the proper optimization of its microstructure geometry. The task for the present investigation is to produce several microstructured surfaces with different geometry and test them with several liquids. This investigation must show the effects of:

- microstructure geometry,
- system pressure,
- liquid properties

on the boiling heat transfer. Experiments must be conducted for nucleate pool boiling mode with heat fluxes below critical values.

3. EXPERIMENTAL

3.1. Experimental apparatus

Experimental installation

To accomplish the planned investigation, an apparatus developed by Mitrovic and Fauser [43] was modified and used to investigate heat transfer from the microstructured surface with pool boiling. It represents a closed loop for the test fluid, Figure 3.1.1. The test tube was horizontally arranged in the test liquid in the container A. Below this container, a pre-heater D was situated to ensure the saturation state of the condensate leaving the condenser B. Bubbles generated by the pre-heater were channeled along the inside surface of the test container, without any effect on the boiling inception or heat transfer on the test tube. Evaporator C was used to rise and regulate the system pressure.

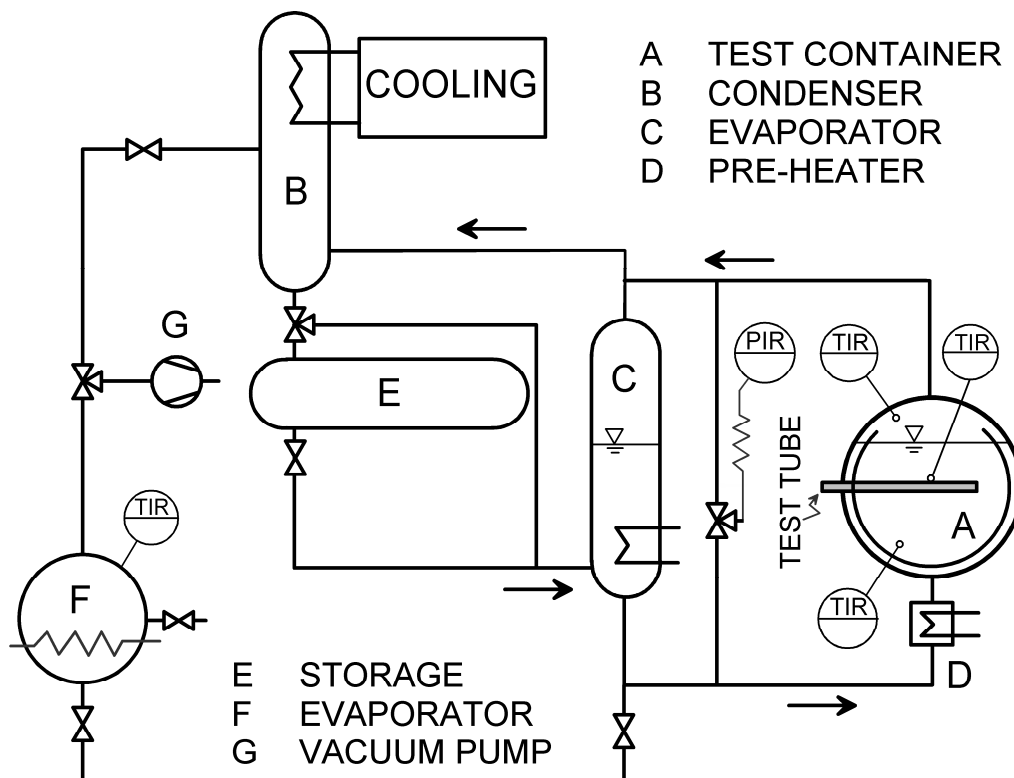


Figure 3.1.1: Principal schema of the test apparatus.

To change the test tube in the apparatus, storage tank E for liquid was used. Filling of the installation with liquid was done by distillation using vacuum pump G, the evaporator F and the condenser B.

With exception of the test tube and the glass windows in the container A, all parts of the apparatus were made of stainless steel. Thermal interaction of the apparatus and the surroundings was sufficiently damped by insulation, Figure 3.1.2. The installation allows conduction experiments at pressures between ≈ 0 bar and 10 bar and saturation temperatures between 0° and 120° .

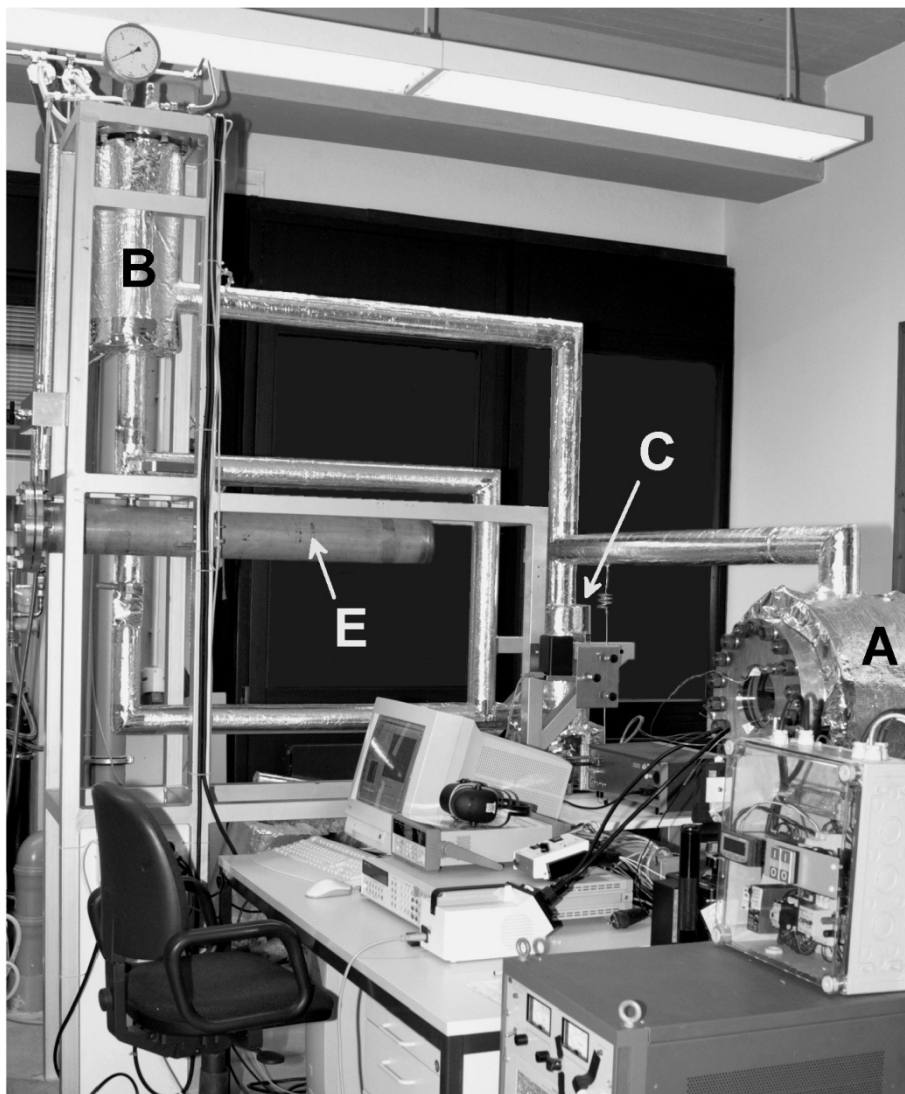


Figure 3.1.2: Photo of the experimental installation.

Test Tube

A copper tube of 18 mm outer diameter was used as the test tube. It was provided with a heating cartridge, Figure 3.1.3. Holes for thermocouples (chromel-alumel, jacket diameter 0.5 mm) were generated by electrolytic deposition. For this purpose, 4 channels of 0.6 mm depth and 0.6 mm width were milled equidistantly on the tube circumference, and a PTFE-tubing (outer \varnothing 0.6 mm) were placed into each channel along the whole length. In a successive galvanization process, an about 1.5 mm thick copper layer was deposited on the outer tube surface. The PTFE-tubing, embedded into this layer, were then pulled in the axial direction, thus decreasing their diameter, and withdrawn. After machining and polishing the tube, its diameter was determined and the microstructure was generated on its outer surface as illustrated in Figure 3.1.4. The average tube diameter was 18.2 mm.

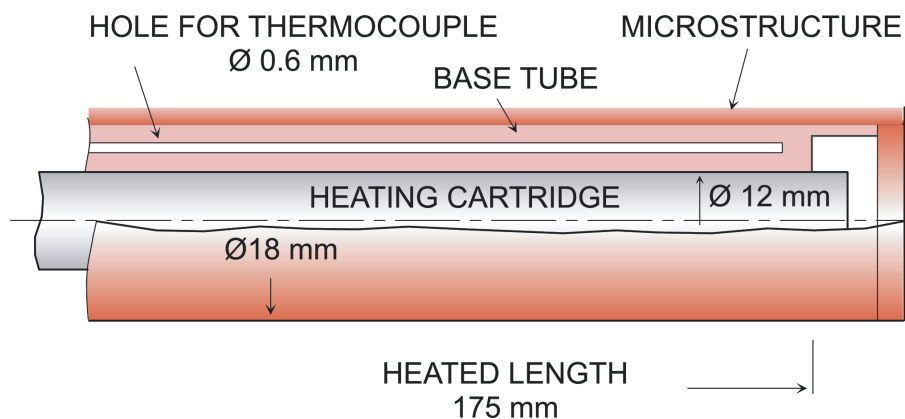


Figure 3.1.3: Construction of the test tube.



Figure 3.1.4: Photo of the test tube A428, provided with microstructure.

The test tube was provided with 2 kW heating cartridge coaxially placed inside of it. Connected to the DC power supply (HP 6479C), this arrangement allows heat fluxes up to 175 kW/m^2 . The heat flow rate was obtained by measuring the voltage and current, the latter by using a $20 \text{ m}\Omega$ standard shunt. To measure the wall temperature, four thermocouples were positioned underneath the surface structure on the top, bottom and sides of the test tube with junctions in the middle of the heated length. One of the side thermocouples was used for safety purposes and operated by a separate relay, disconnecting the power supply at specified wall temperature, thus preventing film boiling. Two thermocouples were located in the liquid and vapor to control their states and to obtain the wall superheat. All of the thermocouples were calibrated by using a standard PT100 resistance thermometer. The temperature in the vapor phase was measured additionally by a calibrated PT100 resistance thermometer that also served for controlling purposes.

In each experimental run, the following signals were taken: one pressure signal, 5 thermocouples voltages (3 in the test tube, 1 in the liquid and 1 in the vapor), PT100 electrical resistance, voltage and current of the tube heating cartridge, and voltage and current of additional cartridge heaters in the evaporator C. These signals were recorded using the Agilent 3458A multimeter via a nanovolt switch, and proceeded to a PC.

Creation and properties of microstructures

The microstructure investigated in the present work, has been developed in cooperation with a partner from industry, company “ μ -Technik” (earlier “SDK-Technik”) from Quedlinburg, Germany and Joint Institute for Nuclear Research from Dubna, Russia. The microstructure consists of cylindrical pins as basic elements with diameters of $0.1 \text{ }\mu\text{m}$ to $25 \text{ }\mu\text{m}$, heights of $10 \text{ }\mu\text{m}$ to $100 \text{ }\mu\text{m}$, while the number density of the pins can be varied from $1 \times 10^4 \text{ cm}^{-2}$ to $1 \times 10^9 \text{ cm}^{-2}$. The structure can be easily generated on cylindrical specimens like tubes in almost all electrochemically depositable materials.

The main steps of the microstructure production are illustrated in Figure 3.1.5. The very first step is the irradiation of a thin (less than 100 μm) polycarbonate foil with heavy ions. Passing through the foil, ions break intermolecular bindings on their way, leaving behind the so-called ion traces. These traces are then widened to pores by a combination of UV-irradiation and chemical etching processes. The density, the inclination and the diameter of the pores can be altered by variation of the density and the inclination of the ion beam and the post-processing duration, respectively. Preparation and processing of polycarbonate foil was done in the Laboratory for Nuclear Reactions of Joint Institute for Nuclear Research in Dubna, Russia.

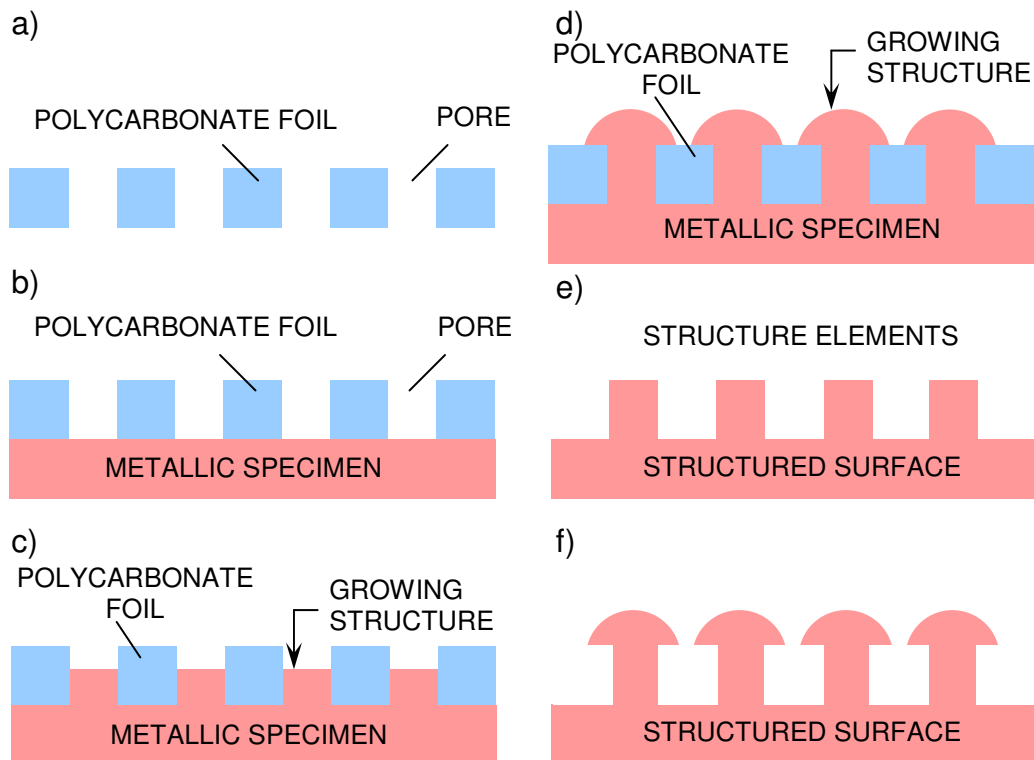


Figure 3.1.5: Microstructure generation steps: (a) Preprocessed polycarbonate foil, (b) foil attached to a specimen, (c) electrodeposition process, (d) structure elements with torospherical tops, (e) and (f) structure after foil stripping.

To generate a structure, the prepared foil is attached to the specimen and the ensemble is subjected to an electrolytic process, in which the pores become filled by ion deposition. In a further etching step, the foil is completely

removed, leaving behind pins metallically connected to the surface of the specimen. The height of the pins can be varied by the duration of the electrodeposition, but is limited by the foil thickness. Appropriate managing of the galvanic deposition may result in different shapes of tops of the elements. The whole process permits an almost continuous variation of the structure dimensions. As an example, Figure 3.1.6 illustrates structure obtained in this way. These photos show the structures generated under the same conditions as the ones actually used in experiments. Microstructures with such properties can be generated in almost all electrochemically depositable materials. For the purposes of the present investigation, both the base surface (tube) and the generated structure were made of copper because of its high thermal conductivity and advantages regarding the electrodeposition.

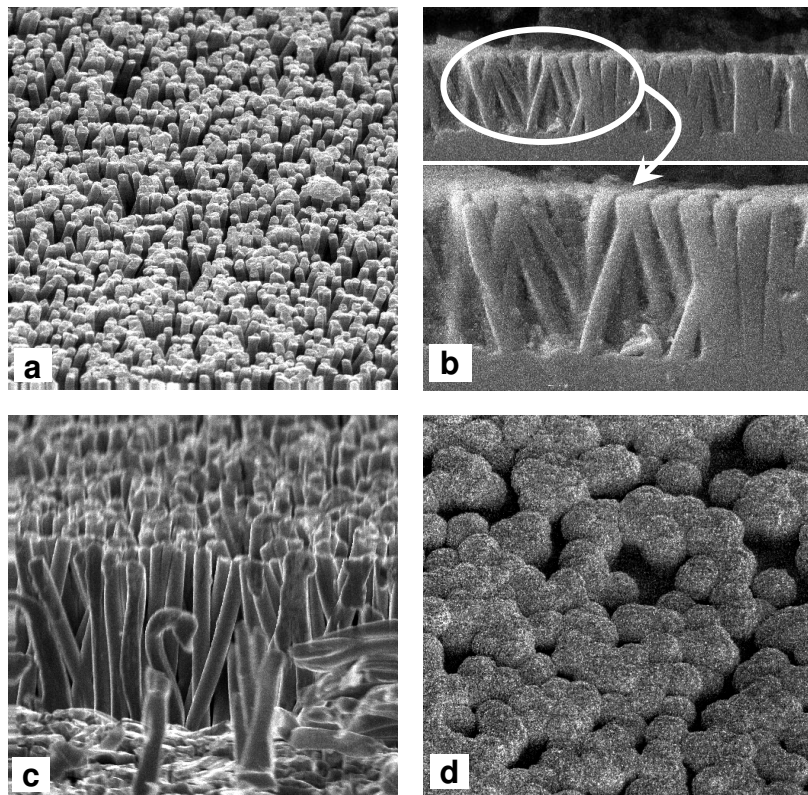


Figure 3.1.6: Photos of some of microstructures used in the experiments [5].

- a) structure A4 28, zoom 500x;
- b) structure A4 28, zoom 500x (upper image), 1000x (lower image);
- c) structure A4 28, zoom 1000x (side view);
- d) structure A4 18, zoom 1000x.

Table 3.1 lists some geometry properties of the structures used in the experiments. The diameter of the pins varied from 3.4 μm to 17.8 μm at pins densities up to $5 \cdot 10^6 \text{ cm}^{-2}$. The inclination of the pins is measured with respect to the normal of the bare surface.

Table 3.1: Geometrical parameters of tested surfaces.

Structure	Pins height μm	Pins density cm^{-2}	Pins diameter μm	Structure volumetric porosity %	Pins inclination angle degree
A4 01	74	$1.17 \cdot 10^6$	4.5	18	0
A4 18	68	$1.2 \cdot 10^5$	11.7	13	0
A4 19	64	$5.6 \cdot 10^5$	8.5	31	0
A4 25	51	$7.6 \cdot 10^5$	7.63	34	± 15
A4 26	44	$1.3 \cdot 10^5$	17.8	33	± 15
A4 27	51	$5.7 \cdot 10^5$	8.2	30	± 25
A4 28	55	$5.0 \cdot 10^6$	3.5	46	± 20
A4 31	60	$2.6 \cdot 10^6$	3.4	24	± 45
A4 32	59	$2.6 \cdot 10^6$	3.5	25	+45
A4 35	49	$4.6 \cdot 10^5$	9.5	34	± 45
A4 37	58	$3.3 \cdot 10^6$	3.7	37	+40 / -13

3.2. Measuring procedure

The evacuated apparatus was filled by distillation of the test liquid. Traces of remaining air were removed by venting the condenser at elevated pressure. The measurements were started after the system has reached equilibrium. The voltage at the cartridge heater in the test tube was first increased in steps of 10V from 0V up to 200V (heat flux up to 125 kW/m²) and then decreased in steps of 25V back to zero. In order to ensure the steady-state after the boiling inception, the voltage increase was suspended for a while. To maintain this state during one experimental run, the coolant temperature and/or the coolant flow rate in the condenser was adjusted according to the variation of the heat flux. System pressure and temperature were varied by changing the energy input (preheater D, test tube, evaporator C) and by changing the coolant temperature or its mass flow rate through the condenser B, Figure 3.1.1. The saturation temperature was kept constant within ± 0.05 K in each experimental run. On reaching the steady-state at the chosen heat flux, all signals were taken and saved to a file for further processing.

The experiments were performed in nucleate boiling mode with refrigerant R141b at pressures of 1 bar to 5 bar (saturation temperatures 32°C to 87°C, respectively) in steps of 1 bar, with refrigerant R134a at pressures of 5 bar to 9 bar (saturation temperatures 16°C to 36°C, respectively) and with highly wetting liquid FC-3284 at pressures of 0.5 bar to 1.5 bar (saturation temperatures 29° to 62°, respectively) in steps of 0.5 bar. The critical temperature of the refrigerant R141b is 208.3°C, the critical pressure 44 bar, those of R134a are 101.1 °C and 40.6 bar, respectively and estimated values of FC-3284 are 160°C and 31 bar. Refrigerants were provided by company Solvay Solkane, and FC-3284 was supplied by company 3M. The liquid properties were guaranteed to be stable by the producers.

3.3. Estimation of measuring uncertainties

The uncertainties of measurements were estimated by the method of Kline and McClintock [47] for heat flux and temperature. Full measuring

uncertainty consists of two parts, systematical and accidental ones. For heat flux it is found as mean square:

$$\delta q = \sqrt{(\delta q_{\text{sys}})^2 + (\delta q_{\text{acc}})^2} \quad (3.3.1)$$

Measurements of the heat flux on the test tube were indirect, i.e. voltage U and current I were measured, using Agilent 3458A digital multimeter, and length L and diameter D of the test tube were measured, using the micrometric device. The heat flux was found as:

$$q = \frac{U \cdot I}{L \cdot \pi \cdot D} \quad (3.3.2)$$

The systematical uncertainty appears always, despite the number of conducted experiments, because it arises due to the procedure of measurement. For the heat flux measurements it is expressed by the equation (3.3.2). Therefore, the relative systematical uncertainty is found as:

$$\delta q_{\text{sys}} = \sqrt{(\delta U)^2 + (\delta I)^2 + (\delta D)^2 + (\delta L)^2} \quad (3.3.3)$$

In accordance with specification of the multimeter manufacturer, the relative measuring uncertainty of voltage and current is given by:

$$\delta U = (14 \cdot U_{\text{Max}} + 3 \cdot U_{\text{Range}}) \cdot 10^{-6} \quad (3.3.4)$$

$$\delta I = (14 \cdot I_{\text{Max}} + 3 \cdot I_{\text{Range}}) \cdot 10^{-6} \quad (3.3.5)$$

where U_{Max} and I_{Max} are maximal values, measured in experiment, and U_{Range} and I_{Range} are corresponding measuring ranges of the multimeter. For conducted experiments these values are: $U_{\text{Max}} = 3.5 \text{ mV}$; $U_{\text{Range}} = 100 \text{ mV}$ for voltage, and $I_{\text{Max}} = 6.7 \text{ A}$; $I_{\text{Range}} = 9 \text{ A}$ for current. Correspondingly, relative uncertainties of measurements are: $\delta U = 0.0349 \%$ and $\delta I = 0.0121 \%$.

For analogue measurements with a micrometric device, the absolute uncertainty is equal to a half of the scale interval, what results in relative uncertainties for tube diameter and length of $\delta D = 0.56 \%$; $\delta L = 0.29 \%$. Using equation (3.3.3) and values of relative uncertainties, listed above, one finally

obtains the relative systematical uncertainty of the heat flux measurements equal to $\delta q_{\text{sys}} = 0.63 \%$.

The accidental part of the measuring uncertainty is determined by the number of conducted measurement, and it obeys Student's t-distribution. It occurs due to numerous chaotical factors, influencing the measuring procedure. For measurements of the heat flux, the cumulative probability of 99.5% was taken, and the corresponding Student's coefficient of 4.604 was used for calculation of the accidental uncertainty for 5 measurement. Then one obtains the accidental part of the measuring uncertainty of the heat flux of $\delta q_{\text{acc}} = 1.29 \%$. Therefore, the full measuring uncertainty of the heat flux in accordance with equation (3.3.1) is equal to $\delta q = 1.44 \%$.

Heat losses in axial directions of the test tube were ignored, as the heat generation was homogenous along the cartridge length (except for the cold ends) and the thermocouples were arranged in the middle of the heated tube section. Due to special construction of the tube, the end losses did not affect the temperature field in the middle of the tube. More information about estimation of the axial losses can be obtained in Hartmann [54].

Tube wall and fluid bulk temperatures systematical uncertainties can be attributed to the errors arising from thermocouple calibration by a platinum resistance thermometer and thermocouple resolution. The resistance of the thermometer was measured by the digital multimeter Agilent 3458A, and the corresponding relative uncertainty is given by the following relation:

$$\delta R = (15 \cdot R_{\text{Max}} + 1 \cdot R_{\text{Range}}) \cdot 10^{-6} \quad (3.3.6)$$

Using corresponding $R_{\text{Max}} = 135 \Omega$; $R_{\text{Range}} = 1000 \Omega$ the systematical uncertainty of $\delta R = 0.3025 \%$ is obtained. The systematical uncertainty of temperature measurements is given by:

$$\delta T_{\text{sys}} = \sqrt{(\delta R)^2 + (\delta U)^2} \quad (3.3.7)$$

Substituting numerical values into equation (3.3.7) one obtains the relative systematical uncertainty of temperature measurement of $\delta T_{\text{sys}} = 0.31\%$. The corresponding accidental uncertainty is $\delta T_{\text{acc}} = 0.64\%$, and the full uncertainty of temperature measurements is $\delta T = 0.71\%$. Therefore, the full measuring uncertainty of measurements of temperature difference is $\delta\vartheta = 1.42\%$.

Pressure was measured directly, using the piezo-electrical device Althen 1000-200. The full relative uncertainty in accordance with the manufacturer specification is 0.01% with the maximal measureable pressure of 13.8 bar.

3.4. Experimental program

Three liquids, refrigerants R141b and R134a, and a highly wetting liquid FC-3284, were used at overall pressure range from 0.5 bar up to 9 bar. Table 3.2 gives an idea about the accomplished experimental program. A cross in Table 3.2 means a conducted measurement for the given conditions. Experimental results were obtained as boiling curves for three thermocouples positions underneath the test tube surface: top, side and bottom. Pressure curves (i. e. dependence of surface superheat on applied pressure at a constant heat flux) were obtained as well, Table 3.2.

In experiments single tubes provided with different microstructures were tested as well as tandem tubes, arranged in the same vertical plane one below the other, Figure 3.4.1. The measurements with tandem tubes were aimed to obtain the effect of rising two-phase flow generated by the lower tube on heat transfer of the upper tube (Table 3.3). In this case the following experimental procedure was employed:

- a) The heat flux on the upper tube was varied at several different heat fluxes fixed on the lower tube.
- b) The heat fluxes of both tubes were varied simultaneously.

c) Several different heat fluxes on the upper tube were kept constant and that on the lower tube was varied, i.e. the mirrored experiment to case a) was undertaken.

Experiments a) and c) modeled the situation when a real heat exchanger with microstructured tubes would be working in a non-stationary mode. It is possible in transition “start and stop” regime. Experiment b) modeled more common in industry case of stationary long time operation.

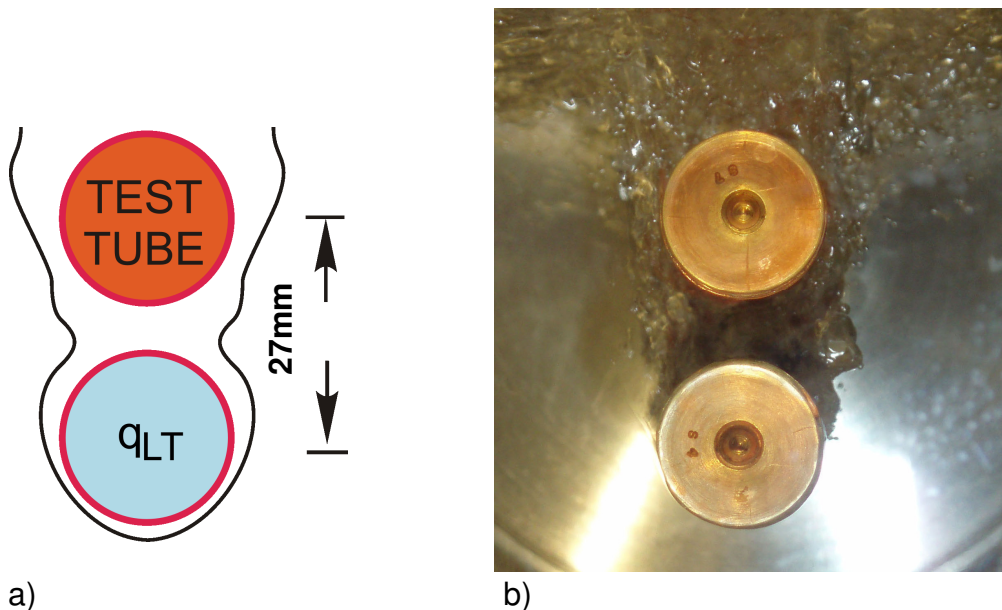


Figure 3.4.1: Tandem tubes configuration:

- a) Sketch of the arrangement,
- b) Photo of the modified experimental installation.

To estimate the microstructure efficiency the enhancement factor was calculated. It is determined as ratio of the heat transfer coefficient measured in experiments to the heat transfer coefficient, calculated in accordance with recommendations of VDI Heat Atlas [44] for a smooth tube under the same conditions. As experimental the spatial-temporal average value of three heat transfer coefficients on the test tube circumference was used. Values were taken for increasing and decreasing heat fluxes. Closed symbols on figures correspond to increase of heat flux while opened symbols – to decrease of it.

Table 3.2: Conducted experiments with single tubes.

Tube Nr.	R141b							
	Pressure p, bar							
	1.0	2.0	3.0	4.0	5.0			
A4 18	x	x						
A4 28	x	x	x	x	x			
Tube Nr.	FC-3284			R134a				
	Pressure p, bar							
	0.5	1.0	1.5	5.0	6.0	7.0	8.0	9.0
A4 28	x	x	x	x	x	x	x	x
A4 19				x	x	x	x	x
A4 01				x	x	x	x	x
A4 37	x	x	x	x	x	x	x	x
A4 35	x	x	x	x	x	x	x	x
A4 31	x	x	x	x	x	x	x	x
A4 32	x	x	x	x	x	x	x	x
A4 25	x	x	x	x	x	x	x	x
A4 26	x	x	x	x	x	x	x	x
A4 27	x			x	x	x	x	x
Tube Nr.	R134a							
	Heat flux q, kW/m ² (pressure as parameter)							
	10		30		70		120	
A4 19	x		x		x		x	
A4 01	x		x		x		x	

Table 3.3: Conducted experiments with tandem tubes.

Tandem A4 25 +		R134a													
		p = 5 bar				p = 7.5 bar				p = 9 bar					
		$q_{LT} = q_{Test\ tube}$	$q_{LT} = 8\ kW/m^2$	$q_{LT} = 50\ kW/m^2$	$q_{LT} = 125\ kW/m^2$	$q_{Test\ tube} = 8\ kW/m^2$	$q_{Test\ tube} = 32\ kW/m^2$	$q_{Test\ tube} = 125\ kW/m^2$	$q_{LT} = q_{Test\ tube}$	$q_{LT} = 8\ kW/m^2$	$q_{LT} = 50\ kW/m^2$	$q_{LT} = 125\ kW/m^2$	$q_{Test\ tube} = 8\ kW/m^2$	$q_{Test\ tube} = 32\ kW/m^2$	$q_{Test\ tube} = 125\ kW/m^2$
A428		X	X	X	X	X	X	X	X	X	X	X	X	X	X
A437		X	X	X	X				X	X	X	X			
Tandem A4 25 +		FC-3284													
		p = 0.5 bar				p = 1.0 bar				p = 1.5 bar					
		$q_{LT} = q_{Test\ tube}$	$q_{LT} = 8\ kW/m^2$	$q_{LT} = 50\ kW/m^2$	$q_{Test\ tube} = 32\ kW/m^2$	$q_{LT} = q_{Test\ tube}$	$q_{LT} = 8\ kW/m^2$	$q_{LT} = 50\ kW/m^2$	$q_{Test\ tube} = 32\ kW/m^2$	$q_{LT} = q_{Test\ tube}$	$q_{LT} = 8\ kW/m^2$	$q_{LT} = 50\ kW/m^2$	$q_{Test\ tube} = 32\ kW/m^2$	$q_{LT} = q_{Test\ tube}$	$q_{LT} = 8\ kW/m^2$
A428		X	X	X	X	X	X	X	X	X	X	X	X	X	X
A437		X	X	X	X				X	X	X	X			

4. RESULTS AND DISCUSSION

Numerical results of experiments are given in the Appendix in tabular form. Listed are the values of the heat flux and the wall superheat. These results will be illustrated as examples in the following.

4.1. Experiments with single tubes

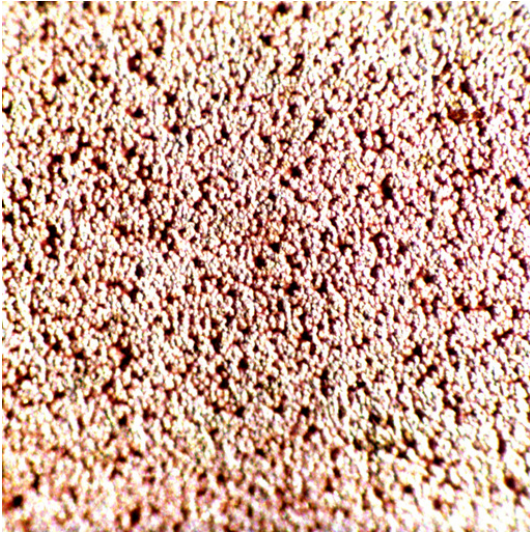
Refrigerant R141b

The refrigerant R141b ($\text{CCl}_2\text{F-CH}_3$) is a high-purity colorless liquid at atmospheric pressure, which is slightly ethereal, has a wide range of applications. Because of its low gas phase thermal conductivity R141b is the best available replacement to R11 in many applications. Compared to R11, R141b is approximately ten times less harmful to stratospheric ozone and is therefore recognized as a viable solution allowing the rapid phase-out of CFCs. R141b has a more polar molecule than R11, and therefore has a slight solvent effect. The result is a slightly weaker inferior dimensional stability when R11 is simply substituted by R141b. This HCFC is not categorized as toxic according to the Dangerous Substances Regulations. R141b is compatible with the most commonly used metals and alloys due to its very high stability.

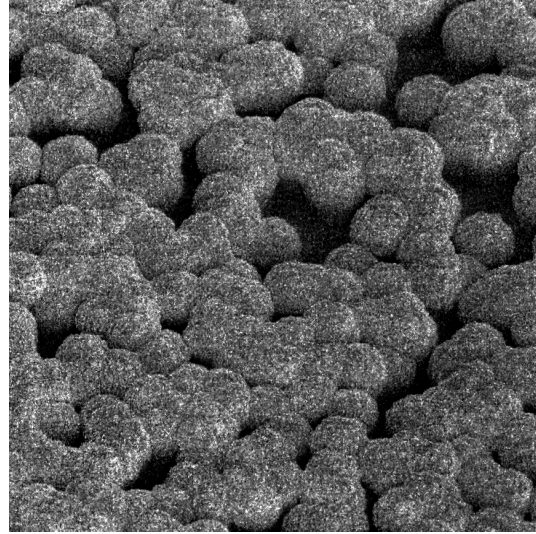
Microstructure A418

Microstructured surface A418 was used as a reference for the further experiments. Photographs of this structure obtained with SEM and a magnifying microscope are presented in Figure 4.1.1. Pins of this microstructure had hemispherical tops, obtained at longer galvanization time (see Chapter 3.1).

This microstructure has shown relatively low boiling inception superheats between 6 K and 10 K at heat fluxes about 5 kW/m^2 , and weak dependence of the surface superheat on the applied heat flux in the developed boiling mode, Figure 4.1.2.



A418 zoom 64x



A418 zoom 500x

Figure 4.1.1: Photos of the microstructure A418.

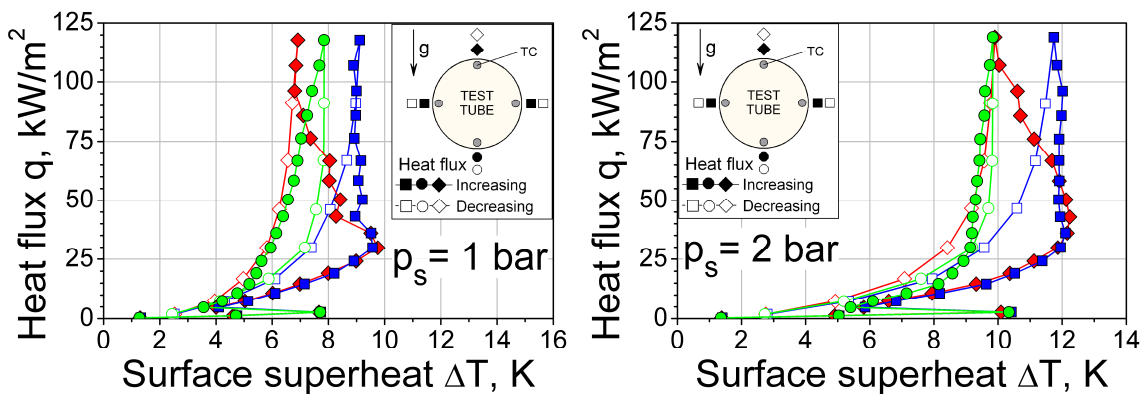


Figure 4.1.2: Boiling characteristics of A418 with R141b at 1 bar and 2 bar.

At heat fluxes above 30 kW/m^2 the surface superheat remains practically constant, i.e. unaffected by the heat flux. For the top of the tube an interesting effect was observed, namely the temperature decrease with the increased heat flux. The superheat at the top forming of the tube has decreased from 10 K down to 6 K at 1 bar and from 12 K to 9 K at 2 bar, Figure 4.1.2. This effect was later observed for other surfaces too, and it will be discussed below in more details. Figure 4.1.3 represents photographs of the surface at boiling inception and the maximal heat flux. It seems that the microstructured surface serves large amount of nucleation sites, thus promoting nucleate boiling strongly.



a)



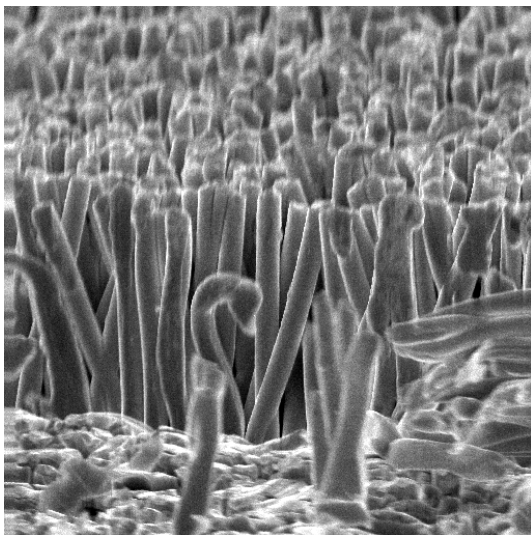
b)

Figure 4.1.3: Boiling of R141b on the structure A418, $p = 2$ bar:

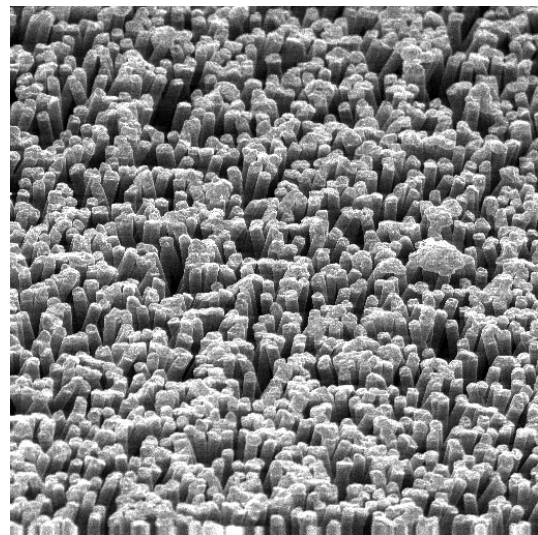
- a) $q = 4.8 \text{ kW/m}^2$;
 b) $q = 120 \text{ kW/m}^2$.

Microstructure A428

Figure 4.1.4 depicts SEM photos of structure A428 which was tested with R141b boiling at pressures in range between 1 bar and 5 bar with 1 bar step. Experimental results of those tests are represented at Figure 4.1.5.



A428 zoom 1000x



A428 zoom 500x

Figure 4.1.4: SEM photos of the microstructure A428.

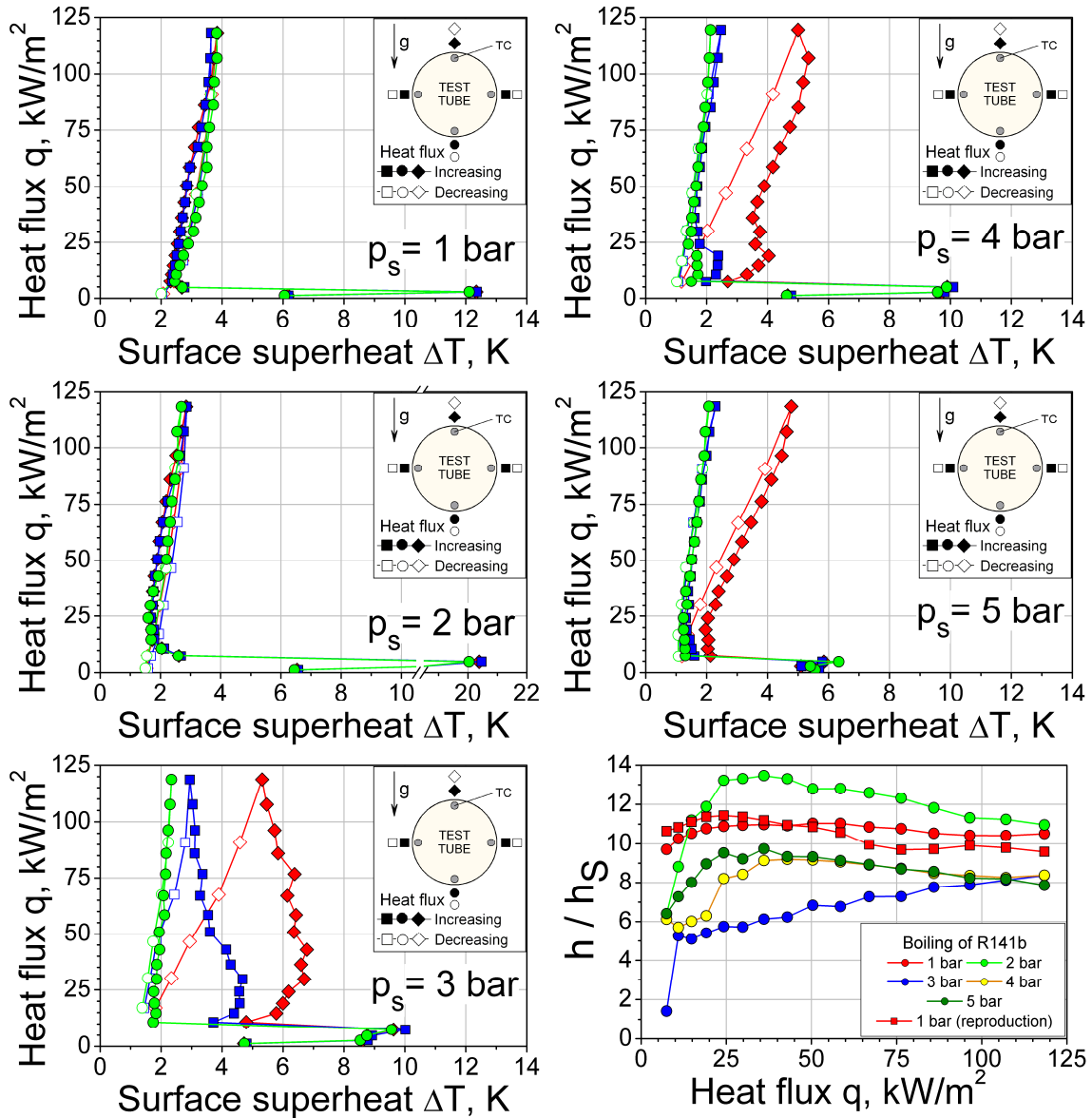


Figure 4.1.5: Boiling characteristics of A428 with R141b at different pressures.

Boiling inception of R141b on the microstructure A428 occurred at superheats in range between 5 K and 20 K and heat flux about 5 kW/m². After boiling establishment the whole boiling surface was homogeneously covered with vapor bubbles. Some visual impressions of boiling events are documented on photographs in Figure 4.1.6. Vapor bubbles of diameters ranging from 50 μ m to 1 mm were observed on the surface. Individual vapor bubbles have been identified visually on the surface up to the highest heat flux (120 kW/m²) applied in the experiments, Figure 4.1.6d.

Boiling of R141b on A428 at all pressures is characterized by the steep curves, with little temperature deviation of the tube top at pressures of 4 bar and 5 bar, Figure 4.1.5. At 3 bar noticeable decrease of surface superheat was observed, especially for the tube top, as earlier for surface A418. The enhancement factor in dependence on the heat flux with pressure as parameter is presented in Figure 4.1.5. Its highest value of 13.5 was found at 2 bar.

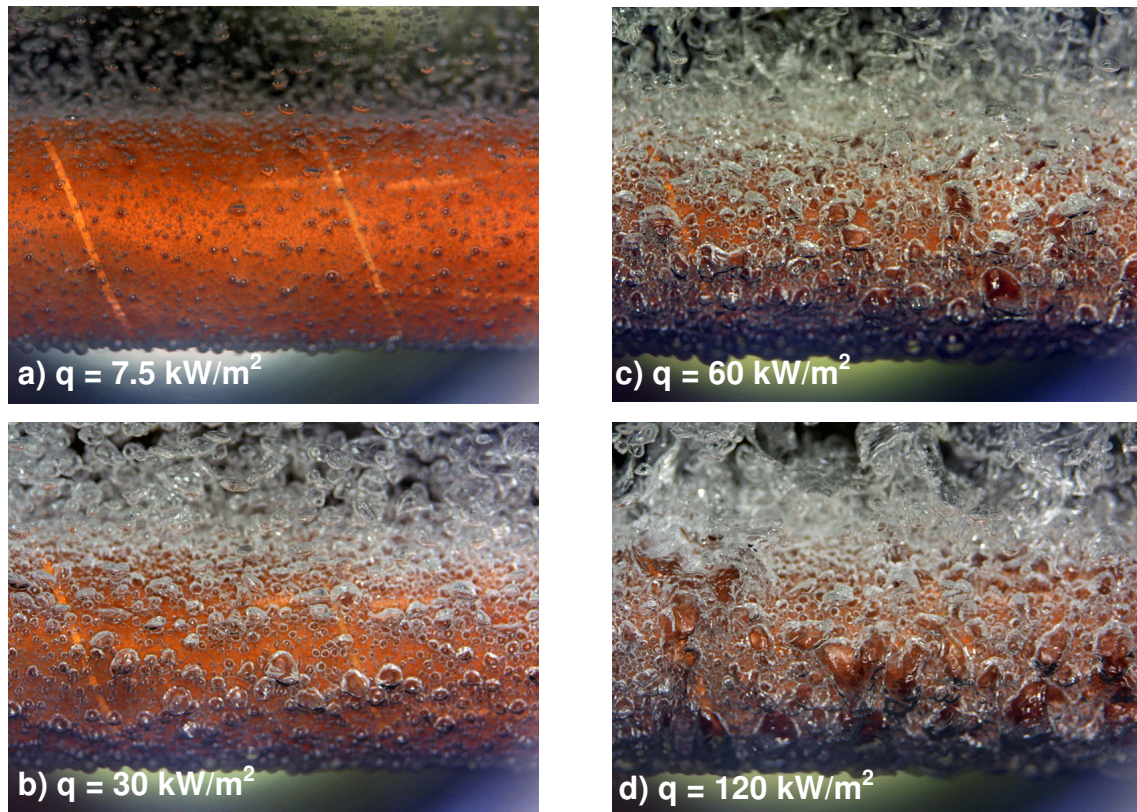


Figure 4.1.6: Boiling of R141b on the structure A428, $p = 2$ bar.

After two weeks of intense boiling at different pressures and heat fluxes, the measurements were repeated at 1 bar. The comparison of the results with previous data is illustrated in Figure 4.1.5 in terms of enhancing factor. As the difference between measurements lies mostly in the range of experimental uncertainty, the boiling behavior did not change significantly and the aging effect can largely be neglected. This result allows expecting a stable boiling behavior of the novel structure over a long period of time.

As can be concluded from the above presented measurements, the superheat of microstructured surface A428 with boiling refrigerant R141b is

weakly affected by the applied heat flux, Figure 4.1.5. This boiling characteristic can roughly be explained by the fact that most of the available nucleation sites become activated at a relatively low heat flux (Figure 4.1.6a). Further raise of the heat flux increases both the departure diameter and frequency of the bubbles, but not so sensitively the density of nucleation sites. The liquid flows between neighboring pins while they act as cavities, supplied with enough liquid even at high heat fluxes. In addition, the pins pierce the bubble surface in the wedge region, generating a long three-phase line with strong evaporation. Thus, the wall temperature remains almost unaffected by the heat flux.

Refrigerant R134a

The refrigerant R134a is a not toxic, not flammable, chemically and thermally stable liquid. It is very well studied and widely used in home and industry applications, serving as a substitute for R12. One can find lots of experimental data with in literature, so it is a good reference liquid.

Microstructure A428

Microstructured surface A428 was tested with R134a boiling at pressures in range between 5 bar and 9 bar with 1 bar step. Experimental results of those tests are represented at Figure 4.1.7. In all experiments with R134a boiling curves are characterized by a steep vertical section corresponding to the nucleate boiling mode (see Figure 4.1.7). Surface temperature of A428 is not affected during boiling by the heat flux above approximately 40 kW/m^2 . However, below this value boiling process at all pressures is characterized by a kind of re-establishing process: surface temperature in this region intensely rises up to a certain value, subsequently remaining almost constant or even decreases by further heat flux increase.

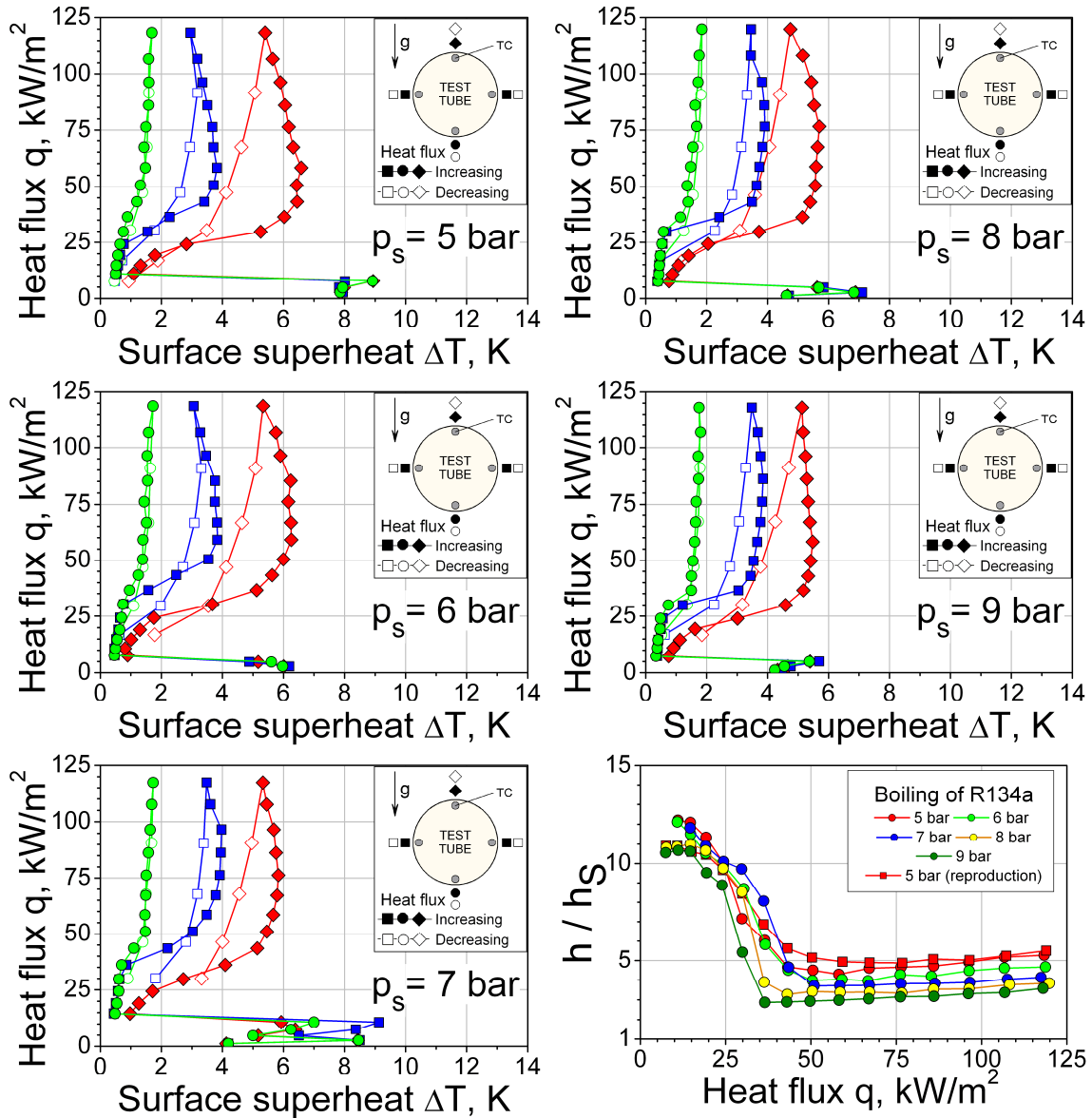


Figure 4.1.7: Boiling characteristics of A428 with R134a at different pressures.

Boiling-reestablishing process at low heat fluxes can be attributed to the changing bubble dynamics with the rising heat flux at a fixed pressure (see the series of photographs in Figures 4.1.8 – 4.1.12). At relatively low heat fluxes (up to 40 kW/m^2) surface is covered with a throng of small vapor bubbles. They effectively decrease surface temperature and hold it at $1 \text{ K} - 2 \text{ K}$ above the saturation value. Further increase of the heat flux (up to the maximal value of 120 kW/m^2) leads to the bubble coalescence and rise of the surface

temperature. Its value remains later constant between 1.5 K for the bottom of the tube and 6 K for the top of it.

The value of enhancement factor for A428 with R134a boiling at a fixed pressure between 5 bar and 9 bar decreases from 10 to 12 for heat fluxes below 40 kW/m^2 down to 2 to 6 for heat fluxes above this value (see Figure 4.1.7). At the same time the enhancement factor is decreasing with the increasing pressure and it is practically independent on a heat flux (above 40 kW/m^2) for all experimental conditions. This feature renders the structure to be very attractive for practical application with fluctuating thermal loads. Change in the heat flux does not lead to any change in the performance above 40 kW/m^2 ; therefore system remains in a state of an indifferent equilibrium.

As a reference to surfaces with the reentrant channels, Figure 2.2.18 can be used. After comparison it is seen, that performance of the tested microstructured surface (A428) has a significant difference: it is much more efficient, stable and independent of heat flux in the fully developed boiling region.

Boiling hysteresis for this microstructure is relatively low and can be identified only for the top and side of the tube. Difference in surface superheats between top, side and bottom of the tube can be explained by bubble coalescence. Rising bubbles slide along the tube surface from the bottom to the top, joining with others and increasing the amount of vapor in the microstructure. This subsequently deteriorates the heat transfer from the surface to the bulk liquid. One may predict that if such structure is applied to a flat surface, its heat transfer behavior would be close to the tube bottom, as it would be depleted from the coalescence process caused by the rising bubbles.

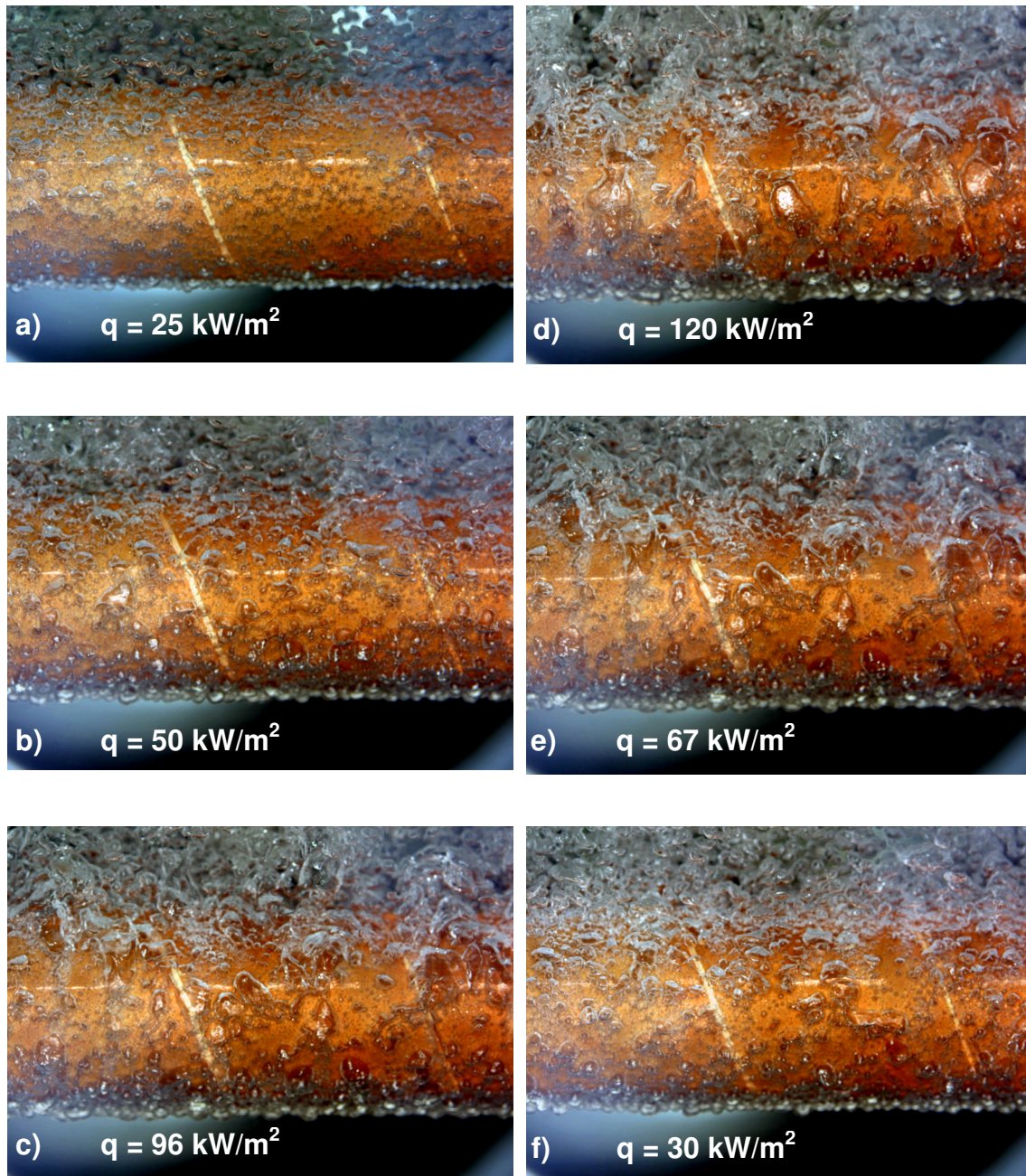


Figure 4.1.8: Boiling of R134a on the structure A428, $p = 5 \text{ bar}$.

a) to d) – increasing heat flux

e) to f) – decreasing heat flux

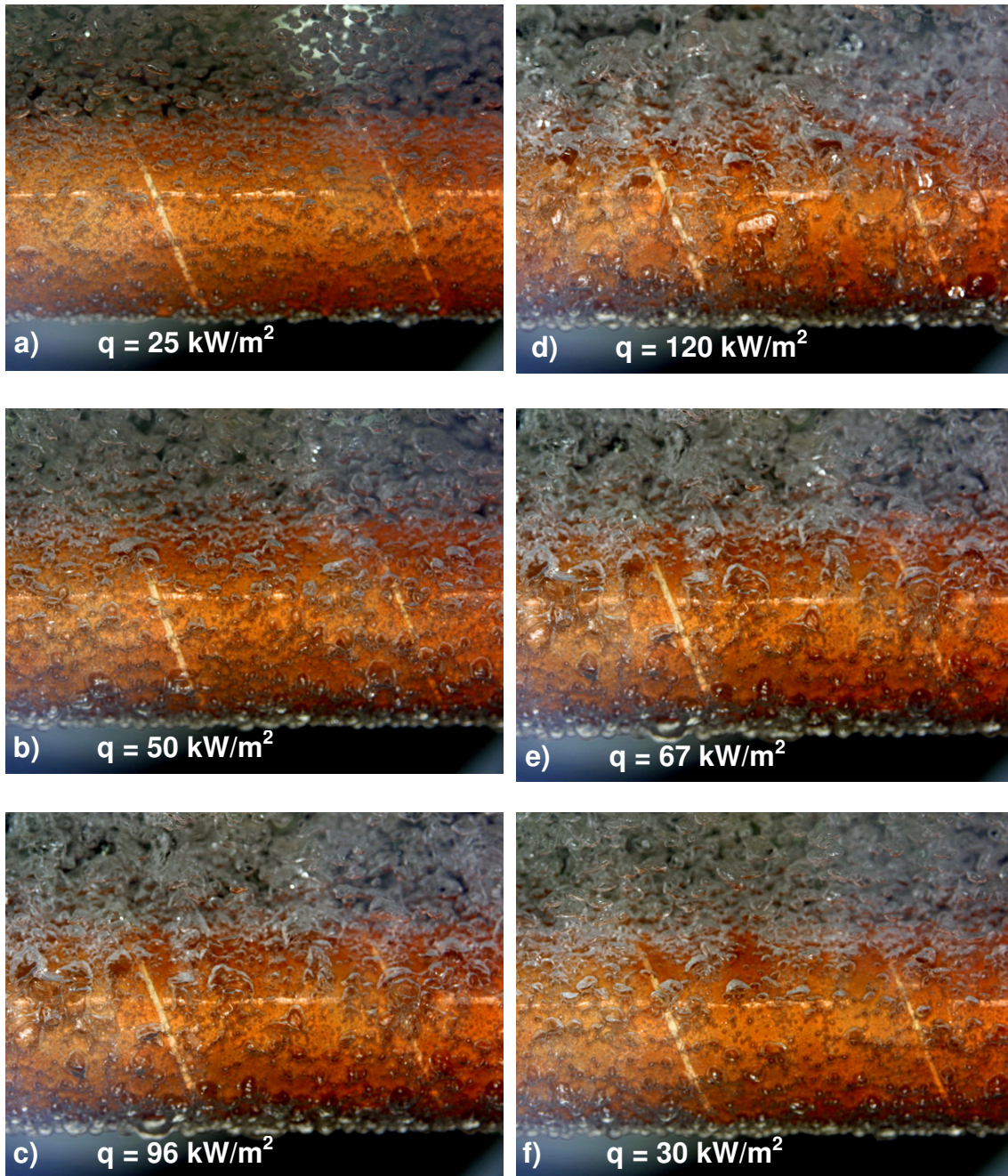


Figure 4.1.9: Boiling of R134a on the structure A428, $p = 6 \text{ bar}$.

a) to d) – increasing heat flux

e) to f) – decreasing heat flux

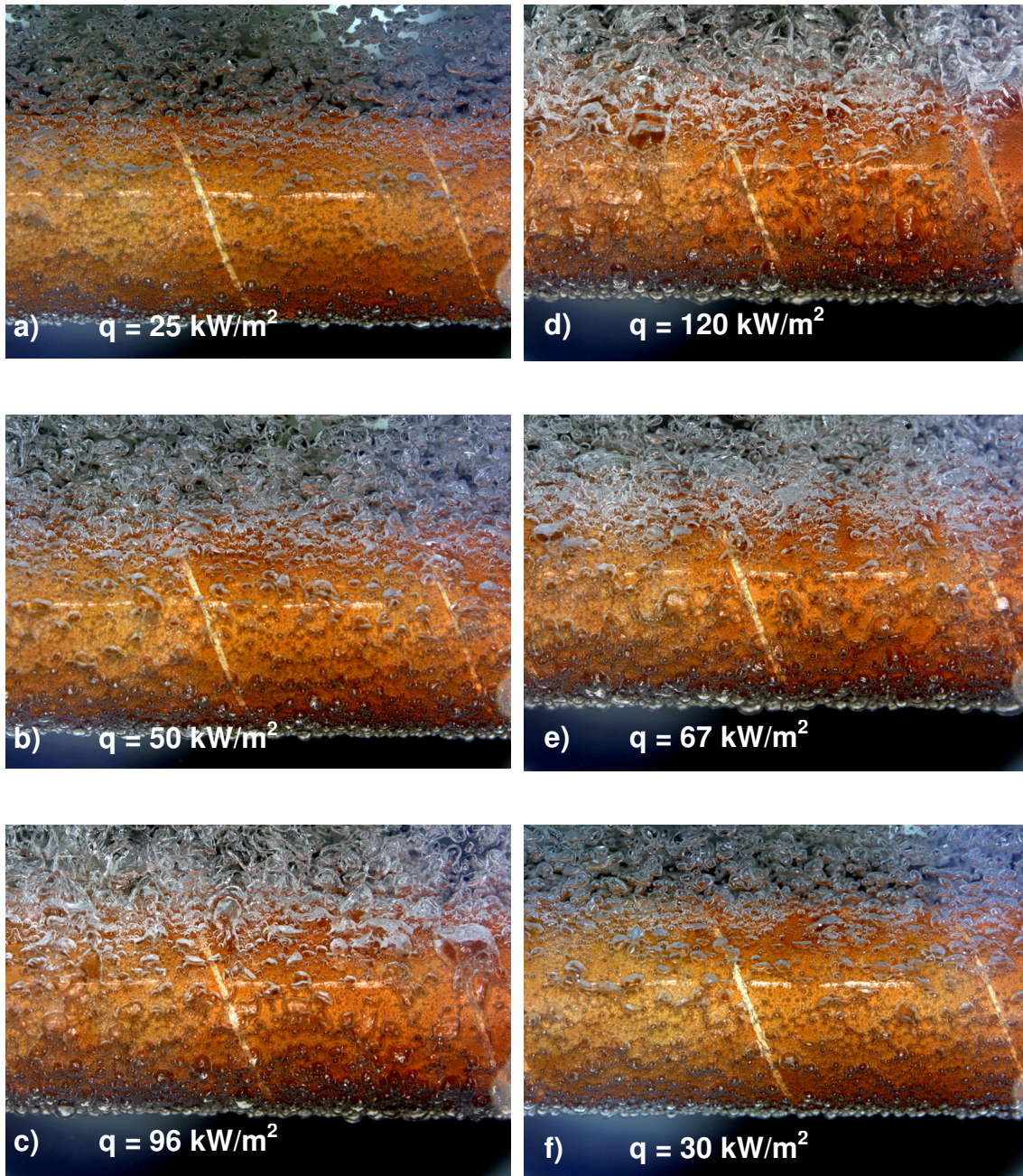


Figure 4.1.10: Boiling of R134a on the structure A428, $p = 7 \text{ bar}$.

a) to d) – increasing heat flux

e) to f) – decreasing heat flux

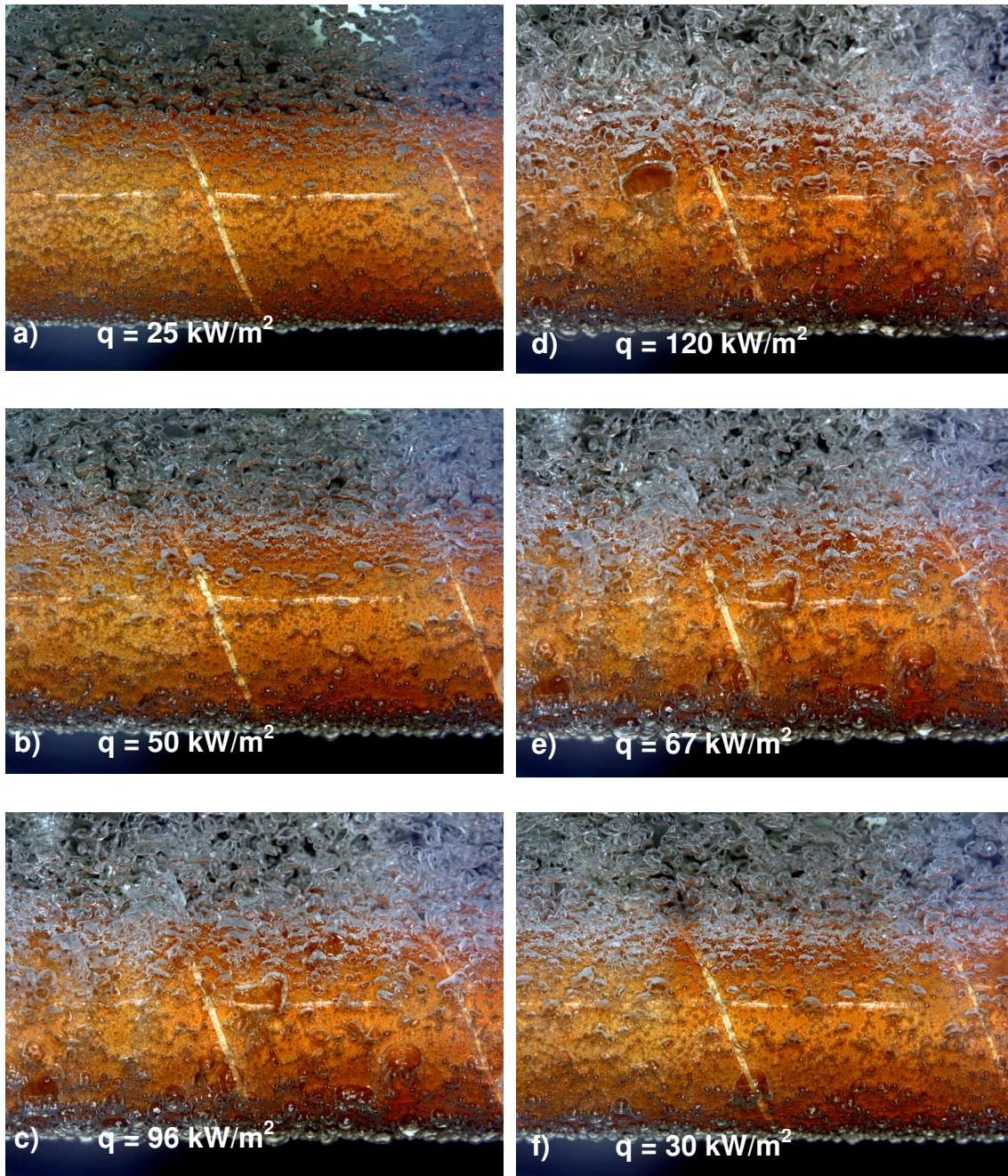


Figure 4.1.11: Boiling of R134a on the structure A428, $p = 8 \text{ bar}$.

- a) to d) – increasing heat flux
- e) to f) – decreasing heat flux

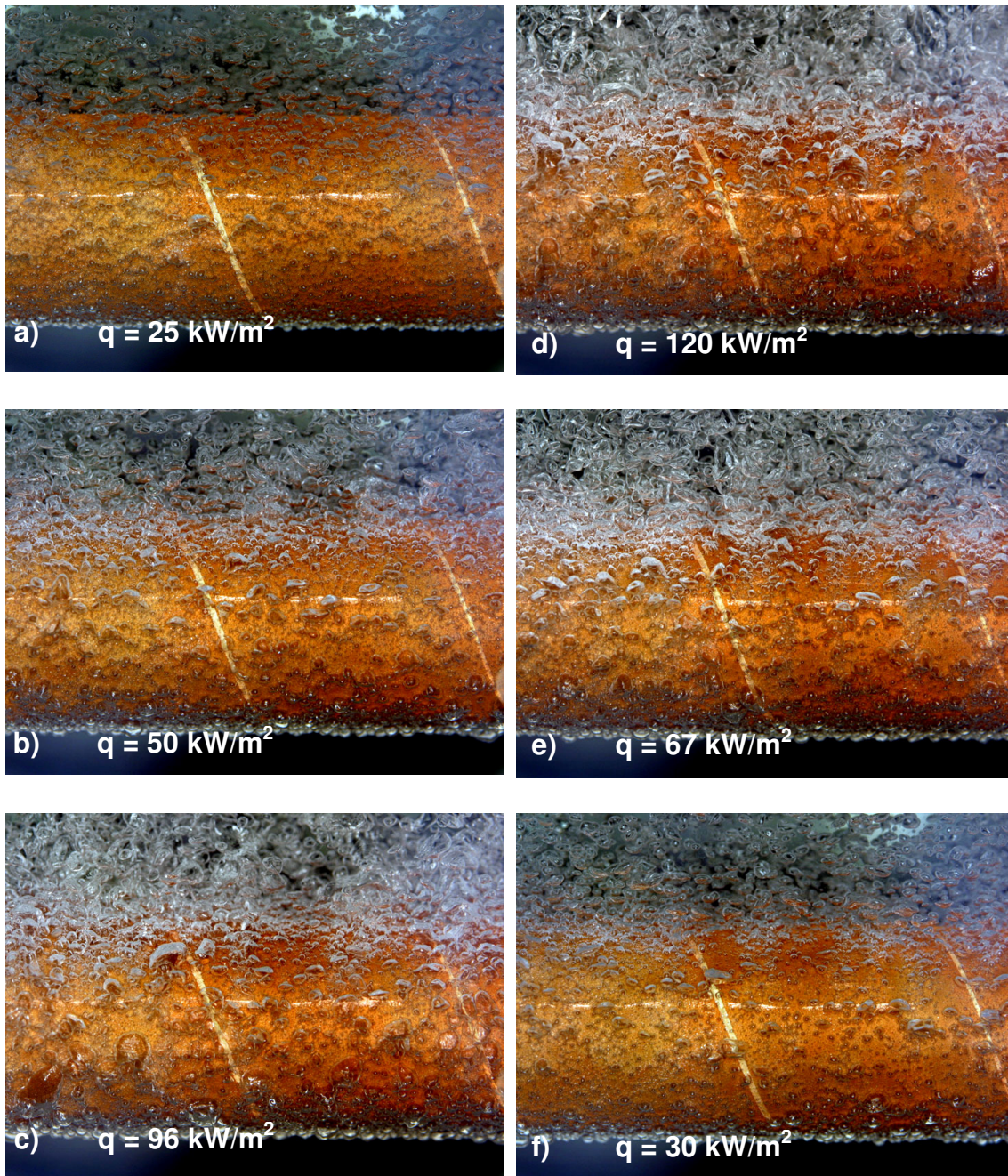


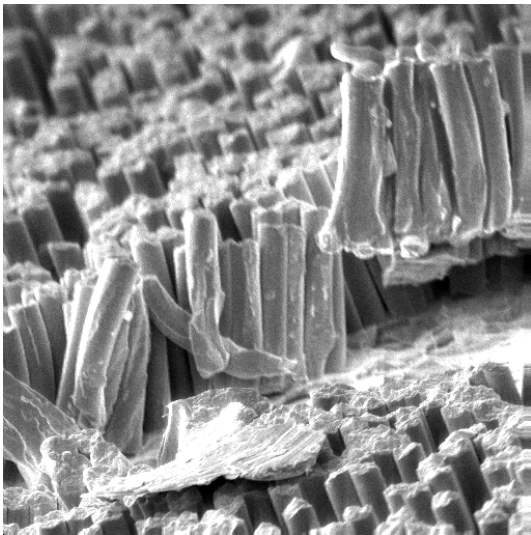
Figure 4.1.12: Boiling of R134a on the structure A428, $p = 9 \text{ bar}$.

a) to d) – increasing heat flux

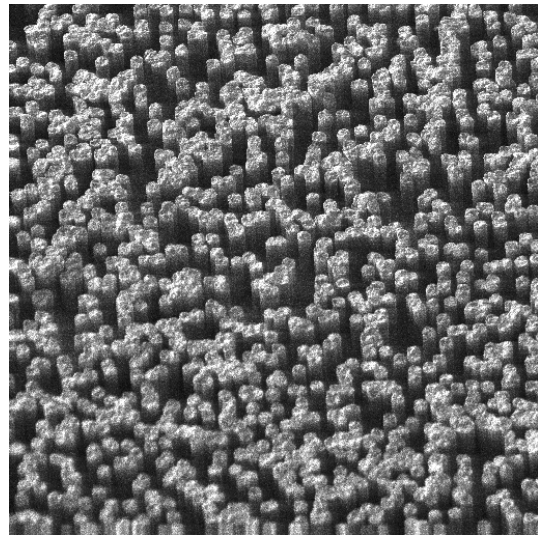
e) to f) – decreasing heat flux

Microstructure A419

Next investigated structure A419 is represented in Figure 4.1.13. It was tested with refrigerant R134a at pressures of 5 bar to 9 bar with the increase step of 1 bar. Experimental results for this structure are presented in Figure 4.1.14. Boiling inception for A419 occurred at lower superheats than for A428 for all pressures. Boiling hysteresis for this structure was even lower than for the previous one and it is noticeable only for the top of the tube. The spatial temperature gradient was lower as well and was suppressed by the increasing pressure (see Figure 4.1.14).



A419 zoom 1000x



A419 zoom 500x

Figure 4.1.13: SEM photo of the microstructure A419.

Boiling process on the tube with microstructure A419 has no reestablishing zone like for A428. Boiling curves for pressures between 5 bar and 9 bar have almost straight vertical section from the boiling inception up to the maximal heat flux.

Enhancement factor for A419 does not have two zones as well and it is slightly increasing with the increasing heat flux. As for A428 it is decreasing with the increasing pressure and its values lie between 2 and 3.5 for appointed experimental conditions.

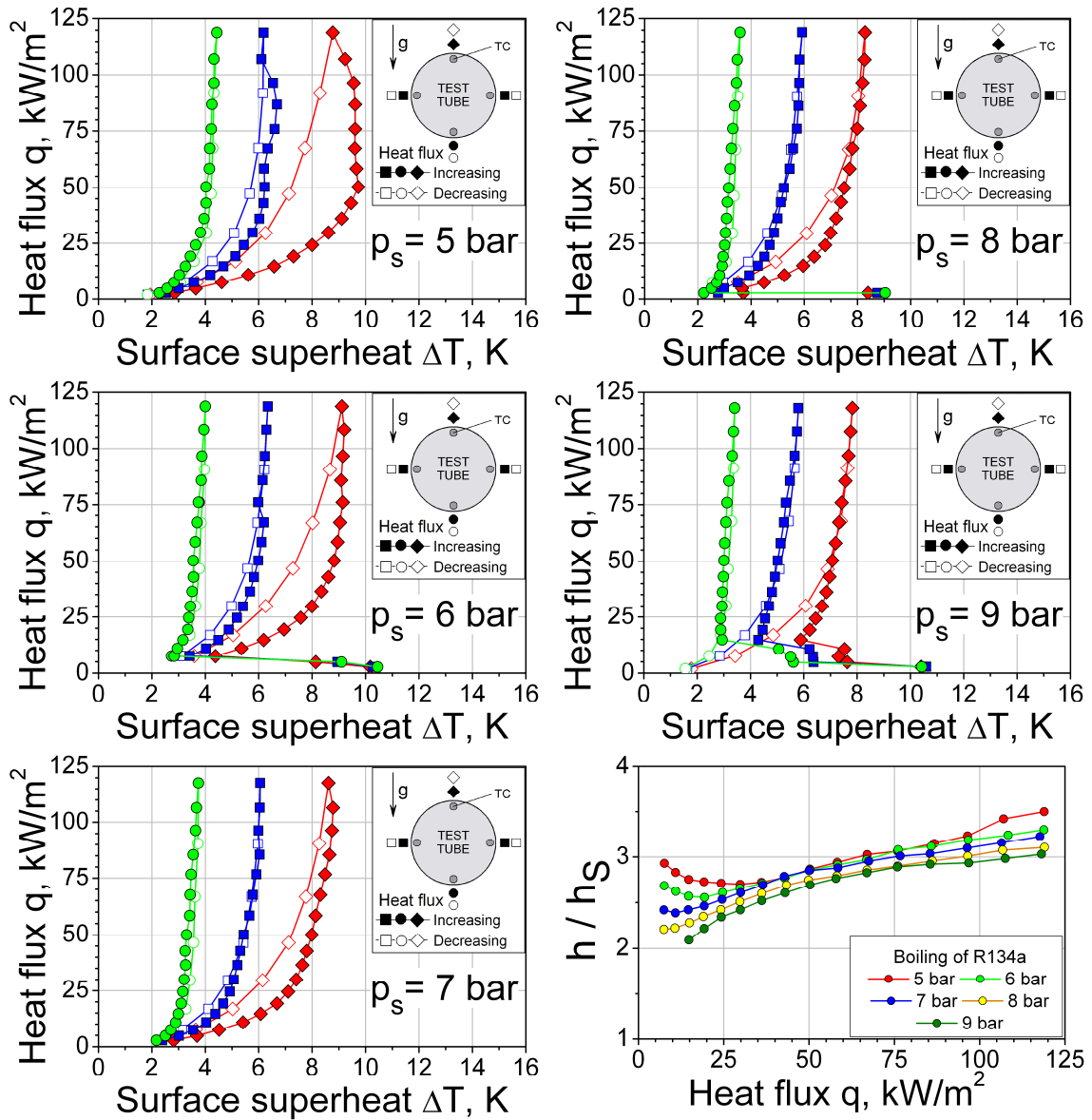


Figure 4.1.14: Boiling characteristics of A419 with R134a at different pressures.

A series of additional experiments was conducted with this microstructure. In these experiments under a constant heat flux the system pressure was varied from 5 bar up to 9 bar with 0.5 bar step. The purpose was to determine the behavior of the surface temperature under fluctuating pressure and to reveal the relation between the critical radius of a nucleus and the surface superheat, the latter being a function of a collective nucleation. The results are represented in Figure 4.1.15. Tests were undertaken for four different heat fluxes: 10 kW/m^2 , 30 kW/m^2 , 70 kW/m^2 and 120 kW/m^2 . As it can be taken from the Figure 4.1.15, at all heat fluxes the temperature of the surface decreases with the increasing pressure. It means that with the increasing pressure the structure provides smaller vapor bubbles that effectively cool it down at all heat fluxes. When the critical nucleus decreases with the increasing pressure, the microstructure becomes more and more effective, as bubbles can be created not only between pins, but in other micro cavities of the surface.

A reader should not be confused by the fact that earlier it was mentioned (and will be mentioned below again for other surfaces) that the enhancement factor decreases with the increasing pressure. Explanation is very simple. The enhancement factor – is a *relative* quantity, showing how good the structure in comparison with a smooth tube is. By contrast, Figure 4.1.15 represents *absolute* values of the superheat for the given conditions. A smooth surface becomes more effective with the increasing pressure as more cavities on it can be activated; therefore it becomes closer in performance to the structured one. In other words at high pressures the structured surface becomes too “rough”.

It is noticeable from Figure 4.1.15 that there is a temperature gradient along the tube circumference despite the great copper heat conductivity. This is mainly due to the coalescence of bubbles sliding along the tube and ones newly created.

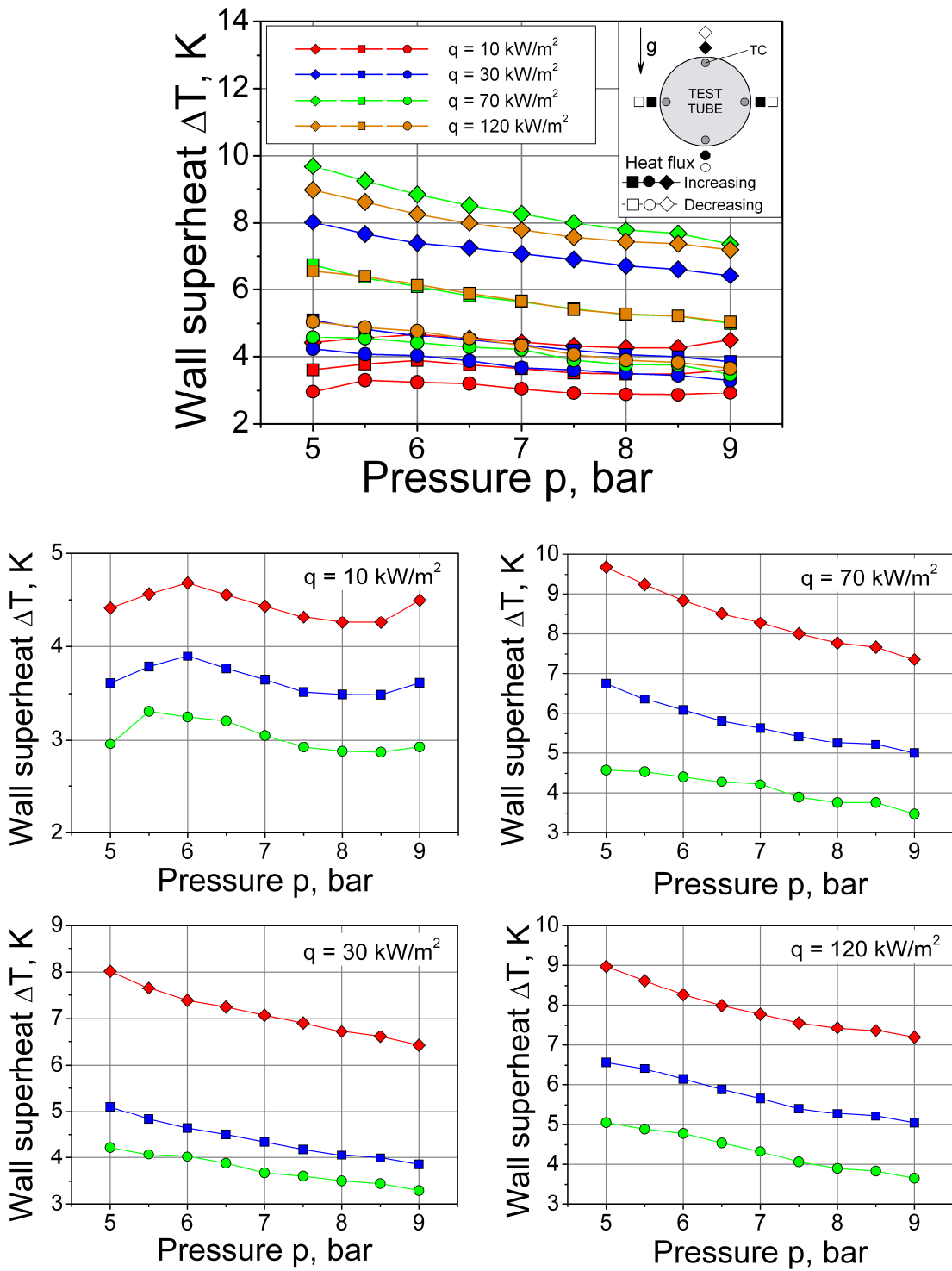
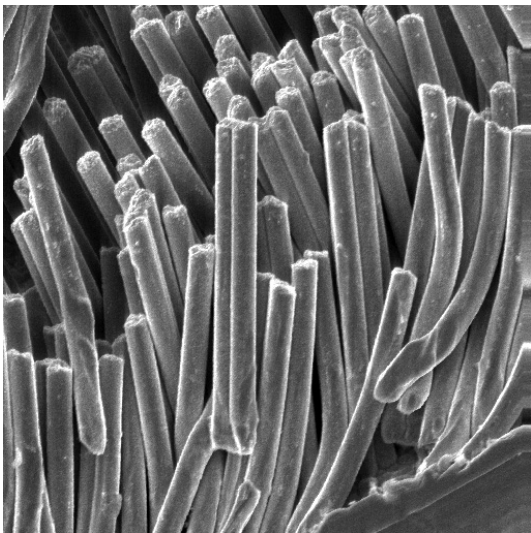


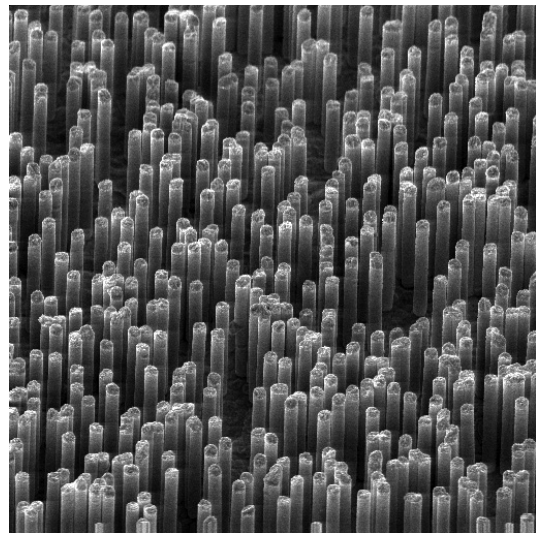
Figure 4.15: Wall superheat of the microstructure A419 with R134a at different heat fluxes.

Microstructure A401

Structure A401 was tested under same condition as previous. It is represented in Figure 4.1.16 and the experimental results at Figures 4.1.17, 4.1.18 and 4.1.19. Overall boiling behavior for A401 is the same as for A419. Boiling inception occurs at superheats below 6 K. Rise of the heat flux does not lead to any significant increase of the surface superheat. Increasing pressure causes suppression of the surface temperature gradient and hysteresis. The heat transfer enhancement factor for this structure lies between 3.5 and 4.5, i.e. somewhat higher than for A419 but lower than for A428. Main tendencies remain the same: the enhancement factor is increasing slightly with the increasing heat flux and decreases with rising pressure. Difference between values of the enhancement factor for A401 at different pressures is practically negligible.



A401 zoom 1000x



A401 zoom 500x

Figure 4.1.16: SEM photo of the structure A401.

Structure A401 was tested at a fixed heat flux under the changing pressure. As and structure A419, A401 shows decrease of the surface superheat at increasing pressure. The highest surface superheats are observed for average heat fluxes. For the lowest heat flux a series of photographs were obtained, representing the bubble dynamics on the tested structure at different pressures, Figure 4.1.19. Unlike other type of surfaces the investigated one demonstrates high number of nucleation sites even at low heat fluxes.

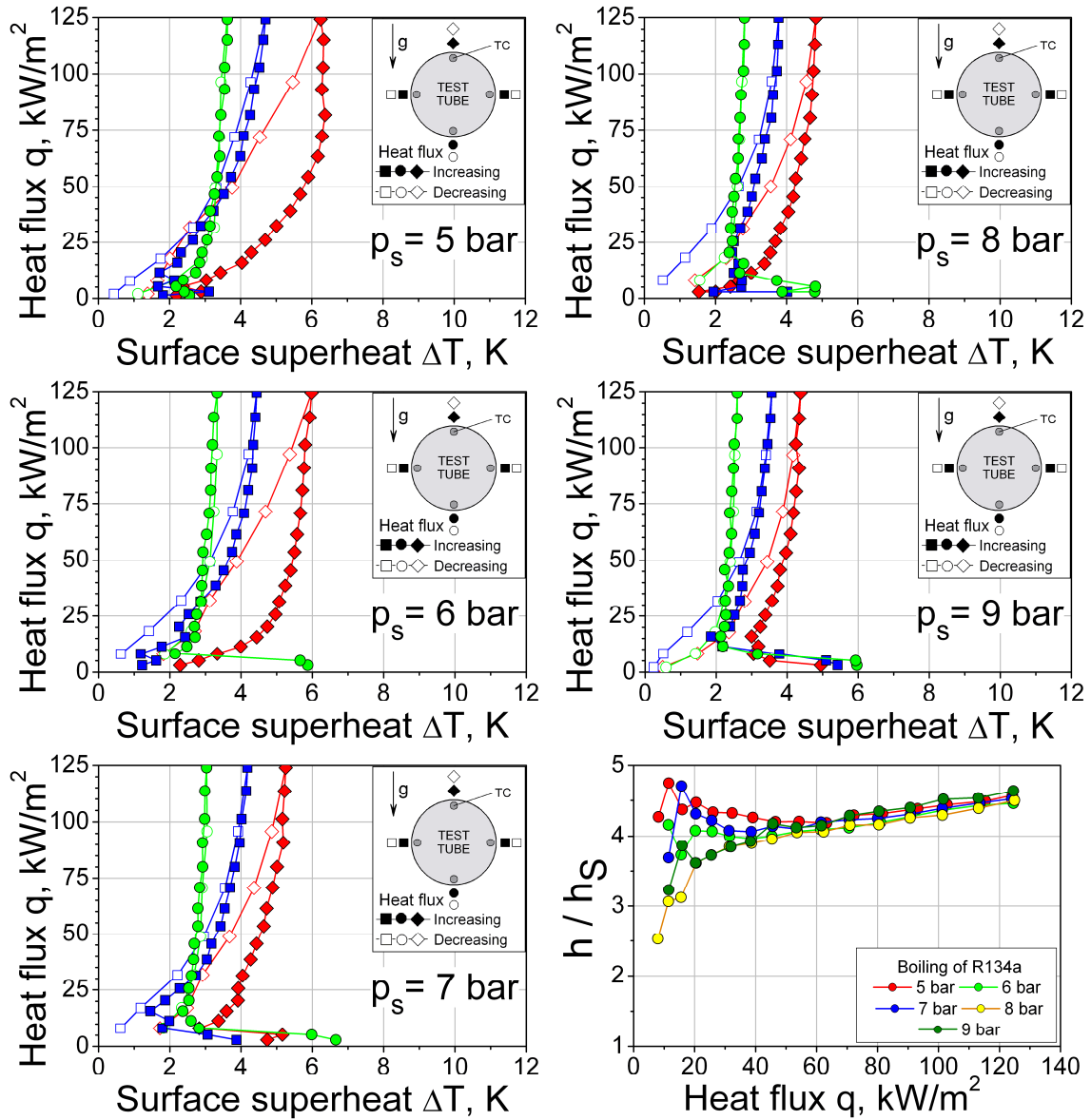


Figure 4.1.17: Boiling characteristics of A401 with R134a at different pressures.

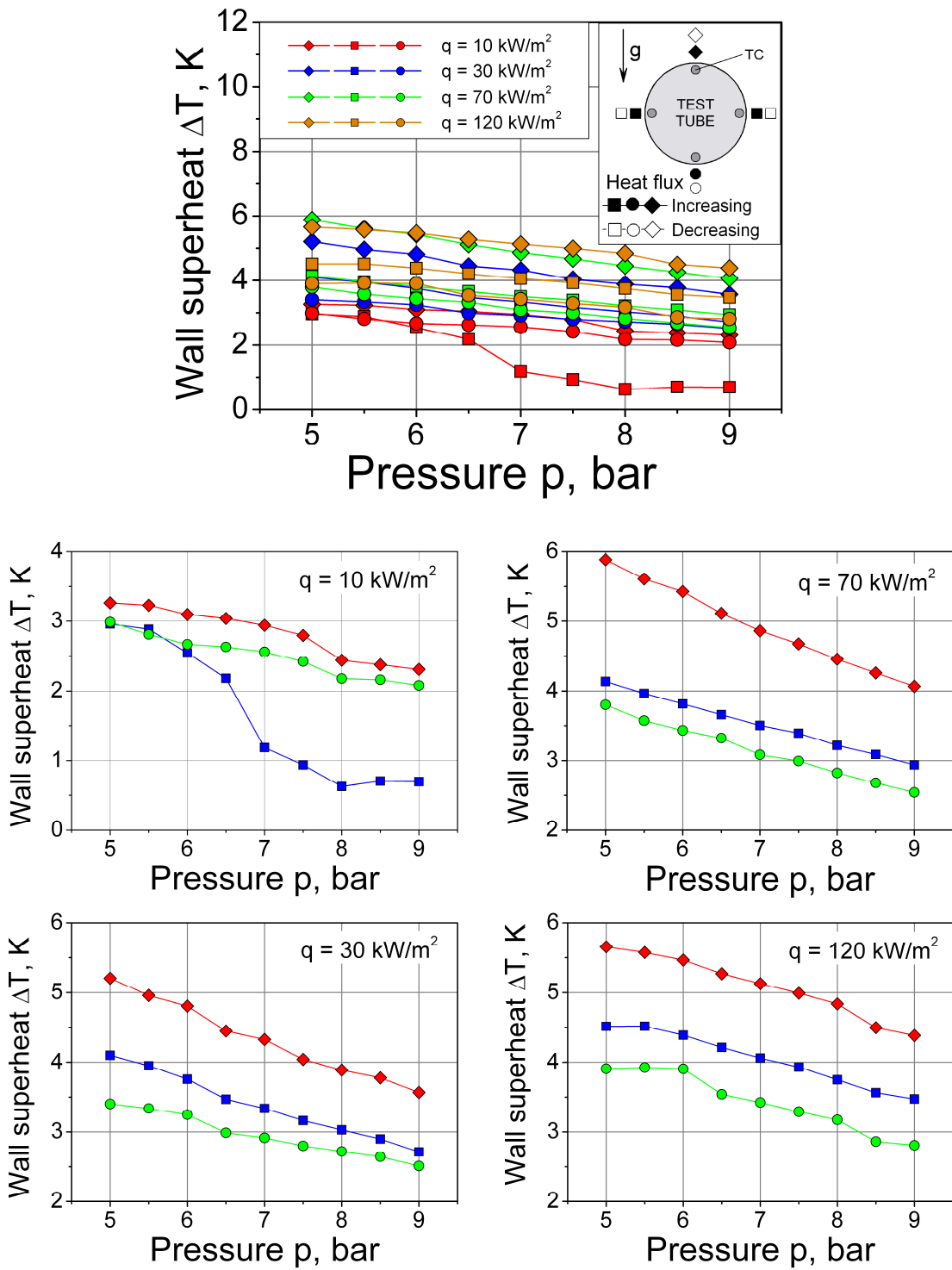


Figure 4.1.18: Wall superheat of the microstructure A401 with R134a at different pressures.

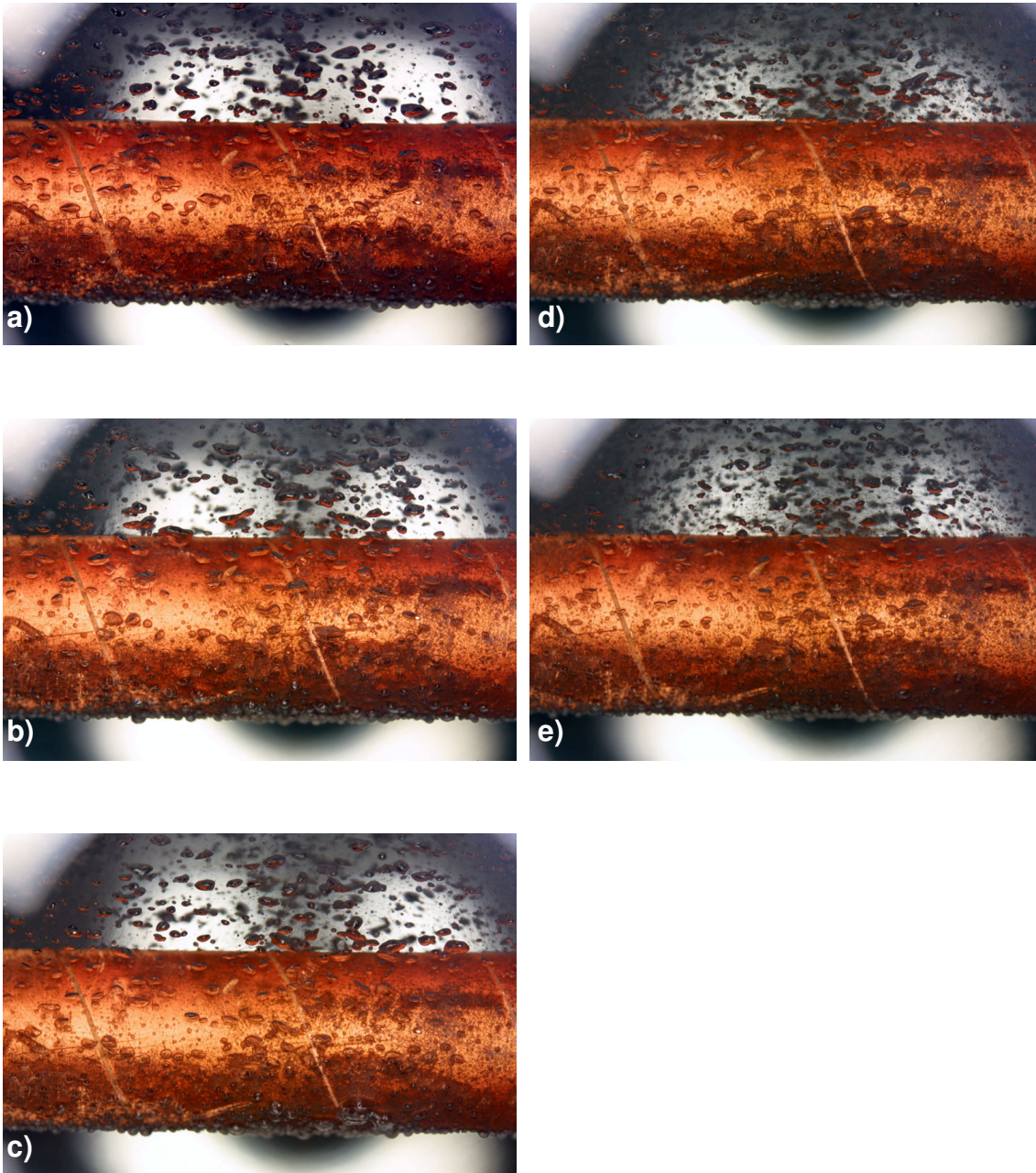
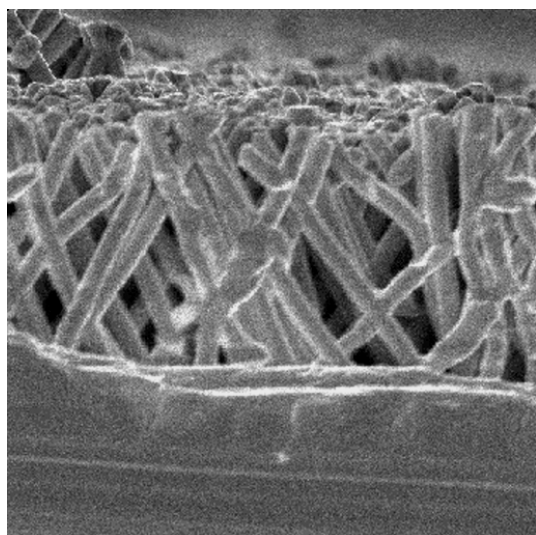
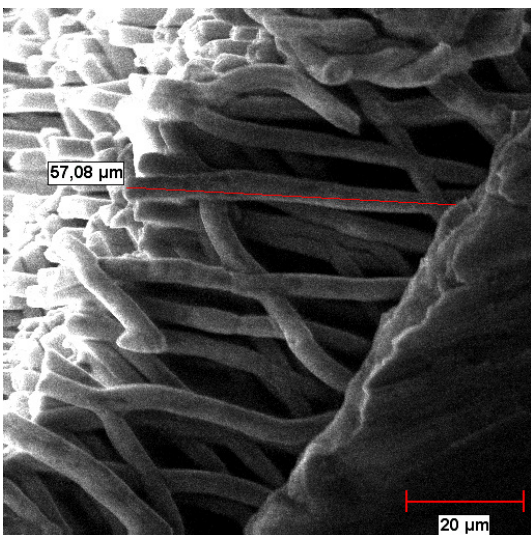
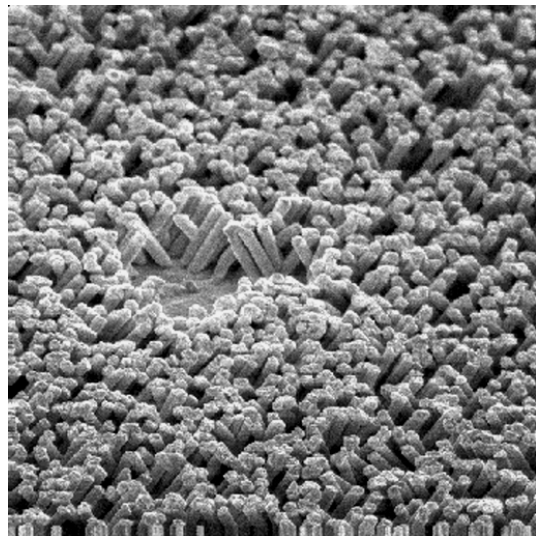
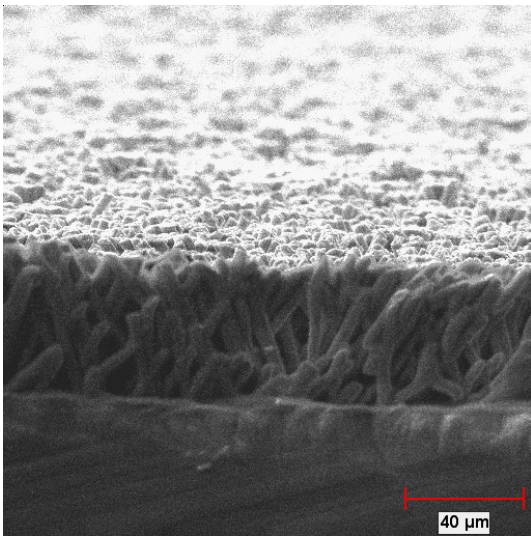


Figure 4.1.19: Boiling of R134a on structure A401, $q = 10 \text{ kW/m}^2$.
a) $p = 5 \text{ bar}$, b) $p = 6 \text{ bar}$, c) $p = 7 \text{ bar}$, d) $p = 8 \text{ bar}$, e) $p = 9 \text{ bar}$.

Microstructure A437

Structure A437 was tested in the same way as previous. SEM images of A437 are shown in Figure 4.1.20. Boiling curves and the enhancement factor are given in Figure 4.1.21. Boiling inception for this structure occurred at very low superheats between 1 K and 7 K. The surface superheat remained at even lower values than for surfaces A428, A419 and A401 (see Figures 4.1.7, 4.1.14, and 4.1.17 for comparison).



A437 zoom 1000 x

A437 zoom 500 x

Figure 4.1.20: SEM photos of the microstructure A437.

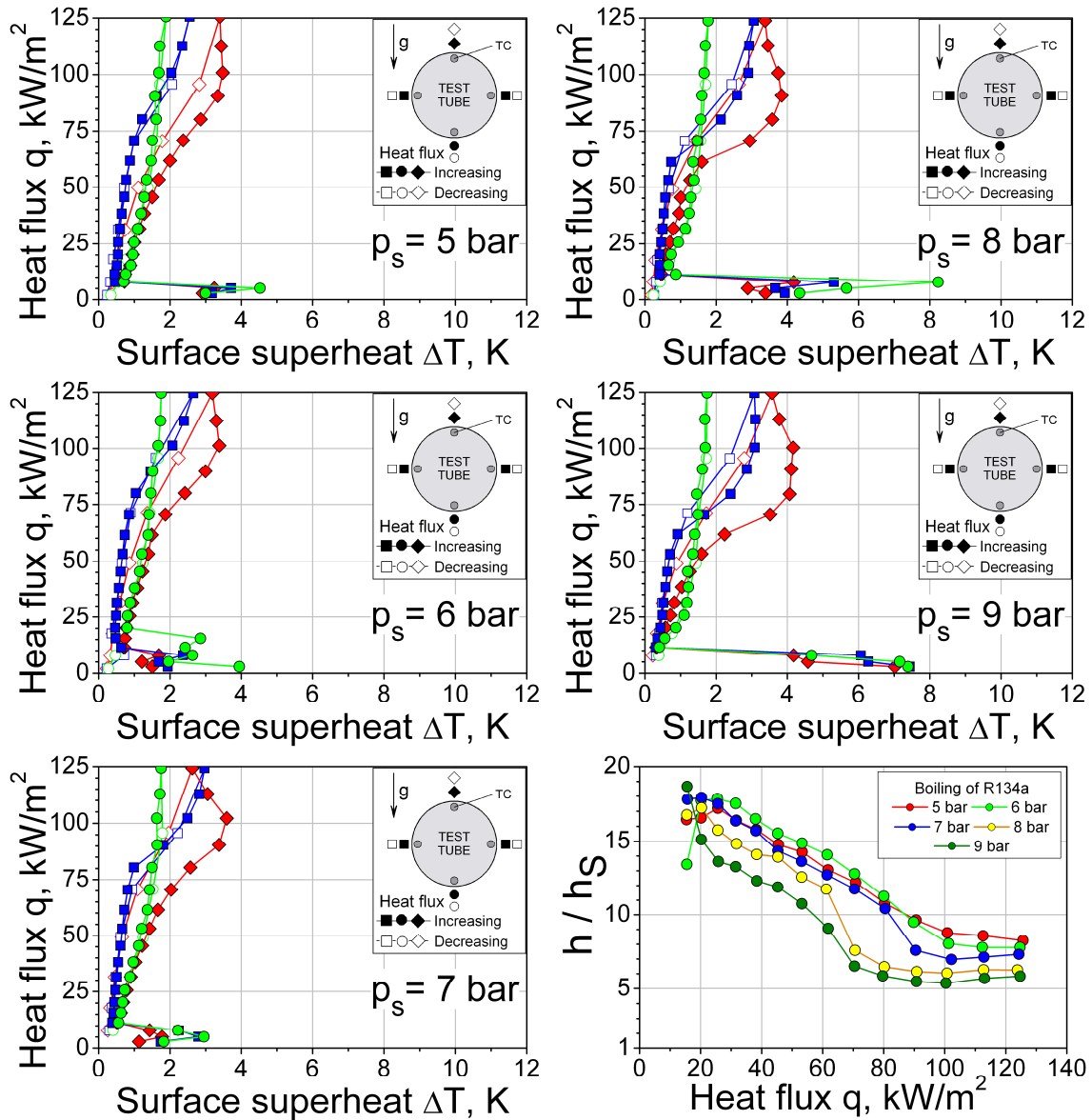


Figure 4.1.21: Boiling characteristics of A437 with R134a at different pressures.

As it can be seen, boiling behavior of microstructure A437 is close to structure A428 (see Figure 4.1.7). Boiling process upon the A437 is characterized by the reestablishing process as well. The difference is that this process occurs up to higher heat fluxes, particularly 90 kW/m². The enhancement factor decreases from 13 – 19 down to 5 – 10, above 90 kW/m² remaining unaffected by the heat flux. Higher value of the factor corresponds to lower pressures. This is the common tendency for all tested microstructured surfaces for all boiling modes. Difference between surface superheats of

microstructure A437 at the idem heat fluxes and different pressures lies close to the experimental uncertainty, causing small deviation for the spatial-temporal average values of temperature, used for calculation of the enhancement factor.

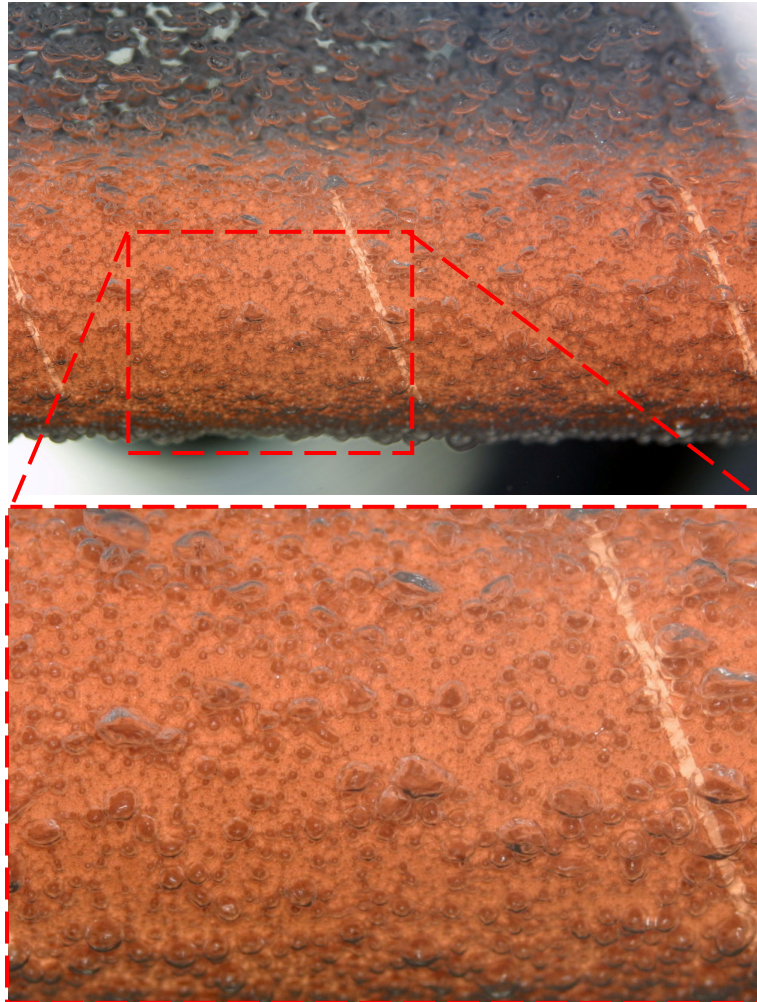


Figure 4.1.22: Bubble chains on A437, boiling R134a at 7 bar, 57 kW/m².

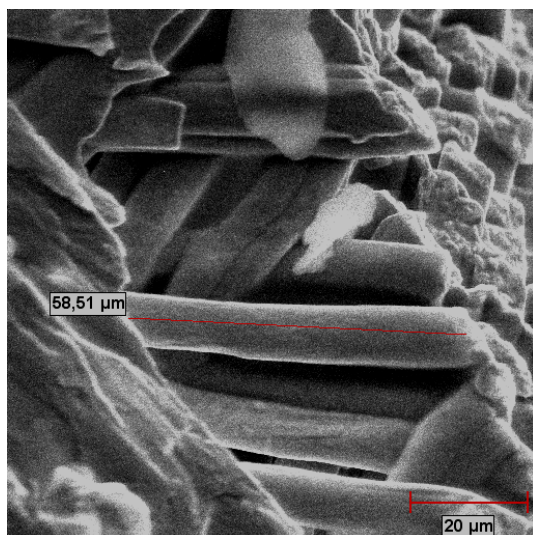
A nucleation criterion (2.1.2) shows preferable evaporation in the surface cavities or near another nucleus. Theoretically it happens due to smaller interfacial areas which must be built, and correspondingly lower surface energy in comparison with nucleation in the bulk liquid. Experimentally this fact is confirmed by all tested microstructure. Figure 4.1.22 represent photos of the boiling R134a at 7 bar and 54 kW/m² on A437. As it can be seen, preferable nucleation near neighboring sites leads to the building of bubbles chains upon the surface. Generally speaking it is observed for all microstructured surfaces

tested in the present work, however in different degree. Concurrent interaction of processes of interface creation and heat transfer between the nucleation site and the bubble determines building of these chains. The microstructure A437 acts in a way allowing all close to each other nucleation sites to produce bubbles for given conditions.

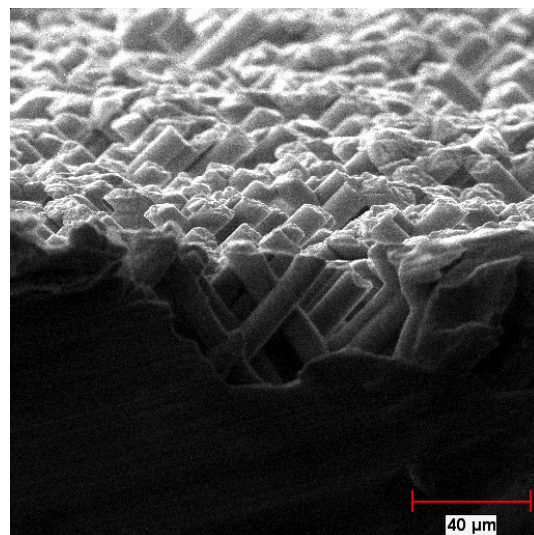
A new approach employing the theory of chaos has risen recently for the boiling process modeling. Chaotic nature of boiling is known. It is acknowledged among researchers that nucleation occurs due to the fluctuation of the liquid density. Although there are no common criteria for quantitative characterization of this process, and just several models exist in modern literature, the experimental example shown in Figure 4.1.22 gives an idea about probability distribution of density and pressure fluctuation in liquid and subsequent nucleation upon a heat transfer surface. The order (bubbles chains) appears in the chaos (of fluctuations).

Microstructure A435

Next investigated with R134a microstructured surface was A435. It is depicted in Figure 4.1.23.



A435zoom 1000 x



A435 zoom 500

Figure 4.1.23: SEM photos of the microstructure A435.

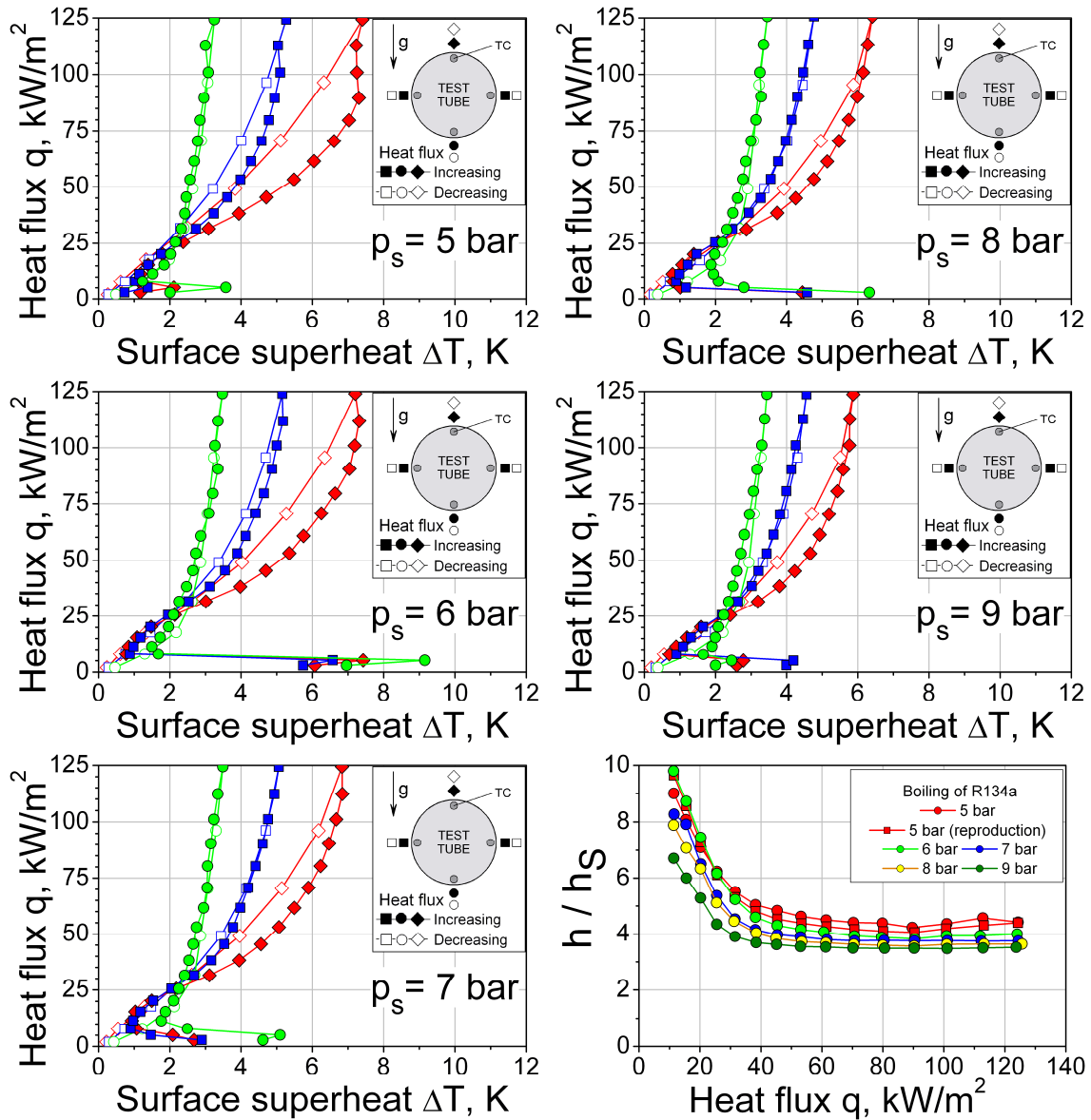


Figure 4.1.24: Boiling characteristics of A435 with R134a at different pressures.

Same tendencies for microstructure A435 were found as and for the above described structures. The boiling inception occurred at low heat fluxes below 5 kW/m² and the surface superheats from 1 K to 9 K. Boiling reestablishing occurred at heat fluxes below 40 kW/m², and above this value the surface superheat remained largely unaffected by the heat flux. Surface temperature gradients and hysteresis were suppressed by the increasing pressure. The microstructure A437 was tested for the long time performance stability and was found to be practically not influenced by the working

conditions. As well as the microstructure A428, A435 could be recommended for use in the fluctuating power output, as its enhancement is independent on the applied heat flux.

Critical heat fluxes for structures A435 and A437 although were not measured directly, seem to be very large, as separate vapor bubbles together with bubbles chains could be seen upon the surface up to the maximal experimental heat flux of 125 kW/m^2 , Figure 4.1.25.

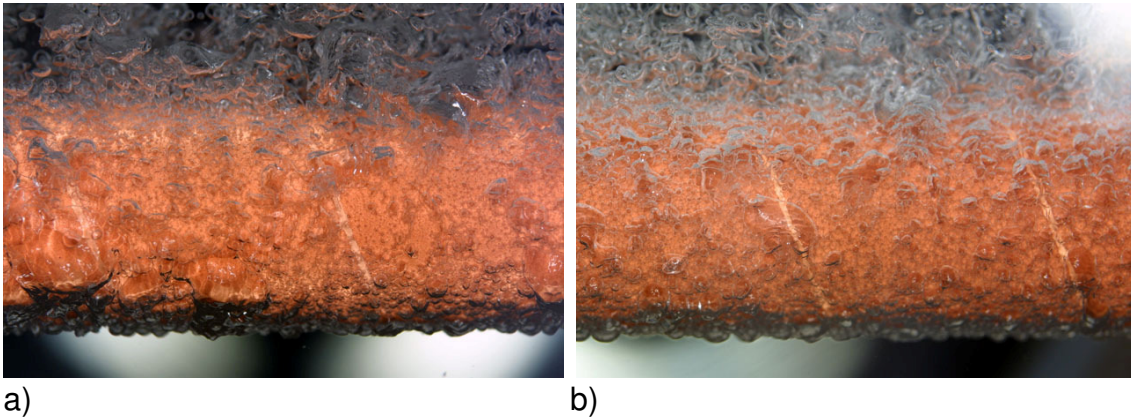
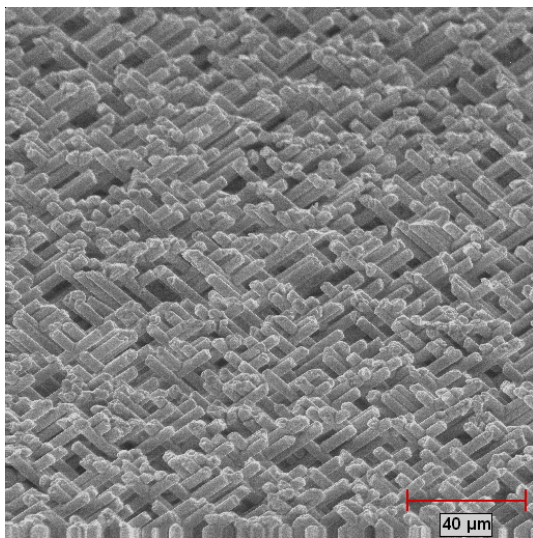


Figure 4.1.25: Boiling of R134a at $p = 5 \text{ bar}$ and $q = 125 \text{ kW/m}^2$,

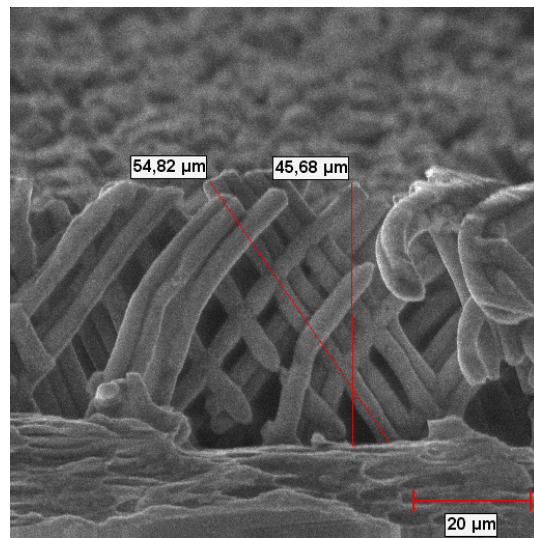
- a) Microstructure A435
- b) Microstructure A437.

Microstructure A431

The following microstructure A431 with inclined pins, Figure 4.1.26, was tested with the refrigerant R134a as well. As well as other microstructures with inclined pins, A431 has demonstrated two zones on boiling curves and the boiling reestablishing process, Figure 4.1.27. Subsequently the values of the enhancement factors decreased from 10 – 17 in the highly effective low heat flux region down to 4 – 8, further remaining unaffected by applied heat flux, Figure 4.1.27.



A431zoom 500 x



A431 zoom 1000

Figure 4.1.26: SEM photos of the microstructure A431.

For microstructured surfaces with inclined pins the inclination angles seem to determine the value of the heat flux, in vicinity to which the reestablishing of the boiling process takes place. This experimentally determined fact will be analyzed in more detail below.

For engineering purposes one may note that the boiling inception occurred at the surface superheats between 5 K and 12 K and at heat fluxes about 5 kW/m² as earlier. Separate vapor bubbles and bubble chains could be observed upon the microstructured surface A431 over the whole range of applied heat fluxes, Figure 4.1.28. Investigation of the boiling crisis upon such surfaces could be an interesting research project in the future.

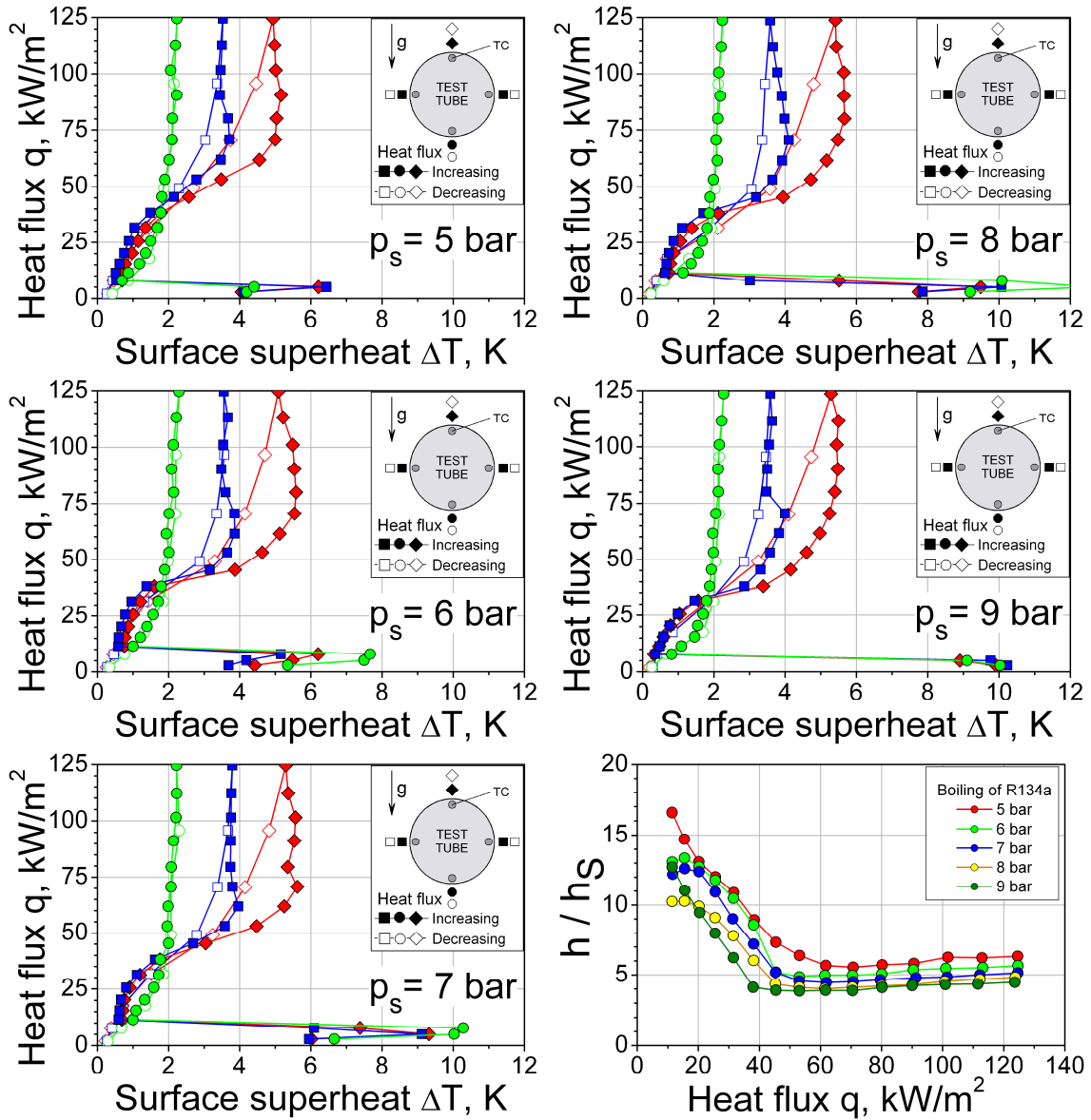
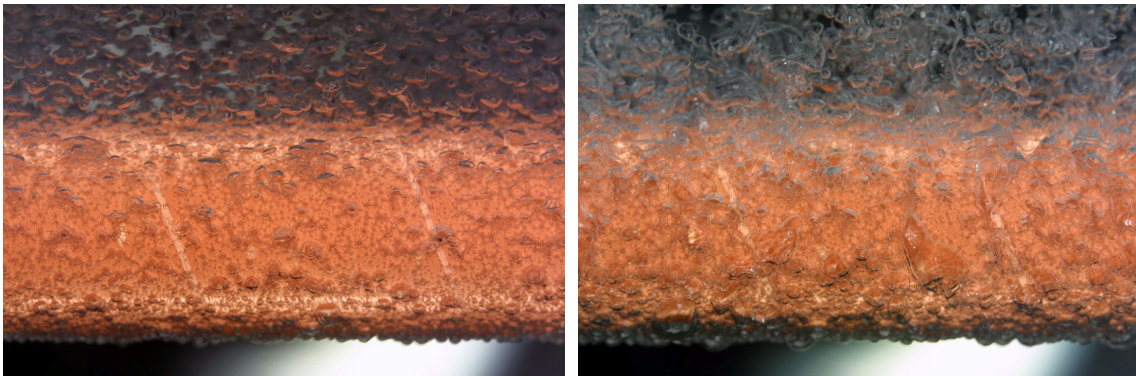


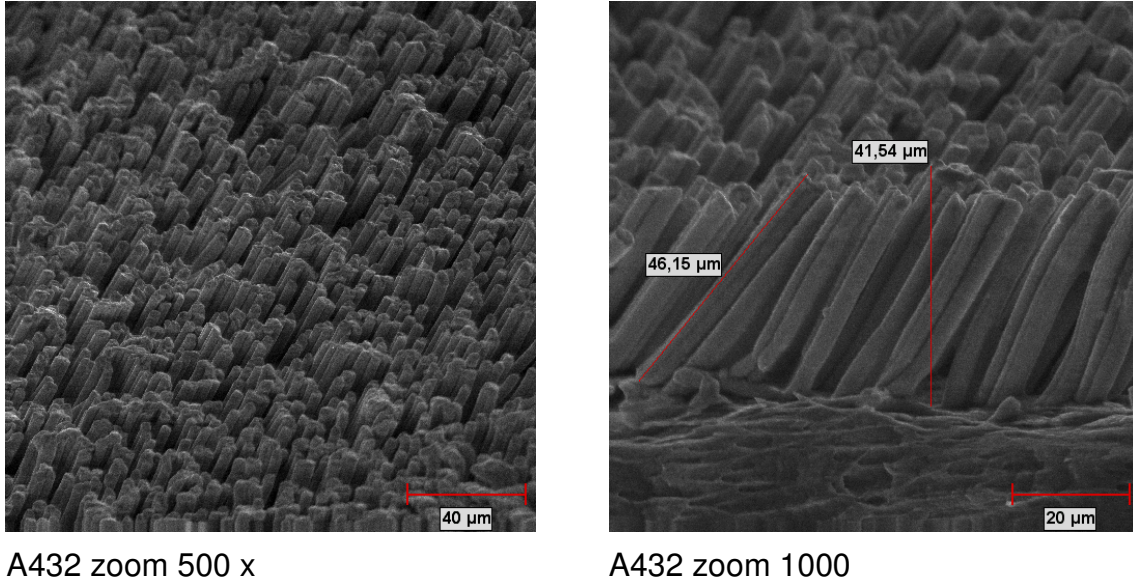
Figure 4.1.27: Boiling characteristics of A431 with R134a at different pressures.



a) b)
Figure 4.1.28: R134a boiling on A431 at 7 bar: a) $q=25$ kW/m², b) $q=125$ kW/m².

Microstructure A432

The surface A432 with mono-inclined pins was next in the measuring program. Its SEM photographs are represented in Figure 4.1.29.



A432 zoom 500 x

A432 zoom 1000

Figure 4.1.29: SEM photos of the microstructure A432.

Boiling curves of R134a with A432 at pressures from 5 bar up to 9 bar are presented in Figure 4.1.30, as well as the enhancement factor dependence on the applied heat flux. Although the microstructure A432 had inclined pins, its behavior is more typical for a microstructure with straight pins. There are no boiling reestablishing was observed and the enhancement factor was slightly rising from 3 – 4.5 to 4 – 5 with the increasing heat flux, Figure 4.1.30. This happens due to the micro configuration of the structure with mono-inclined pins. Microstructures A435, A437 and A428 had bi-inclined pins, intersecting at a given angle, forming thus bi-cavity pattern of the surface, what resulted in the two zones boiling curves and boiling reestablishing. Especially good this can be observed in comparison with A431, microstructure that had absolutely the same geometry as and A432, however with bi-inclined pins, Figures 4.1.27 and 4.1.30. Theoretical explanation of this phenomenon will be given in the work later.

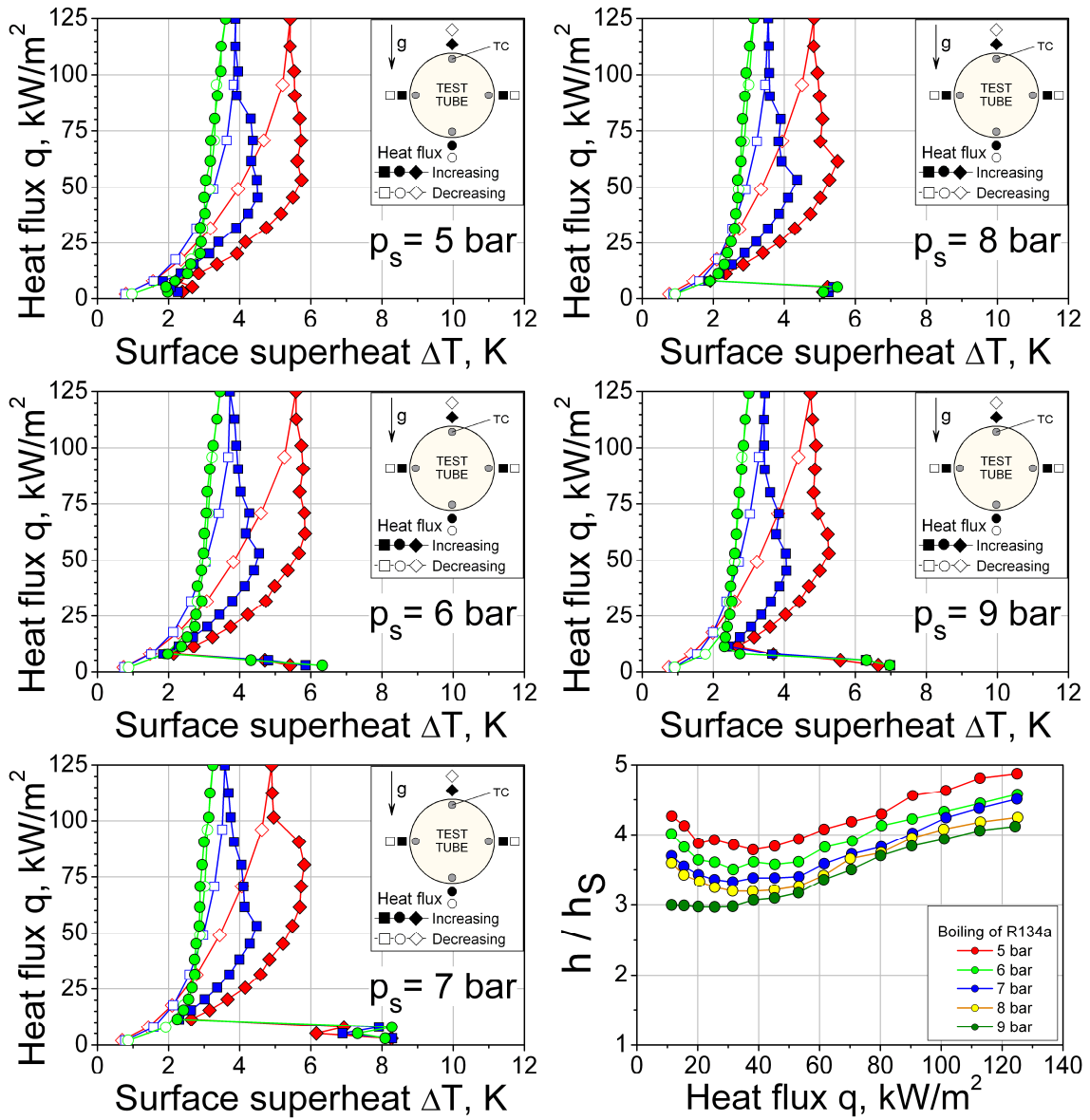
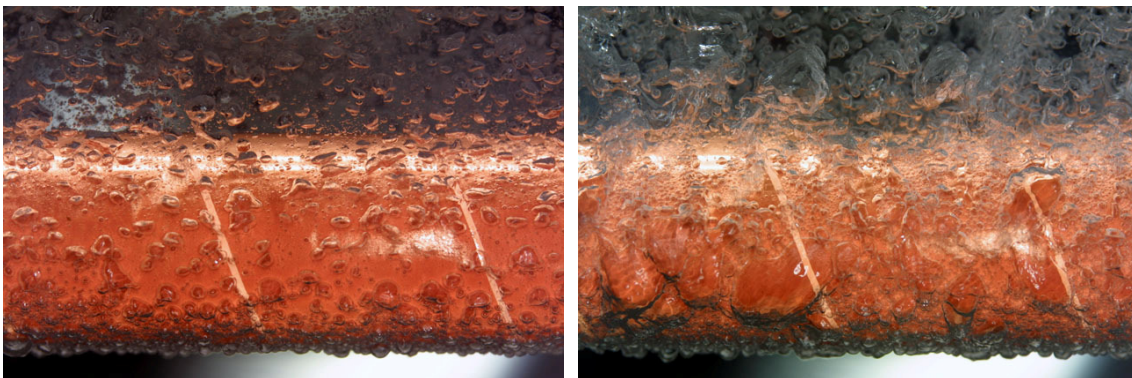


Figure 4.1.30: Boiling characteristics of A432 with R134a at different pressures.

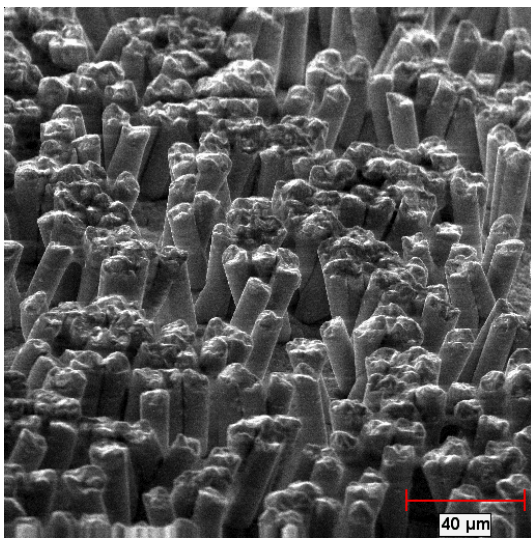


a) b)
Figure 4.1.31: R134a boiling on A432 at 8 bar: a) $q=25 \text{ kW/m}^2$, b) $q=125 \text{ kW/m}^2$.

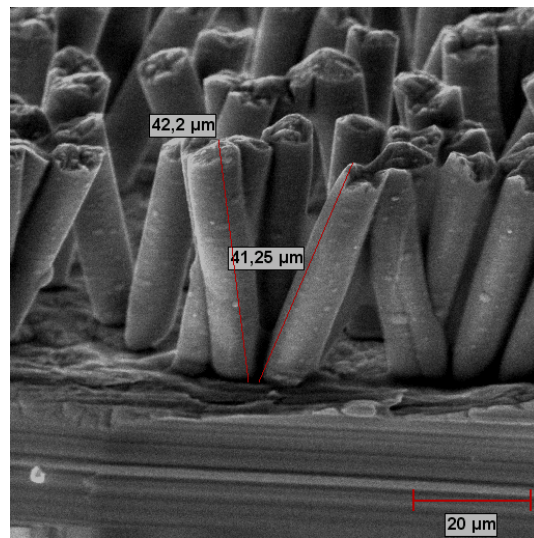
The surface superheat of microstructure A432 was largely independent on the heat flux, Figure 4.1.30. Boiling inception occurred at superheats between 2 K and 8 K and at heat fluxes below 5 kW/m². Figure 4.1.31 represents photographs of boiling R134a at 8 bar on A432.

Microstructure A425

SEM photographs of the next tested microstructure A425 are represented in Figure 4.1.32.



A425 zoom 500 x



A425 zoom 1000

Figure 4.1.32: SEM photos of the microstructure A425.

Experimental results for the microstructure A425 are presented in Figure 4.1.33. Boiling curves of R134a are steep and the surface superheat is weakly influenced by the heat flux. Although A425 is the bi-inclined microstructure, it has boiling reestablishment only for the low pressure region, and noticeable for 5 bar. The enhancement factor is narrowing the range of its values from 2 – 4 for low heat fluxes to 2.5 – 3 for higher ones, being weakly affected by the middle heat fluxes, Figure 4.1.33. The microstructured surface A425 has approximately 10 times lower pins density as other bi-inclined surfaces, investigated in the present work. Therefore the boiling reestablishing can only be noticed at low pressures, when the critical vapor bubble radius is relatively

large. For pressures above 5 bar pins act as isolated and their inclination has almost no effect on initial nucleation.

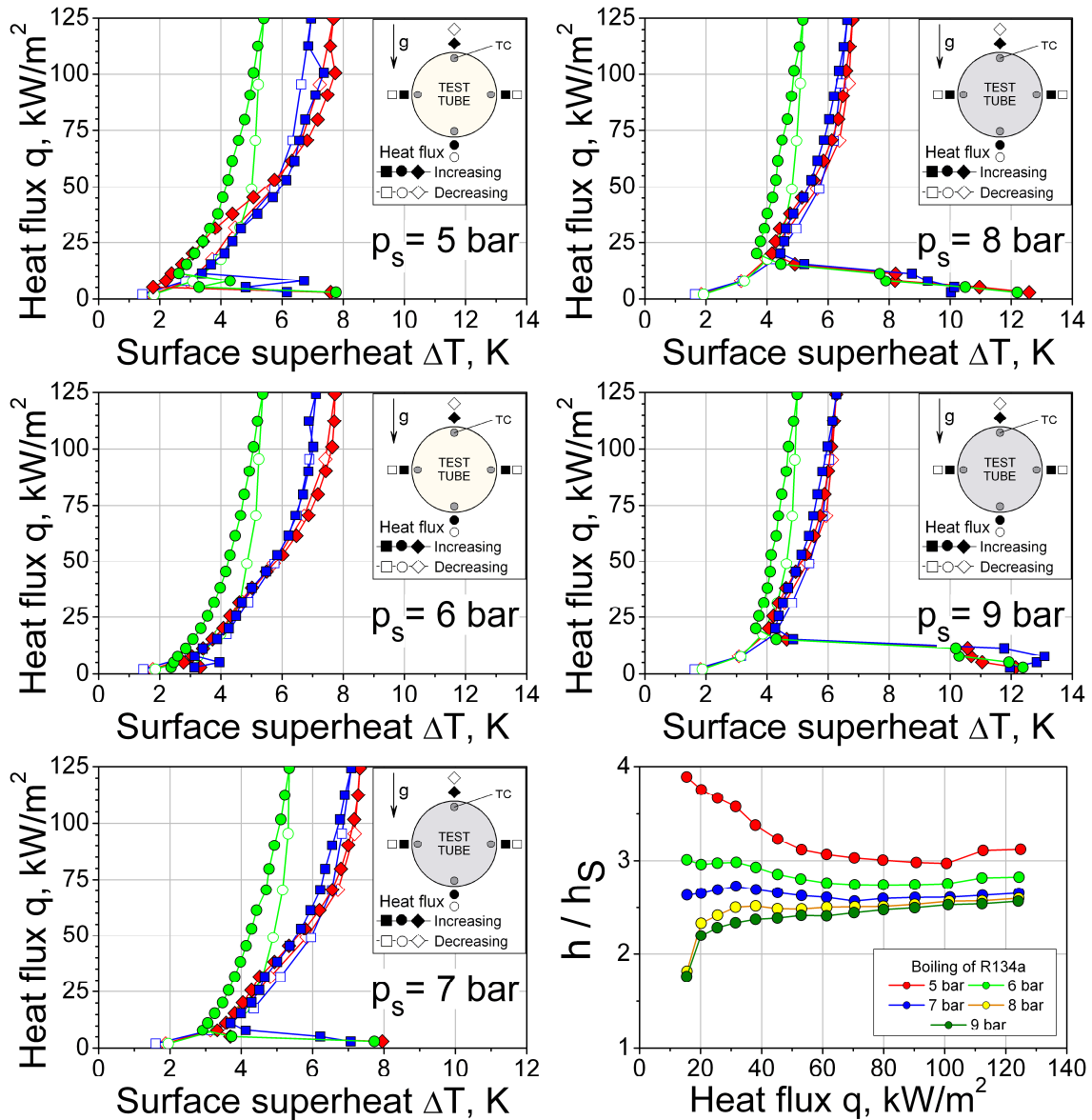
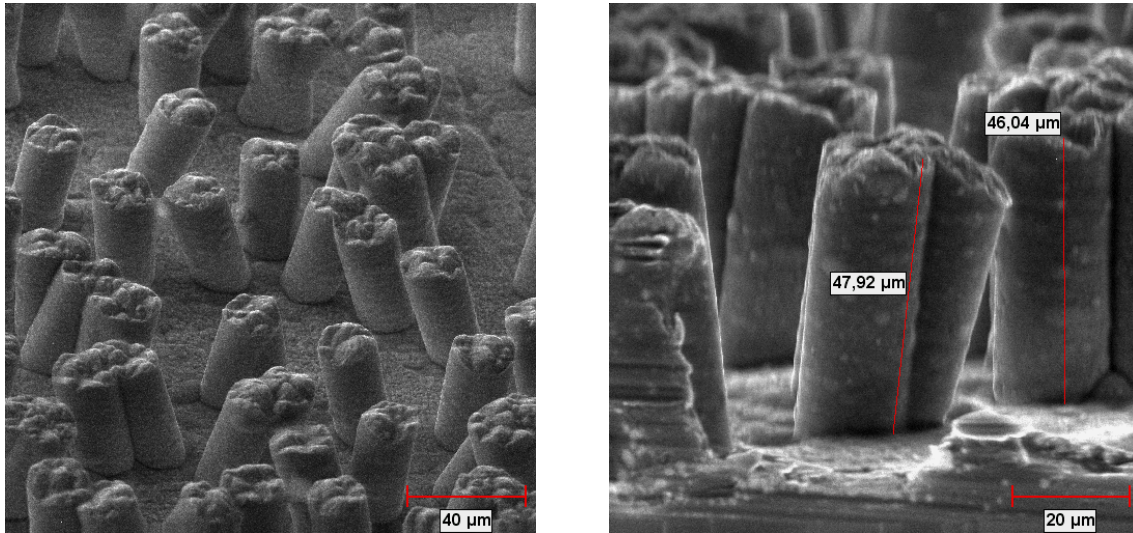


Figure 4.1.33: Boiling characteristics of A425 with R134a at different pressures.

Boiling inception occurred at the superheats of 3 K to 12 K with higher values for higher pressures. Boiling process at the pressures of 8 bar and 9 bar is characterized by an undeveloped region at the heat fluxes below 15 kW/m². Nevertheless, the microstructure A425 is effective and its superheats never exceeded the saturation temperatures at more than 8 K.

Microstructure A426

The next microstructured surface with bi-inclined rarified pins is presented at Figure 4.1.34.



A426 zoom 500 x

A426 zoom 1000

Figure 4.1.34: SEM photos of the microstructure A426.

Heat transfer of the boiling R134a from A426 has proved the earlier discovered tendencies for this type of surfaces. Weak influence of the applied heat flux on the surface superheat, influence of the rarefied bi-inclined pins, suppressed boiling hysteresis, and low surface spatial-temporal temperature gradients were observed for A426 as well as for other investigated surfaces. This particular microstructure was not extremely effective due to the low pins density and has demonstrated the slightly rising enhancement factor from 1.8 – 2.6 for low heat fluxes to 2.6 – 2.9 for higher ones, Figure 4.1.35.

Boiling inception occurred at the superheats from 2 K to 11 K and heat fluxes of about 5 kW/m². The higher values of inception superheat and heat flux are typical for boiling at high pressures. That is why a small region of undeveloped boiling took place on the microstructured surface. In engineering praxis, however, this can totally be neglected.

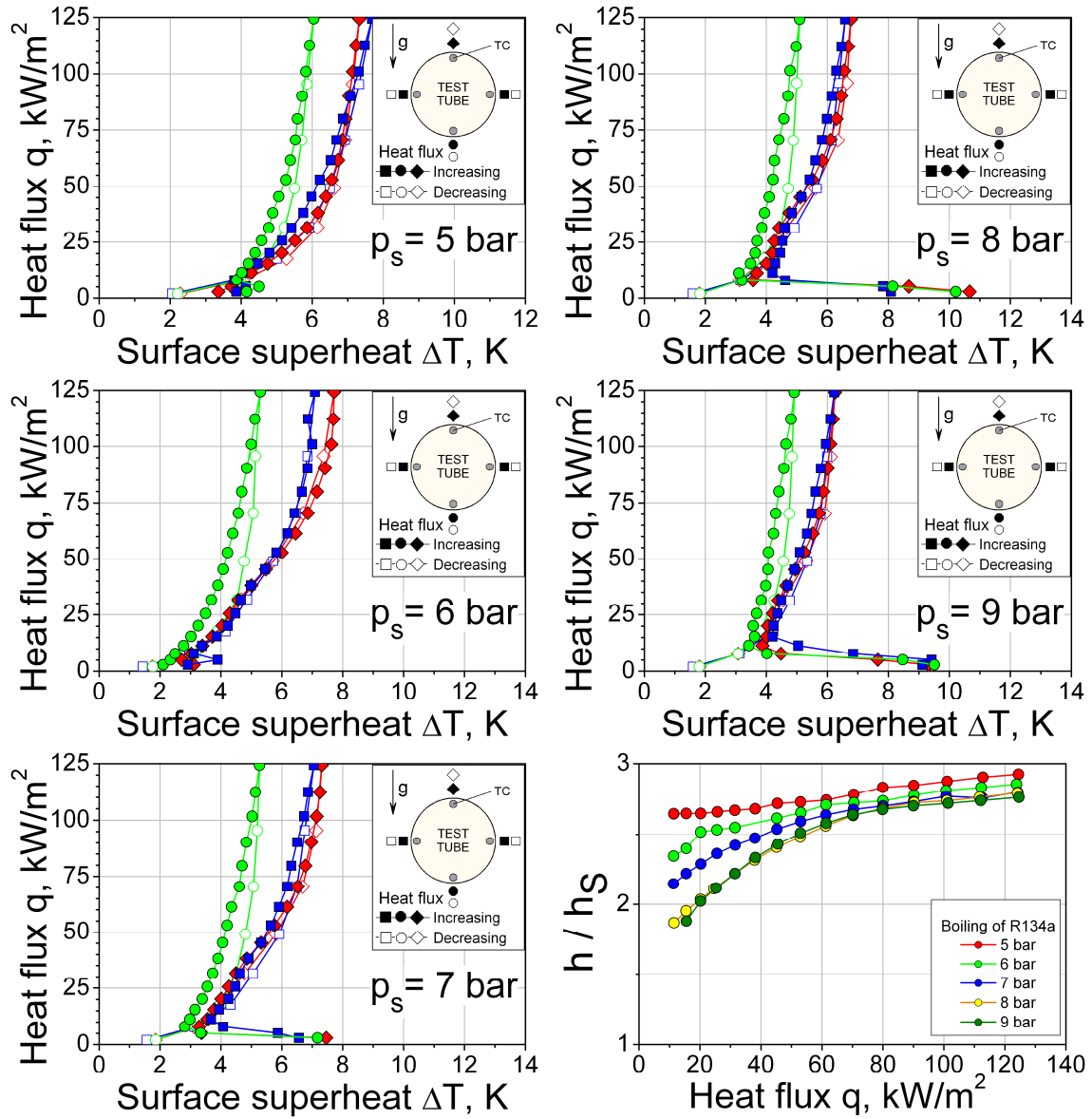
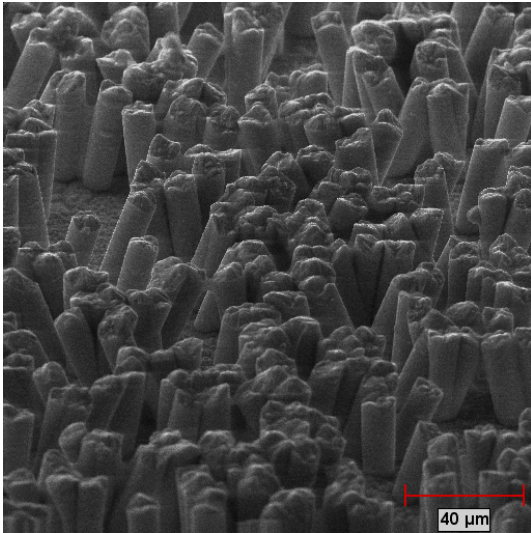


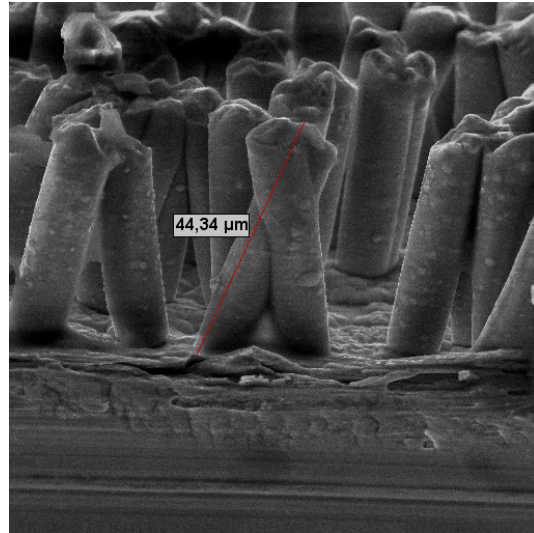
Figure 4.1.35: Boiling characteristics of A426 with R134a at different pressures.

Microstructure A427

Last microstructure tested with R134a boiling at pressures in range between 5 bar and 9 bar was A427, it is depicted in Figure 4.1.36.



A427 zoom 500 x



A427 zoom 1000

Figure 4.1.36: SEM photos of the microstructure A427.

Experimental results are presented in Figure 4.1.37, proving the above discussed common boiling properties. This structure efficiency was found to be independent on the heat flux with the enhancement factor 2.2 – 3.3 in dependence on the pressure, Figure 4.1.37. Boiling inception occurred at the maximal superheat of 9 K and heat flux of 10 kW/m².

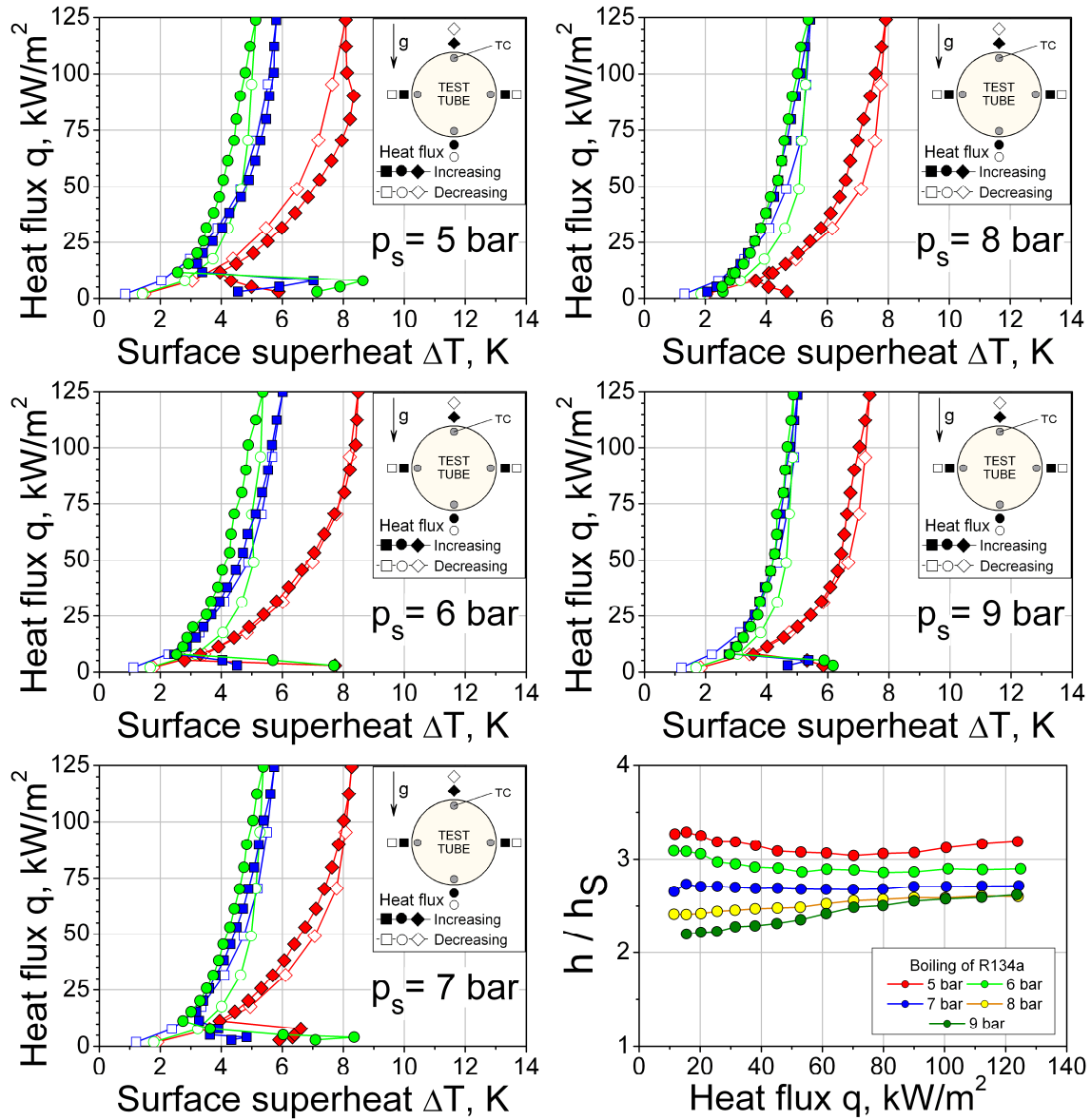


Figure 4.1.37: Boiling characteristics of A427 with R134a at different pressures.

Electronic liquid FC-3284

FC-3284 is a commercially available product for company 3M™. It is positioned by the producer as a substitute for its another product, FC-72. FC-3284 is a clear, colorless, thermally stable, fully-fluorinated liquid for use in many single phase heat transfer applications in the semiconductor manufacturing industry. It is suitable for a variety of applications such as etchers, ion implanters, testers, rectifiers and others. Because Fluorinert™ liquid FC-3284 is primarily a single compound, its composition will not shift or fractionate with time.

Microstructure A428

The microstructure A428 was the only one tested with all three liquids, employed in the study, finally with FC-3284 at pressures of 0.5 bar, 1.0 bar and 1.5 bar. Maximal heat flux in experiments with this fluid was decreased, as it had been noticed the heat flux $q = 75 \text{ kW/m}^2$ to be critical. Boiling inception of FC-3284 on A428 occurred at surface superheats of 11 K – 15 K, Figure 4.1.38. Like for two previously tested liquids, the surface superheats were weakly influenced by the applied heat flux. For FC-3284 the surface temperature in experiments never exceeded the saturation temperature for a given pressure for more than 6 K, Figure 4.1.38. Due to high wettability of FC-3284, vapor bubbles arising upon the surface are larger as for refrigerants. Therefore bubbles joint each other, causing the crisis to occur earlier, Figure 4.1.39.

Microstructure A428 with boiling FC-3284 has demonstrates enhancement factor to be from 2 for undeveloped boiling at low heat fluxes up to 5 for the developed mode, Figure 4.1.38. For pressures of 1 bar and 1.5 bar the enhancement factor is slightly rising with the increasing heat flux. Principal dependence of the enhancement on pressure remains for this liquid the same: the absolute values of heat transfer coefficients are increasing with increasing pressure, while values related to ones of a smooth tube, decrease, Figure 4.1.38.

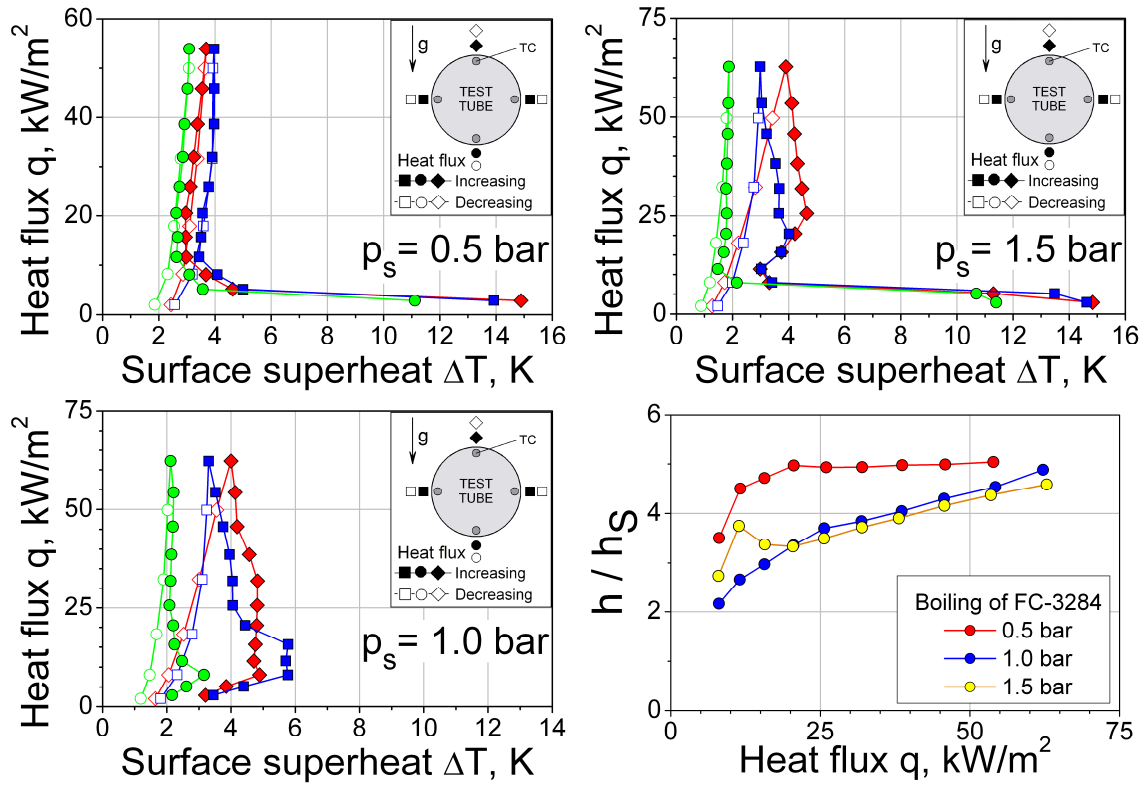


Figure 4.1.38: Boiling characteristics of A428 with FC-3284 at different pressures.

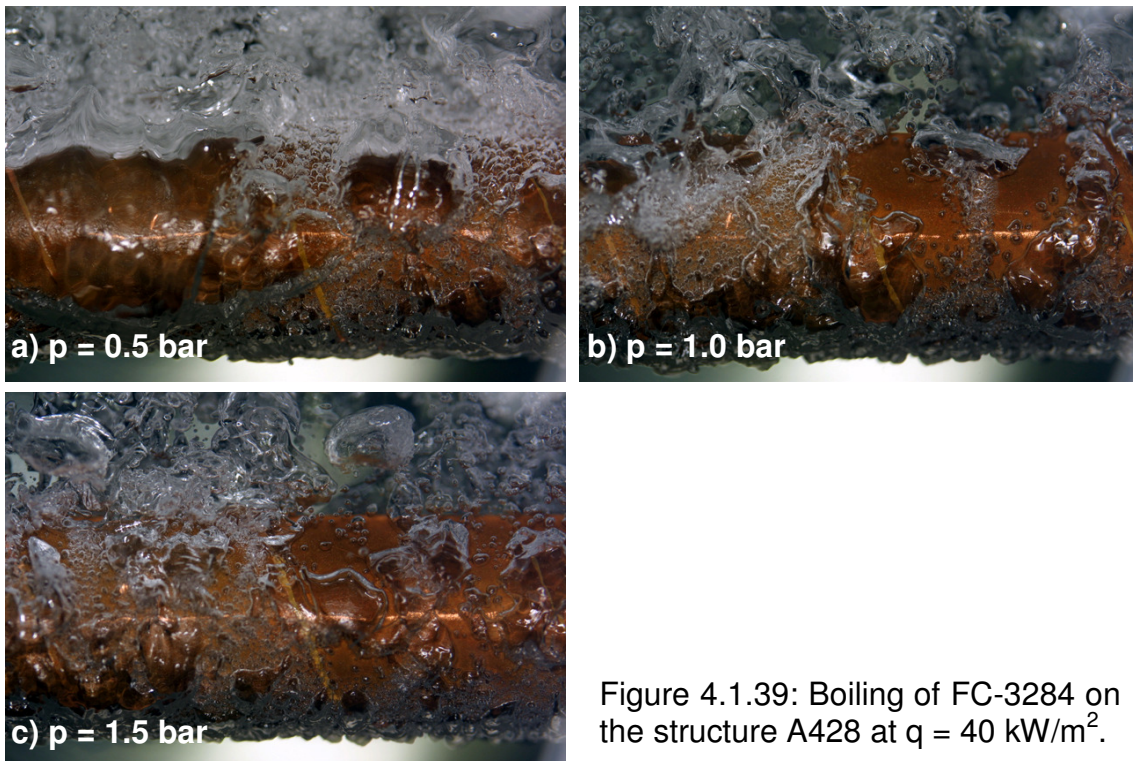


Figure 4.1.39: Boiling of FC-3284 on the structure A428 at $q = 40 \text{ kW/m}^2$.

Microstructure A437

Microstructure A437 which was found to be one of the most effective with boiling R134a was tested with FC-3284 as well. Experimental results are represented in Figure 4.1.40 as boiling curves. Measurements were conducted at heat fluxes starting from 5 kW/m^2 , so boiling inception occurred at the very first given heat flux, except for at underpressure of 0.5 bar, Figure 4.1.40.

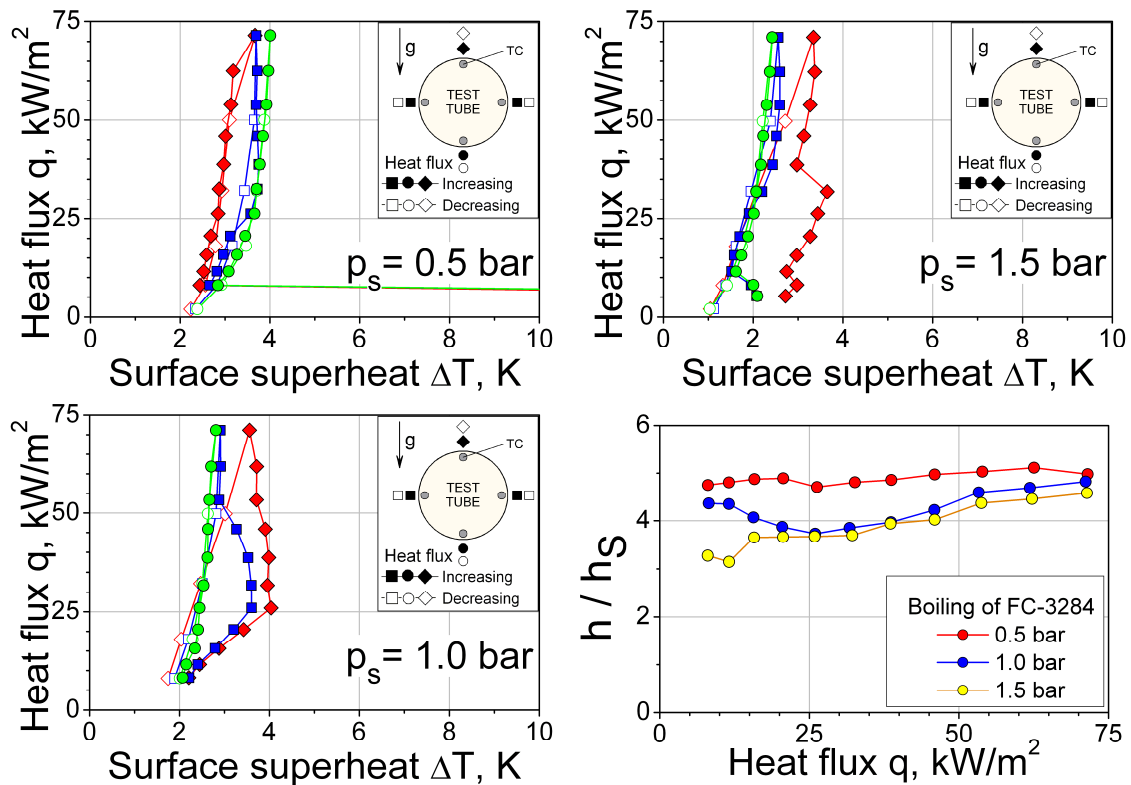


Figure 4.1.40: Boiling characteristics of A437 with FC-3284 at different pressures.

The surface superheats as well as the enhancement factor for microstructure A437 with boiling FC-3284 remained largely unaffected by the applied heat flux. Therefore, except for the low critical heat flux and a bit lower relative efficiency in comparison with a smooth tube, boiling process of FC-3284 was the same as for refrigerants. Both of those facts are explained by the higher wettability of the FC and subsequent change in the bubble dynamics.

Microstructure A435

Microstructure A435 was tested with FC-3284 for idem experimental conditions. Boiling inception occurred at the superheats of 2 K except for pressure of 1.5 bar, as at this pressure a small region of undeveloped boiling took place, Figure 4.1.41.

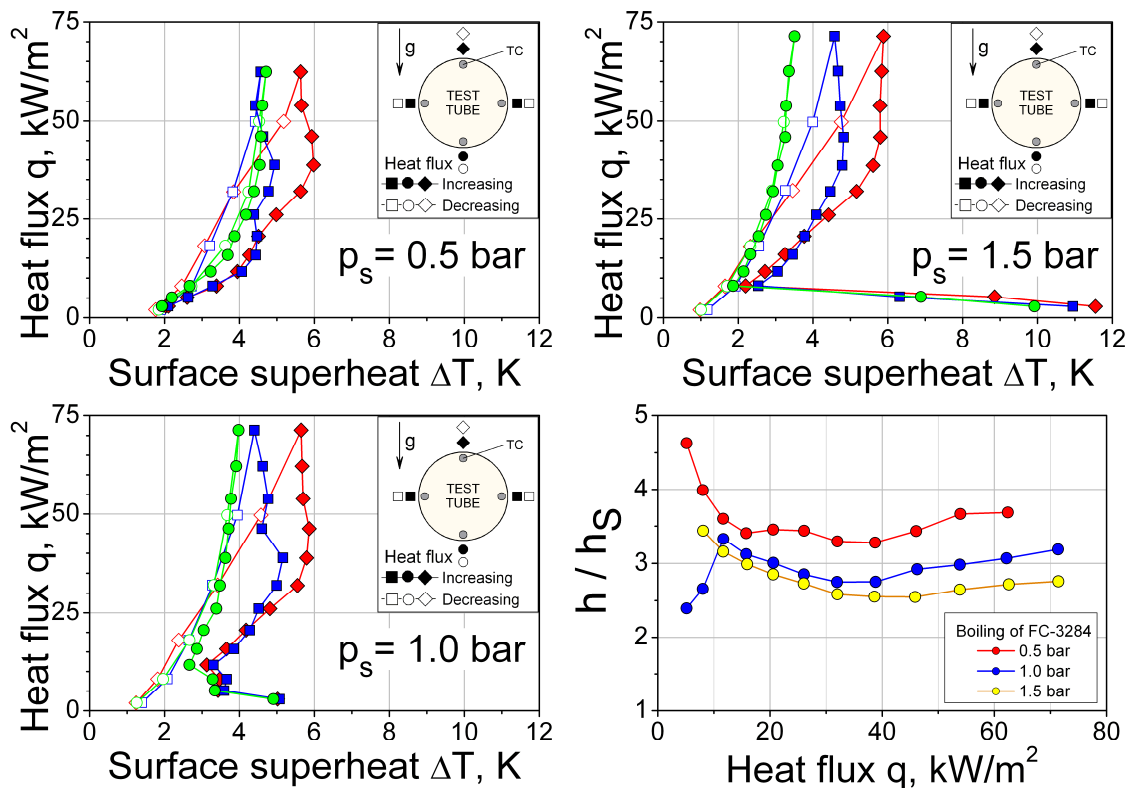


Figure 4.1.41: Boiling characteristics of A435 with FC-3284 at different pressures.

One may note that the microstructure A435 as well as A428 was tested at 0.5 bar only up to the heat flux of 65 kW/m². It was done, as the pre-critical condition has been detected at this pressure. The method of detection will be discussed in more detail below; it is based on the measuring of temperature oscillation of the surface. Right before the crisis the amplitude of temperature oscillations rises greatly, as larger vapor masses are formed and leave the surface. Liquid flow cools down the surface shortly after that, supplying nucleation sites with liquid in the repeating process. This is especially the case

for an underpressure boiling, as vapor bubbles are large, and they join each other more intensively, forming larger vapor conglomerates.

This method seems to be universal and can be recommended for detection and prevention of the boiling crisis.

Microstructure A431

Microstructured surface A431 was tested with FC-3284 under the same conditions as the above presented surfaces. Experiments with FC has found a little higher surface superheats as with refrigerants, Figure 4.1.42. Independency of the surface temperature on the applied heat flux holds for A431 as well. The efficiency with FC-3284 is somewhat lower in comparison with refrigerants, as and for other tested surfaces. However, the principle behavior is same: relative efficiency decreases with increasing pressure, and for A431 slightly rises with the increasing heat flux, Figure 4.1.42.

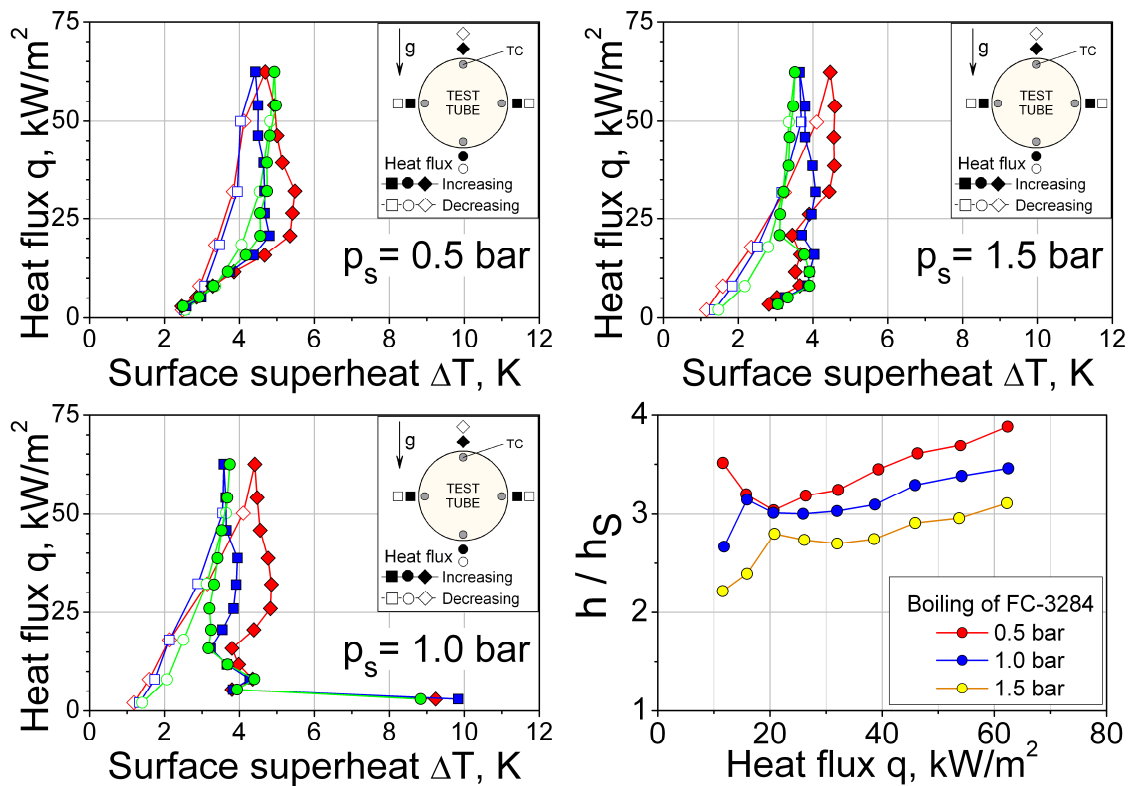


Figure 4.1.42: Boiling characteristics of A431 with FC-3284 at different pressures.

Microstructure A432

Microstructure A432 was tested with FC-3284 and has shown same heat transfer behavior as the whole family of novel microstructures. The only difference was existence of an undeveloped boiling region at all pressures, set in the experiments, Figure 4.1.43. This subsequently has mirrored in the dependence on the enhancement factor on the applied heat flux, Figure 4.1.43. There is a region below 20 kW/m² with relatively low (from 2 to 4.5) efficiency. Above this value of heat flux both the surface superheat and enhancement factor remains unaffected by the heat flux.

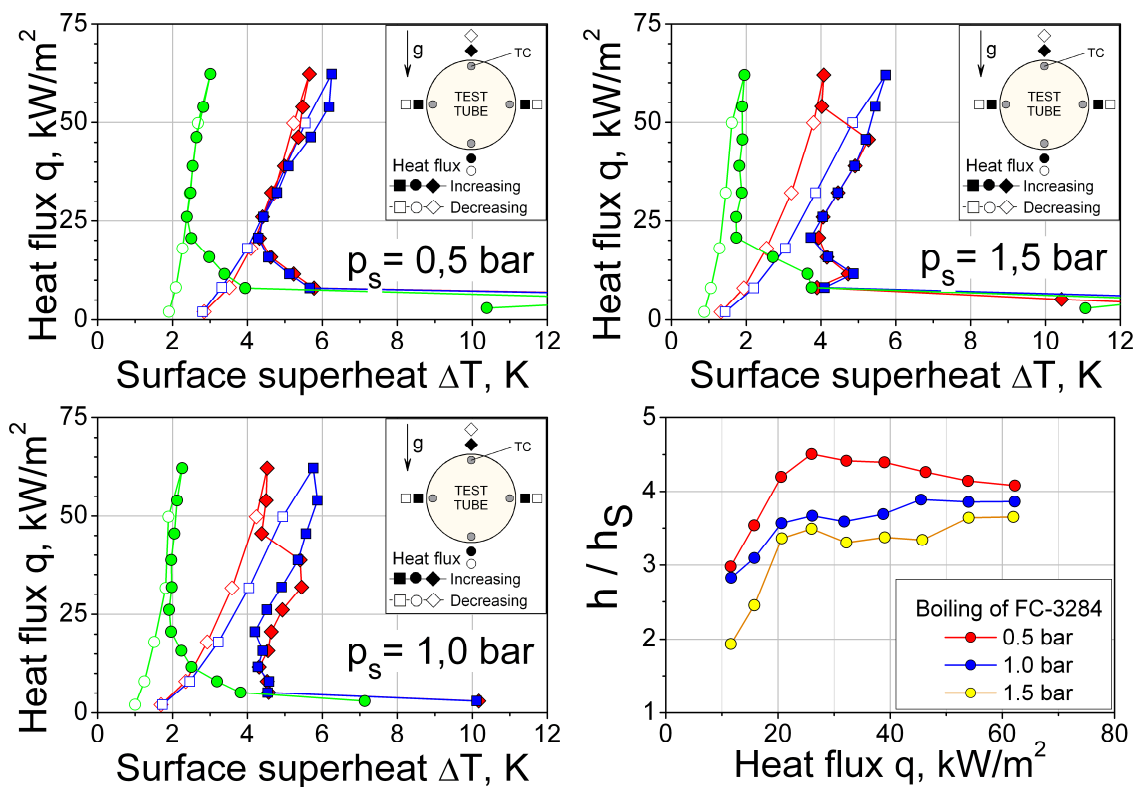


Figure 4.1.43: Boiling characteristics of A432 with FC-3284 at different pressures.

The explanation of such behavior lies in the specific geometry of the microstructure A432. It is the only surface with mono-inclined pins. In combination with high wettability of FC-3284 it prevents the tested liquid from penetrating in between the pins during boiling at normal gravity. Bottom of the test tube experiences this effect in the lower degree, as liquid is pressed by the

additional pressure of the liquid column towards the surface. It causes the bottom of the tube be the coolest place of the surface. This is especially significant at lower heat fluxes and boiling inception. Visual confirmation is represented in Figure 4.1.44: the tube bottom is covered with lots of small bubbles, while side and top have lack of them.



Figure 4.1.44: Boiling of FC-3284 on the structure A432 at $p=1$ bar, $q = 40 \text{ kW/m}^2$.

Microstructure A425

Microstructured surface A425 has demonstrated high surface superheats up to 11 K with boiling FC-3284, Figure 4.1.45. The enhancement factor of A425 was weakly influenced by the pressure as well as by the applied heat flux. This microstructure was approximately two times better as a technically smooth surface with boiling FC-3284 under idem conditions. Boiling reestablishing with FluorinertTM was observed for A425 only at the lowest pressure of 0.5 bar, as and with the refrigerant R134a at 5 bar, see Figure 4.1.33.

Despite the relatively high superheats, the microstructured surface A425 was producing many vapor bubbles at all heat fluxes, see Figure 4.1.46 for example. Due to high wettability of FC-3284, occurring vapor bubbles are larger than for R134a, even at low heat fluxes. This was one of the reasons why the boiling crisis occurred at lower heat fluxes as for the refrigerant.

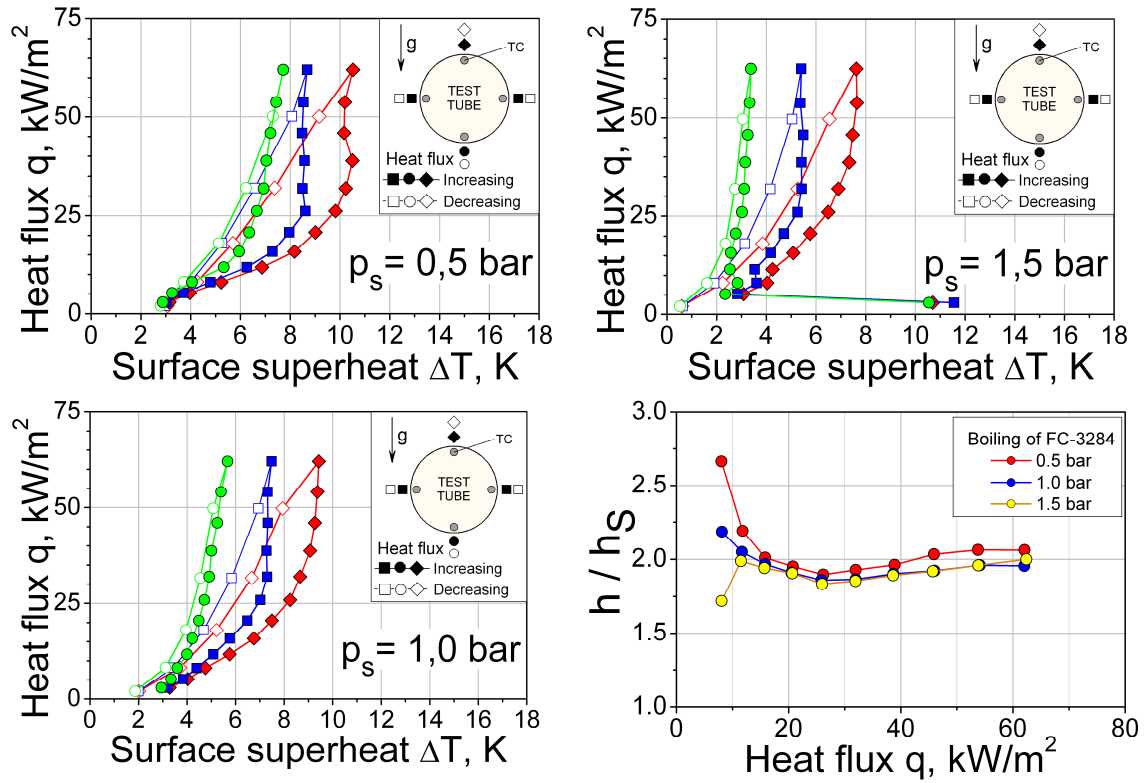


Figure 4.1.45: Boiling characteristics of A425 with FC-3284 at different pressures.



Figure 4.1.46: Boiling of FC-3284 on A425 at $p = 0,5 \text{ bar}$, $q = 3 \text{ kW/m}^2$.

Microstructure A426

Last microstructured surface tested with FC-3284 was A426. This surface has closed the experimental program with single tubes and has confirmed the earlier determined experimentally tendencies. As all other surfaces with all tested liquids, A426 has demonstrated weak dependency of the surface superheat on the heat flux, not exceeding the liquid saturation temperature at more than 10 K. Dependency of the enhancement factor on the pressure was same as earlier, namely decreasing with increasing pressure, being practically independent on the applied heat flux, Figure 4.1.47.

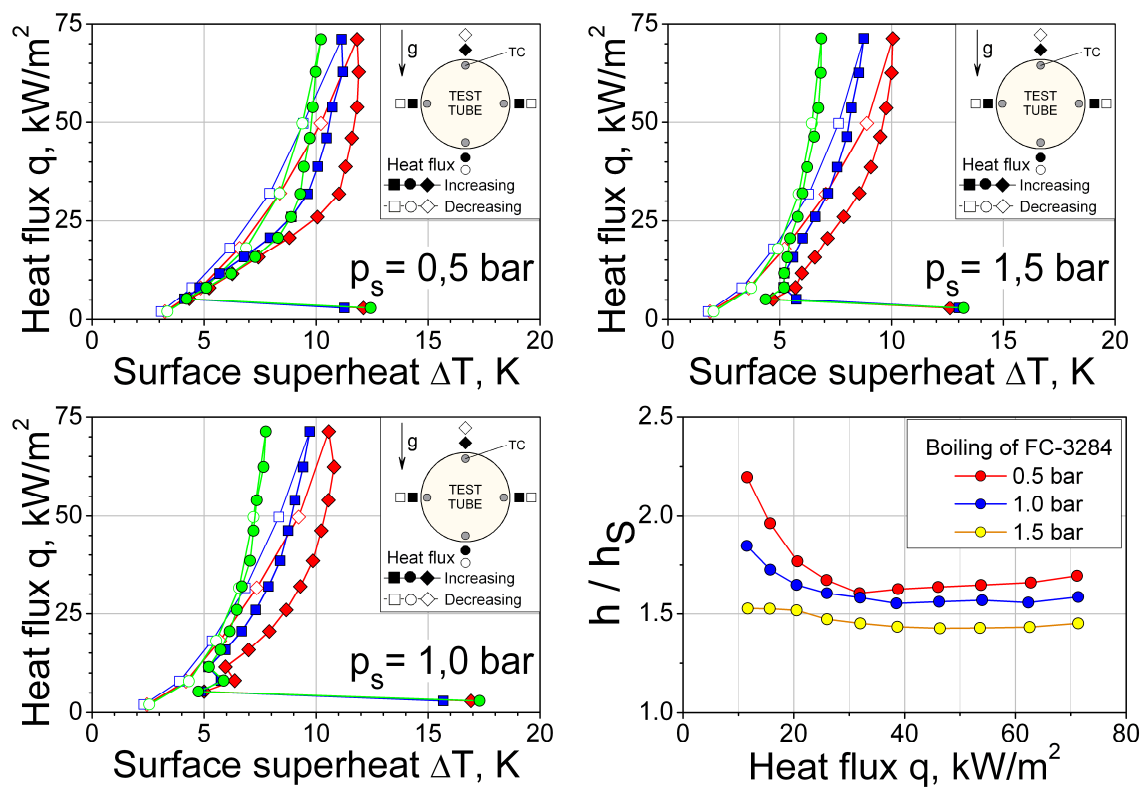


Figure 4.1.47: Boiling characteristics of A426 with FC-3284 at different pressures.

Boiling reestablishing was observed for A426 with FC-3284 at pressures of 0.5 bar and 1 bar, remaining practically hidden at 1.5 bar and at higher pressures, in earlier experiments with the refrigerant R134a, Figure 4.1.35.

4.2. Special boiling effects on microstructured surface

Before summarizing the experimental results it would be useful to remind and analyze the common properties for the family of novel microstructures, the unique as well as the known ones.

Constancy of the wall superheat

One of the main features of the novel microstructured surface is the constancy of the wall superheat, independently on the applied heat flux. Such behavior although somewhat astonishing was observed in a different degree for all surfaces tested in the present work. This feature can be used in many applications critical to the stability of the performance, cooling of electronic components taking as an example. The constancy of the heated wall superheat was detected with all tested liquids, allowing expecting the same behavior for any other liquid under a certain conditions. Figure 4.2.1 represents some typical boiling curves for different microstructures, test liquids and system pressures, covering roughly the whole range of parameters, varied in the present experimental program.

Explanation of the wall superheat constancy is that new microstructured surface serves the great number of potential nucleation sites. Homogeneously applied microstructures form mono- or bi-cavity patterns on the heat transfer surface. Using equation (2.1.2) one immediately finds the corresponding superheat, required for activation of a single cavity. As all of the cavities have approximately same size, they become activated at the same heat flux. Further increase of the heat flux results in changing of the dynamical characteristics of vapor bubbles, but not in activation of additional nucleation sites. Therefore, the nucleation sites density remains the same, holding the surface temperature at a constant value.

This effect will be considered in the work later one more time, theoretically.

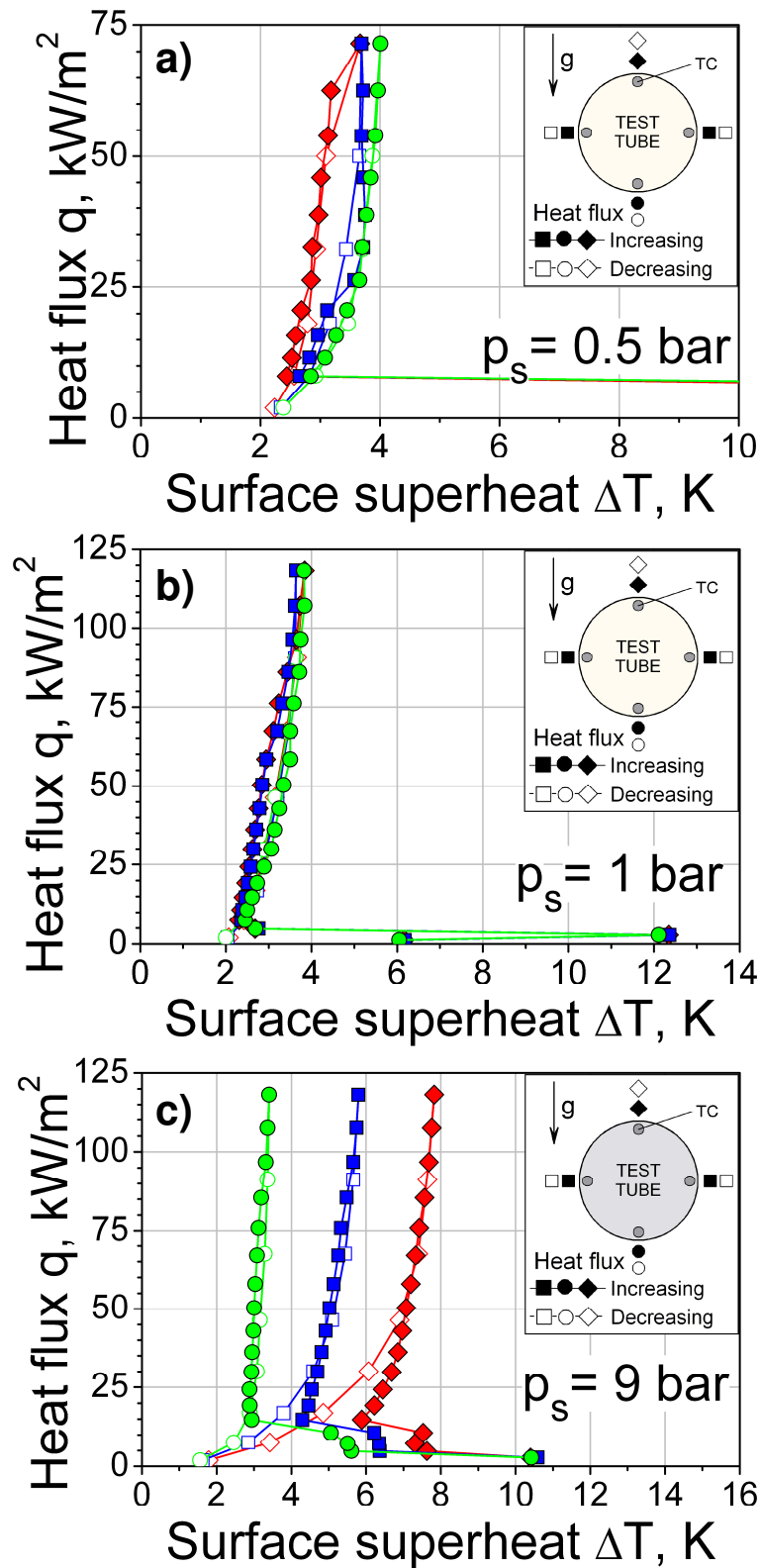


Figure 4.2.1: Constancy of the wall superheat,

- a) Microstructure A437, FC-3284, $p = 0.5$ bar;
- b) Microstructure A428, R141b, $p = 1$ bar;
- c) Microstructure A419, R134a, $p = 9$ bar.

The effect of the wall superheat constancy has extended itself and resulted for several microstructures under certain conditions in the **decrease of the surface superheat with the increasing heat flux**. This feature is absolutely unique to the knowledge of the author. Basically it means that a microstructured surface cools itself down while being heated up. Figure 4.2.2 represents this experimentally discovered effect for different structures, liquids and pressures.

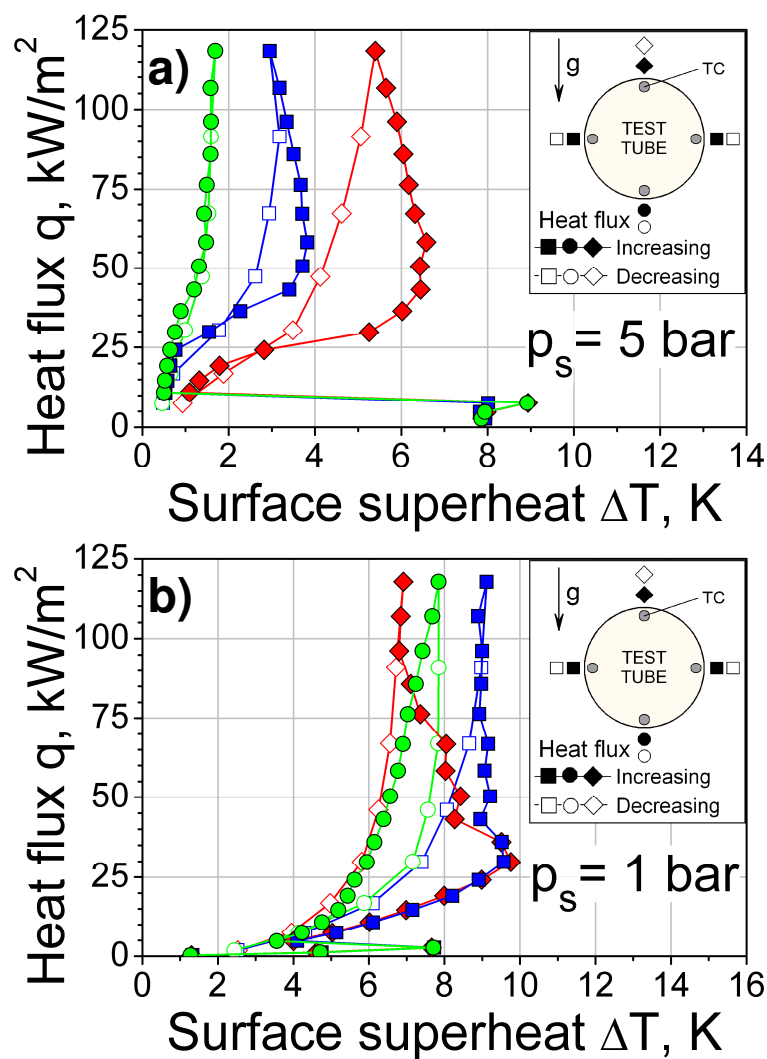


Figure 4.2.2: Decrease of the surface superheat with the increasing heat flux,

- a) Microstructure A428, R134a, $p = 5$ bar;
- b) Microstructure A418, R141b, $p = 1$ bar.

Some possible explanations of this phenomenon can be found in Mitrovic [4]. This quite unique behavior is explained from positions of heat and mass transfer in the wedge region of a growing vapor bubble, pierced by a large number of micro pins, Figure 4.2.3.

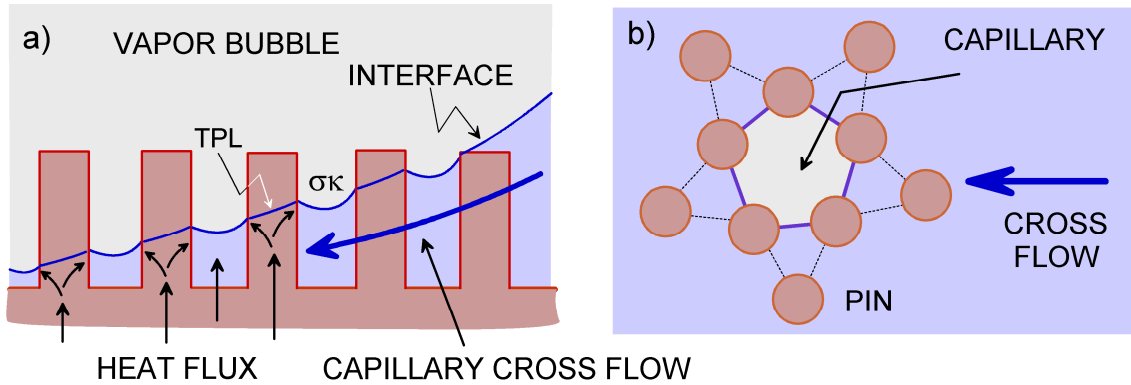


Figure 4.2.3: Fluid flow in the wedge region of a vapor bubble growing on the microstructured surface [4].

With increase of the heat flux the amount of vapor inside the microstructure increases as well. Subsequently, the number of pins, penetrating the growing vapor bubbles increases. The most effective evaporation is known to occur along the three phase line (TPL). Thus increase of the heat flux finally leads to the increase of the TPL length. Suddenly at higher heat fluxes additional heat sinks arise that cool down the surface even more effectively. This is especially the case for the top forming of the test tube, where amount of vapor is maximal. As confirmed by the measurements (Figure 4.2.2) the effect of cooling at rising heat flux the most sound for the top forming of the test tube.

Boiling inception as a front

For majority of known enhanced surfaces the boiling process starts spontaneously in a single spot with preferable physical-chemical conditions, spreading later along the whole surface with the increasing heat flux. For the novel microstructured surface it was discovered in the present study that at low pressures, i.e. the highest relative efficiency, the boiling process starts as a fast moving front along the entire surface.

Boiling process of R141b with A428 at 1 bar was preceded by strong convection, resulting in ascending streams of liquid (Fig. 4.2.4a). A video of the boiling inception was obtained using a standard digital camera with 25 frames per second. As it can be seen from the pictures, nucleation starts on the right side of the tube and moves as a boiling front to the left. The boiling front consists of relatively large single bubbles as well as of bubble conglomerates, the occurrence of which results in a measurable pressure jump in the system. After the boiling front passes the heated tube section from right to left, extremely active boiling establishes on the tube surface for about 0.32 s, characterized by swarms of bubbles. At the same time, the boiling front becomes reflected from the left end of the tube, and instead of bubble conglomerates, smaller bubbles form the front that now moves in the reverse direction, see Figure 4.2.4e. The transient flow took about 0.88 s. After that time span, stable nucleate boiling establishes on the whole tube surface. In the repeated experiment, the nucleation was initiated on the left side of the tube and, unlike Figure 4.2.4, the boiling front moves to the right, Figure 4.2.5.

Boiling inception of R141b with A428 at 2 bars was approximately the same as at 1 bar (Figure 4.2.4) with a boiling front moving from right to left (Figure 4.2.6). The main difference was that there were two boiling fronts instead of a single one reflected from the end of the tube. The first front, like for 1 bar, was reflected from the left end of the tube; the second front has followed the first one and moved in the same direction, see Figure 4.2.6e. Approximately in the middle of the test tube they met each other and overlapped. Afterwards stable nucleate boiling has established on the whole tube surface.

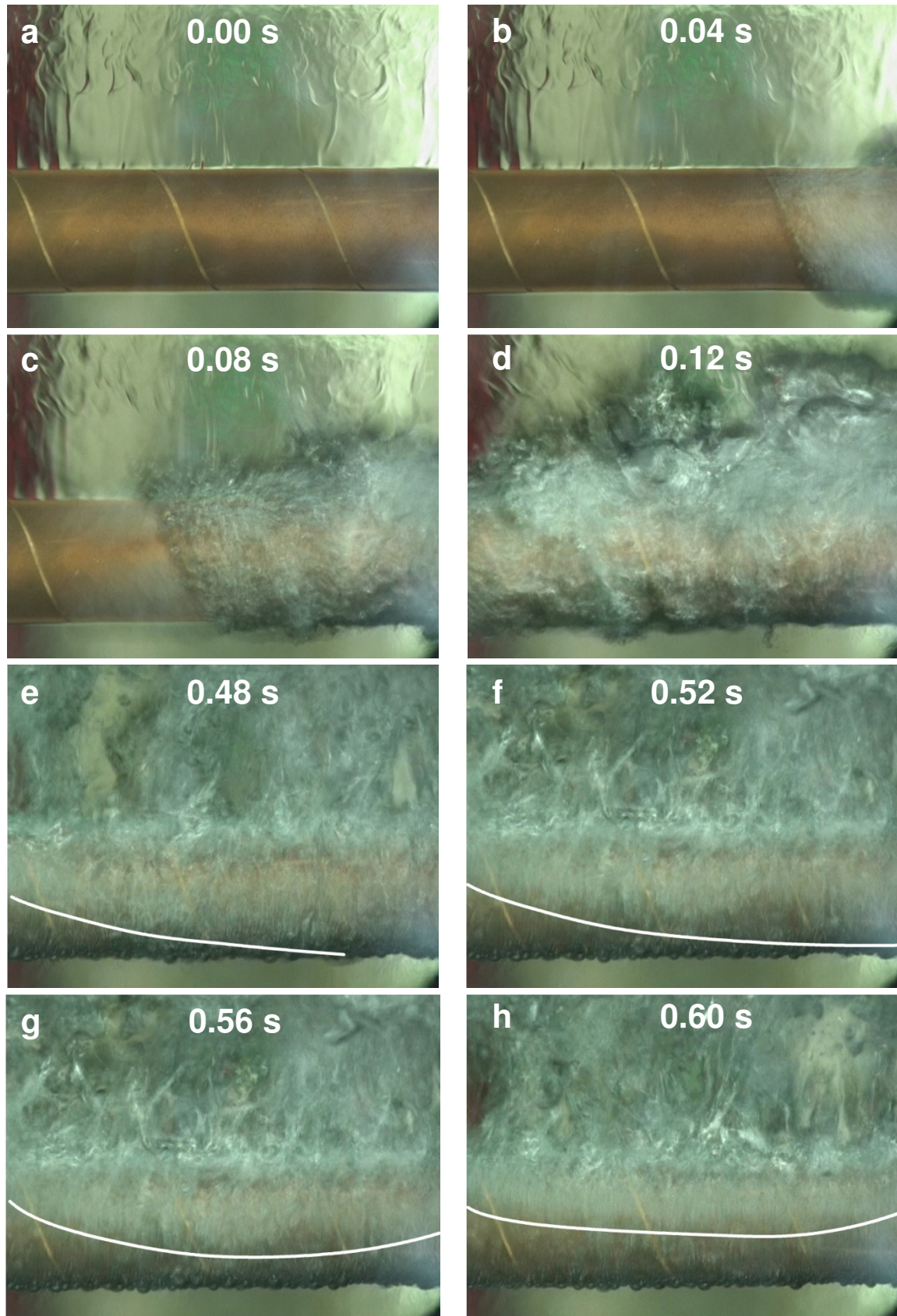


Figure 4.2.4: Front boiling inception of R141b with A428 at 1 bar, $q = 3.8 \text{ kW/m}^2$.

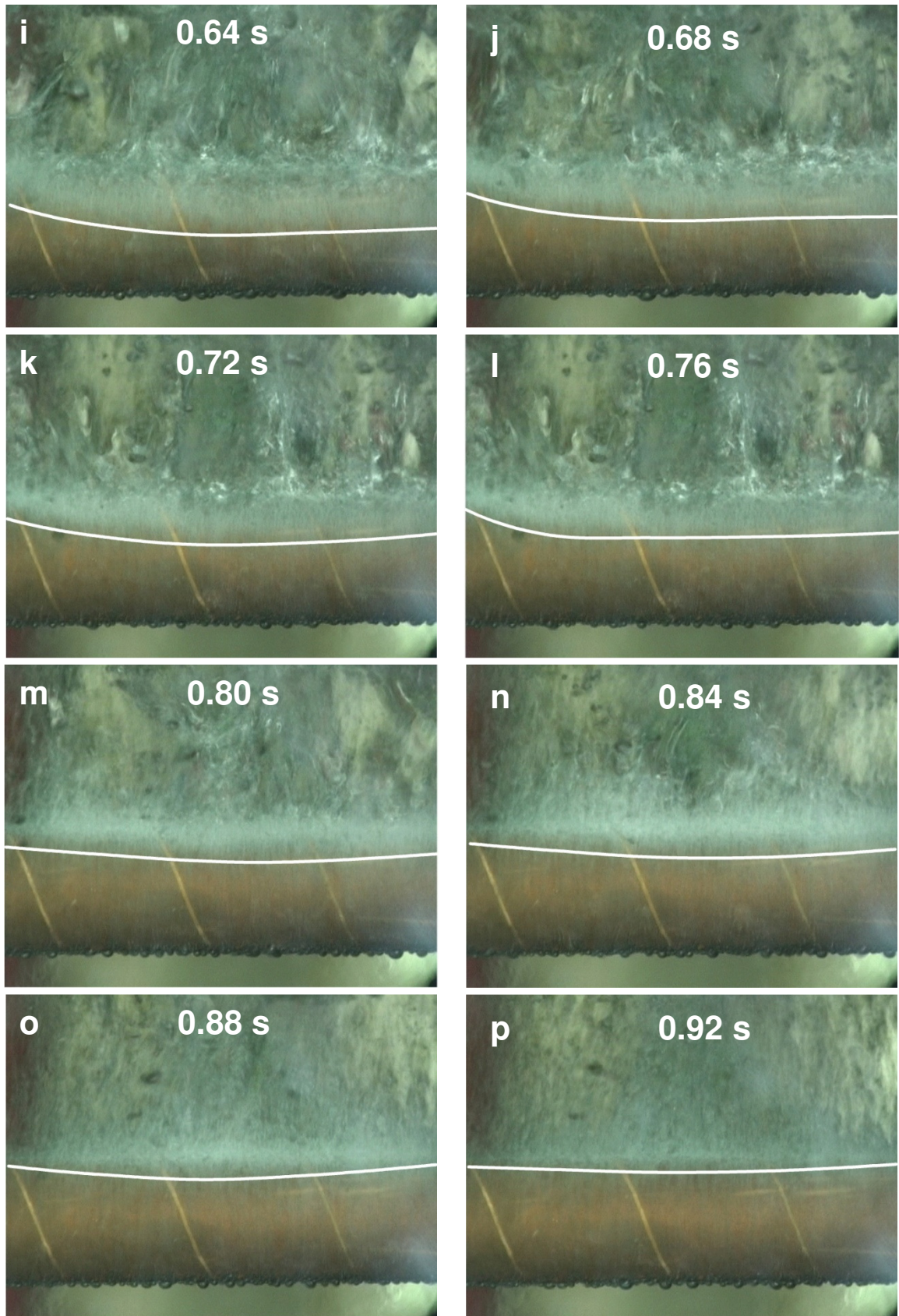


Figure 4.2.4: continue.

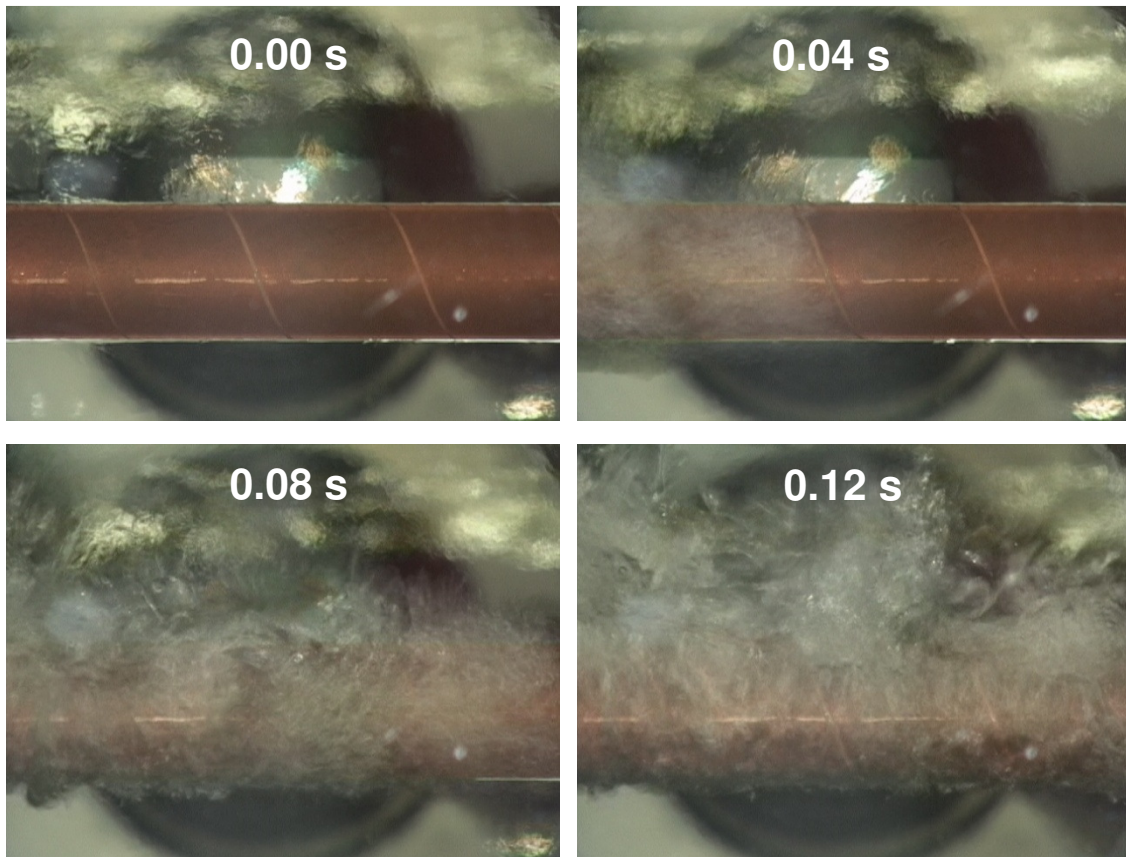


Figure 4.2.5: Boiling inception of R141b with A428 at 1 bar in a repeated run.

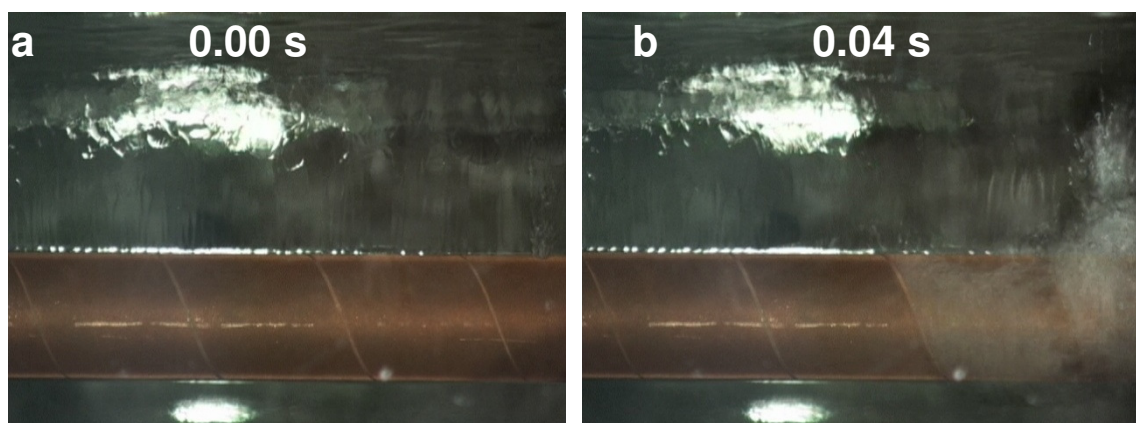


Figure 4.2.6: Double front boiling onset of R141b with A428 at 2 bar, $q=6.2$ kW/m².

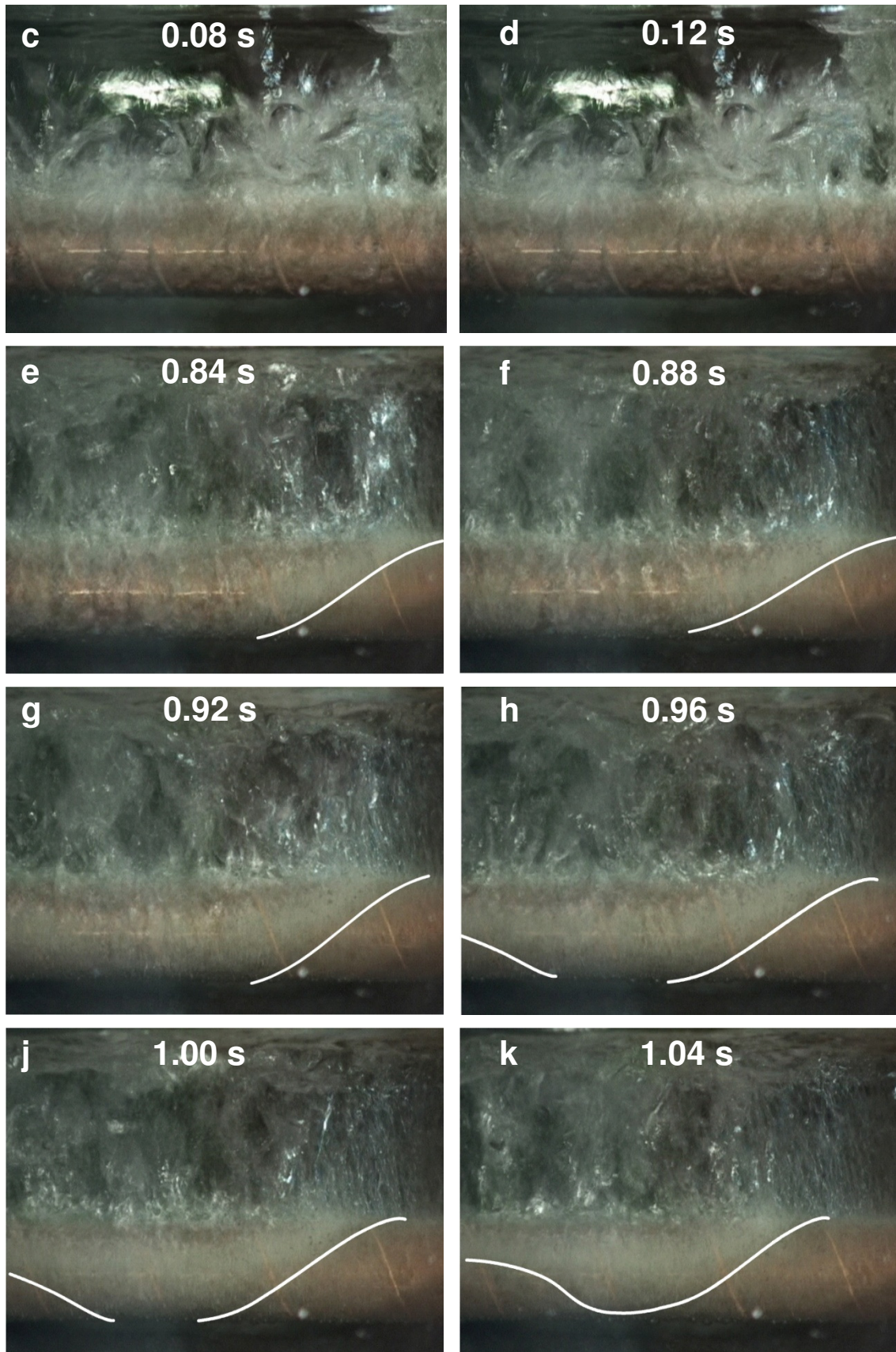


Figure 4.2.6: continue.

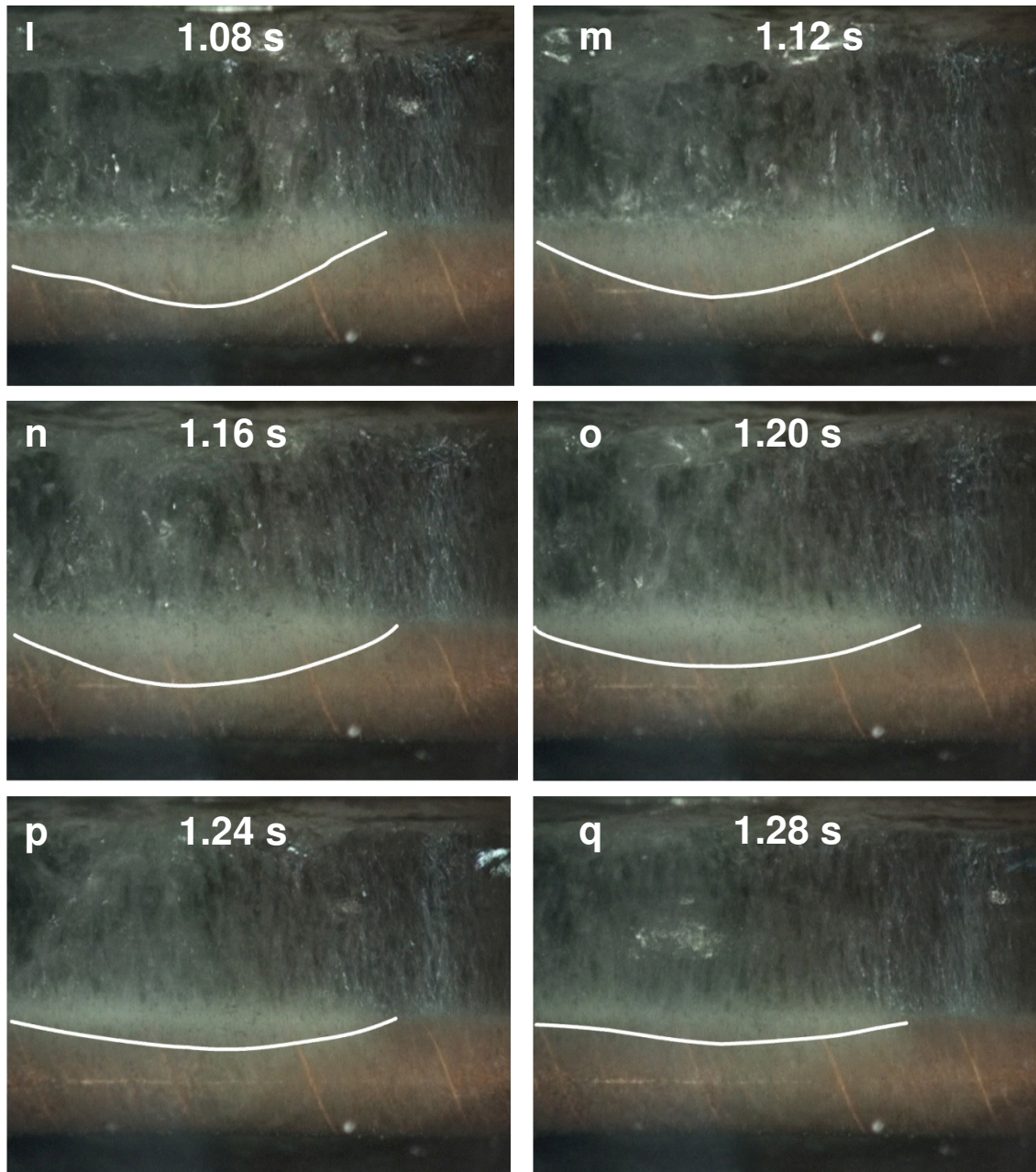


Figure 4.2.6: continue.

Boiling inception as a front was typical for the refrigerant R141b. For the refrigerant R134a it was not observed, as experiments with this fluid were conducted at higher pressures, starting from 5 bar. The third tested liquid Fluorinert™ FC-3284 has demonstrated boiling inception as a fast moving front too, as it was tested at pressures starting from 0.5 bar, Figure 4.2.7.

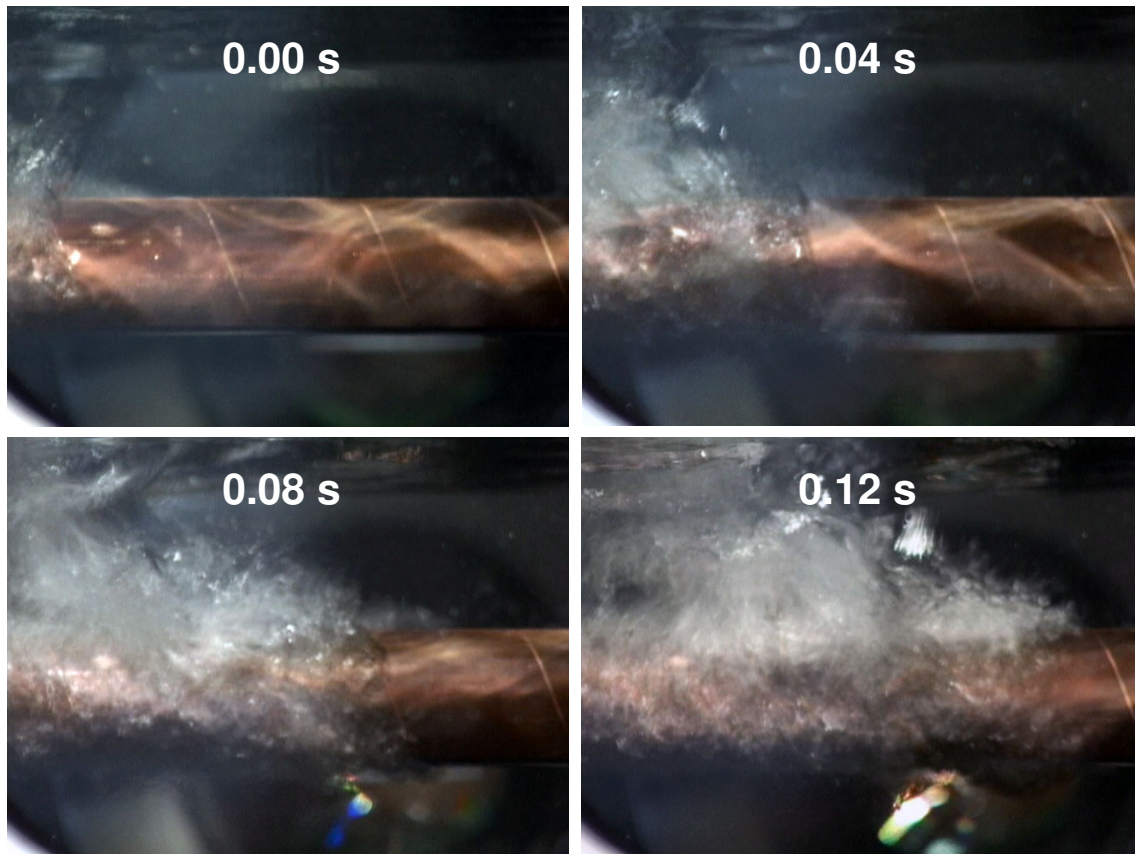


Figure 4.2.7: Boiling inception of FC-3284 with A428 at 0.5 bar.

Boiling front propagation velocities, which can be roughly estimated from Figures 4.2.4 – 4.2.8, lie between 50 cm/s and 100 cm/s. Propagation velocity of a boiling front seems to depend on the microstructure geometry, and to be less dependent on type of the liquid. However, exact determination of such dependency was not a goal of the present study. Boiling inception as two fronts observed for R141a at 2 bar with A428 is a manifestation of the bi-cavity pattern of the microstructure.

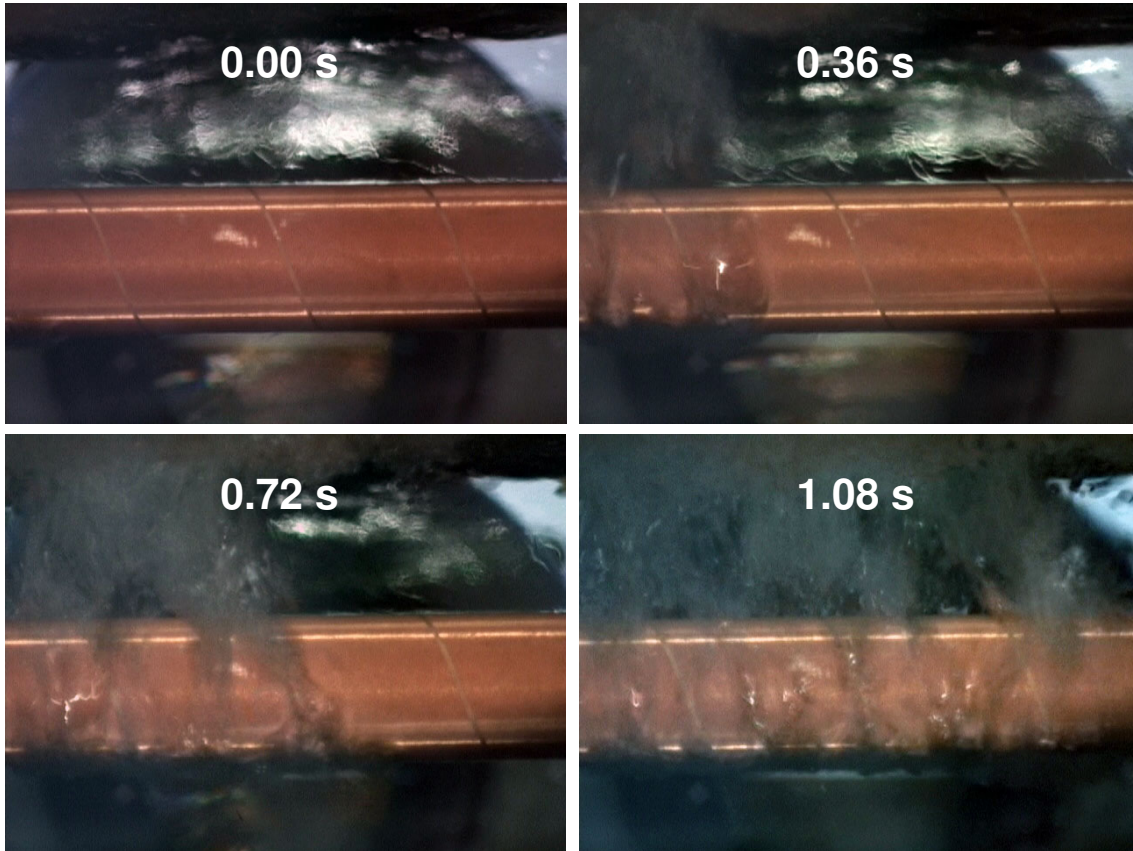


Figure 4.2.8: Boiling inception of FC-3284 with A435 at 0.5 bar.

Boiling crisis

As mentioned earlier, the electronic liquid FC-3284 employed in the present study has a very high wettability towards metallic surfaces. Due to this property, larger vapor bubbles are formed in this liquid in comparison with refrigerants. This condition leads to occurrence of earlier boiling crisis already at moderate heat fluxes. Heat flux of 75 kW/m^2 was experimentally detected to be critical for majority of surfaces tested with FC-3284.

Surface temperature oscillations during boiling are well-known phenomena. Vapor bubbles cool down the surface locally at a nucleation site during their origin and growth. Then temperature is gained back by nucleation site, after bubble detaches from it. In the present study it was detected that right before boiling crisis amplitudes of temperature oscillation of the microstructured surface are much larger than at lower heat fluxes, Figure 4.2.9.

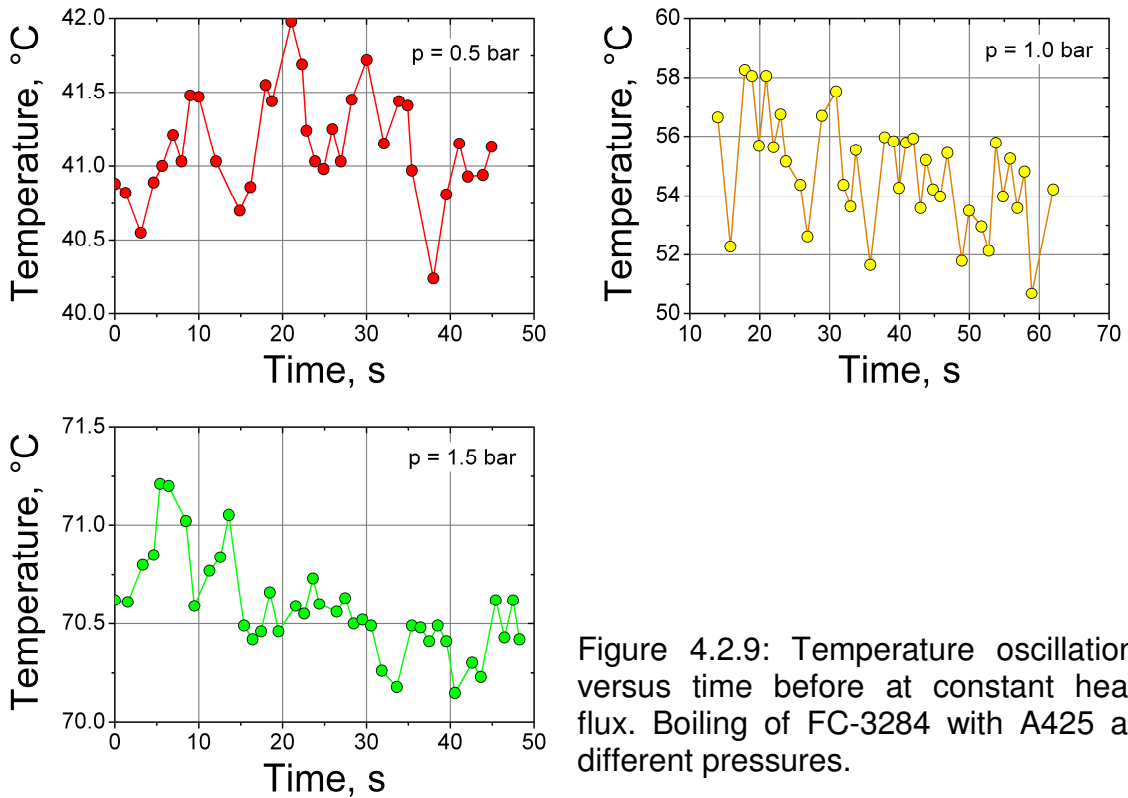


Figure 4.2.9: Temperature oscillation versus time before at constant heat flux. Boiling of FC-3284 with A25 at different pressures.

Amplitude-frequency characteristics of the surface temperature pre-crisis oscillations seem to depend on the geometry of the surface. Figure 4.2.10 gives temperature time signals for microstructure A437 for comparison.

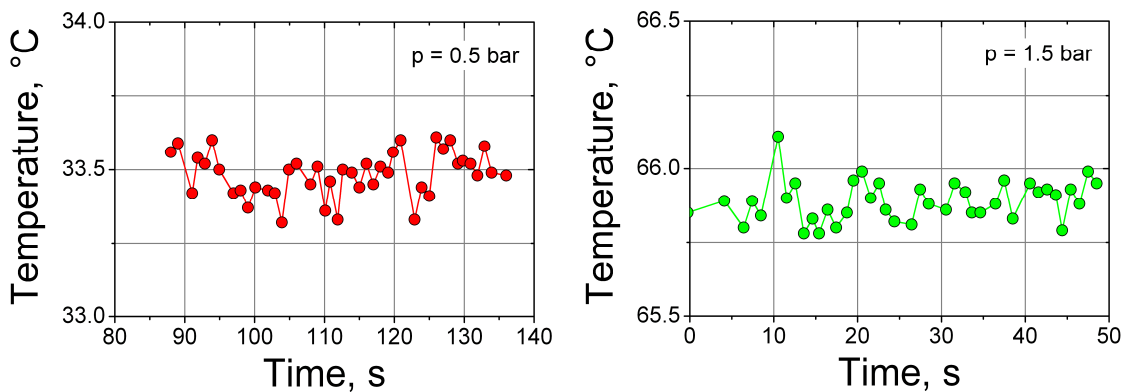


Figure 4.2.10: Temperature oscillation in time before boiling crisis of FC-3284 with A437 at different pressures.

Explanation of such behavior although seldom met in literature is quite simple. The process of bubbles join is especially intensive near the critical heat flux. Large amounts of vapor occurring and leaving the surface cause its

temperature to oscillate with greater amplitude as in separate bubbles boiling mode. This feature could be used in industrial apparatus for detecting and preventing the arising of the boiling crisis and burn-out of heat transfer surfaces.

For further analysis the mathematical apparatus of autocorrelation and chaotic dynamic was used, [51, 52]. Attractor based on the experimental measurements is represented in Figure 4.2.11. It shows that for a given time delay after the beginning of observation, amplitudes and frequencies are located in a relatively narrow field of the phase space. It makes possible to predict the developing crisis when measured parameters tend to tighten near a certain phase area.

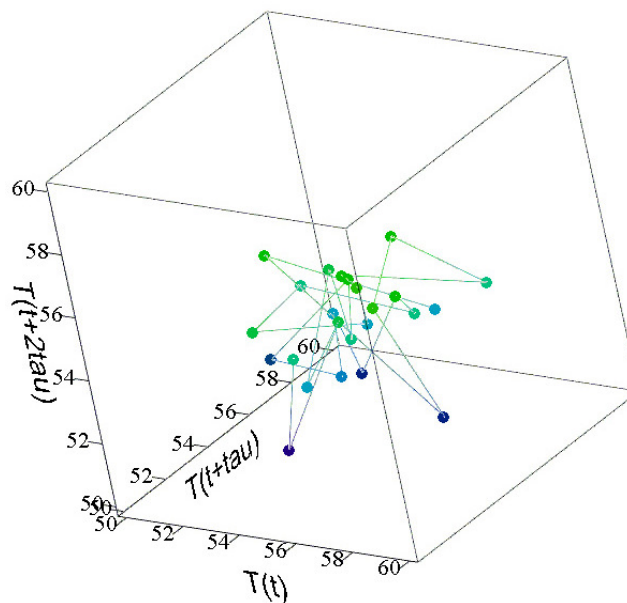


Figure 4.2.11: Attractor based on the measured temperature oscillations for microstructure surface A425 with boiling FC-3284 at 1 bar.

Another conclusion can be drawn basing the experimental observations: the critical heat flux depends on the microstructured surface geometry, as not every tested surface has exhibited 75 kW/m^2 to be the critical heat flux. The dependency of surface properties on the critical heat flux is not taken into account by the known approach of Kutateladze [45], considering instead the instability of Taylor “cold phase above the hot one”. Another approach, being developed for several last years by Bar-Cohen [46], takes into account wider

range of influencing parameters, namely fluid properties, pressure, subcooling, heater geometry, and “controversial” effects of surface property.

Boiling hysteresis

Term “hysteresis” for boiling process means non equality of surface temperatures at equal heat fluxes during increase and decrease of the heat load. Experimentally was found that boiling hysteresis for microstructured surface depends on pressure, liquid properties and the microstructure geometry, as a consequence of the change in nucleation conditions.

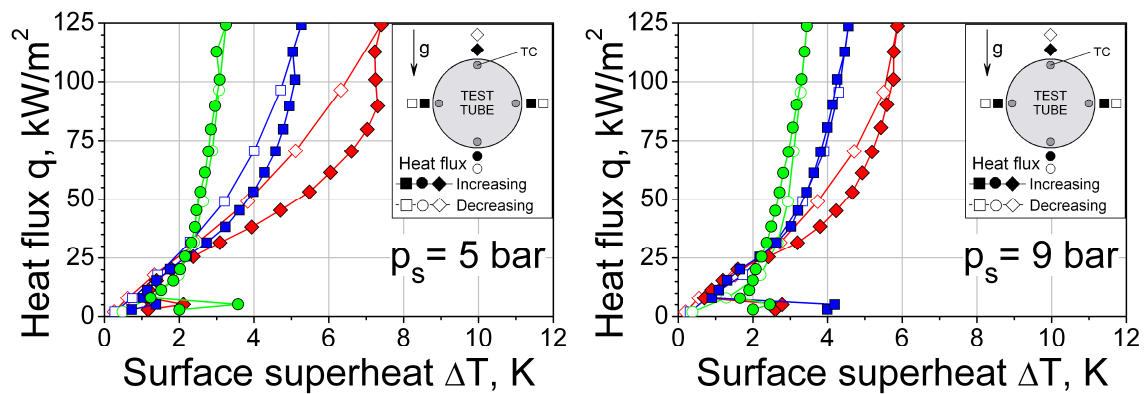


Figure 4.2.12: Boiling hysteresis of R134a at different pressures on A435.

It was found that higher pressures suppress the hysteresis and surface temperature gradients for boiling R134a, Figure 4.2.12. It happens due to decrease of critical nucleus diameter with increasing pressure, consequently smaller departure diameters of vapor bubbles, and following reduction of amount of vapor inside the microstructure. Therefore during the decrease of the heat flux at constant pressure arising bubbles do not have advantage to be created near the vapor rests inside the microstructure. So boiling curves for higher pressures typically look like depicted in Figure 4.2.12 on the right.

At lower pressures the situation is a bit different. After reaching the maximal heat flux, there are lots of vapor rests in the microstructure, especially on the top forming of the test tube. Even after decrease of the heat flux, trapped vapor sufficiently supports further nucleation, Figure 4.2.12 on the left. It was

mentioned above that nucleation criterion (2.1.2) is easier to fulfill near an already existing interface.

Because of the same reasons geometry of the microstructure affects the hysteresis. Different number of micro pins on the microstructured surface grants different nucleation conditions and vapor trapping capabilities for a given liquid boiling at a constant pressure. That is why microstructures with higher pin densities (especially with inclined pins) demonstrated sounder hysteresis, Figure 4.2.13.

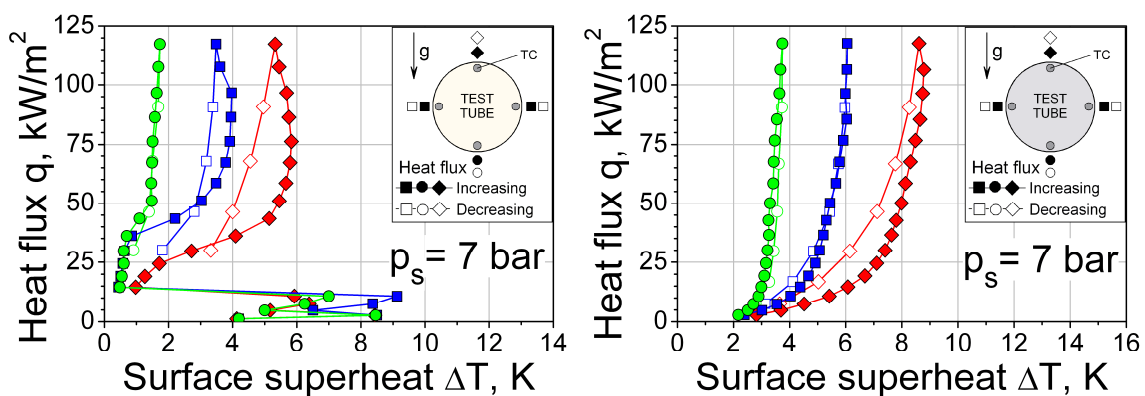


Figure 4.2.13: Hysteresis of R134a at 7 bar, A428 (left) and A419 (right).

Considering hysteresis with different liquids, boiling on microstructured surface with fixed geometry at idem pressures, it is possible to compare R141b with FC-3284 at 1 bar (Figures 4.1.5 and 4.1.38), and R134a with R141b at 5 bar (Figures 4.1.7 and 4.1.5) for tube A428. As it can be seen, in dependence on the liquid properties, determining the critical nucleus diameter, same structure can have “dense” or “not dense” pin structure. Whenever the structure becomes “dense” enough, the hysteresis becomes significant as well.

Developing this idea, one may predict that testing several different liquids at certain but different pressures, determining the equal critical nucleus diameter, must result in practically coinciding boiling characteristics and hysteresis as well.

4.3. Summary on the single tubes experiments

Effect of microstructure geometry on heat transfer

Summarizing the above presented experimental results, the following conclusion can be obtained. Figure 4.3.1 represents the dependence of the average enhancement factor in the developed boiling region of R134a on total length of the available TPL of a microstructured surface.

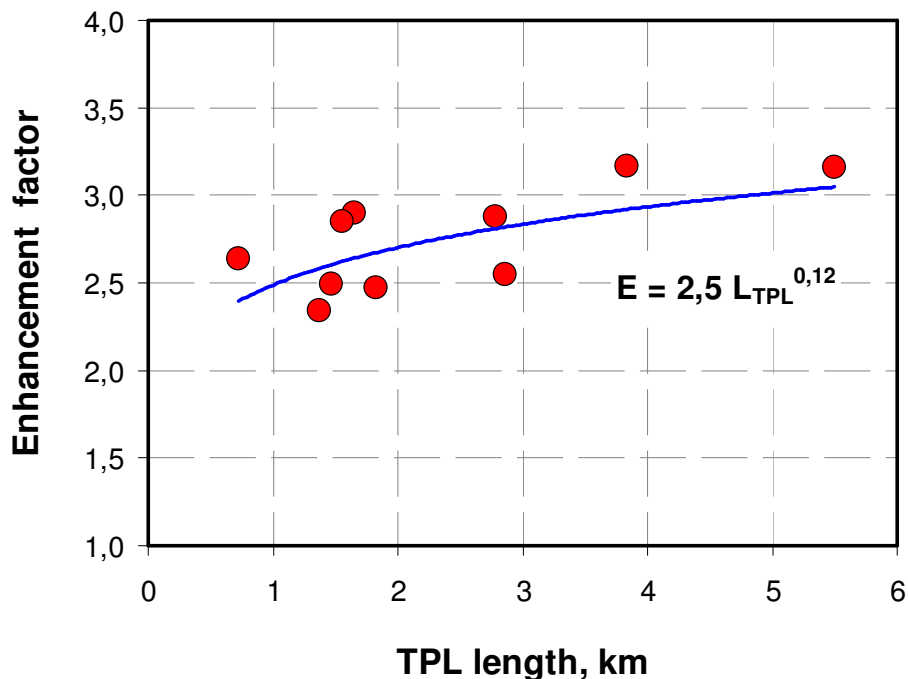


Figure 4.3.1: Dependence of average enhancement factor on total TPL length.

Total length of the TPL is calculated as follows:

$$L_{TPL} = N \cdot \pi \cdot d_{pin} \quad (4.3.1)$$

Numerical values represented in Figure 4.3.1 are not mistaken, if one would try to walk around every pin on microstructured surface A428 he would have to cover a distance over 5,5 km. The heated length with micro pins however for all surfaces used in the present study was only 175 mm. In reality the TPL length seem to be even larger as bubbles have curved surfaces, so the TPL is formed not perpendicularly to a pin, but lengthways of it. Although some separate information can be found in literature on dependence of the boiling

heat transfer on the TPL length, the work by Mitrovic [4] was the first one proving this dependence theoretically.

Approximating the heat transfer performance of the microstructured surface numerically, the formula (4.3.2) was obtained:

$$h/h_S = 2.5 \cdot L_{TPL}^{0.12} \quad (4.3.2)$$

where h is the heat transfer coefficient for the microstructured surface, h_S is the heat transfer coefficient for a smooth surface under idem conditions, and the L_{TPL} is the total length of the TPL in km, calculated using (4.3.1). Although one is free in choice of an approximating curve, the power function with exponent less than 1 seem to be the most appropriate: at a certain number, pins form too dense microstructure, and some of the enhancement mechanisms become unavailable.

Pressure effect on heat transfer

As it was mentioned in Chapter 2, an important conclusion from the approach (2.1.1) – (2.1.2) is that only the surface cavities with sizes deduced from equation (2.1.2), can affect the initial nucleation. For larger cavities, the energy barrier (2.1.2) becomes equal to the one for the bulk liquid with the corresponding nucleus diameter according to (2.1.1). For different liquids and pressures equation (2.1.1) gives the value of the critical vapour bubble radius in range between $1 \cdot 10^{-6}$ m and $1 \cdot 10^{-5}$ m. Therefore, cavities of such sizes are preferable for initial nucleation in general. Some experimental validation of this result can be found in literature, see Figure 2.1.2 for details.

Microstructured surfaces investigated in this work grant cavities with characteristic sizes equal to distance between neighbouring pins:

$$l \approx 1/\sqrt{N} \quad (4.3.3)$$

where N is the micro pin density. For the microstructure A437 as an example equation (4.3.3) gives the cavity size of $5.5 \cdot 10^{-6}$ m. One should note that this quantity is scarcely reachable for surfaces manufactured by other technologies. At lower pressures the critical bubble radius increases, reducing the difference

between values, obtained from equations (4.3.3) and (2.1.1). This explains why the microstructure is more efficient at low pressures: even more nucleation sites can be activated, as their sizes become large enough to support the density fluctuation and form a vapor bubble.

The reasoning, presented above, shows the interlinking between effects of the microstructure geometry and the pressure. These two factors can not be considered separately from each other.

Liquid effect on heat transfer

It is well known (see Labuntsov [7]) that dependence of the heat transfer coefficient on the liquid properties is weak in case of surface tension, for mostly fluids:

$$h \sim \sigma^{0.3} \quad (4.3.4)$$

Figure 4.3.2 represents experimental data on the heat transfer coefficient dependence on the heat flux, the so-called “h-q curve”. It can be seen that difference between heat transfer coefficients for two liquids for a given pressure is not large. It is correct to compare experimental results only if they are taken for idem reduced pressures (reduced pressure is absolute pressure divided by critical one). However, experiments were conducted for fixed values of the absolute pressure. But relatively close values of critical pressures for the tested liquids allow direct comparison. Figure 4.3.3 represents comparison of the relation of the measured heat transfer coefficients for different liquids with values calculated using (4.3.4). Experimental heat transfer coefficients were averaged using the same procedure, as for calculation of the enhancement factor, explained in the Chapter 4. Deviation of measured values with calculated is not significant because of the mentioned difference in reduced pressures, the averaging procedure itself and the boiling reestablishing process at low heat fluxes. Despite of this, good agreement with (4.3.3) was found.

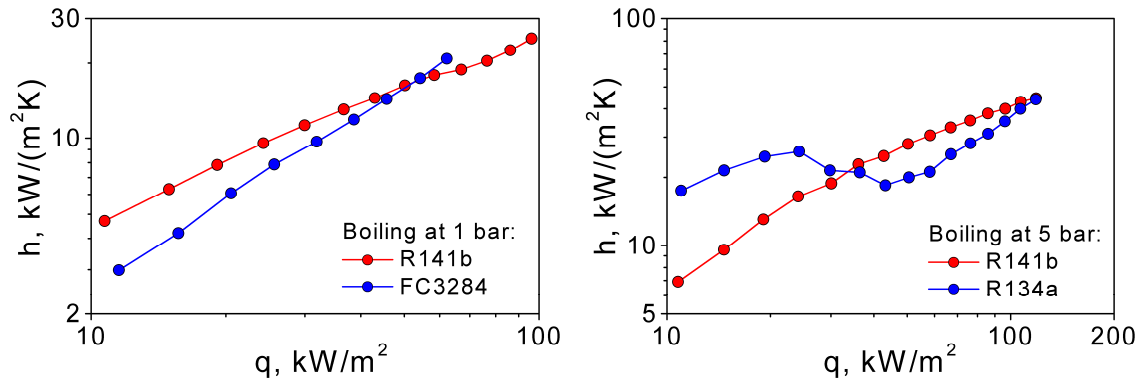


Figure 4.3.2: Comparison of the boiling heat transfer for microstructure A428:
 Left: 1 bar boiling of R141b and FC-3284;
 Right: 5 bar boiling of R141b and R134a.

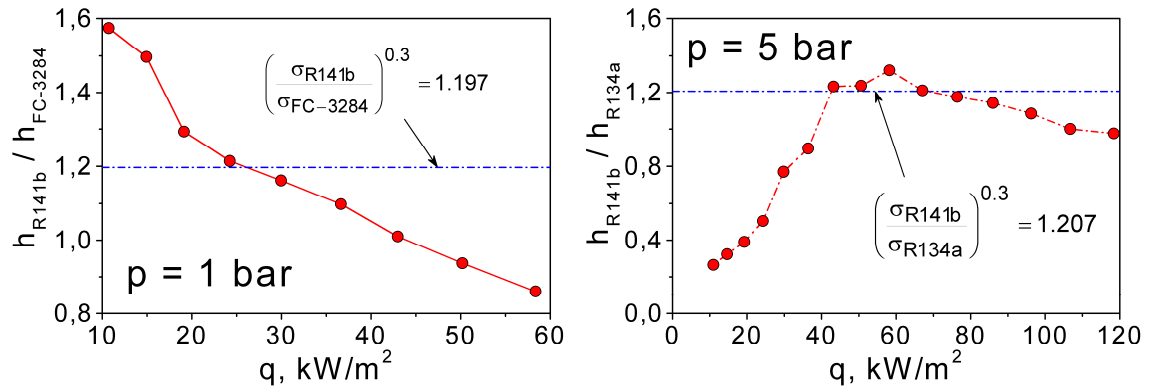


Figure 4.3.3: Comparison of measurement for microstructure A428 with (4.3.4):
 Left: 1 bar boiling of R141b and FC-3284;
 Right: 5 bar boiling of R141b and R134a.

Conclusion on the single tube experiments

The novel microstructured surfaces were tested with refrigerants R141b, R134a and FC-3284 in nucleate pool boiling mode at pressures between 0.5 bar to 9 bar in the single tube configuration. Basing the obtained experimental results the following conclusions can be outlined:

Surface superheat of the novel microstructured surface during nucleate pool boiling remains largely unaffected by the applied heat flux. This unique property is attributed to very large lengths of the TPL (three phase line). TPL acts as an extremely efficient heat sink, and it makes the surface temperature to be practically independent on the applied heat flux. In several boiling modes the TPL length was so long that the surface superheat was decreasing with the increasing heat flux.

For boiling on surfaces with bi-cavity patterns (i.e. surfaces with cavities of two characteristic sizes) the surface superheat experiences a sharp step-like change, later remaining unaffected by the heat flux. This process is called “boiling re-establishing”. During it the smaller cavities become activated at a certain superheat at first. Later, when the surface reaches the activation temperature for the larger cavities, they become activated as well. However, as cavities of both sizes are formed by the same near by pins, only a larger one acts. Thus the larger bubbles occur on the surface, what was observed visually, Figures 4.1.8 – 4.1.12.

The efficiency of heat transfer of the microstructured surface in comparison with a technically smooth tube under idem conditions was found to be higher by the factors range up to 18 in several boiling modes. The enhancement factor depends on the geometry of the microstructured surface, system pressure and properties of the liquid. This dependency on the microstructure geometry is generalized by the equation (4.3.4). The enhancement factor decreases with increasing pressure. At lower pressures the critical bubble radius increases, reducing the difference between values, obtained from equations (2.1.1) and (4.3.3). Therefore, the microstructure is

more efficient at low pressures: even more nucleation sites can be activated, as their sizes become large enough to support density fluctuations and form a vapor bubble. The most effective boiling modes were accompanied by the boiling inception as a front. The velocity of the front depends on the microstructure geometry as well.

Appearance of the bubble chains on the microstructured surfaces was observed in several boiling modes, Figure 4.1.22. It confirms the correctness of the nucleation criteria expressed by equation (2.1.2): it is easier for a new bubble to arise near an existing interface. This phenomenon also sets thinking about boiling as a chaotic process with deterministic behavior. The order of bubbles chains appears in the chaos of the fluid density fluctuations.

Temperature oscillations of the surface were detected near the crisis during boiling of the highly wetting fluid FC-3284. The amplitudes and frequencies of temperature oscillations rise significantly near crisis in comparison with boiling at lower heat fluxes. The reason is that greater masses of vapor form and detach from the surface in comparison with separate bubbles boiling mode. Both amplitudes and frequencies of oscillations depend on the microstructure geometry. For microstructures with larger number of pins the decrease of amplitudes of temperature oscillation was noted. The phase portrait (attractor) was plotted after the experimental data, showing that some time after the beginning of observations the amplitudes and the frequencies tend to tighten near a narrow phase area. This allows recommending this method for detection and prevention of boiling crisis in industrial apparatus.

Boiling hysteresis is expressed stronger for structures with higher micropins density due to their better vapor trapping abilities. Higher pressures suppress the hysteresis as well as the surface temperature gradients.

Comparison of experimental data on boiling heat transfer between different liquids has shown relatively good agreement with literature data, expressed with the equation (4.3.4).

4.4. Experiments with tandem tubes

The purpose of the tandem tube experiments was to determine the influence of the lower tube on the heat transfer performance of the upper one. As follows from the Table 3.3 the experiments were conducted with two liquids, R134a and FC-3284, at pressures of 5 bar, 7.5 bar, 9 bar and 0.5 bar, 1.0 bar, 1.5 bar, correspondingly. Two types of experiments have been conducted. First, for the lower tube (indexed as 1) three different heat fluxes were set (minimal one for the boiling inception, maximal one for the fully developed boiling and one in between) while the upper tube (indexed as 2) experienced the whole range of heat fluxes. Second type of experiments was the opposite of the first, the heat flux for the upper tube was kept constant while heat flux for the lower tube was changing. One additional set of experiments have been conducted, when both test tubes had equal heat fluxes. Experiments of first and second types model a situation when a heat exchanger with microstructured tubes operates in non-stationary, “start and stop”-alike modes. Experiments with equal for both tubes heat fluxes model a common in industry practice case of stationary long time operation.

It was found during experiments that different system parameters (pressure, heat flux, liquid properties and microstructure geometry) bring nearly no difference in results. Therefore, the experimental program has been slightly reduced, like one notes from the Table 3.3.

Refrigerant R134a

Tandem A428 + A425

The microstructured tube A425 has been chosen as the lower for all experiments in tandem tube configuration. Figure 4.4.1 represents boiling curves of R134a at 5 bar with upper tube A428 and at heat fluxes of 8 kW/m², 50 kW/m² and 125 kW/m² on lower tube (A425). It can be seen that the heat flux of the lower tube has very weak influence on the heat transfer characteristics of the upper tube. However, the upper tube superheats slightly

increase with the rising heat flux on the lower tube. When the amount of vapor generated by the lower tube is not too large, it promotes the heat transfer of the upper tube, as new bubbles can be created near the trapped vapor rests. Moderate vapor masses worsen the creation of bubbles on the upper tube as they block some of nucleation sites. Described above mechanism of the TPL enlargement for high heat fluxes becomes turned on for largest amounts of vapor generated by the lower tube, so the superheat of the upper tube slightly decreasing. Nevertheless, the highest value of the wall superheat for the upper tube was only 6 K. It was observed only at the top of the upper tube in the region of moderate heat fluxes on the lower tube.

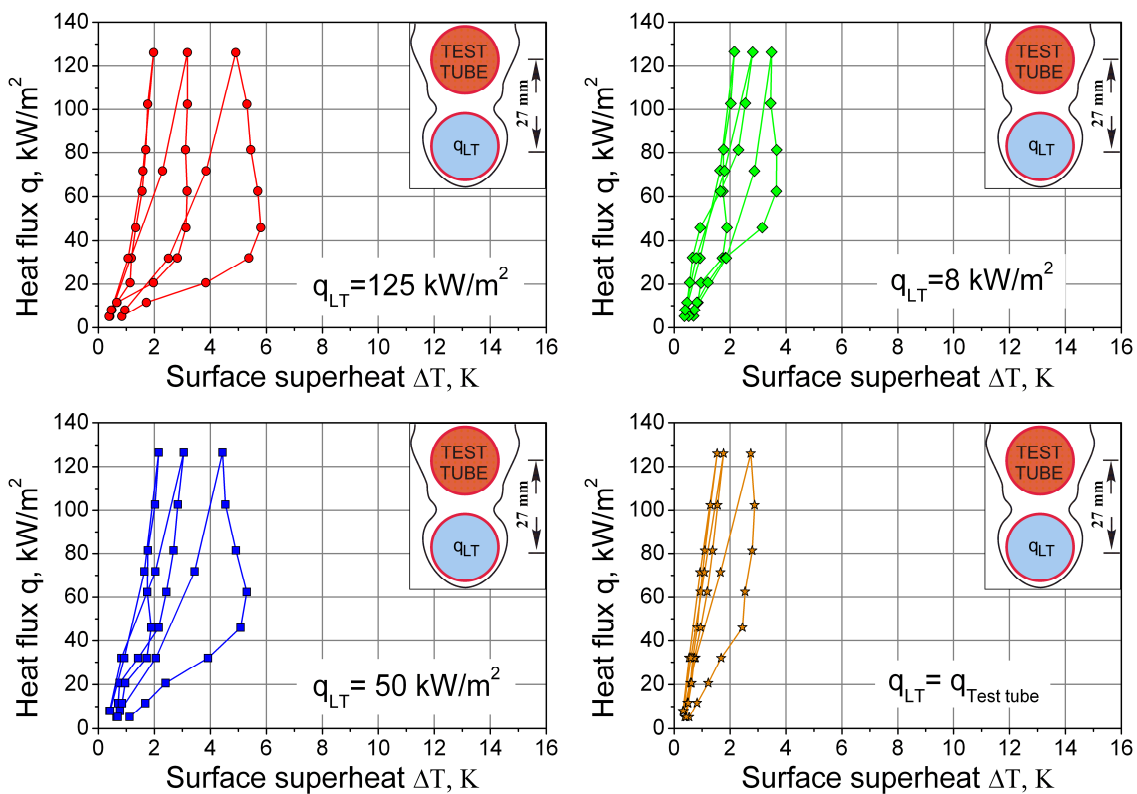
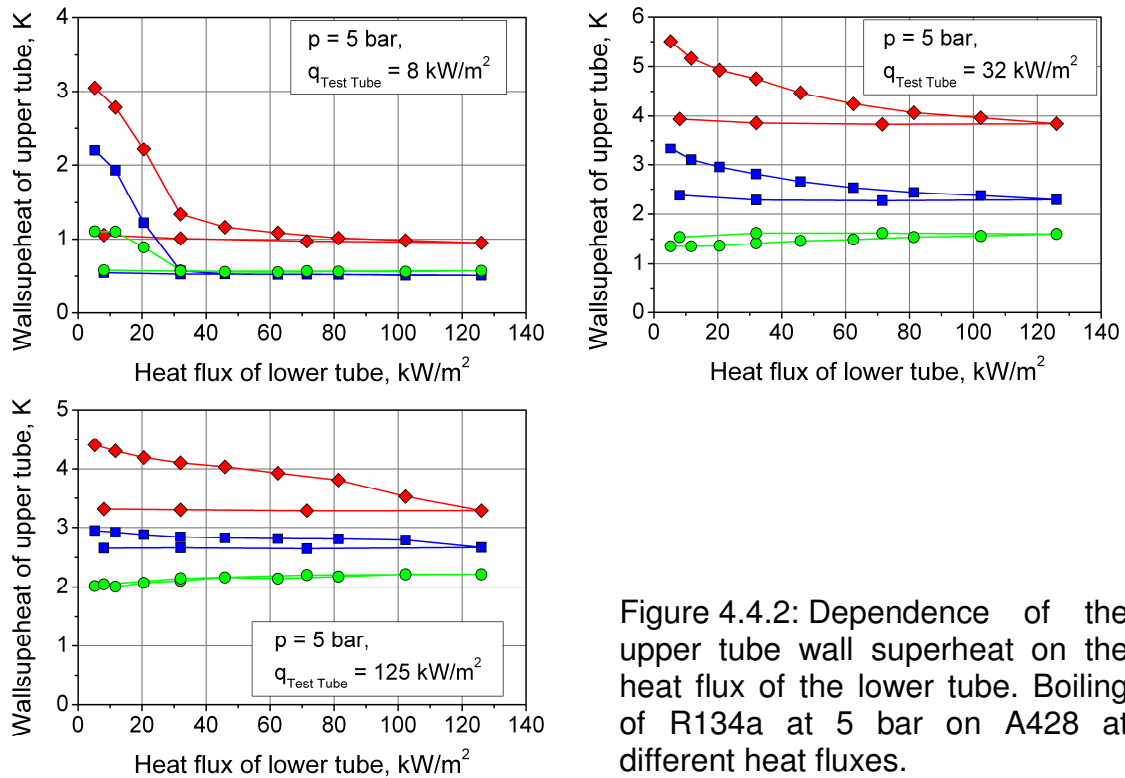


Figure 4.4.1: Boiling curves of R134a at 5 bar with upper tube A428 at different heat fluxes on the lower tube A425.

Figure 4.4.2 represents data on wall superheats of the upper tube A428 at the heat fluxes of 8 kW/m², 32 kW/m², and 125 kW/m² in dependence on the heat flux of the lower tube A425 (results of the above mentioned experiments of second type). As it can be seen, the region of the temperature change of the

upper tube depends on its heat flux. At lowest heat flux of 8 kW/m^2 the temperature of the upper tube changes up to 30 kW/m^2 fixed on the lower tube. With increase of the upper tube heat flux, this region expands. For the heat flux of 125 kW/m^2 the temperature changing of the upper tube is observed until the maximal heat flux of the lower tube equal to 125 kW/m^2 .



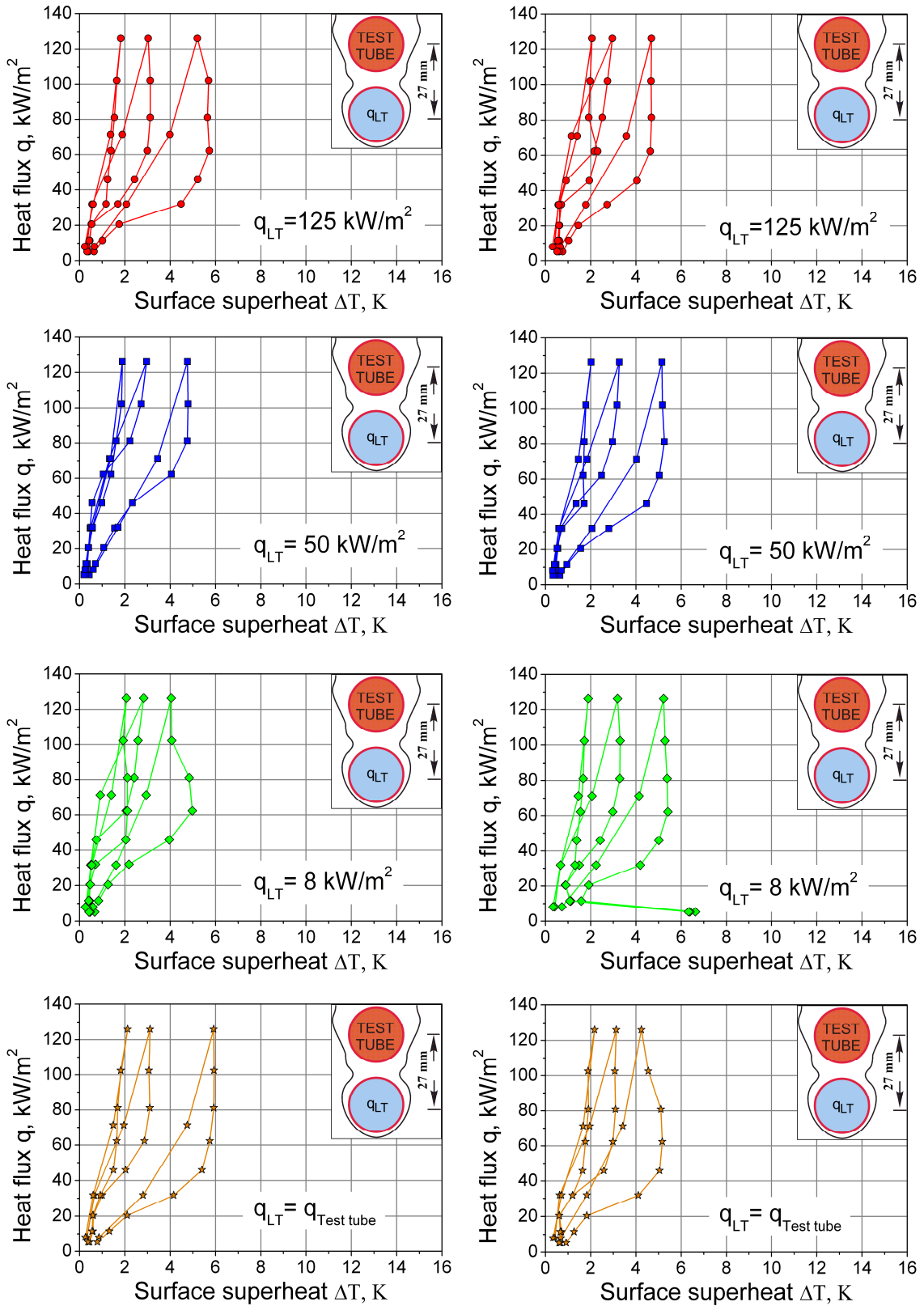


Figure 4.4.3: Boiling curves of R134a at 7.5 bar (left) and 9 bar (right) for the upper tube A428 at different heat fluxes on the lower tube A425.

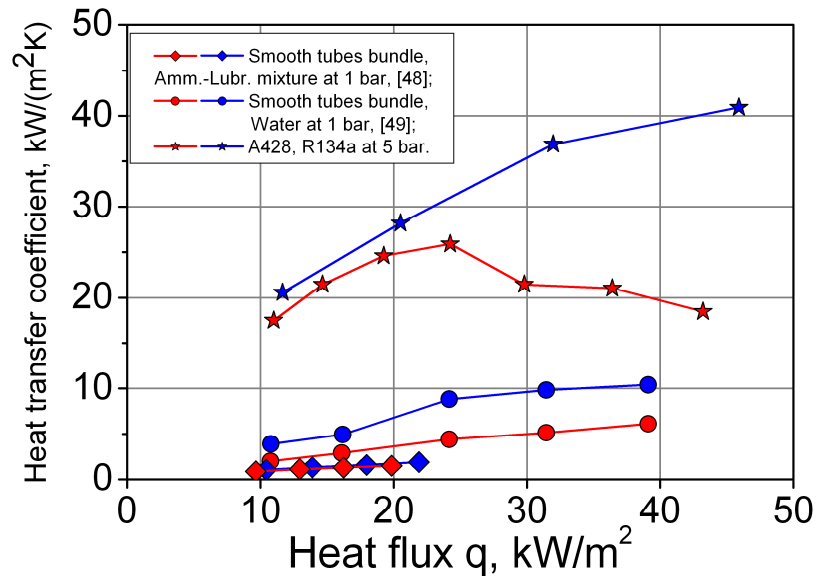


Figure 4.4.4: Comparison of tandem tubes experiments (A428 with R134a boiling at 5 bar) with data from literature [48, 49].

Tandem A437 + A425

Another tube tested in tandem configuration was A437. The microstructured surfaces A428 and A437 have been chosen as they have the largest density of micropins and showed to be the most effective out of all tested surfaces. Figure 4.4.5 represents boiling curves of R134a in tandem configuration A437+A425 at pressures of 5 bar, 7.5 bar and 9 bar.

As can clearly be seen from the presented experimental results, the tandem tube configuration is characterized by the extremely low surface superheats and small variance of measured values for different boiling modes. Difference for the microstructured surface A437 in the single and tandem tube configuration is not significant, see Figure 4.1.21. The surface superheat does not depend on the applied heat flux for all experimental regimes. The maximal surface superheat detected for the A437 in the tandem mode was only 4 K. Hysteresis remains approximately on the same level, as for the single tube. Boiling re-establishing is less expressed, as it is partly compensated by vapour bubbles rising from the lower tube. Physics of those processes has been revealed in previous chapters, so experiments for tandem of A437 with A425 were further confirmation of conclusions obtained earlier.

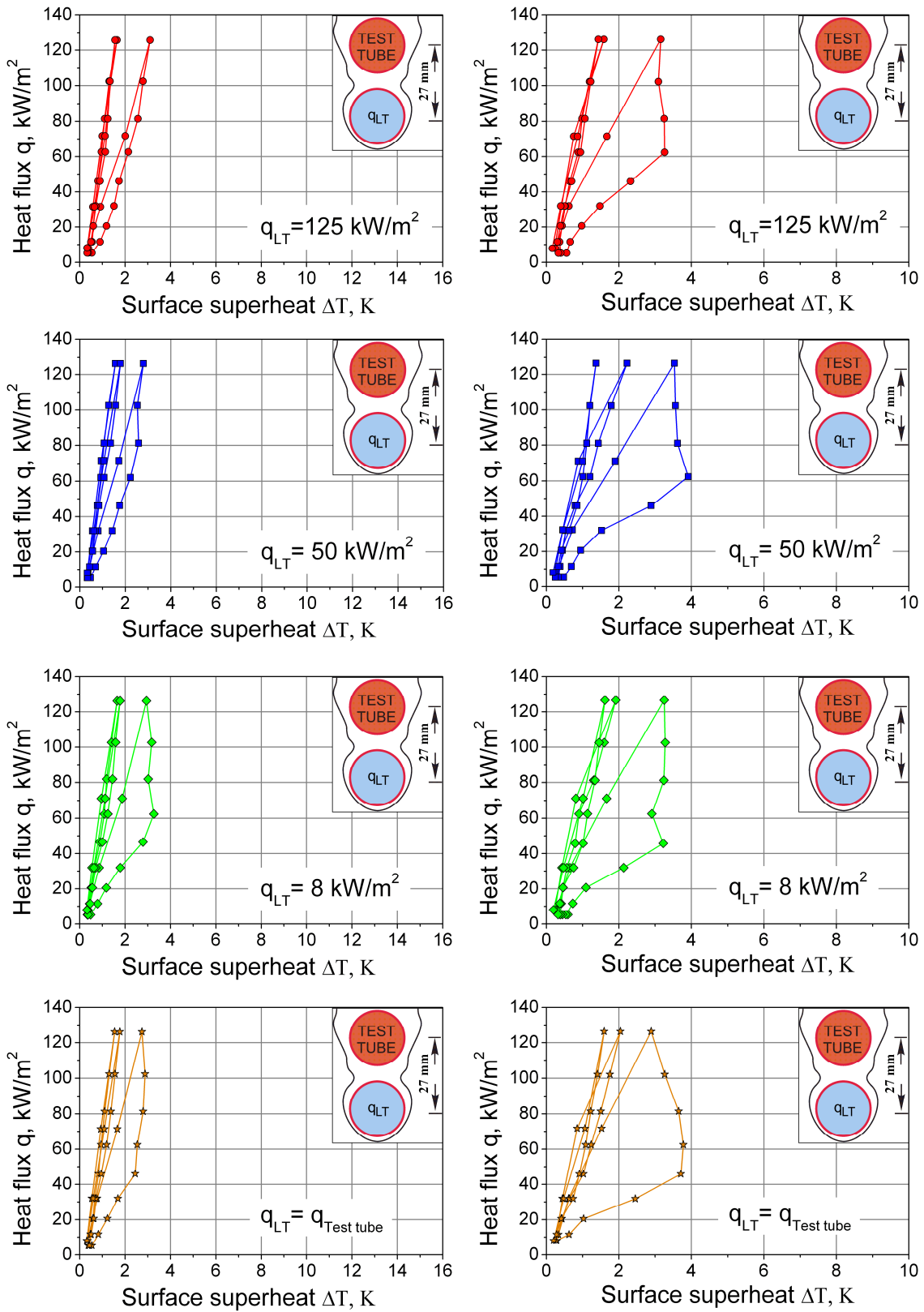


Figure 4.4.5a: Boiling curves of R134a at 5 bar (left) and 7.5 bar (right) for the upper tube A437 at different heat fluxes on the lower tube A425.

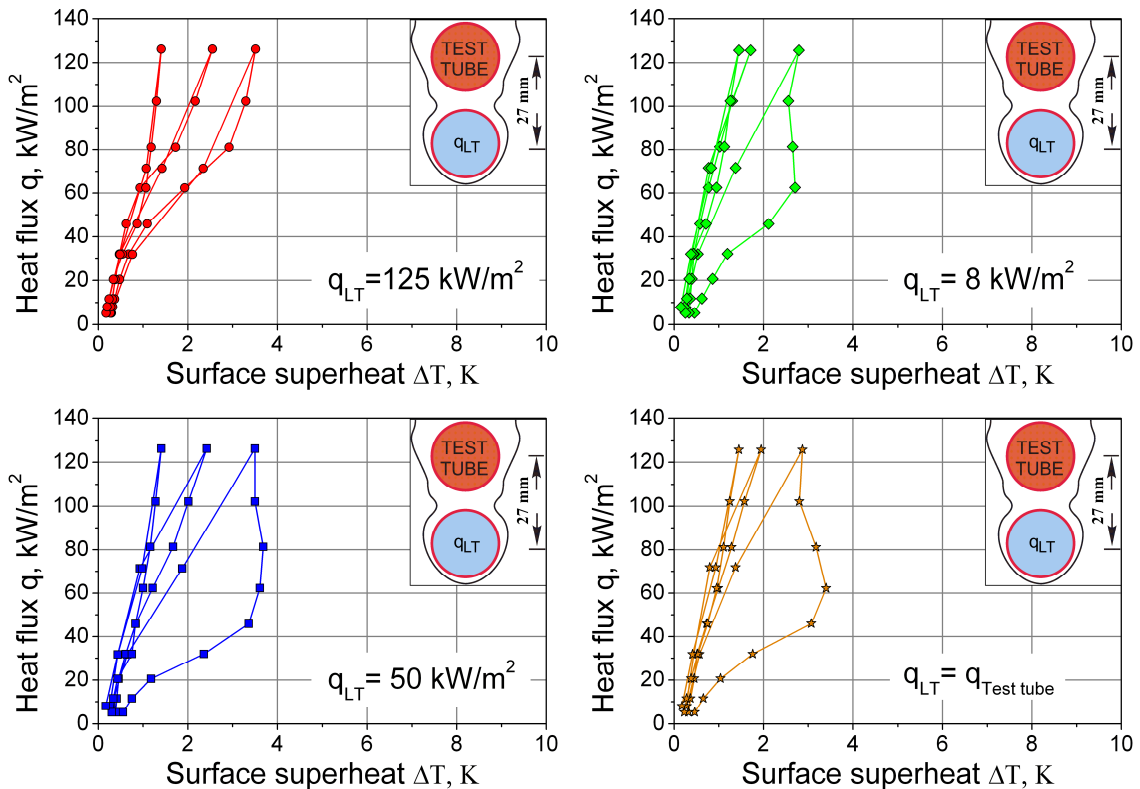


Figure 4.4.5b: Boiling curves of R134a at 9 bar for the upper tube A437 at different heat fluxes on the lower tube A425.

Electronic fluid FC-3284

Tandem A428 + A425

Same experimental program has been accomplished for the second liquid, the highly wetting fluorocarbon FC-3284. Experimental results are represented in Figure 4.4.6 as boiling curves for pressures of 0.5 bar, 1.0 bar and 1.5 bar. These measurements largely confirm the conclusions obtained previously. The maximal heat flux was limited to 65 kW/m² due to earlier crisis and presence of the lower tube. The largest surface superheat reached in experiments was 6 K for boiling at 0.5 bar. Figure 4.4.7 depicts the upper tube wall superheat in dependence on the heat flux of the lower tube. Only one heat flux on the upper tube was chosen for FC-3284 versus 3 for R134a, because the relatively small influence of this heat flux has been detected. Difference

between measurements for various thermocouples position is very small; i. e. there is almost no surface temperature gradients.

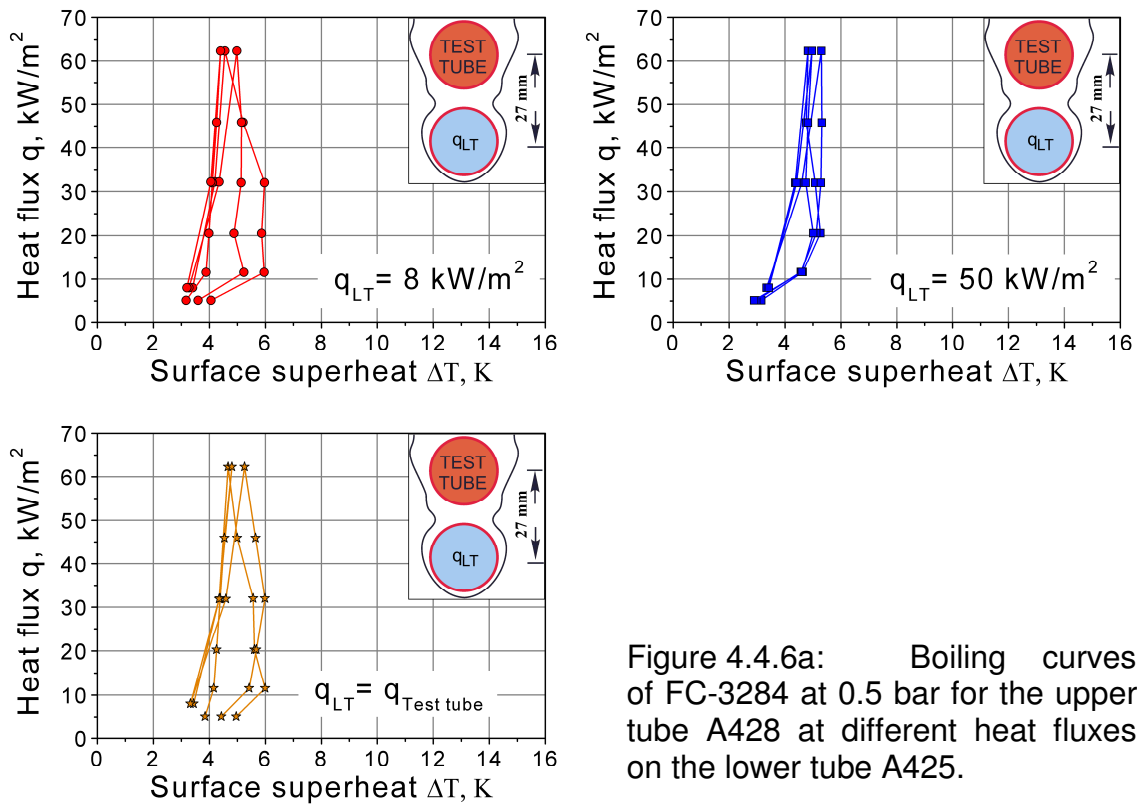


Figure 4.4.6a: Boiling curves of FC-3284 at 0.5 bar for the upper tube A428 at different heat fluxes on the lower tube A425.

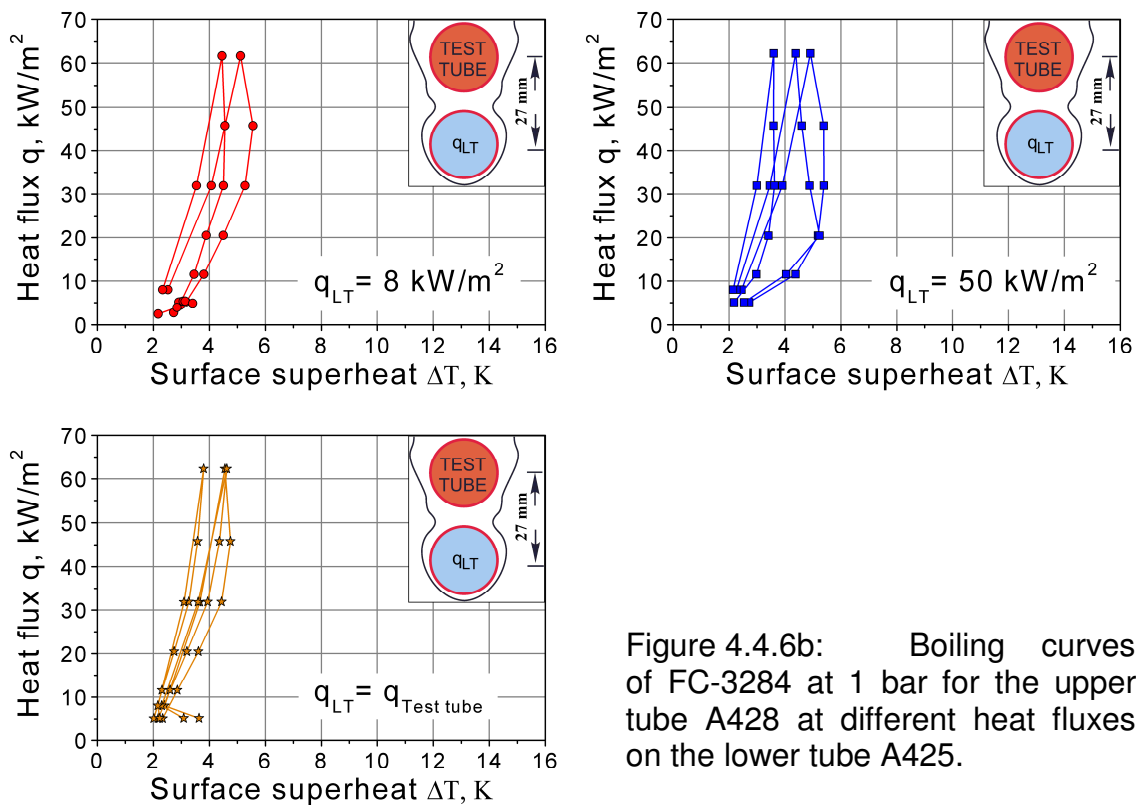


Figure 4.4.6b: Boiling curves of FC-3284 at 1 bar for the upper tube A428 at different heat fluxes on the lower tube A425.

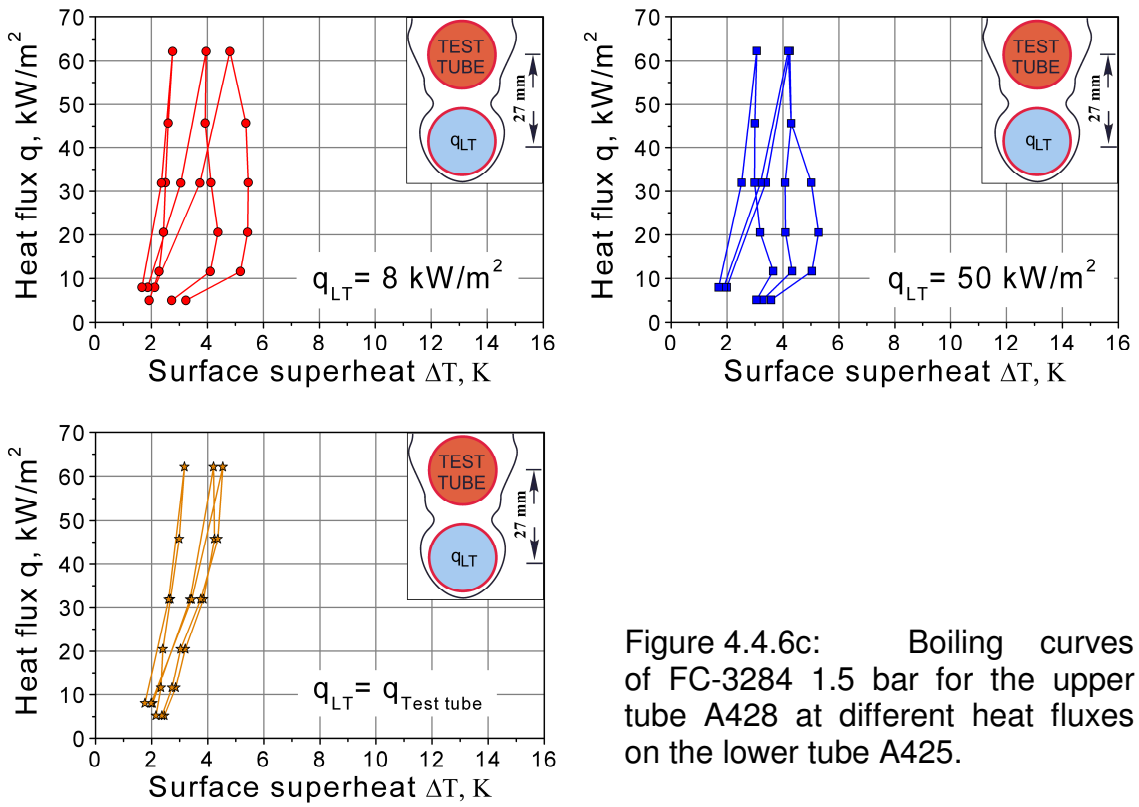


Figure 4.4.6c: Boiling curves of FC-3284 1.5 bar for the upper tube A428 at different heat fluxes on the lower tube A425.

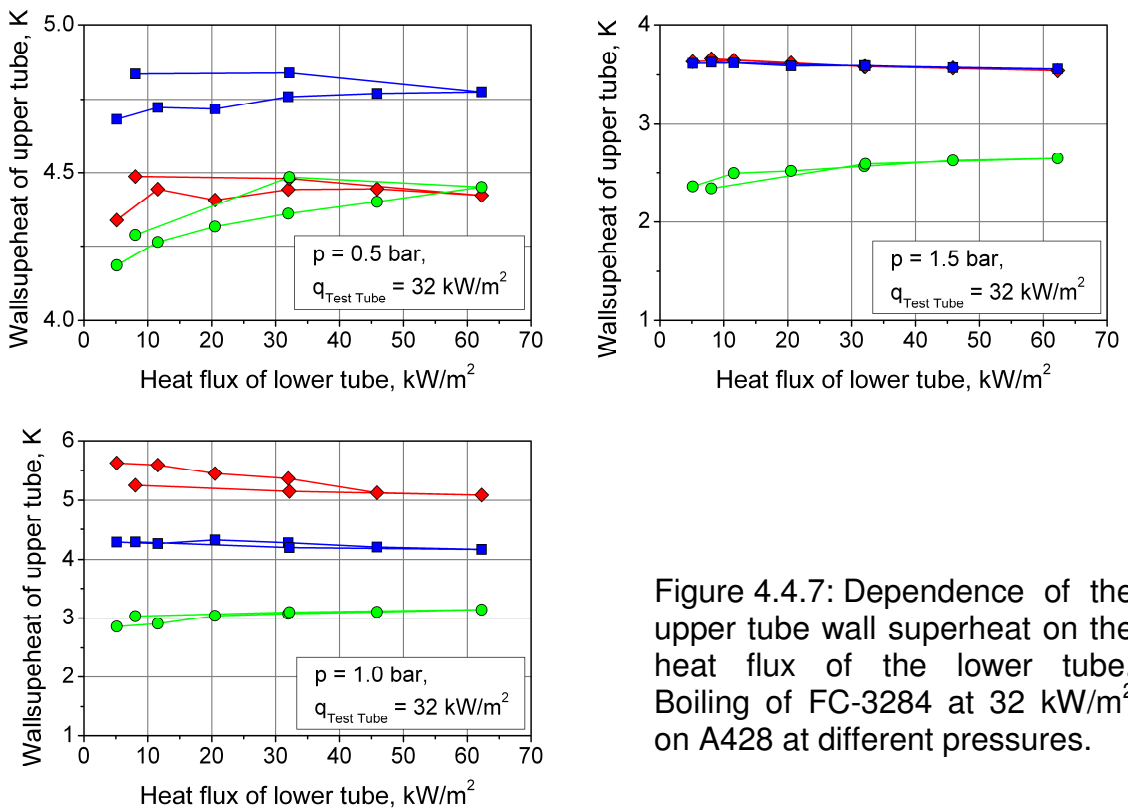


Figure 4.4.7: Dependence of the upper tube wall superheat on the heat flux of the lower tube. Boiling of FC-3284 at 32 kW/m^2 on A428 at different pressures.

Experimental results (Figures 4.4.6 and 4.4.7) show good principal agreement with data for another liquid R134a, and keep all features of the microstructured surface, discovered in the single tube mode (hysteresis, constancy of the wall superheat, high efficiency). To recommend the liquid FC-3284 for the real industrial application would not be, however, completely correct. The main disadvantage of liquid FC-3284 – low critical heat flux – is even worsening in the tandem tube configuration. Comparing the results for FC-3284 with A428 in tandem with A425 with single A428 tests (Figure 4.1.38) one sees the increase of the wall superheats up to 2 K.

Tandem A437 + A425

The microstructured surface A437 was tested in tandem with A425 with FC-3284 at pressures of 0.5 bar and 1.5 bar due to weak dependence of results on pressure. As follows from the Figures 4.4.8 and 4.4.9, the experimental data largely agree with those for single tube A437 and for tandem of A428+A425, see corresponding figures above.

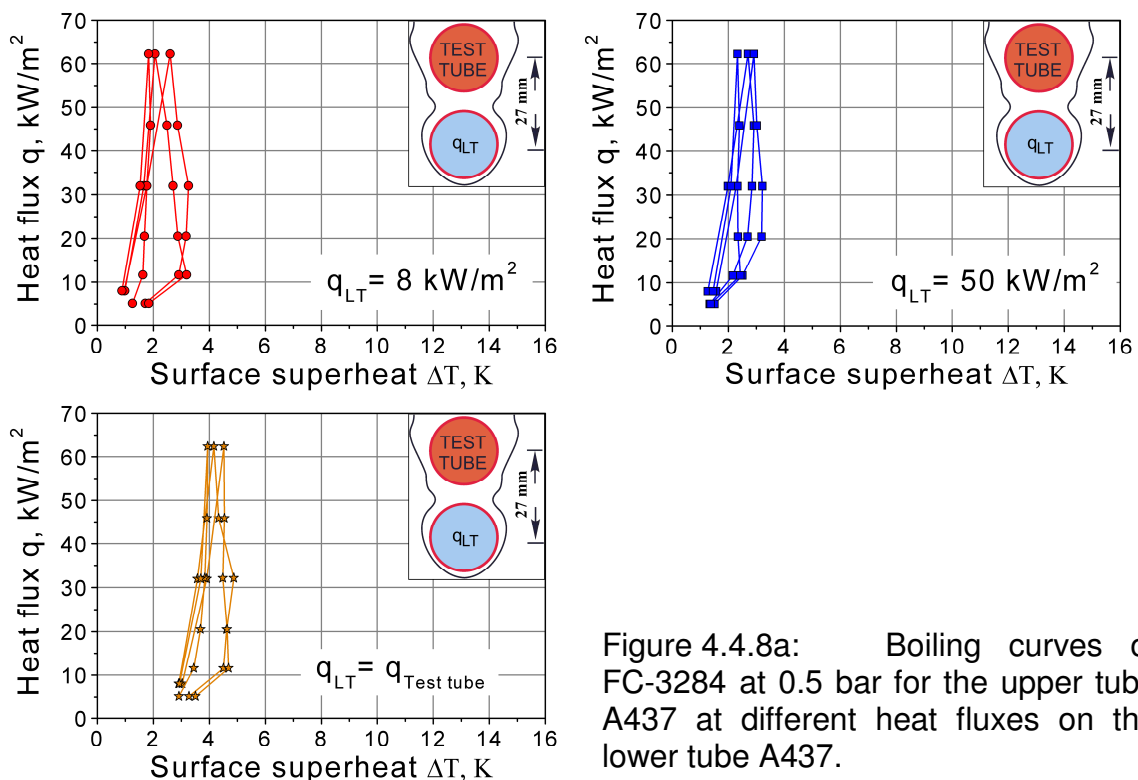


Figure 4.4.8a: Boiling curves of FC-3284 at 0.5 bar for the upper tube A437 at different heat fluxes on the lower tube A437.

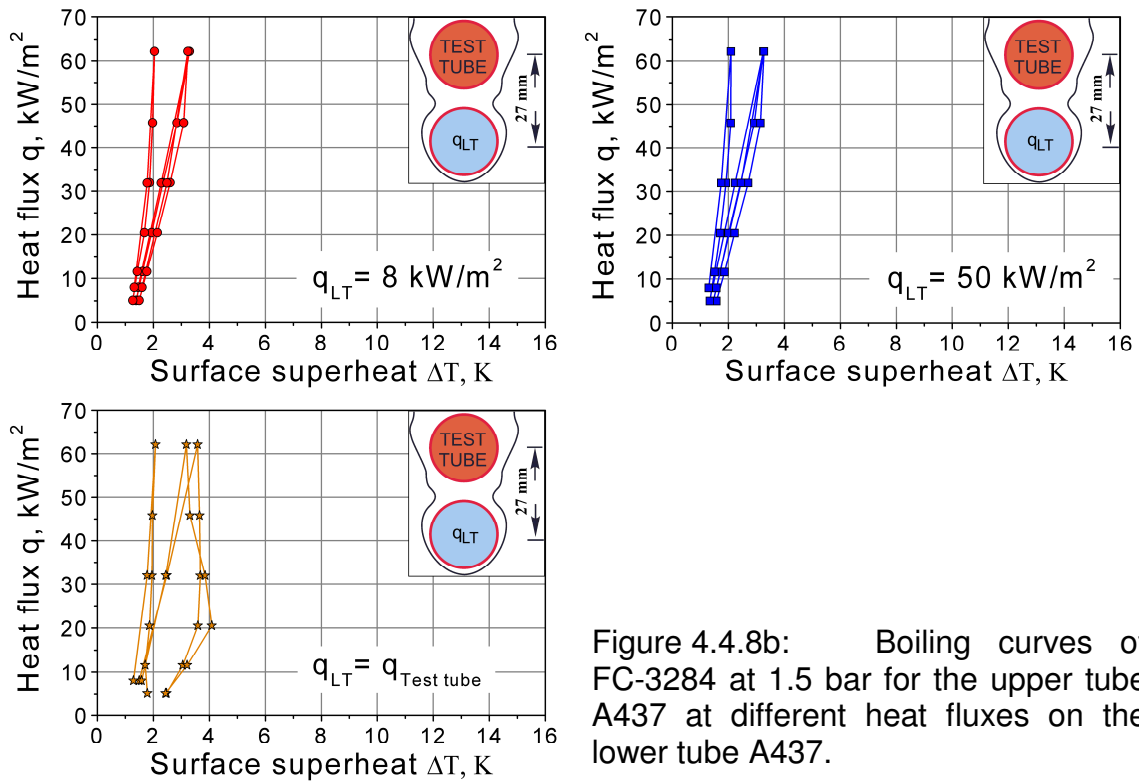


Figure 4.4.8b: Boiling curves of FC-3284 at 1.5 bar for the upper tube A437 at different heat fluxes on the lower tube A437.

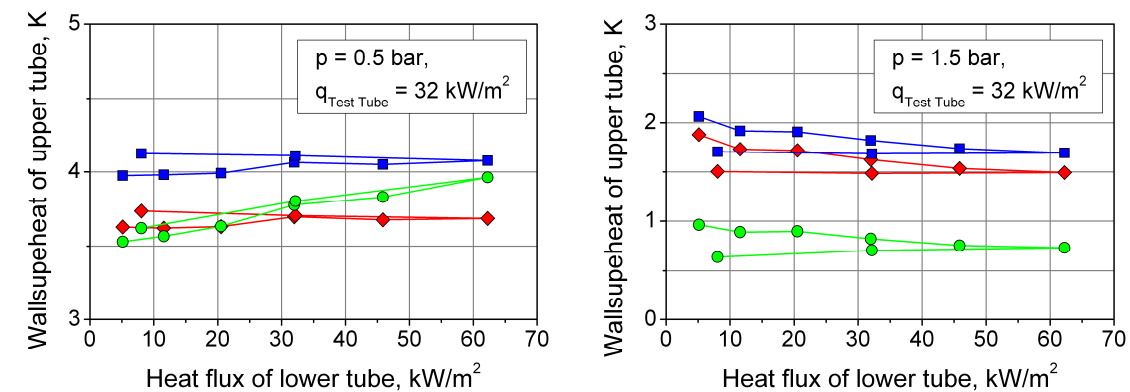


Figure 4.4.9: Dependence of the upper tube wall superheat on the heat flux of the lower tube. Boiling of FC-3284 at 32 kW/m² on A437 at different pressures.

The rest of experimental measurements are presented in the Appendix in tabular form, as they show further confirmation of the above presented conclusions and lie closely to each other. Some intermediate conclusions concerning the experimental results will be discussed in the next sub-chapter.

Conclusion on the tandem tube experiments

Tandem tube experiments have shown high compactness of results of measurements for different boiling modes. The independence of the surface superheats on the heat flux applied to the test tube has been observed for all pressures. This feature is attributed to the great number of vapor bubbles, produced by the microstructure. Low dependence of the upper tube superheats on the heat flux of the lower tube was observed. For industrial practice it means no significant temperature gradients in a heat exchanger, and simultaneous stable and effective work of all microstructured tubes, regardless their positions in the bundle, entering position of liquids into the heat exchanger and working pressure.

Higher heat transfer coefficients have been found for the upper tube, than for lower tube, what has good agreement with data from literature, Figure 4.4.4. Presence of the lower tube generally promotes heat transfer of the upper tube. Vapor bubbles generated on the lower tube are efficiently trapped by the microstructure of the upper tube, helping in creation of new bubbles.

Effects of boiling reestablishing, hysteresis and the most important the constancy of the wall superheat were detected for the tandem configuration in the same degree as for the single tube experiment.

The microstructured surfaces have demonstrated very high effectiveness in tandem configuration, stability of the performance, very low superheats and independency on non-stationary effects. The microstructured surfaces can be recommended for use in industrial heat exchangers with the corresponding liquid, so the critical heat flux would be large enough. As soon as boiling occurs on a single tube of the bundle, the rest of the tubes becomes activated as well, so no great inception superheats are required for the bundle of microstructured tubes.

5. STATISTICAL MODEL OF HEAT TRANSFER FROM ENHANCED SURFACE

5.1. Suggestions and limitations of the model

A calculation model is proposed in this chapter to evaluate the heat transfer performance of the novel microstructured surfaces. In construction of this model the less possible amount of experimental information should be involved. As input data the micro geometry of an enhanced surface must be used and liquid properties. As output the dependence of applied heat flux on surface superheat should be obtained. This information can easily be expressed in terms of the heat transfer coefficient. The main aim of modeling is not the obtaining of full numerical agreement with measured values, but correct principal behavior of calculated quantities. As some minor effects will be neglected, the fitting of the calculated and experimental values seem to be possible with several empirically determined coefficients. However, it must be a subject of future theoretical investigations. Some other suggestions will be made and properly discussed in this chapter during deduction of model equations.

5.2. Model equations

The heat flux applied to an enhanced surface is normally spent for bubble generation on nucleation sites and free convection of liquid between them:

$$q = q_{\text{conv}} + q_{\text{boil}} \quad (5.2.1)$$

Free convection is known to have heat transfer coefficients by several orders of magnitude lower than those for processes of phase change. The novel microstructure has demonstrated the great number of nucleation sites, so the free convection term in equation (5.2.1) can be neglected. It is suggested that the whole heat flux applied to an enhanced surface is consumed by arising vapor bubbles.

It is known that a distribution close to normal of the bubbles departure diameters exist for a smooth surface [50]. Nevertheless this fact is neglected here, as an effective value of a departure diameter is supposed to be used. Thus, every single vapor bubble needs a certain effective amount of heat power, say q_0 , to overcome the energy barrier (2.1.2), grow and detach from a surface. As there is certain number of active nucleation sites on an enhanced surface, say n^* , the equation (5.2.1) can be expressed through n^* and q_0 as:

$$q = q_0 \cdot n^* \quad (5.2.2)$$

Number of *active* nucleation sites is determined by sizes of *potential* nucleation sites and the surface superheat. Number of *potential* nucleation sites is a given property of the surface, originating from its production technology. Depending on superheat of the surface, more or less number of potential nucleation sites can be activated to produce bubbles.

The continuous distribution of potential nucleation sites on their sizes is assumed. This assumption should be close to reality, because casual deviations always occur, even when one tries to obtain a predetermined cavity size on a surface. The exact shape of the distribution curve varies from surface to surface in dependence on its micro geometry. For the microstructured surface investigated in the present work this distribution is close to δ -function for surfaces with mono-cavity patterns, and a sum of two δ -functions for bi-cavity patterns, Figure 5.2.1a and 5.2.1b. For untreated surface one may suggest the normal distribution of potential nucleation sites versus their sizes, Figure 5.2.1c.

For untreated real surface the expression of the normal distribution of potential nucleation sites on their sizes is given as:

$$n/N = \frac{1}{\Sigma\sqrt{2\pi}} \exp\left(\frac{-(d-d_1)^2}{2\Sigma^2}\right) \quad (5.2.3)$$

where Σ is the dispersion (the capital letter Σ is used here not to interfere with σ for surface tension); d_1 is the mean cavity diameter, and d is the diameter of a random cavity.

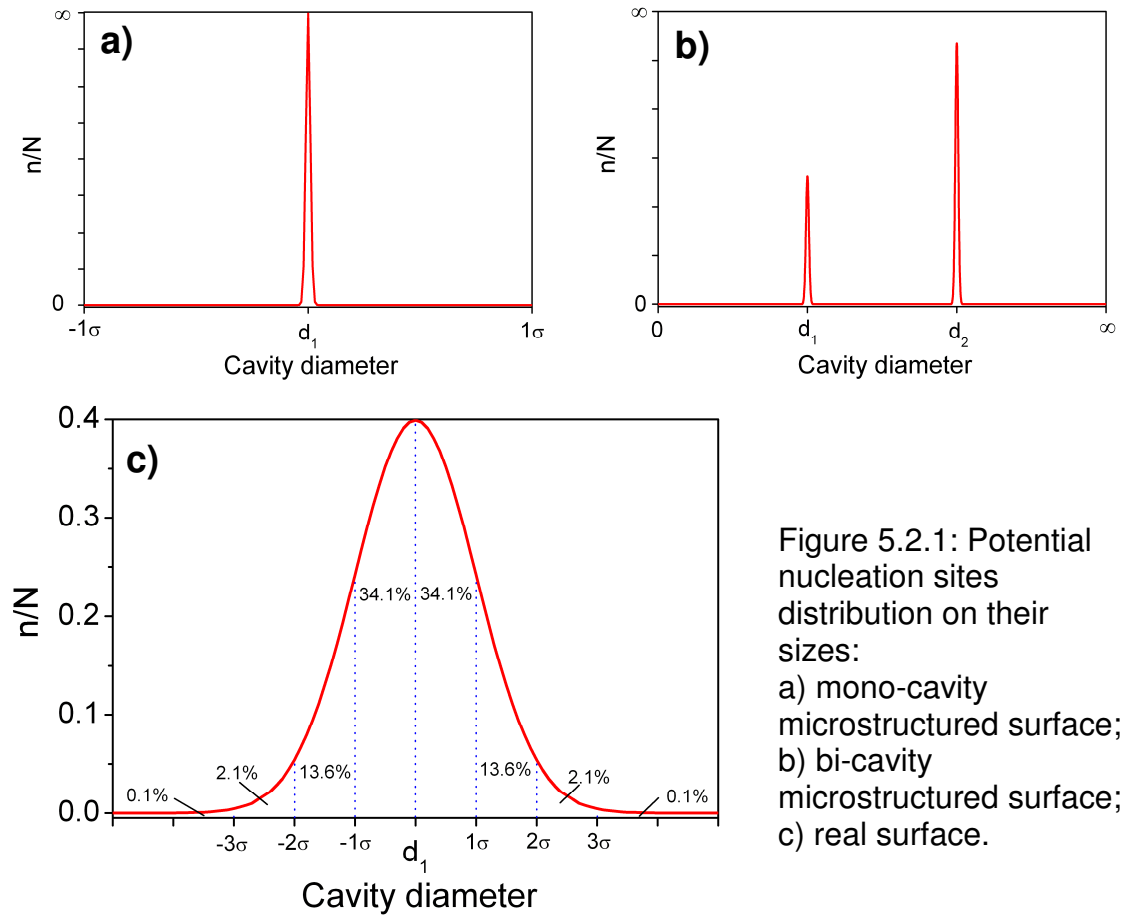


Figure 5.2.1: Potential nucleation sites distribution on their sizes:
 a) mono-cavity microstructured surface;
 b) bi-cavity microstructured surface;
 c) real surface.

The dispersion is determined by the surface treatment technology, and it characterizes the width of diameters interval for majority of cavities, see Figure 5.2.1c. The suggestion of normal distribution should be correct, because no one can predict its shape for an arbitrary surface. Therefore, the normal (or Gaussian) distribution for a random quantity is most likely. This will be checked once again later. Correspondingly, the δ -function distribution for the microstructured surface is following:

$$n/N = \delta(d - d_1) \quad (5.2.4)$$

The choice of the δ -function is obvious. Using the technology of the microstructure production described in Chapter 3, one obtains micropins, almost homogeneously distributed over the surface. In case of straight pins or pins inclined with a same angle, distance between them can be taken as a characteristic cavity size and calculated using equation (4.3.3). For bi-inclined

pins the situation is different, as they form a pattern where two quasi-cavities exist. Figure 5.2.2 clearly illustrates this idea.

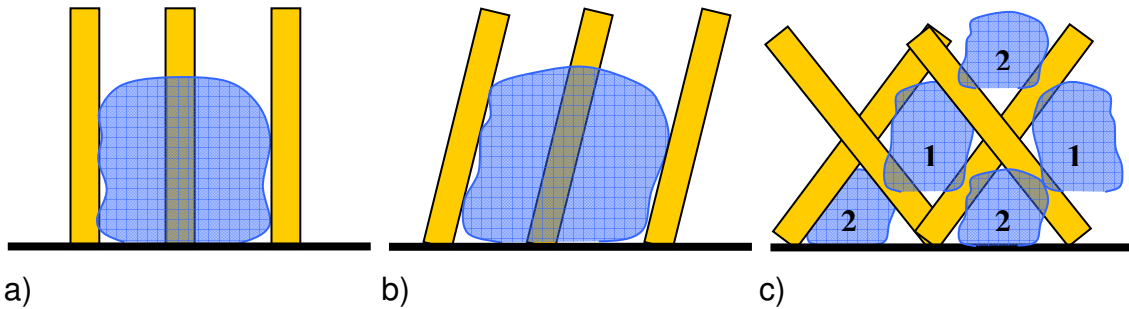


Figure 5.2.2: Nucleation patterns of microstructured surface,
 a) straight pins;
 b) mono-inclined pins;
 c) bi-inclined pins.

For bi- or multy- cavity patterns, equation (5.2.4) can be generalized as:

$$n/N = \sum_i A_i \delta(d-d_i) \quad (5.2.5)$$

In equation (5.2.5) coefficients A_i are percentage numbers of nucleation sites of a given size with obvious normalization condition $\sum_i A_i = 1$. Total number of nucleation site in reality is not infinite. Therefore, instead of Dirac delta function, a normal distribution with a very small dispersion is used to model the novel microstructured surface.

A nucleation site of a certain size can be activated at a corresponding surface superheat. It can be found from equation (2.1.1). According to Labuntsov [7], for relatively low superheats (2.1.1) can also be expressed as:

$$\Delta T = \frac{\sigma T_s}{r \rho_v d} \quad (5.2.6)$$

where r is the latent heat of evaporation. Clearly higher superheats activate more cavities. One must pay attention that a given superheat activates not only cavities of a certain size, but all smaller cavities as well. Therefore, transferring to *active* nucleation sites (n^*) from *potential* (n), one must integrate equation (5.2.3) on size of a cavity, in limits from 0 to d . The function obtained as a result

of this integration is non-elementary and called **complementary error function**:

$$n^*(d) = \int_0^d \frac{n}{N}(l)dl = \frac{1}{2} \operatorname{erfc}\left(\frac{d_1 - d}{\sqrt{2\Sigma}}\right) \quad (5.2.7)$$

Some information about this function can be found, for example, in [53]. It would be useful to give some details about it here as well. The complementary error function is defined in terms of the **error function** (also called the **Gauss error function**):

$$\operatorname{erfc}(x) = 1 - \operatorname{erf}(x) \quad (5.2.8)$$

$$\operatorname{erf}(x) = \frac{2}{\sqrt{\pi}} \int_0^x \exp(-t^2) dt \quad (5.2.9)$$

As follows from equation (5.2.9) one needs to evaluate this function numerically. Summarizing the said above, one obtains the dependence of the applied heat flux on the surface superheat as:

$$q(\Delta T) = q_0 \frac{1}{\sqrt{\pi}} \int_0^D \exp(-t^2) dt \quad (5.2.10)$$

$$D = \frac{d_1 - d}{\sqrt{2\Sigma}} \quad (5.2.11)$$

$$d = \frac{\sigma T_S}{r \rho_V \Delta T} \quad (5.2.12)$$

The system of model equations (5.2.10) – (5.2.12) needs the following information for numerical calculations. Liquid properties: saturation temperature T_S , latent heat of vaporization r , vapor density ρ_V , coefficient of surface tension σ , and surface properties: cavity mean diameter d_1 , dispersion Σ of cavities sizes around d_1 . The quantity q_0 – is more complex, and detailed finding of it can be done using the model proposed by Mitrovic [4]. This lies outside the frames of the proposed model. However, it is important to note that q_0 is dependent on the liquid and surface properties, it increases with the increasing

lengths of the three phase line (TPL). For purpose of presented model it is suggested to be constant.

If information about distribution of cavities number on their sizes is obtained from a side experiments or somehow else, one may follow a simplified procedure, expressed by integration of distribution function in corresponding limits. In this case, one needs to use equation (5.2.7) and substitute its result in equation (5.2.2).

Remembering the given task for modeling one sees that it is successfully accomplished. A model with less possible amount of attracted experimental data is obtained. The only attracted data is information about the surface micro geometry and liquid properties. Numerical experiments will be performed in the next subchapter to validate the proposed model.

5.3. Calculation results

As it was mentioned earlier, for an untreated surface the normal distribution of potential nucleation sites on their sizes is assumed. Figure 5.3.1 represents the boiling curve (q as a function of ΔT), calculated using the system (5.2.10) – (5.2.12), with the accuracy to a constant multiplier.

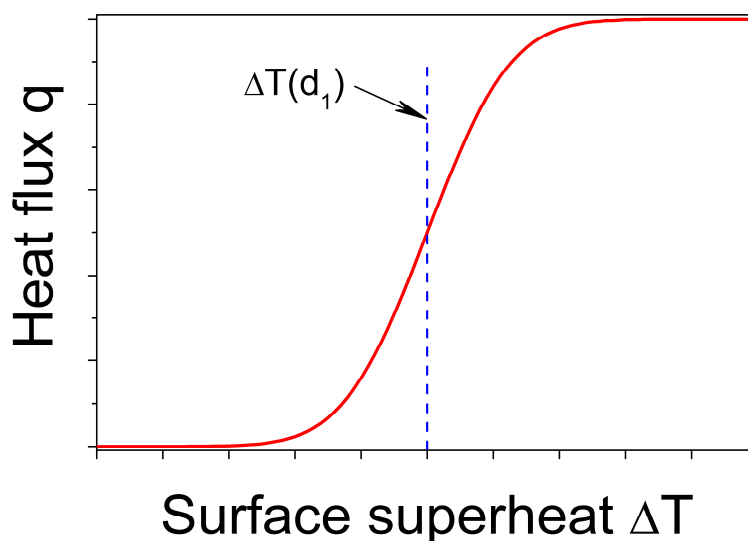


Figure 5.3.1: Boiling curve, evaluated using the proposed system of equations (5.2.10) - (5.2.12).

The axes are left intentionally without numbering, as no information was given earlier on the quantity q_0 . With a blue marker line a superheat is depicted that corresponds to the mean cavity diameter of a real untreated surface, see Figure 5.2.1c. It can be calculated using (5.2.6) or correctly deduced from equation (2.1.2).

One sees the shape of the calculated boiling curve to be the classical one, despite the boiling inception and transfer to film boiling, but those questions were not raised in modeling. It is also seen that very small cavities and very large ones bring no difference in nucleation phenomenon and make almost no contribution into the heat flux.

The next numerical experiment is calculation of the boiling curve for a mono-cavity microstructured cavern. As mentioned earlier, for these surfaces the distribution of cavities on sizes is close to δ -function. It was also mentioned that as in reality the total number of nucleation sites is not infinite, one may choose a very narrow normal distribution instead. The corresponding boiling curve in this case looks as depicted in Figure 5.3.2.

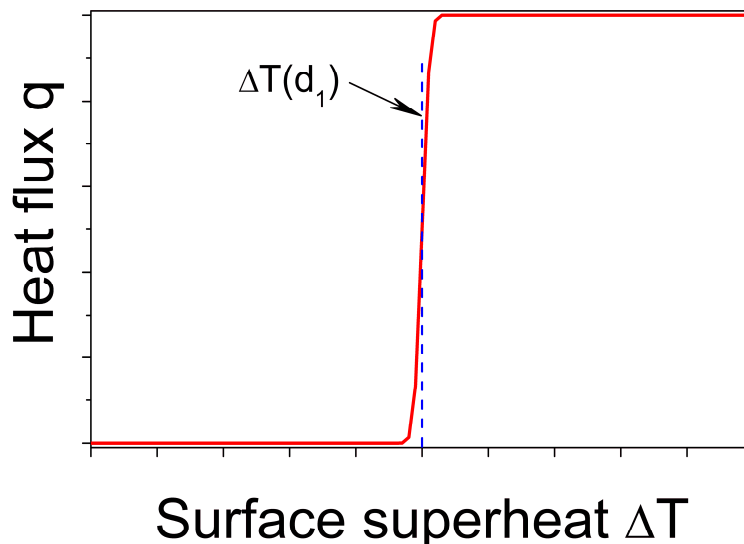


Figure 5.3.2: Calculated boiling curve for a mono-cavity pattern surface.

As all cavities of mono pattern have approximately same size, Figure 5.2.1a, they become activated at a same superheat, Figure 5.3.2. Blue marker in Figure 5.3.2 depicts the superheat corresponding to size of the mono cavity. If one compares Figures 5.3.2 and 4.2.1, they obviously look similar. Continuing

comparing one sees that all microstructured surfaces having the straight mono-spaced pins have boiling curves like one depicted in Figure 5.3.2.

Complicating the calculation experiment, let's move to surfaces with bi-cavity patterns. Let's take a surface with 33% of cavities with characteristic size of d_1 and rest (67%) of cavities with size of d_2 . The difference between d_1 and d_2 is suggested to be relatively small. Correspondingly, coefficient A_1 and A_2 in equation (5.2.5) will be 0.33 and 0.67. The boiling curve calculated for these conditions is represented in Figure 5.3.3.

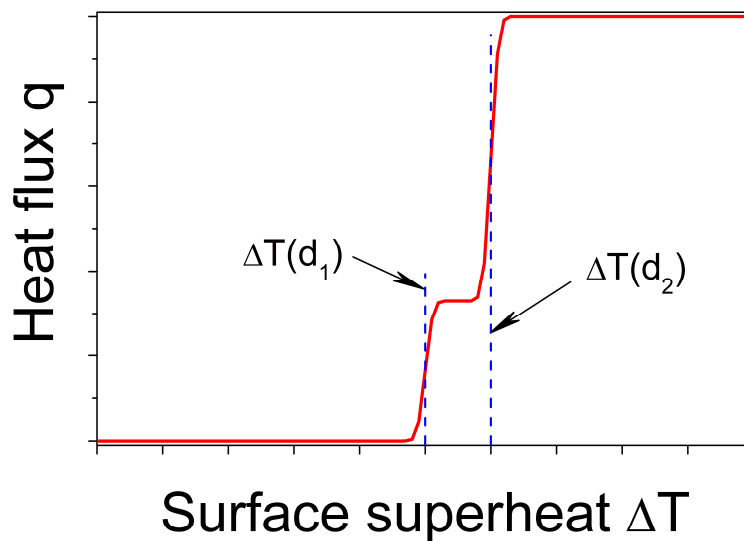


Figure 5.3.3: Calculated boiling curve for a bi-cavity pattern surface.

One sees a step-like change of the temperature between superheats, corresponding to cavities with characteristic sizes d_1 and d_2 . This phenomenon was earlier observed in experiments and called “boiling re-establishing”; see corresponding figures for surfaces with bi-inclined pins. Due to the model analysis re-establishing happens because the cavities with first characteristic size become all active, so no more cavities are available. Because of that temperature “jumps” slightly up, activating the rest of the cavities. Changing the percentage relation between cavities of first and second sizes, one can get different height of “steps” on boiling curves. Changing the ratio between d_1 and d_2 changes the width of the step correspondingly. This analysis will be done in the next subchapter. Thus, successful application of the proposed model was demonstrated. The model gives known results for boundary cases and allows

evaluation of boiling curves for a given conditions. Principal agreement with experiments was demonstrated as well.

5.4. Predictions and extrapolation of the model

It was shown that the proposed model gives the correct principal behavior of the heat flux in dependence on the surface superheat for test cases. Further development of the model is given by equations (5.2.3) and (5.2.5). One may take different functions of cavities distribution and calculate corresponding boiling curves. For example, taking a three-cavity pattern of a surface, the following result may be received, Figure 5.4.1.

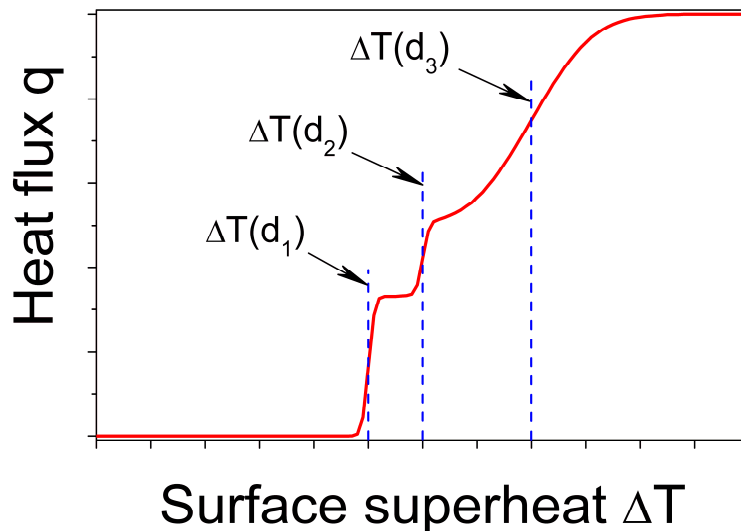


Figure 5.4.1: Predicted boiling curve for a three-cavity pattern surface.

For the case depicted in Figure 5.4.1 an imaginary surface was taken with 3 characteristic cavities with sizes d_1 , d_2 and d_3 , so that $(d_3 - d_2) = 2(d_2 - d_1)$, dispersions $\Sigma_1 = \Sigma_2$ and $\Sigma_3 = 10\Sigma_1$, and coefficients $A_1 = 0.33$, $A_2 = 0.17$ and $A_3 = 0.5$. The following influence of the parameters is observed:

- number of the cavity families is equal to the number of “steps” of the boiling curve;
- difference $(d_i - d_{i-1})$ determines the width of a corresponding step;
- weight coefficients A_i determine the height of a corresponding step;

- dispersions Σ_i determine the slope of the boiling curve in every corresponding region.

To manufacture the described surface, a precise control of cavities sizes must be undertaken. Using the specific production technology of the microstructured surfaces investigated in this work, a variation of number of ion beams and their inclination must be varied.

A boiling curve obtained as a result of calculations using the proposed model is a monotonously growing function. In experiments, however, the decrease of the surface temperature with the increasing heat flux was observed. To obtain this behavior numerically, the following modifications should be done. It was experimentally observed that starting from a certain amount of vapor inside the microstructure (i.e. certain number of active nucleation sites) the surface begin to cool itself down as the length of TPL increases greatly. In terms of the proposed model it means that an equation reverse to (5.2.10) regarding ΔT must be solved with reverse (negative) heat fluxes for some of nucleation sites. Number of active nucleation sites with negative heat fluxes must be proportional to the total number of active nucleation sites with a small, low varying coefficient. This is an important topic for future theoretical studies. For the very first time the reverse heat fluxes were found experimentally by Ilyin [14]. More information about reverse heat fluxes can be obtained from works by Mitrovic [15], and Ustinov et al. [11].

Surprisingly few words can be additionally said about boiling inception and crisis, although, no additional criteria were introduced to account those effects. For all surfaces extremely small or large cavities bring no contribution into the heat transfer. In accordance with Figures 5.3.1 – 5.3.3 and 5.4.1, only cavities of a certain size can be used for initial nucleation. This means also that the lower limit of integration in (5.2.7) can be shifted up. Analogous, when all available cavities of a surface are activated, the surface temperature starts to rise fast, accompanied by no change of the applied heat flux. This confirms the conclusion obtained earlier from experiments that the critical heat flux depends on the surface properties. Due to prediction of the proposed model, the crisis

starts when there are no more cavities available on the surface and the number of active nucleation sites is equal to the number of potential nucleation sites. As distance between neighboring nucleation sites is about several micrometers, created by them vapor immediately form a film.

Another conclusion from the proposed model is that cumulative effects of nucleation dump contribution of a single bubble into the total heat transfer. To explain this idea one must follow through the model equation and see that it is practically unimportant what kind of dependence exists between a cavity size d and its activation superheat ΔT . The main thing is that exists at all. The mentioned dependence is needed only to obtain the numerical values, and can be determined in additional experiments. As the number of potential nucleation sites and subsequently the number of created bubbles is huge, it becomes not so important how exactly each of them was activated. Therefore, the suggestion of constant q_0 is supported. It can adequately model the real situation. Nevertheless, superheat activating a cavity of a certain size must correctly be deduced from equation (2.1.2).

Further development of the model seems to be possible by taking into consideration the fractal dimension of the surface. Doing so, one can obtain the function of distribution of the potential nucleation sites of a surface on their sizes.

6. CONCLUSIONS

The original classification system of enhanced surfaces was proposed basing the common properties of different enhancement methods and consideration of basic physical principles governing the nucleation. Majority of existing enhanced surfaces for nucleate boiling were considered with pro and contra using the proposed classification system.

Modified surfaces can enhance the boiling heat transfer either supporting the initial nucleation which is a probabilistic phenomenon, or by enlarging the length of three phase line (TPL) after a vapour bubble had been created and started to grow. To judge about certain way of enhancement, a characteristic micro geometry scale of structure is proposed to calculate using the fractal dimension. This quantity seems to be the universal and applicable for different kind of microstructures, unlike the roughness parameter.

Eleven novel microstructured surfaces were created using the patented technology and tested with three liquids, refrigerants R141b, R134a and highly wetting electronic liquid FC-3284. Experiments were conducted for nucleate pool boiling mode at pressures ranging from 0.5 bar to 9 bar in the single tube configuration. Surface superheat of a microstructured surface was discovered to be unaffected by the applied heat flux. This unique property is attributed to very large lengths of TPL, provided by great number of micropins piercing a growing bubble. In several boiling modes the TPL lengths were so long that 2 K – 3 K decrease of surface temperature was detected with the increasing heat flux.

For boiling on surfaces with bi-cavity patterns superheat experiences a sharp step-alike change, later remaining unaffected by the heat flux. This process is called “boiling re-establishing”. First, smaller cavities are activated at a certain superheat. Later, when surface reaches the activation temperature for larger cavities, they become activated as well. As cavities of both sizes are formed by the same near by pins, only a larger one acts. Thus the larger bubbles occur on the surface, what was observed visually, Figures 4.1.8 – 4.1.12.

The heat transfer efficiency of the microstructured surface in comparison with a technically smooth tube under idem conditions was found to be by the factors ranging up to 18 times higher in several boiling modes. The enhancement factor depends on the geometry of the microstructured surface, system pressure and properties of the boiling liquid. This dependency on the microstructure geometry is generalized by the equation (4.3.4). The enhancement factor decreases with increasing pressure: at lower pressures the critical bubble radius increases, reducing the difference between values, obtained from equations (2.1.1) and (4.3.3). Therefore, even more nucleation sites can be activated, as their sizes become large enough to support density fluctuations and form a vapor bubble. The most effective boiling modes were accompanied by the boiling inception as a front. The velocity of the front depends on the microstructure geometry.

Appearance of the bubble chains on the microstructured surfaces was observed in all boiling modes, see Figure 4.1.22. It confirms the correctness of the nucleation criteria (2.1.2): it is easier for a new bubble to arise near an existing vapor rest. This phenomenon also sets thinking about boiling as a chaotic process with deterministic behavior. The order of bubbles chains appears in the chaos of the fluid density fluctuations.

Temperature oscillations of the surface were detected experimentally near the crisis during boiling of the highly wetting fluid FC-3284. The amplitudes and the frequencies of oscillations rise significantly right before the crisis, because large vapor masses are formed and detached from the surface. Both amplitudes and frequencies of temperature oscillations depend on the microstructure geometry. For microstructures with larger number of pins the decrease of amplitudes of temperature oscillation was noted. The phase portrait (attractor) was constructed for measured data, showing that some time after the beginning of observations the amplitudes and the frequencies of surface temperature oscillations tend to tighten near a narrow phase area. This allows recommending this method for detection and prevention of boiling crisis in industrial apparatuses.

Boiling hysteresis was found to be expressed stronger for structures with higher micropins density due to their better vapor trapping abilities. Higher pressures suppress the hysteresis as well as the surface temperature gradients.

Comparison of experimental data on boiling heat transfer from a single microstructured tube with different liquids has shown good agreement with literature data, expressed by (4.3.4).

Tandem tube experiments have shown high compactness of results of measurements for different boiling modes. The independence of the surface superheats on the heat flux applied to the test tube has been observed for all pressures. This is attributed to the great number of vapor bubbles, produced by the microstructured surface, same as for a single tube. Weak dependence of the upper tube superheats on the heat flux of the lower tube was observed. For industrial practice it means no significant temperature gradients in a heat exchanger, and simultaneous stable and effective work of all microstructured tubes, regardless their positions in the bundle, entering position of fluids into the heat exchanger, and pressure.

Higher heat transfer coefficients for R134a have been found for the upper tube, than for lower tube, what has good agreement with data from literature, Figure 4.4.4. Presence of the lower tube generally promotes heat transfer of the upper tube, as vapor bubbles generated by lower tube are trapped by the microstructure of the upper one, helping to create new bubbles. For FC-3284, however, the increase of surface temperature of the upper tube in comparison with single tube at 2 K was measured.

Effects of boiling reestablishing, hysteresis and, most important, the constancy of the wall superheat, were detected for the tandem configuration in the same degree as for the single tube experiment.

The microstructured surfaces have demonstrated very high effectiveness in tandem configuration, stability of the performance, very low superheats and independency on non-stationary effects. The microstructured surfaces can be recommended for use in industrial heat exchangers with the corresponding liquid, so its critical heat flux would be large enough. As soon as boiling occurs on a single tube from the bundle, the rest of the tubes becomes activated as

well, so no great inception superheats are required for the bundle of microstructured tubes.

A model is proposed based upon the statistical information of a surface micro geometry and properties of liquid. The proposed model is universal and is not limited to a single class of enhanced surfaces. The only surface specific information required is a function of distribution of cavities on their sizes.

The proposed model gives correct principal dependence of heat flux on surface superheat for a real surface, microstructured surface with mono-cavity pattern and bi-cavity pattern as well. Modeling results show that the superheat of a mono-cavity pattern surface is independent on the heat flux – a fact confirmed by numerous experiments. For bi-cavity pattern the re-establishing is obtained as results of calculation. It happens when all cavities of a smaller characteristic size are active. In subsequent process surface temperature “jumps” up, activating the rest of the cavities.

Varying model parameters (number of distinguished cavities, diameter of these cavities, dispersions of cavities sizes around their diameters, and percent relation between the distinguished cavities) one may obtain any shape of a boiling curve. It seems possible to manufacture a surface with pre-programmed boiling curves.

Modeling results show that boiling crisis starts when there are no more cavities available on the surface and the number of active nucleation sites is equal to the number of potential nucleation sites. As distance between neighboring nucleation sites is about several micrometers, vapor, created by them, immediately forms a film. Principally the mechanisms of boiling crisis and boiling re-establishing are the same.

7. REFERENCES

1. Thome J. R., Enhanced boiling heat transfer, 1990, *Hemisphere, New York*
2. Webb, R. L. (1994) Principles of Enhanced Heat Transfer, *Wiley Int. Publication*
3. Webb R.L., Odyssey of the enhanced boiling surface, *ASME Journal of Heat Transfer*, Vol. 126, 2004, pp. 1051-1059
4. Mitrovic J., How to create an efficient surface for nucleate boiling? *International Journal of Thermal Sciences*, Vol. 45, 2006, pp. 1–15
5. Mitrovic J., Ustinov A., Nucleate boiling heat transfer on a tube provided with a novel microstructure, *Journal of Enhanced Heat Transfer*, Vol. 13(3), 2006, pp. 1–18
6. Mitrovic J., Ustinov A., Boiling features of a novel microstructure, *Proc. of 13th International Heat Transfer Conference*, 2006, Sydney, Australia
7. Labuntsov D.A., Heat transfer during nucleate boiling of liquids, *Teploenergetika*, Vol. 12, 1959, pp. 19-26, in Russian
8. Deriagin B.V. *Doklady AN SSSR*, Vol. 51 # 5, 1946, pp. 357-360, in Russian
9. Deriagin B.V., Churaev N.V., Muller V.M., Surface forces, 1987, Nauka, in Russian
10. Labuntsov D.A., Approximate theory of heat transfer for a developed nucleate boiling, *Izvestia AN SSSR, OTN, Energetika I transport*, Vol. 1, 1963, pp. 58 – 71, in Russian
11. Kuzma-Kichta Y. A., Ustinov A.K., Ustinov A.A., Analysis of interface oscillations during boiling, *Proc of 12th Int. Heat Transfer Conf. Grenoble, France*, 2002, Vol. 3, p. 527
12. Auracher H., Marquardt W., Heat transfer characteristics and mechanisms along entire boiling curves under steady-state and transient conditions, *International Journal of Heat and Fluid Flow*, Vol. 25, 2004, pp. 223–242

13. Judd K., Kenning D.B.R., Ellepola J.H., McSharry P. E., J. v. Harden, Spatial-temporal analysis of nucleate pool boiling: identification of nucleation sites using non-orthogonal empirical functions, *International Journal of Heat and Mass Transfer*, Vol. 45, 2002, pp. 237-253
14. Iliyn I. N., Gritsov V. P., Yaundalders S. R. Holographic interferometry studies of temperature profiles in thermal boundary layer in free convection and bubble boiling, *Proc. of 7th International Heat Transfer Conference*, Vol. 4, 1982, pp. 55-59
15. Mitrovic J., On the profile of the liquid wedge underneath a growing vapor bubble and the reversal of the wall heat flux, *Int. J. Heat Mass Transfer*, Vol.45, 2002, pp. 409-415
16. Shoji M., Studies of boiling chaos: a review, *International Journal of Heat and Mass Transfer*, Vol. 47, 2004, pp. 1105–1128
17. Mosdorf R., Shoji M., Chaos in nucleate boiling – nonlinear analysis and modeling, *International Journal of Heat and Mass Transfer*, Vol. 47, 2004, pp. 1515–1524
18. Franco A., Latrofa E.M., Yagov V.V., Heat transfer enhancement in pool boiling of a refrigerant fluid with wire nets structures, *Experimental Thermal and Fluid Science*, Vol. 30, 2006, pp. 263-275
19. Labuntsov D.A., Yagov V.V., Vapor bubbles dynamics at low pressures, *Trudi MEI*, Vol. 268, 1975, pp. 16-32, in Russian
20. Hwang G.-S., Kaviany M., Critical heat flux in thin, uniform particle coatings, *International Journal of Heat and Mass Transfer*, Vol.49, 2006, pp. 844-849
21. Liter S. G., Kaviany M., Pool-boiling CHF enhancement by modulated porous-layer coating: theory and experiment, *International Journal of Heat and Mass Transfer*, Vol. 44 , 2001, pp. 4287-4311
22. Chang J. Y., You S. M., Enhanced boiling heat transfer from micro-porous surfaces: effects of a coating composition and method, *International Journal of Heat and Mass Transfer* , Vol. 40 (1997) 4449-4460

23. Kuzma-Kichta Yu.A., Komendantov A.S., Bakunin V.G., Bartsch G., Goldschmidt R., Stein M., Enhancement of heat transfer at boiling with porous coated surfaces, *Proc. of 3rd European Thermal Sciences Conference*, 2000, pp. 809-814
24. Nelson R.A., Do we doubt too little? Examples from the thermal sciences, *Experimental thermal and fluid science*, Vol. 25, 2001, pp. 255-267
25. Luke A., Danger E., Gorenflo D., Size distribution of active and potential nucleation sites in pool boiling, *Proc of 12th Int. Heat Transfer Conf. Grenoble, France, 2002, Vol. 3*
26. Mitrovic J., Hartmann F., A new microstructure for pool boiling, *Superlattices and Microstructures*, Vol. 35, 2004. pp. 617-628
27. Barthau G., Hahne E., Second order effects in an experimental study of nucleate pool boiling of R134a, *Proc of 12th Int. Heat Transfer Conf. Grenoble, France, 2002, Vol. 3, pp. 683*
28. Y. Fujita, Q. Bai. Bubble dynamics and heat transfer in boiling. *Proc. of 12th IHTC*, Vol.1 p. 93-104
29. Asano H., Bouyer E., Hanne R., Müller-Steinhagen H., Schäfer D.: Improved Heat Transfer by RF Plasma Produced Structured Surfaces. International Thermal Spray Conference, Orlando, USA, 5-8 May 2003, S.559-566 (2003)
30. Y. Takata, S. Hidaka, H. Yamamoto, M. Masuda and T. Ito. Evaporation of Water Drop on Photo-Induced Hydrophilic Surface, *Proc of 12th Int. Heat Transfer Conf. Grenoble, France, 2002, Vol. 3.*
31. Mueller-Steinhagen H., Zhao Q., Investigation of low fouling surface allows made by ion implantation technology, *Chem. Eng. Science*, Vol. 52, #19, 1997, pp. 3321-3332
32. Solodov A. P., Computer Model of Nucleate Boiling: *Proc. of the International Engineering Foundation, 3rd Conference*, Irsee, Germany. 1997. pp. 231 – 238.

33. Yu B., Cheng P., A Fractal Model for Nucleate Pool Boiling Heat Transfer, *Journal of Heat Transfer*, Vol.124, 2002, pp. 1117-1124
34. Shoji M., Takagi Y. Bubbling features from a single artificial cavity, *Int. Journal of Heat and Mass Transfer*, Vol. 44, 2001, pp. 2763-2776
35. El-Genk M. S., Parker J. L., Enhanced boiling of HFE-7100 dielectric liquid on porous graphite, *Energy Conversion and Management*, Vol. 46, 2005, pp. 2455-2481
36. Webb R.L., Chien L.-H., Visualization of pool boiling on enhanced surfaces, *Experimental Thermal and Fluid Science*, Vol.16, 1998, pp. 332-341
37. Chen Y., Groll M., Mertz R., Kulenovic R., Visualization and mechanisms of pool boiling of propane, isobutane and their mixtures on enhanced tubes with reentrant channels, *International Journal of Heat and Mass Transfer*, Vol. 48, 2005, pp. 2516-2528
38. Guglielmini G., Misale M., Schenone C., Boiling of saturated FC-72 on square pin fin arrays, *Int. J. Therm. Sci.*, Vol.41, 2002, pp. 599-608
39. Wei J.J., Honda H., Effects of fin geometry on boiling heat transfer from silicon chips with micro-pin-fins immersed in FC-72, *International Journal of Heat and Mass Transfer*, Vol. 46, 2003, pp. 4059–4070
40. Kandlikar S. G., Kuan W. K., Willistein D. A., Borrelli J., Stabilization of flow boiling in microchannels using pressure drop elements and fabricated nucleation sites *Journal of Heat Transfer*, Vol. 128, 2006, pp. 389 – 396
41. Hwang U.P., Moran K.F., Boiling heat transfer of silicon integrated circuits chip mounted on a substrate, *ASME HTD*, Vol. 20, 1981, pp. 53–59
42. R.N. Wenzel, Resistance of solid surfaces to wetting by water. *Ind. Eng. Chem.*, Vol. 28, 1936, p. 988
43. Mitrovic J. and Fauser J., Propagation of boiling fronts along horizontally arranged heated tubes, *Trans. IChemE*, Vol.79, Part A, 2001 pp. 363-370
44. Gorenflo D., Pool Boiling, VDI Heat Atlas, *VDI – Verlag*, 1993, Duesseldorf

45. Kutateladze S.S., Heat transfer during boiling and condensation, *Mashgiz*, 1952, p. 231, in Russian
46. Arik M., Bar-Cohen A., Effusivity-based correlation of surface property effects in pool boiling CHF of dielectric liquids, *International Journal of Heat and Mass Transfer*, Volume 46, Issue 20, September 2003, pp. 3755-3764
47. Kline S.J., McClintock F.A., Describing uncertainties in single sample experiments, *Mech. Eng.* Vol. 75, 1953, pp. 3 – 8
48. Zheng, J. X., Jin, G. P., Chyu, M.-C., Ayub, Z. H.; Boiling on a horizontal plain tube bundle with Ammonia/Lubricant mixture subjected to inlet vapor quality; *Proc. of 13th Int. Heat Transfer Conf.*, Sydney, Australia, 2006
49. Akhilesh Gupta; Enhancement of boiling heat transfer in a 5×3 tube bundle; *International Journal of Heat and Mass Transfer* 48 (2005) 3763 – 3772.
50. Kuzma-Kichta Yu.A., Bakunin V.G., Laser methodic of investigation of characteristics of nucleate boiling, *Instruments and Experimental Techniques*, Vol. 41, # 6, 1998, pp. 128-131
51. Schuster H.G., Deterministic chaos – an introduction, *Physik-Verlag*, Weinheim, 1984
52. Berge P., Pomeau Y., Vidal C., The order in the chaos. About deterministic approach to the turbulence, *Hermann*, Paris 1988
53. Abramowitz M, Stegun I.A., eds. Handbook of Mathematical Functions with Formulas, Graphs, and Mathematical Tables, *Dover*, New York, 1972.
54. Hartmann F., Untersuchungen yum Siedeverhalter von Heizflächen mit Mikrostrukturen. Dissertation. Fortschr.-Ber. VDI Reihe 19 Nr. 158. Düsseldorf: *VDI Verlag* 2008.

APPENDICES

Experimental data in table form.

q – Heat flux;

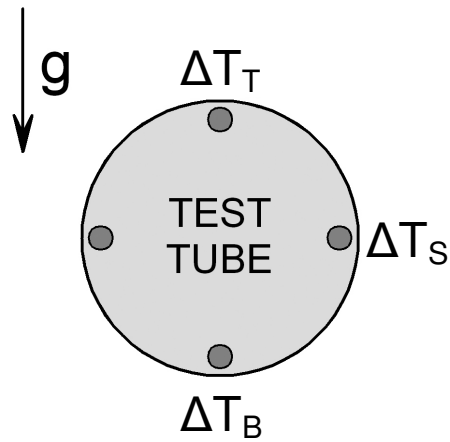
p – Pressure;

ΔT_T – Wall superheat at the top of the test tube;

ΔT_S – Wall superheat at the side of the test tube;

ΔT_B – Wall superheat at the bottom of the test tube;

* – Boiling inception.



Single tube experiments
Refrigerant R141b

q kW/m ²	ΔT_T K	ΔT_S K	ΔT_B K
Structure A418+50, pressure p = 1 bar			
0,3	1,024	1,057	1,059
1,3	3,982	4,107	4,260
* 2,9	8,377	8,415	8,977
5,2	4,148	3,862	4,052
8,1	5,155	4,627	4,862
11,6	6,307	5,482	5,631
15,8	7,541	6,409	6,332
20,6	8,812	7,239	6,962
26,1	10,089	8,133	7,513
32,2	10,800	8,408	7,856
39,0	11,234	8,411	8,143
46,3	11,020	8,383	8,397
54,3	10,974	8,506	8,658
63,0	10,734	8,534	8,891
72,3	10,386	8,538	9,202
82,2	10,195	8,546	9,458
92,7	10,182	8,468	9,634
103,9	9,657	8,151	9,998
115,7	9,430	7,900	10,211
128,2	9,251	7,650	10,491
98,2	8,611	7,744	9,874
73,2	8,167	7,339	9,079
50,3	7,594	6,741	8,237
32,2	6,726	6,019	7,319
17,7	5,649	5,167	6,266
8,1	4,268	3,999	4,678
2,0	2,619	2,543	2,696

q kW/m ²	ΔT_T K	ΔT_S K	ΔT_B K
Structure A418+50, pressure p = 2 bar			
0,3	0,965	1,039	1,025
1,3	4,208	4,364	4,496
2,9	9,112	9,208	9,651
4,0	11,856	12,13	12,68
* 5,2	13,975	14,08	14,78
8,1	5,055	4,506	4,525
11,6	6,109	5,232	5,143
15,8	7,330	5,942	5,662
20,6	8,539	6,715	6,045
26,1	9,710	7,442	6,484
32,2	10,153	7,701	6,681
38,9	10,281	7,833	6,864
46,2	10,191	7,725	7,053
54,2	10,153	7,723	7,221
62,8	10,366	7,835	7,462
72,1	9,997	7,656	7,544
82,1	9,931	7,648	7,792
92,5	9,587	7,393	8,186
103,7	9,461	7,286	8,302
115,4	9,373	7,112	8,639
127,9	9,213	6,971	8,941
98,0	8,629	7,029	8,232
72,1	8,280	6,787	7,720
50,2	7,741	6,308	7,145
32,2	6,715	5,607	6,517
18,1	5,356	4,704	5,642
8,1	3,726	3,476	4,150
2,0	2,156	2,118	2,295

q kW/m ²	ΔT_T K	ΔT_S K	ΔT_B K	q kW/m ²	ΔT_T K	ΔT_S K	ΔT_B K
Structure A428, pressure p = 1 bar				Structure A428, pressure p = 2 bar			
1,2	6,168	6,181	6,048	1,2	6,539	6,577	6,447
* 2,8	12,343	12,364	12,111	2,7	12,62	12,685	12,427
4,8	2,683	2,765	2,690	* 4,8	20,382	20,462	20,041
7,5	2,311	2,359	2,451	7,5	2,612	2,682	2,591
10,8	2,356	2,383	2,500	10,9	2,050	2,127	2,029
14,7	2,413	2,463	2,616	14,8	1,731	1,798	1,695
19,2	2,474	2,516	2,734	19,1	1,725	1,791	1,694
24,3	2,547	2,583	2,893	24,2	1,644	1,694	1,593
29,9	2,617	2,645	3,064	29,8	1,714	1,751	1,662
36,1	2,683	2,708	3,143	36,1	1,752	1,769	1,761
42,9	2,766	2,785	3,250	42,9	1,810	1,819	1,931
50,4	2,834	2,855	3,350	50,4	1,903	1,906	2,200
58,4	2,942	2,950	3,500	58,5	1,973	1,979	2,247
67,2	3,112	3,198	3,502	66,9	2,073	2,090	2,326
76,2	3,235	3,317	3,584	76,3	2,195	2,238	2,381
86,1	3,433	3,462	3,714	85,9	2,335	2,458	2,490
96,5	3,644	3,555	3,746	96,5	2,530	2,658	2,609
107,0	3,729	3,615	3,838	107,1	2,710	2,779	2,550
118,3	3,836	3,637	3,824	118,4	2,856	2,870	2,697
90,7	3,655	3,614	3,633	90,9	2,686	2,779	2,494
67,0	3,414	3,455	3,443	67,0	2,437	2,576	2,329
46,4	3,141	3,206	3,156	46,4	2,214	2,358	2,184
29,7	2,917	2,949	2,888	29,8	1,971	2,112	1,952
16,9	2,693	2,730	2,631	17,2	1,806	1,955	1,791
7,5	2,419	2,432	2,384	7,5	1,578	1,687	1,547
2,0	2,069	2,040	2,001	1,9	1,538	1,585	1,500

q kW/m ²	ΔT_T K	ΔT_S K	ΔT_B K
Structure A428, pressure p = 3 bar			
1,2	4,721	4,804	4,731
2,7	8,620	8,782	8,537
4,8	8,766	8,922	8,757
* 7,5	9,629	10,017	9,558
10,8	4,796	3,717	1,740
14,7	5,779	4,395	1,833
19,1	5,999	4,577	1,782
24,2	6,181	4,563	1,755
29,7	6,692	4,672	1,854
36,2	6,593	4,284	1,862
42,9	6,782	4,133	1,954
50,8	6,359	3,603	1,939
58,4	6,423	3,543	2,111
67,0	6,142	3,278	2,079
76,8	6,380	3,359	2,148
86,0	5,838	3,101	2,166
96,3	5,724	3,113	2,231
107,6	5,465	3,034	2,292
118,7	5,316	2,943	2,343
90,9	4,588	2,793	2,236
67,5	3,892	2,438	2,015
46,5	2,940	1,849	1,736
30,1	2,334	1,645	1,560
17,1	1,814	1,445	1,380

q kW/m ²	ΔT_T K	ΔT_S K	ΔT_B K
Structure A428, pressure p = 4 bar			
1,2	4,657	4,777	4,629
2,7	9,720	9,813	9,583
* 4,9	9,896	10,096	9,882
7,5	2,692	1,981	1,498
10,7	3,321	2,309	1,716
14,8	3,700	2,363	1,689
19,1	4,033	2,379	1,681
24,2	3,598	1,773	1,400
29,8	3,750	1,710	1,501
36,0	3,511	1,605	1,512
43,1	3,664	1,646	1,580
50,2	3,890	1,696	1,656
58,6	4,174	1,781	1,721
66,8	4,413	1,853	1,818
76,4	4,733	1,961	1,898
85,0	5,012	2,13	1,951
96,4	5,165	2,237	2,043
107,1	5,342	2,369	2,094
119,6	5,000	2,474	2,131
90,9	4,176	2,069	2,020
66,5	3,319	1,757	1,732
47,0	2,628	1,541	1,524
30,2	2,026	1,366	1,338
16,7	1,542	1,223	1,183
7,4	1,175	1,075	1,025

q kW/m ²	ΔT_T K	ΔT_S K	ΔT_B K
Structure A428, pressure $p = 5$ bar			
1,2	5,620	5,694	5,564
2,8	5,097	5,111	5,401
* 4,8	5,845	5,797	6,336
7,5	2,126	1,599	1,303
10,8	2,038	1,509	1,292
14,7	2,055	1,444	1,277
19,1	1,963	1,348	1,248
24,1	2,040	1,319	1,241
30,1	2,289	1,422	1,357
36,1	2,392	1,391	1,320
42,7	2,665	1,481	1,455
50,3	2,891	1,519	1,510
58,3	3,161	1,589	1,600
66,9	3,458	1,668	1,683
76,3	3,803	1,782	1,747
85,8	4,121	1,848	1,815
96,4	4,465	1,999	1,921
107,0	4,623	2,090	1,958
118,6	4,777	2,291	2,077
90,5	3,918	1,853	1,866
66,7	3,039	1,565	1,594
46,7	2,318	1,351	1,316
30,2	1,787	1,23	1,177
16,8	1,374	1,124	1,063
7,4	1,191	1,136	1,075

Refrigerant R134a

q kW/m ²	ΔT_T K	ΔT_S K	ΔT_D K
Structure A428, pressure p = 5 bar			
2,70	7,882	7,944	7,855
4,80	7,977	7,820	7,94
* 7,70	8,937	8,013	8,922
11,0	1,090	0,538	0,501
14,7	1,318	0,583	0,523
19,3	1,790	0,651	0,575
24,2	2,821	0,768	0,645
29,8	5,251	1,547	0,756
36,4	6,022	2,269	0,888
43,2	6,445	3,408	1,200
50,6	6,431	3,711	1,313
58,2	6,579	3,822	1,480
67,1	6,317	3,706	1,430
76,4	6,175	3,672	1,493
86,0	6,051	3,506	1,579
96,3	5,899	3,347	1,590
106,7	5,646	3,179	1,582
118,4	5,396	2,951	1,691
91,6	5,062	3,178	1,591
67,2	4,617	2,935	1,532
47,3	4,121	2,618	1,378
30,4	3,487	1,777	0,989
16,9	1,881	0,717	0,656
7,60	0,931	0,477	0,463

q kW/m ²	ΔT_T K	ΔT_S K	ΔT_B K
Structure A428, pressure p = 6 bar			
2,80	6,007	6,189	5,973
* 4,80	5,171	4,881	5,604
7,70	0,896	0,469	0,459
10,8	0,808	0,465	0,497
14,8	1,006	0,522	0,553
19,1	1,297	0,595	0,636
24,3	1,754	0,644	0,695
30,3	3,666	0,761	0,740
36,6	5,118	1,573	0,959
43,3	5,627	2,486	1,245
50,4	5,995	3,540	1,387
59,1	6,257	3,832	1,396
66,7	6,246	3,826	1,514
76,2	6,156	3,751	1,435
85,3	6,232	3,759	1,549
96,4	5,901	3,464	1,534
106,7	5,748	3,273	1,580
118,7	5,333	3,059	1,724
90,8	5,081	3,311	1,636
66,6	4,639	3,083	1,580
46,9	4,124	2,712	1,398
29,6	3,540	1,978	1,090
16,9	1,779	0,629	0,583

q kW/m ²	ΔT_T K	ΔT_S K	ΔT_B K
Structure A4 28, pressure p = 7 bar			
1,20	4,130	4,190	4,192
* 2,70	8,436	8,501	8,461
4,80	5,171	6,505	5,000
7,60	6,382	8,370	6,245
10,8	5,924	9,127	6,998
14,6	0,974	0,443	0,482
19,1	1,262	0,509	0,545
24,4	1,710	0,575	0,606
29,7	2,718	0,623	0,607
36,1	4,091	0,857	0,696
43,5	5,138	2,203	1,095
51,0	5,456	3,028	1,479
58,5	5,663	3,486	1,463
67,2	5,788	3,782	1,491
76,3	5,834	3,911	1,503
86,3	5,756	3,949	1,577
96,6	5,681	3,971	1,631
108	5,452	3,610	1,685
117	5,324	3,484	1,733
90,6	4,961	3,384	1,682
67,8	4,550	3,180	1,500
46,4	3,998	2,803	1,388
30,0	3,318	1,807	0,907

q kW/m ²	ΔT_T K	ΔT_S K	ΔT_B K
Structure A4 28, pressure p = 8 bar			
1,20	4,654	4,702	4,623
* 2,60	6,886	7,105	6,835
4,80	5,626	5,834	5,683
7,60	0,767	0,379	0,402
10,7	0,873	0,415	0,434
14,7	1,075	0,443	0,449
19,1	1,408	0,484	0,476
24,3	2,048	0,554	0,534
29,8	3,719	0,680	0,586
36,3	5,143	2,417	1,142
43,1	5,397	3,489	1,397
50,4	5,564	3,638	1,360
58,6	5,589	3,730	1,480
67,2	5,642	3,832	1,551
76,6	5,695	3,909	1,676
86,0	5,528	3,893	1,623
96,4	5,433	3,813	1,720
108	5,154	3,456	1,759
120	4,749	3,458	1,844
90,7	4,405	3,322	1,817
67,3	4,055	3,136	1,715
46,2	3,585	2,833	1,554
30,2	3,087	2,272	1,252
16,7	1,189	0,479	0,463

q kW/m ²	ΔT_T K	ΔT_S K	ΔT_B K
Structure A428, pressure p = 9 bar			
1,20	4,328	4,48	4,236
2,80	4,663	4,759	4,553
* 5,00	5,393	5,694	5,373
7,40	0,754	0,378	0,335
11,1	0,909	0,396	0,380
14,6	1,123	0,419	0,404
19,4	1,620	0,496	0,473
24,0	3,013	0,564	0,486
29,9	4,587	1,217	0,744
36,5	5,176	3,047	1,500
42,9	5,333	3,441	1,504
49,7	5,413	3,542	1,550
58,2	5,478	3,660	1,607
66,9	5,386	3,768	1,637
76,2	5,329	3,818	1,659
86,1	5,282	3,853	1,736
96,1	5,243	3,776	1,723
107	5,163	3,681	1,801
118	5,131	3,483	1,751
91,0	4,698	3,285	1,782
67,2	4,252	3,065	1,724
47,1	3,767	2,767	1,581
30,1	3,172	2,243	1,361
16,9	1,844	0,623	0,525

q kW/m ²	ΔT_T K	ΔT_S K	ΔT_B K
Structure A419, pressure p = 5 bar			
2,73	2,854	2,501	2,282
4,81	3,645	3,006	2,573
* 7,59	4,618	3,582	2,834
10,9	5,611	4,187	3,029
14,8	6,578	4,680	3,260
19,2	7,302	5,125	3,445
24,2	7,998	5,444	3,645
29,8	8,607	5,772	3,828
36,1	9,106	6,022	3,953
43,0	9,456	6,183	4,032
50,3	9,727	6,225	4,029
58,3	9,655	6,202	4,156
67,0	9,596	6,344	4,166
75,9	9,610	6,599	4,227
86,8	9,609	6,684	4,250
96,5	9,555	6,540	4,329
107	9,231	6,101	4,330
120	8,770	6,185	4,436
91,9	8,291	6,160	4,328
67,2	7,734	5,986	4,282
47,2	7,132	5,662	4,218
29,6	6,249	5,081	4,049
17,0	5,127	4,272	3,580
7,49	3,684	3,219	3,078
1,91	1,943	1,842	1,839

q kW/m ²	ΔT_T K	ΔT_S K	ΔT_B K
Structure A419, pressure p = 6 bar			
2,71	10,18	10,28	10,43
* 4,85	8,137	8,943	9,105
7,54	4,374	3,410	2,739
10,9	5,352	4,031	2,958
14,7	6,186	4,492	3,162
19,4	6,946	4,878	3,349
24,7	7,572	5,189	3,383
29,8	7,992	5,413	3,441
36,4	8,346	5,676	3,515
42,9	8,604	5,824	3,561
50,3	8,827	5,984	3,546
58,4	8,952	6,107	3,628
66,9	9,046	6,196	3,698
76,1	9,141	5,978	3,771
85,8	9,086	6,151	3,848
96,7	9,149	6,232	3,875
108	9,204	6,288	3,949
119	9,113	6,342	4,000
90,7	8,665	6,216	3,974
66,7	8,018	5,955	3,838
46,6	7,277	5,583	3,777
29,9	6,263	4,983	3,635
16,9	5,043	4,184	3,418
7,56	3,591	3,123	2,841

q kW/m ²	ΔT_T K	ΔT_S K	ΔT_B K
Structure A419, pressure p = 7 bar			
2,84	2,816	2,390	2,176
* 4,85	3,693	3,013	2,510
7,48	4,517	3,548	2,711
10,8	5,414	4,035	2,896
14,6	6,077	4,377	2,995
19,3	6,684	4,673	3,102
24,5	7,102	4,920	3,158
30,0	7,400	5,069	3,211
36,5	7,632	5,206	3,266
42,7	7,799	5,311	3,248
50,0	7,988	5,438	3,303
58,5	8,127	5,653	3,417
67,5	8,305	5,781	3,435
76,7	8,481	5,910	3,472
85,5	8,645	6,038	3,548
96,4	8,744	5,987	3,635
106	8,786	6,043	3,670
118	8,610	6,055	3,741
90,4	8,262	5,972	3,726
66,7	7,770	5,739	3,616
46,4	7,119	5,431	3,559
29,6	6,145	4,848	3,428
16,9	5,026	4,119	3,274
7,60	3,641	3,132	2,785

q kW/m ²	ΔT_T K	ΔT_S K	ΔT_B K
Structure A419, pressure p = 8 bar			
* 2,73	3,706	2,758	2,225
4,83	3,662	2,987	2,514
7,49	4,487	3,503	2,712
10,7	5,248	3,937	2,824
15,0	5,954	4,257	2,915
19,1	6,371	4,500	2,955
24,2	6,782	4,702	3,012
29,7	6,991	4,868	3,043
36,2	7,195	4,996	3,084
43,4	7,376	5,124	3,112
49,8	7,496	5,235	3,161
58,2	7,703	5,452	3,220
67,0	7,812	5,583	3,263
76,0	7,986	5,722	3,318
86,1	8,091	5,784	3,382
96,5	8,188	5,809	3,457
107	8,266	5,821	3,485
119	8,284	5,921	3,588
90,4	8,030	5,729	3,508
66,5	7,673	5,501	3,419
46,3	7,017	5,160	3,363
29,5	6,089	4,619	3,299
16,8	4,923	3,901	3,064

q kW/m ²	ΔT_T K	ΔT_S K	ΔT_B K
Structure A419, pressure p = 9 bar			
2,76	10,40	10,60	10,42
* 4,82	7,624	6,364	5,609
7,33	7,301	6,347	5,506
10,7	7,524	6,218	5,060
14,8	5,886	4,298	2,938
19,3	6,221	4,460	2,890
24,3	6,448	4,548	2,882
29,9	6,681	4,698	2,934
36,2	6,846	4,807	2,951
43,0	6,968	4,919	2,987
50,3	7,072	5,019	3,008
57,9	7,194	5,132	3,033
67,0	7,326	5,256	3,081
75,9	7,423	5,328	3,125
85,5	7,563	5,480	3,195
96,8	7,679	5,658	3,316
108	7,756	5,746	3,364
118	7,823	5,796	3,409
91,2	7,636	5,658	3,367
67,5	7,388	5,439	3,290
46,4	6,892	5,093	3,160
30,0	6,070	4,587	3,083
16,9	4,851	3,791	2,885
7,59	3,427	2,849	2,458
1,88	1,783	1,625	1,558

q kW/m ²	ΔT_T K	ΔT_S K	ΔT_B K
Structure A401, pressure p = 5 bar			
1,32	2,196	1,818	2,563
2,94	2,885	3,111	2,414
* 5,24	2,374	1,678	2,185
8,13	3,032	2,137	2,386
11,5	3,431	1,720	2,735
15,9	4,033	2,222	2,848
20,5	4,299	2,322	2,918
26,1	4,688	2,657	3,054
32,3	5,002	2,882	3,138
39,1	5,391	3,238	3,143
46,5	5,670	3,527	3,263
54,3	5,895	3,729	3,340
63,3	6,168	3,990	3,414
72,2	6,285	4,083	3,388
81,6	6,372	4,268	3,443
93,2	6,283	4,381	3,550
103	6,314	4,529	3,550
115	6,333	4,639	3,626
124	6,247	4,699	3,625
96,3	5,463	4,280	3,449
71,8	4,537	3,826	3,403
49,5	3,759	3,318	3,291
31,7	2,577	2,670	3,258
17,8	2,011	1,752	2,912
7,78	1,658	0,889	2,123
1,98	1,383	0,438	1,111

q kW/m ²	ΔT_T K	ΔT_S K	ΔT_B K
Structure A401, pressure p = 6 bar			
3,03	2,289	1,224	5,872
* 5,06	2,813	1,617	5,658
8,14	3,329	1,183	2,150
11,4	3,988	1,775	2,481
15,6	4,436	2,431	2,710
20,2	4,733	2,260	2,691
25,7	4,964	2,530	2,753
31,5	5,068	2,857	2,879
38,6	5,237	3,287	2,898
45,3	5,388	3,513	2,918
53,7	5,500	3,746	2,932
61,3	5,568	3,868	3,035
70,7	5,662	4,085	3,102
81,0	5,722	4,201	3,149
90,8	5,764	4,313	3,157
101	5,795	4,340	3,198
114	5,924	4,405	3,231
125	5,975	4,438	3,331
97,1	5,364	4,214	3,326
71,3	4,686	3,772	3,236
49,4	3,876	3,123	3,127
32,0	3,119	2,323	2,891
18,3	2,696	1,415	2,609
8,01	1,821	0,627	1,861

q kW/m ²	ΔT_T K	ΔT_S K	ΔT_B K
Structure A401, pressure p = 7 bar			
* 2,86	4,735	3,874	6,660
5,17	5,159	3,061	5,981
8,11	2,825	1,790	2,822
11,5	3,366	1,987	2,593
15,7	3,590	1,457	2,364
20,4	3,911	1,871	2,536
25,6	3,917	2,280	2,531
31,3	4,043	2,733	2,607
38,6	4,266	3,040	2,666
45,6	4,432	3,167	2,688
53,5	4,635	3,425	2,791
61,4	4,717	3,538	2,789
70,7	4,884	3,691	2,840
80,0	5,009	3,825	2,921
90,8	5,184	3,959	2,920
101	5,156	4,014	2,979
114	5,220	4,147	2,983
124	5,250	4,179	3,032
95,9	4,862	3,918	3,045
70,6	4,359	3,549	2,909
48,9	3,673	2,954	2,860
31,7	2,918	2,217	2,682
17,1	2,482	1,185	2,333
8,13	1,723	0,615	1,815

q kW/m ²	ΔT_T K	ΔT_S K	ΔT_B K
Structure A401, pressure p = 8 bar			
* 1,89	2,004	4,017	4,790
2,89	1,533	1,948	3,873
5,19	2,418	2,725	4,807
7,94	2,654	2,745	3,723
11,4	3,000	2,515	2,677
15,5	3,375	2,648	2,791
20,5	3,541	2,471	2,388
25,5	3,686	2,519	2,476
31,4	3,827	2,698	2,426
38,7	4,046	2,903	2,469
45,4	4,186	3,024	2,519
53,6	4,254	3,119	2,564
62,3	4,404	3,305	2,640
70,9	4,512	3,391	2,640
80,5	4,656	3,572	2,694
90,7	4,713	3,620	2,721
101	4,755	3,726	2,788
113	4,795	3,763	2,813
125	4,823	3,776	2,818
96,7	4,558	3,584	2,742
70,7	4,109	3,223	2,678
50,0	3,549	2,650	2,615
31,3	2,769	1,890	2,513
18,2	2,299	1,149	2,252
8,10	1,424	0,521	1,560

q kW/m ²	ΔT_T K	ΔT_S K	ΔT_B K
Structure A401, pressure p = 9 bar			
* 3,04	4,949	5,422	5,963
5,08	3,512	5,099	5,927
8,02	3,049	3,778	3,168
11,5	3,190	2,175	2,187
15,9	2,999	1,854	2,130
20,3	3,241	2,395	2,237
25,5	3,384	2,517	2,276
31,9	3,575	2,674	2,260
38,4	3,727	2,737	2,346
45,6	3,797	2,753	2,241
53,4	3,969	2,952	2,369
61,6	4,097	3,09	2,434
70,8	4,176	3,206	2,380
80,5	4,251	3,284	2,438
90,8	4,335	3,374	2,490
102	4,242	3,449	2,513
113	4,340	3,533	2,593
125	4,381	3,564	2,594
96,8	4,172	3,402	2,527
71,4	3,880	3,142	2,487
49,2	3,438	2,649	2,397
31,7	2,799	2,043	2,221
17,9	2,362	1,188	1,977
8,19	1,475	0,514	1,416
2,08	0,494	0,242	0,591

q kW/m ²	ΔT_T K	ΔT_S K	ΔT_B K
Structure A437, pressure p = 5 bar			
2,83	2,924	3,176	2,999
* 5,06	3,242	3,711	4,524
7,99	0,721	0,460	0,707
11,4	0,742	0,452	0,763
15,3	0,886	0,513	0,903
20,1	0,953	0,544	0,962
25,6	1,001	0,548	0,992
31,6	1,138	0,599	1,100
38,2	1,274	0,648	1,191
45,4	1,503	0,722	1,274
53,3	1,684	0,775	1,348
61,7	2,002	0,880	1,473
70,7	2,368	0,999	1,507
80,2	2,860	1,220	1,615
90,7	3,340	1,629	1,578
100	3,480	2,038	1,691
112	3,435	2,343	1,715
125	3,400	2,552	1,890
95,7	2,820	2,057	1,716
70,4	1,781	0,994	1,630
49,7	1,112	0,720	1,388
31,1	0,733	0,547	1,073
18,0	0,513	0,412	0,790
7,89	0,384	0,326	0,558
1,99	0,292	0,243	0,347

q kW/m ²	ΔT_T K	ΔT_S K	ΔT_B K
Structure A437, pressure $p = 6$ bar			
2,86	1,505	1,938	3,944
5,05	1,212	1,685	1,960
* 7,95	1,688	2,365	2,636
11,4	0,715	0,636	2,425
15,5	0,734	0,476	2,857
20,2	0,786	0,462	0,800
25,5	0,868	0,491	0,811
31,5	0,943	0,523	0,885
38,0	1,082	0,568	1,012
45,3	1,229	0,618	1,152
53,2	1,390	0,674	1,214
61,5	1,487	0,732	1,389
70,5	1,867	0,855	1,411
80,0	2,418	1,043	1,468
89,8	2,994	1,457	1,515
101	3,381	2,070	1,672
112	3,300	2,394	1,735
124	3,189	2,653	1,754
95,8	2,237	1,606	1,670
71,2	1,364	0,898	1,435
49,1	0,863	0,653	1,241
31,5	0,592	0,510	0,944
17,7	0,394	0,362	0,638
7,88	0,327	0,717	0,472
2,03	0,234	0,228	0,275

q kW/m ²	ΔT_T K	ΔT_S K	ΔT_B K
Structure A437, pressure $p = 7$ bar			
2,88	1,134	1,743	1,823
5,08	1,774	2,795	2,954
* 7,98	1,431	2,248	2,225
11,4	0,522	0,382	0,559
15,7	0,622	0,423	0,631
20,3	0,687	0,442	0,673
25,7	0,783	0,472	0,731
31,5	0,903	0,509	0,881
38,1	1,030	0,546	0,972
45,4	1,219	0,616	1,124
53,1	1,427	0,663	1,210
61,5	1,662	0,722	1,369
70,5	2,033	0,815	1,426
80,4	2,574	0,991	1,497
90,5	3,376	1,812	1,645
102	3,590	2,491	1,630
112	3,055	2,823	1,717
124	2,624	2,971	1,754
95,7	1,961	2,217	1,788
70,7	1,090	0,940	1,522
49,2	0,650	0,618	1,251
31,5	0,456	0,480	0,881
17,9	0,330	0,374	0,591
7,90	0,256	0,304	0,404

q kW/m ²	ΔT_T K	ΔT_S K	ΔT_B K
Structure A437, pressure $p = 8$ bar			
2,90	3,388	3,928	4,343
5,06	2,886	3,658	5,661
* 7,86	4,181	5,306	8,235
11,3	0,462	0,416	0,868
15,5	0,538	0,420	0,667
20,3	0,587	0,417	0,734
25,7	0,702	0,458	0,940
31,8	0,798	0,499	1,135
38,4	0,961	0,530	1,243
45,3	1,006	0,572	1,290
53,1	1,271	0,659	1,376
61,2	1,594	0,738	1,351
70,6	2,945	1,496	1,470
80,2	3,572	2,132	1,566
90,9	3,839	2,587	1,599
101	3,741	2,903	1,664
113	3,455	2,930	1,696
124	3,373	3,059	1,777
95,8	2,633	2,438	1,705
70,6	1,437	1,118	1,564
49,1	0,767	0,670	1,428
31,5	0,485	0,493	1,150
17,6	0,299	0,351	0,686
8,01	0,242	0,312	0,432
1,97	0,186	0,258	0,243

q kW/m ²	ΔT_T K	ΔT_S K	ΔT_B K
Structure A437, pressure $p = 9$ bar			
2,87	7,016	7,437	7,390
5,06	4,577	6,273	7,155
* 7,91	4,177	6,063	4,681
11,6	0,325	0,310	0,404
15,6	0,433	0,357	0,557
20,3	0,576	0,436	0,868
25,8	0,713	0,490	1,102
31,5	0,824	0,515	1,183
38,4	1,036	0,580	1,225
45,3	1,258	0,627	1,199
53,2	1,588	0,709	1,348
61,8	2,237	0,919	1,398
70,5	3,515	1,668	1,494
79,7	4,064	2,406	1,459
90,7	4,109	2,864	1,612
100	4,160	3,082	1,695
113	3,772	3,104	1,684
125	3,569	3,075	1,744
95,6	2,791	2,386	1,722
71,0	1,724	1,196	1,515
48,9	0,883	0,692	1,429
31,4	0,504	0,483	1,162
17,7	0,344	0,407	0,761
7,8	0,224	0,313	0,390

q kW/m ²	ΔT_T K	ΔT_S K	ΔT_B K
Structure A435, pressure p = 5 bar			
2,90	1,170	0,730	2,005
* 5,10	2,114	1,380	3,575
8,00	1,129	1,034	1,237
11,4	1,179	1,147	1,520
15,4	1,392	1,394	1,843
20,2	1,800	1,755	2,023
25,6	2,373	2,200	2,156
31,5	3,085	2,734	2,326
38,2	3,937	3,233	2,422
45,3	4,706	3,610	2,461
53,2	5,481	3,984	2,568
61,4	6,043	4,280	2,689
70,4	6,605	4,574	2,783
79,8	7,028	4,778	2,846
89,7	7,305	4,943	2,956
101	7,248	5,099	3,080
113	7,230	5,035	2,997
124	7,401	5,265	3,250
96,5	6,321	4,713	3,063
70,6	5,108	4,004	2,885
49,1	3,828	3,214	2,640
31,8	2,502	2,292	2,397
17,8	1,333	1,426	1,985
7,90	0,620	0,745	1,204
2,00	0,261	0,279	0,488

q kW/m ²	ΔT_T K	ΔT_S K	ΔT_B K
Structure A435, pressure p = 6 bar			
2,88	6,065	5,739	6,959
* 5,15	7,422	6,572	9,154
7,97	0,770	0,879	1,678
11,4	0,844	0,983	1,497
15,5	1,082	1,175	1,730
20,2	1,475	1,455	1,968
25,6	2,139	1,949	2,105
31,5	3,009	2,530	2,265
38,2	3,975	3,126	2,473
45,3	4,693	3,549	2,646
53,1	5,351	3,892	2,734
60,6	5,751	4,127	2,869
70,6	6,253	4,414	3,100
79,6	6,637	4,644	3,205
90,5	7,039	4,867	3,351
101	7,187	5,000	3,268
112	7,312	5,176	3,353
124	7,202	5,154	3,475
95,6	6,342	4,693	3,236
70,4	5,268	4,137	3,055
49,0	4,026	3,372	2,861
31,6	2,637	2,427	2,618
17,8	1,338	1,453	2,179
8,02	0,607	0,755	1,296
1,98	0,235	0,283	0,461

q kW/m ²	ΔT_T K	ΔT_S K	ΔT_B K
Structure A435, pressure p = 7 bar			
* 2,85	2,680	2,897	4,614
5,08	2,082	1,468	5,096
7,93	1,067	0,903	2,492
11,5	0,936	0,973	1,763
15,4	1,031	1,177	1,876
20,3	1,494	1,537	2,109
25,5	2,178	2,043	2,256
31,5	3,112	2,680	2,413
38,2	3,943	3,163	2,538
45,4	4,555	3,525	2,656
53,0	5,061	3,774	2,751
61,7	5,491	3,980	2,947
70,7	5,887	4,198	3,045
80,4	6,228	4,406	3,060
90,4	6,462	4,609	3,151
101	6,668	4,759	3,239
112	6,840	4,933	3,347
124	6,830	5,060	3,490
96,3	6,172	4,696	3,298
70,4	5,141	4,148	3,069
49,1	3,957	3,437	2,859
31,6	2,617	2,529	2,697
17,7	1,301	1,479	2,127
7,9	0,546	0,728	1,227
1,97	0,222	0,297	0,432

q kW/m ²	ΔT_T K	ΔT_S K	ΔT_B K
Structure A435, pressure p = 8 bar			
* 2,86	4,442	4,575	6,326
5,12	1,012	1,172	2,800
7,96	0,801	0,893	2,083
11,3	0,795	0,987	1,943
15,5	1,067	1,219	1,875
20,2	1,393	1,467	1,978
25,4	2,072	1,989	2,196
31,2	2,863	2,478	2,314
38,5	3,731	2,940	2,487
44,9	4,256	3,271	2,622
53,4	4,764	3,553	2,774
61,3	5,142	3,76	2,853
70,5	5,467	3,973	2,999
79,9	5,740	4,144	3,138
90,3	5,987	4,300	3,284
101	6,149	4,463	3,249
113	6,278	4,609	3,354
126	6,409	4,770	3,459
95,5	5,876	4,453	3,229
70,5	4,957	4,023	3,067
49,1	3,922	3,373	2,905
31,5	2,689	2,563	2,672
17,5	1,344	1,561	2,138
7,89	0,517	0,716	1,208
1,97	0,170	0,265	0,376

q kW/m ²	ΔT_T K	ΔT_S K	ΔT_B K
Structure A435, pressure p = 9 bar			
2,97	2,599	3,99	2,003
* 5,03	2,783	4,189	2,455
7,87	0,700	0,902	1,658
11,4	0,896	1,086	1,903
15,5	1,198	1,307	1,996
20,2	1,596	1,649	2,075
25,5	2,415	2,179	2,232
31,5	3,192	2,629	2,371
38,4	3,797	3,023	2,493
45,2	4,228	3,207	2,601
53,0	4,660	3,437	2,713
61,2	4,928	3,631	2,813
70,2	5,190	3,814	2,953
80,6	5,427	3,993	3,068
90,3	5,586	4,131	3,169
101	5,764	4,259	3,303
113	5,772	4,461	3,382
124	5,869	4,558	3,445
95,6	5,504	4,301	3,281
70,4	4,711	3,909	3,090
49,1	3,731	3,331	2,939
31,6	2,729	2,603	2,662
17,8	1,523	1,731	2,206
7,96	0,553	0,786	1,288
1,94	0,195	0,316	0,382

q kW/m ²	ΔT_T K	ΔT_S K	ΔT_B K
Structure A431, pressure p = 5 bar			
2,83	4,055	4,100	4,197
* 5,05	6,211	6,441	4,406
7,93	0,690	0,532	0,696
11,4	0,684	0,515	0,869
15,4	0,777	0,624	1,183
20,2	0,971	0,750	1,356
25,6	1,143	0,882	1,499
31,6	1,350	1,042	1,685
38,3	1,784	1,486	1,787
45,4	2,567	2,155	1,813
53,1	3,479	2,785	1,894
61,7	4,553	3,470	2,014
70,7	4,995	3,709	2,095
80,2	5,032	3,675	2,109
90,6	5,163	3,448	2,234
102	5,013	3,466	2,059
113	4,983	3,501	2,196
125	4,937	3,526	2,237
95,8	4,459	3,368	2,154
70,4	3,735	3,035	2,106
49,2	2,689	2,293	1,873
31,5	1,444	1,236	1,719
17,8	0,815	0,757	1,461
7,93	0,459	0,435	0,875
2,01	0,300	0,265	0,421

q kW/m ²	ΔT_T K	ΔT_S K	ΔT_B K
Structure A431, pressure $p = 6$ bar			
2,89	4,419	3,684	5,347
5,10	5,479	4,187	7,495
* 7,91	6,201	5,156	7,663
11,5	0,756	0,588	1,002
15,5	0,766	0,602	1,211
20,3	0,864	0,672	1,397
25,6	1,002	0,780	1,568
31,5	1,204	0,960	1,716
38,1	1,600	1,378	1,793
45,4	3,864	3,160	1,890
53,1	4,632	3,645	2,010
61,5	5,122	3,857	1,934
70,5	5,538	3,854	2,015
80,0	5,583	3,602	2,144
90,4	5,532	3,481	2,086
101	5,489	3,536	2,133
113	5,218	3,67	2,218
125	5,085	3,552	2,292
96,8	4,705	3,567	2,206
70,4	4,146	3,348	2,191
49,1	3,295	2,876	1,990
31,5	1,410	1,309	1,852
17,7	0,732	0,707	1,322
7,86	0,452	0,463	0,762
1,99	0,265	0,276	0,344

q kW/m ²	ΔT_T K	ΔT_S K	ΔT_B K
Structure A431, pressure $p = 7$ bar			
2,89	6,017	5,946	6,658
* 5,06	9,319	9,116	10,025
7,83	7,381	6,089	10,285
11,6	0,688	0,595	1,001
15,5	0,709	0,623	1,087
20,3	0,752	0,661	1,329
25,5	0,902	0,809	1,586
31,3	1,196	1,109	1,724
38,1	1,758	1,617	1,768
45,3	3,040	2,690	2,002
53,1	4,471	3,584	1,960
61,9	5,253	3,962	1,987
70,7	5,620	3,797	2,072
79,6	5,347	3,741	2,079
91,3	5,533	3,746	2,141
101	5,565	3,755	2,210
112	5,362	3,765	2,226
125	5,296	3,794	2,225
95,9	4,825	3,671	2,304
70,5	4,150	3,376	2,068
49,1	3,238	2,793	2,068
31,6	1,515	1,476	1,855
17,7	0,705	0,727	1,353
7,78	0,386	0,412	0,672
1,96	0,230	0,265	0,296

q kW/m ²	ΔT_T K	ΔT_S K	ΔT_B K	q kW/m ²	ΔT_T K	ΔT_S K	ΔT_B K
Structure A431, pressure p = 8 bar				Structure A431, pressure p = 9 bar			
2,92	7,750	7,853	9,189	* 2,84	9,917	10,234	10,032
* 5,05	9,483	10,067	12,644	5,01	8,902	9,763	9,103
7,90	5,511	3,012	10,084	7,88	0,32	0,355	0,815
11,4	0,738	0,631	1,137	11,5	0,464	0,479	1,089
15,5	0,776	0,672	1,364	15,6	0,588	0,585	1,461
20,2	0,874	0,740	1,564	20,5	0,786	0,759	1,547
25,5	1,054	0,872	1,674	25,5	1,037	0,991	1,696
31,5	1,381	1,109	1,811	31,5	1,561	1,461	1,797
38,1	2,118	1,707	1,869	38,0	3,384	2,853	1,884
45,3	3,941	3,188	1,892	45,4	4,151	3,309	1,933
53,1	4,720	3,641	1,990	53,1	4,600	3,577	1,988
61,4	5,162	3,916	2,100	61,6	4,973	3,829	1,973
70,5	5,475	4,104	2,060	70,5	5,248	3,995	2,054
80,1	5,661	3,982	2,112	80,1	5,392	3,475	2,125
90,1	5,648	3,908	2,184	90,0	5,478	3,495	2,116
101	5,645	3,778	2,140	101	5,445	3,549	2,157
112	5,434	3,660	2,212	112	5,495	3,635	2,218
124	5,410	3,580	2,239	124	5,285	3,583	2,275
95,6	4,800	3,435	2,126	95,5	4,735	3,459	2,152
70,5	4,246	3,355	2,080	70,1	4,085	3,249	2,142
48,9	3,568	3,058	2,028	49,0	3,247	2,847	2,045
31,5	2,102	1,903	1,932	31,4	1,842	1,897	1,993
17,7	0,680	0,695	1,296	17,7	0,716	0,845	1,692
7,87	0,363	0,396	0,595	7,95	0,337	0,408	0,670
1,97	0,189	0,244	0,236	1,96	0,196	0,285	0,257

q kW/m ²	ΔT_T K	ΔT_S K	ΔT_B K
Structure A432, pressure p = 5 bar			
2,93	2,390	2,265	1,976
* 5,12	2,665	2,056	1,927
7,97	2,209	1,840	2,185
11,5	2,841	2,347	2,532
15,6	3,359	2,710	2,627
20,3	3,923	3,147	2,890
25,5	4,162	3,403	2,918
31,8	4,748	3,901	2,893
38,1	5,156	4,236	3,023
45,3	5,495	4,505	2,997
53,2	5,736	4,485	3,045
61,5	5,617	4,323	3,176
70,6	5,726	4,370	3,190
80,4	5,684	4,309	3,297
90,6	5,549	3,912	3,376
102	5,528	3,955	3,470
113	5,414	3,879	3,482
125	5,417	3,882	3,604
95,6	5,206	3,831	3,347
70,6	4,674	3,636	3,291
49,1	3,952	3,255	3,155
31,5	3,177	2,785	2,954
17,7	2,348	2,196	2,636
7,93	1,565	1,584	2,014
1,96	0,801	0,786	0,971

q kW/m ²	ΔT_T K	ΔT_S K	ΔT_B K
Structure A432, pressure p = 6 bar			
2,85	5,413	5,849	6,320
* 5,05	4,707	4,803	4,319
7,94	2,144	1,848	1,978
11,4	2,704	2,286	2,365
15,5	3,234	2,688	2,522
20,2	3,743	3,088	2,742
25,6	4,225	3,430	2,771
31,7	4,732	3,794	2,937
38,4	4,982	4,142	2,812
45,4	5,348	4,404	2,929
53,1	5,661	4,545	2,984
61,7	5,837	4,171	3,007
70,8	5,816	4,271	3,059
80,4	5,684	4,026	3,088
90,5	5,784	3,954	3,163
101	5,735	3,905	3,254
113	5,586	3,854	3,360
125	5,579	3,728	3,451
95,9	5,256	3,679	3,225
70,6	4,596	3,410	3,118
49,2	3,822	3,042	3,029
31,6	3,072	2,631	2,811
17,8	2,277	2,134	2,551
7,90	1,479	1,512	1,898
2,00	0,735	0,754	0,878

q kW/m ²	ΔT_T K	ΔT_S K	ΔT_B K	q kW/m ²	ΔT_T K	ΔT_S K	ΔT_B K
Structure A432, pressure p = 7 bar				Structure A432, pressure p = 8 bar			
* 2,90	8,264	8,285	8,087	2,88	5,093	5,253	5,099
5,08	6,154	6,889	7,315	* 5,05	5,214	5,377	5,495
7,95	6,930	7,914	8,279	7,88	1,919	1,856	1,904
11,4	2,640	2,301	2,246	11,4	2,350	2,181	2,139
15,5	3,153	2,632	2,421	15,4	2,843	2,520	2,310
20,3	3,659	3,016	2,562	20,6	3,398	2,883	2,399
25,5	4,152	3,366	2,661	25,6	3,875	3,212	2,502
31,5	4,583	3,707	2,736	31,5	4,296	3,540	2,605
38,2	4,835	3,990	2,732	38,0	4,731	3,848	2,636
45,3	5,214	4,284	2,777	45,2	5,010	4,105	2,691
53,2	5,481	4,477	2,863	53,3	5,267	4,365	2,688
61,5	5,691	4,137	2,879	61,3	5,499	3,926	2,782
70,6	5,723	4,106	2,886	70,1	5,018	3,838	2,783
80,3	5,813	4,049	2,946	80,3	5,074	3,899	2,827
90,6	5,667	3,840	2,998	90,4	4,996	3,595	2,892
102	4,956	3,746	3,132	101	4,932	3,575	2,929
113	4,914	3,689	3,165	113	4,828	3,568	3,023
125	4,897	3,583	3,247	125	4,833	3,547	3,143
96,1	4,622	3,507	3,095	95,6	4,497	3,465	2,997
70,6	4,062	3,286	3,022	70,2	3,939	3,229	2,875
49,1	3,437	2,975	2,882	49,0	3,343	2,910	2,713
31,5	2,787	2,591	2,743	31,3	2,730	2,543	2,613
17,7	2,099	2,133	2,434	17,7	2,099	2,138	2,328
7,90	1,429	1,581	1,924	7,86	1,446	1,611	1,880
1,95	0,694	0,782	0,864	1,98	0,761	0,881	0,927

q kW/m ²	ΔT_T K	ΔT_S K	ΔT_B K	q kW/m ²	ΔT_T K	ΔT_S K	ΔT_B K
Structure A432, pressure $p = 9$ bar				Structure A425, pressure $p = 5$ bar			
* 2,87	6,643	6,983	6,968	* 2,90	7,590	6,158	7,763
5,09	5,579	6,296	6,319	5,12	1,782	4,814	3,287
7,92	3,693	3,660	2,750	8,01	2,194	6,722	4,302
11,4	2,687	2,431	2,318	11,4	2,388	3,381	2,627
15,5	3,148	2,752	2,341	15,4	2,732	3,677	2,877
20,2	3,595	3,067	2,398	20,2	3,077	4,119	3,139
25,6	4,035	3,355	2,466	25,5	3,408	4,379	3,416
31,5	4,422	3,624	2,526	31,5	3,813	4,655	3,636
38,3	4,692	3,864	2,489	38,0	4,376	5,192	3,898
45,2	4,999	4,058	2,542	45,3	5,063	5,699	4,062
53,1	5,249	4,046	2,610	53,1	5,751	6,139	4,236
61,4	5,221	3,770	2,653	61,3	6,323	6,409	4,370
70,5	4,951	3,850	2,672	70,4	6,817	6,564	4,577
80,8	4,828	3,604	2,733	79,7	7,166	6,761	4,776
90,3	4,860	3,451	2,802	90,7	7,483	7,094	4,952
101	4,892	3,436	2,853	101	7,736	7,366	5,066
113	4,797	3,428	2,899	113	7,577	6,856	5,206
124	4,741	3,460	3,000	125	7,681	6,952	5,402
95,9	4,397	3,285	2,809	95,5	7,233	6,622	5,223
70,4	3,825	3,034	2,699	70,3	6,626	6,338	5,131
49,2	3,226	2,723	2,604	49,1	5,709	5,745	5,007
31,5	2,598	2,370	2,464	31,9	4,465	4,651	4,628
17,7	1,982	1,995	2,269	17,7	3,715	3,918	4,000
7,89	1,373	1,544	1,777	7,81	2,917	2,839	3,084
2,00	0,749	0,891	0,917	1,98	1,758	1,435	1,813

q kW/m ²	ΔT_T K	ΔT_S K	ΔT_B K	q kW/m ²	ΔT_T K	ΔT_S K	ΔT_B K
Structure A425, pressure p = 6 bar				Structure A425, pressure p = 7 bar			
* 2,86	3,320	3,135	2,374	* 2,93	7,951	7,068	7,729
5,06	2,776	3,957	2,462	5,13	3,693	6,215	3,730
7,92	3,060	3,144	2,591	7,99	3,325	4,126	2,913
11,4	3,413	3,408	2,854	11,4	3,574	3,700	3,058
15,5	3,726	3,875	3,084	15,6	3,817	3,990	3,254
20,2	4,079	4,261	3,342	20,2	4,041	4,287	3,478
25,5	4,307	4,495	3,567	25,6	4,285	4,504	3,642
31,7	4,601	4,689	3,775	31,6	4,516	4,657	3,815
38,1	5,018	5,013	3,979	38,1	4,927	5,006	3,975
45,3	5,496	5,480	4,159	45,2	5,337	5,354	4,136
52,9	6,005	5,845	4,297	53,1	5,780	5,675	4,290
61,4	6,466	6,212	4,470	61,3	6,190	5,940	4,429
70,5	6,865	6,436	4,642	70,4	6,546	6,214	4,699
79,9	7,167	6,684	4,761	79,8	6,790	6,349	4,776
90,2	7,425	6,864	4,927	90,3	6,994	6,546	4,927
101	7,640	7,021	5,067	102	7,162	6,766	5,109
112	7,704	6,874	5,194	112	7,272	6,901	5,221
124	7,726	7,108	5,367	124	7,322	7,083	5,344
95,7	7,415	6,893	5,237	95,6	7,176	6,822	5,312
70,4	6,720	6,485	5,146	70,3	6,707	6,540	5,159
48,9	5,730	5,750	4,848	49,1	5,832	5,956	4,891
31,8	4,703	4,901	4,627	31,5	4,806	5,097	4,595
17,7	3,959	4,187	3,986	17,7	4,046	4,351	4,065
7,88	3,040	2,988	3,253	7,90	3,133	3,159	3,300
1,98	1,773	1,463	1,854	2,00	1,877	1,600	1,951

q kW/m ²	ΔT_T K	ΔT_S K	ΔT_B K	q kW/m ²	ΔT_T K	ΔT_S K	ΔT_B K
Structure A425, pressure p = 8 bar				Structure A425, pressure p = 9 bar			
* 2,85	12,587	10,030	12,198	* 2,81	12,143	11,961	12,384
5,13	10,958	10,135	10,496	5,10	11,045	12,838	11,923
7,91	8,192	9,268	7,892	7,85	10,693	13,090	10,294
11,3	8,213	8,747	7,693	11,5	10,571	11,771	10,185
15,5	4,912	5,220	4,453	15,5	4,645	4,857	4,305
20,2	4,165	4,441	3,663	20,1	4,061	4,272	3,633
25,5	4,284	4,568	3,785	25,5	4,209	4,381	3,736
31,5	4,420	4,615	3,915	31,4	4,391	4,521	3,895
38,1	4,756	4,865	4,010	38,0	4,625	4,695	4,012
45,2	5,141	5,201	4,184	45,2	4,936	4,942	4,106
53,1	5,519	5,450	4,291	53,0	5,254	5,134	4,139
61,4	5,849	5,653	4,353	61,3	5,532	5,373	4,304
70,5	6,123	5,864	4,494	70,3	5,737	5,519	4,374
79,9	6,333	6,035	4,668	80,0	5,881	5,655	4,483
90,1	6,480	6,193	4,804	90,1	5,998	5,816	4,631
101	6,592	6,358	4,886	101	6,099	5,984	4,704
112	6,708	6,513	5,063	112	6,195	6,145	4,873
124	6,796	6,629	5,178	124	6,267	6,272	4,988
95,9	6,678	6,425	5,093	95,4	6,126	6,035	4,912
70,2	6,367	6,183	4,971	70,2	5,937	5,828	4,828
49,1	5,635	5,711	4,812	48,9	5,326	5,386	4,639
31,4	4,701	4,962	4,549	31,4	4,574	4,821	4,341
17,7	3,979	4,278	4,014	17,8	3,971	4,268	3,866
7,94	3,153	3,198	3,260	7,86	3,077	3,147	3,141
1,98	1,843	1,643	1,923	1,97	1,818	1,628	1,881

q kW/m ²	ΔT_T K	ΔT_S K	ΔT_B K	q kW/m ²	ΔT_T K	ΔT_S K	ΔT_B K
Structure A426, pressure p = 5 bar				Structure A426, pressure p = 6 bar			
2,85	3,357	3,864	4,151	* 2,86	3,107	2,919	2,102
* 5,09	3,729	4,135	4,504	5,06	2,714	3,893	2,341
8,07	3,873	3,808	3,871	7,92	3,025	3,106	2,498
11,4	4,286	4,041	4,018	11,4	3,391	3,382	2,772
15,5	4,743	4,461	4,206	15,5	3,720	3,864	3,018
20,2	5,141	4,796	4,391	20,2	4,051	4,229	3,254
25,7	5,513	5,150	4,575	25,5	4,295	4,478	3,495
31,4	5,851	5,419	4,771	31,7	4,576	4,658	3,688
38,1	6,160	5,747	4,887	38,1	5,000	4,989	3,899
45,4	6,383	5,979	5,056	45,3	5,474	5,450	4,075
53,0	6,546	6,215	5,259	52,8	5,992	5,825	4,221
61,5	6,727	6,519	5,385	61,4	6,451	6,189	4,393
70,4	6,841	6,681	5,527	70,5	6,855	6,417	4,569
79,9	6,935	6,863	5,584	79,9	7,154	6,662	4,685
90,1	7,041	7,076	5,717	90,2	7,415	6,844	4,853
101	7,144	7,311	5,821	101	7,631	7,001	4,994
113	7,229	7,478	5,923	112	7,695	6,855	5,121
124	7,329	7,681	6,045	124	7,718	7,091	5,296
95,5	7,141	7,321	5,855	95,7	7,378	6,848	5,137
70,3	6,920	6,923	5,701	70,4	6,700	6,457	5,063
49,1	6,614	6,495	5,502	48,9	5,705	5,718	4,761
31,7	6,146	5,908	5,223	31,8	4,670	4,862	4,533
17,6	5,275	5,002	4,685	17,7	3,925	4,149	3,893
7,97	4,052	3,804	3,980	7,88	3,017	2,961	3,170
1,98	2,287	2,062	2,210	1,98	1,746	1,435	1,770

q kW/m ²	ΔT_T K	ΔT_S K	ΔT_B K	q kW/m ²	ΔT_T K	ΔT_S K	ΔT_B K
Structure A426, pressure $p = 7$ bar				Structure A426, pressure $p = 8$ bar			
* 2,93	7,458	6,560	7,172	* 2,85	10,663	8,088	10,213
5,13	3,362	5,870	3,335	5,13	8,670	7,827	8,146
7,99	3,286	4,075	2,810	7,91	3,565	4,621	3,201
11,3	3,560	3,674	2,980	11,3	3,686	4,201	3,102
15,6	3,779	3,939	3,151	15,5	4,002	4,292	3,480
20,2	4,016	4,249	3,389	20,2	4,201	4,457	3,635
25,6	4,264	4,470	3,556	25,5	4,264	4,528	3,701
31,6	4,494	4,621	3,728	31,5	4,422	4,597	3,854
38,1	4,849	4,909	3,905	38,1	4,752	4,840	3,942
45,2	5,319	5,322	4,054	45,2	5,114	5,153	4,094
53,1	5,761	5,642	4,207	53,1	5,508	5,419	4,218
61,3	6,171	5,906	4,347	61,4	5,826	5,608	4,267
70,4	6,520	6,173	4,608	70,5	6,105	5,825	4,414
79,8	6,770	6,314	4,693	79,9	6,303	5,983	4,577
90,3	6,968	6,504	4,837	90,1	6,451	6,142	4,713
102	7,145	6,733	5,028	101	6,547	6,292	4,780
112	7,251	6,864	5,136	112	6,683	6,465	4,977
124	7,311	7,054	5,269	124	6,774	6,584	5,095
95,6	7,126	6,755	5,198	95,9	6,642	6,367	4,995
70,3	6,679	6,496	5,066	70,2	6,344	6,139	4,887
49,1	5,808	5,918	4,803	49,1	5,602	5,655	4,716
31,5	4,775	5,053	4,500	31,4	4,678	4,919	4,463
17,7	4,024	4,316	3,979	17,7	3,948	4,227	3,919
7,90	3,115	3,130	3,218	7,94	3,122	3,149	3,165
2,00	1,851	1,564	1,861	1,98	1,806	1,591	1,822

q kW/m ²	ΔT_T K	ΔT_S K	ΔT_B K	q kW/m ²	ΔT_T K	ΔT_S K	ΔT_B K
Structure A426, pressure p = 9 bar				Structure A427, pressure p = 5 bar			
* 2,81	9,325	9,118	9,506	* 2,92	5,877	4,550	7,137
5,10	7,655	9,419	8,473	5,11	4,991	5,901	7,892
7,85	4,479	6,845	4,019	7,89	4,320	7,028	8,647
11,5	3,872	5,045	3,426	11,7	3,956	3,377	2,568
15,5	4,015	4,202	3,614	15,5	4,487	3,212	2,924
20,1	4,055	4,241	3,568	20,3	5,045	3,395	3,207
25,5	4,214	4,360	3,682	25,6	5,519	3,718	3,418
31,4	4,390	4,494	3,835	31,5	5,987	4,031	3,510
38,0	4,653	4,697	3,982	38,1	6,419	4,262	3,750
45,2	4,944	4,924	4,056	45,3	6,838	4,648	3,935
530	5,243	5,096	4,071	53,0	7,221	4,907	4,067
61,3	5,519	5,333	4,234	61,3	7,608	5,117	4,216
70,3	5,727	5,482	4,307	70,3	7,948	5,284	4,424
80,0	5,864	5,611	4,409	79,9	8,219	5,471	4,493
90,1	6,000	5,790	4,576	90,1	8,341	5,577	4,621
101	6,094	5,951	4,642	101	8,117	5,726	4,791
112	6,185	6,107	4,807	112	8,090	5,738	4,942
124	6,251	6,228	4,916	124	8,078	5,804	5,131
95,4	6,113	5,993	4,842	95,4	7,635	5,532	4,994
70,2	5,916	5,778	4,750	70,3	7,184	5,136	4,878
49,0	5,307	5,339	4,563	48,9	6,476	4,631	4,658
31,4	4,552	4,772	4,261	31,4	5,464	3,880	4,219
17,8	3,957	4,228	3,793	17,7	4,385	2,977	3,726
7,88	3,075	3,122	3,079	7,87	3,047	2,034	2,807
1,97	1,804	1,592	1,806	1,98	1,479	0,850	1,417

q kW/m ²	ΔT_T K	ΔT_S K	ΔT_B K	q kW/m ²	ΔT_T K	ΔT_S K	ΔT_B K
Structure A427, pressure p = 6 bar				Structure A427, pressure p = 7 bar			
* 2,84	7,729	4,517	7,696	2,86	5,905	4,331	7,087
5,12	2,793	4,037	5,691	* 4,08	6,332	4,834	8,355
7,89	3,307	2,456	2,533	5,19	6,407	3,629	6,027
11,4	3,903	2,872	2,742	7,93	6,608	3,903	3,636
15,4	4,415	3,171	2,876	11,5	3,948	3,275	2,743
20,1	4,914	3,418	3,067	15,4	4,441	3,178	3,011
25,7	5,387	3,673	3,512	20,2	4,889	3,406	3,303
31,6	5,811	3,947	3,664	25,6	5,308	3,601	3,520
37,9	6,209	4,187	3,889	31,4	5,689	3,816	3,735
45,6	6,644	4,476	4,032	38,1	6,063	4,085	3,915
53,4	7,047	4,714	4,277	45,3	6,396	4,299	4,061
61,5	7,378	4,864	4,325	53,1	6,752	4,507	4,280
70,4	7,707	5,134	4,429	61,3	7,101	4,716	4,427
80,0	8,036	5,338	4,677	70,1	7,381	4,891	4,597
90,0	8,213	5,534	4,810	79,8	7,630	5,080	4,743
101	8,402	5,666	4,884	90,0	7,846	5,232	4,835
112	8,445	5,819	5,127	100	8,016	5,391	5,043
125	8,486	6,015	5,362	112	8,182	5,611	5,166
95,9	8,214	5,670	5,290	124	8,273	5,738	5,375
70,1	7,772	5,322	5,000	95,5	8,073	5,499	5,268
49,0	6,990	4,887	5,062	70,3	7,781	5,192	5,137
31,3	6,010	4,095	4,673	49,0	7,062	4,738	4,981
17,7	4,830	3,287	4,053	31,6	6,105	4,103	4,634
7,86	3,440	2,268	3,156	17,7	4,948	3,346	4,013
1,98	1,770	1,119	1,668	7,84	3,612	2,378	3,227

q kW/m ²	ΔT_T K	ΔT_S K	ΔT_B K	q kW/m ²	ΔT_T K	ΔT_S K	ΔT_B K
Structure A427, pressure p = 8 bar				Structure A427, pressure p = 9 bar			
* 2,88	4,677	2,063	2,578	* 2,84	5,852	4,689	6,170
5,07	4,069	2,370	2,551	5,09	5,318	5,367	5,884
7,92	3,662	2,769	2,811	7,94	3,558	2,758	2,791
11,4	4,084	2,989	2,892	11,4	4,016	2,969	3,025
11,4	4,209	2,898	2,977	15,5	4,554	3,217	3,239
15,4	4,627	3,154	3,254	20,3	5,009	3,393	3,478
20,2	5,029	3,396	3,471	25,5	5,439	3,607	3,707
25,5	5,434	3,622	3,626	31,5	5,788	3,764	3,780
31,4	5,791	3,809	3,822	38,0	6,081	3,940	4,005
38,0	6,110	4,013	3,985	45,1	6,322	4,125	4,133
45,3	6,404	4,258	4,139	52,9	6,443	4,271	4,267
52,8	6,601	4,391	4,381	61,3	6,540	4,362	4,327
61,3	6,753	4,511	4,504	70,3	6,628	4,454	4,328
70,2	6,987	4,668	4,587	79,9	6,743	4,564	4,545
79,8	7,189	4,810	4,728	90,0	6,870	4,631	4,600
90,0	7,410	4,970	4,852	100	7,042	4,769	4,676
100	7,587	5,121	5,028	112	7,221	4,904	4,800
112	7,780	5,278	5,129	124	7,364	5,010	4,877
124	7,918	5,443	5,375	95,8	7,220	4,902	4,845
95,3	7,752	5,310	5,291	70,3	7,018	4,665	4,744
70,1	7,561	5,136	5,168	48,8	6,670	4,344	4,638
48,9	7,103	4,653	5,075	31,2	5,849	3,804	4,352
31,3	6,163	4,097	4,613	17,7	4,739	3,129	3,803
17,6	4,964	3,283	3,937	7,83	3,438	2,204	3,048
7,85	3,621	2,428	3,149	1,91	1,836	1,210	1,688

Electronic fluid FC-3284

q kW/m ²	ΔT_T K	ΔT_S K	ΔT_B K
Structure A428, pressure p = 0,5 bar			
* 2,88	14,88	13,919	11,113
5,17	4,628	4,999	3,564
8,09	3,679	4,080	3,088
11,6	2,968	3,432	2,633
15,7	2,949	3,502	2,673
20,5	2,959	3,560	2,620
26,0	3,118	3,778	2,740
32,0	3,240	3,900	2,857
38,7	3,380	3,968	2,918
45,9	3,543	3,978	3,021
53,9	3,686	3,969	3,082
50,0	3,642	3,930	3,070
31,6	3,366	3,908	2,780
17,9	3,097	3,589	2,546
8,20	2,859	3,199	2,314
2,01	2,434	2,568	1,857

q kW/m ²	ΔT_T K	ΔT_S K	ΔT_B K
Structure A428, pressure p = 1,5 bar			
* 2,92	14,83	14,622	11,397
5,15	11,29	13,48	10,692
7,96	3,312	3,407	2,156
11,4	2,990	3,026	1,477
15,7	3,744	3,733	1,692
20,4	4,226	4,016	1,774
25,6	4,649	3,650	1,793
32,0	4,476	3,667	1,772
38,1	4,314	3,536	1,800
45,7	4,207	3,216	1,834
53,5	4,118	3,041	1,855
62,8	3,905	2,985	1,875
49,7	3,427	2,919	1,790
32,3	2,815	2,762	1,636
18,1	2,211	2,387	1,414
7,97	1,719	1,994	1,193
2,02	1,274	1,472	0,878

q kW/m ²	ΔT_T K	ΔT_S K	ΔT_B K
Structure A428, pressure p = 1,0 bar			
* 2,92	3,203	3,446	2,164
5,16	3,848	4,394	2,607
8,06	4,888	5,770	3,157
11,5	4,712	5,707	2,473
15,7	4,756	5,775	2,235
20,5	4,800	4,438	2,203
25,6	4,812	4,050	2,085
31,9	4,826	4,047	2,117
38,6	4,564	3,957	2,146
45,7	4,187	3,754	2,193
54,4	4,126	3,516	2,211
62,2	3,997	3,303	2,119
49,8	3,551	3,244	2,028
32,3	3,009	3,102	1,901
18,2	2,522	2,787	1,680
8,01	2,055	2,323	1,466
2,03	1,642	1,806	1,189

q kW/m ²	ΔT_T K	ΔT_S K	ΔT_B K
Structure A437, pressure p = 0,5 bar			
2,96	12,88	15,194	14,936
* 5,33	19,48	23,328	23,093
8,04	2,439	2,655	2,842
11,6	2,523	2,816	3,081
15,8	2,591	2,960	3,266
20,6	2,684	3,115	3,448
26,3	2,845	3,571	3,656
32,6	2,866	3,721	3,706
38,7	2,970	3,749	3,775
46,0	3,011	3,724	3,844
53,9	3,130	3,693	3,923
62,6	3,181	3,716	3,968
71,5	3,666	3,691	4,008
50,0	3,095	3,654	3,874
32,2	2,928	3,432	3,704
18,1	2,787	3,161	3,469
8,12	2,562	2,820	2,923
2,00	2,237	2,341	2,382

q kW/m ²	ΔT_T K	ΔT_S K	ΔT_B K
Structure A437, pressure p = 1,5 bar			
* 5,28	2,718	2,077	2,094
8,12	2,974	1,954	2,004
11,5	2,746	1,518	1,615
15,6	2,969	1,577	1,737
20,5	3,270	1,698	1,885
26,3	3,439	1,910	2,014
32,0	3,648	2,196	2,069
38,6	2,974	2,435	2,173
46,0	3,130	2,517	2,226
53,8	3,269	2,593	2,303
62,3	3,373	2,595	2,371
71,0	3,342	2,558	2,426
49,7	2,712	2,384	2,215
32,1	2,078	1,952	2,067
18,0	1,619	1,618	1,749
7,99	1,324	1,390	1,419
2,03	1,045	1,121	1,034

q kW/m ²	ΔT_T K	ΔT_S K	ΔT_B K
Structure A437, pressure p = 1,0 bar			
* 8,20	2,208	2,214	2,069
11,6	2,447	2,406	2,153
15,7	2,879	2,791	2,344
20,5	3,424	3,206	2,412
26,0	4,037	3,603	2,448
31,7	3,954	3,598	2,535
38,6	3,984	3,524	2,624
45,9	3,908	3,269	2,635
53,3	3,712	2,880	2,664
61,9	3,714	2,915	2,703
71,2	3,555	2,909	2,812
49,8	3,015	2,813	2,631
32,2	2,470	2,511	2,508
18,0	2,037	2,196	2,293
8,02	1,747	1,891	2,006

q kW/m ²	ΔT _T K	ΔT _S K	ΔT _B K
Structure A435, pressure p = 0,5 bar			
* 2,92	2,103	2,091	1,930
5,14	2,604	2,629	2,198
8,04	3,388	3,282	2,670
11,6	3,946	4,062	3,231
15,8	4,266	4,435	3,689
20,6	4,508	4,469	3,869
26,1	4,981	4,386	4,174
32,0	5,630	4,776	4,387
38,8	5,976	4,940	4,541
46,1	5,926	4,629	4,574
54,0	5,655	4,424	4,607
62,4	5,633	4,568	4,711
49,9	5,178	4,419	4,526
31,9	3,845	3,823	4,243
18,1	3,069	3,208	3,620
8,00	2,458	2,723	2,719
2,02	1,765	1,898	1,848
q kW/m ²	ΔT _T K	ΔT _S K	ΔT _B K
Structure A435, pressure p = 1,0 bar			
* 2,94	5,017	5,073	4,904
5,14	3,427	3,590	3,344
8,04	3,465	3,658	3,286
11,7	3,125	3,306	2,665
15,8	3,655	3,850	2,866
20,6	4,174	4,274	3,047
26,1	4,812	4,515	3,383
32,0	5,549	4,990	3,480
38,8	5,790	5,160	3,625
46,3	5,860	4,597	3,710
53,9	5,696	4,765	3,779
62,2	5,671	4,620	3,913
71,4	5,646	4,397	3,975
49,7	4,573	3,946	3,677
32,0	3,419	3,28	3,318
18,0	2,376	2,649	2,667
8,08	1,818	2,073	1,964
2,00	1,239	1,391	1,260

q kW/m ²	ΔT _T K	ΔT _S K	ΔT _B K
Structure A435, pressure p = 1,5 bar			
* 2,86	11,55	10,946	9,919
5,32	8,853	6,314	6,883
8,08	2,198	2,536	1,864
11,7	2,716	3,055	2,142
15,9	3,250	3,457	2,325
20,6	3,762	3,780	2,546
26,0	4,415	4,088	2,740
32,0	5,164	4,460	2,931
38,6	5,605	4,781	3,054
45,9	5,799	4,818	3,260
53,9	5,791	4,727	3,280
62,6	5,836	4,669	3,356
71,4	5,886	4,578	3,505
49,8	4,754	3,993	3,217
32,3	3,454	3,259	2,905
18,0	2,324	2,551	2,326
8,01	1,646	1,926	1,706
2,01	0,981	1,174	1,006

q kW/m ²	ΔT_T K	ΔT_S K	ΔT_B K
Structure A431, pressure p = 0,5 bar			
* 2,92	2,456	2,581	2,491
5,21	2,856	2,979	2,921
8,05	3,285	3,259	3,309
11,6	3,850	3,746	3,688
15,8	4,670	4,378	4,171
20,7	5,347	4,803	4,555
26,4	5,413	4,672	4,552
32,2	5,482	4,669	4,739
39,3	5,143	4,646	4,733
46,3	5,001	4,496	4,811
54,0	4,938	4,498	4,970
62,4	4,690	4,424	4,934
50,0	4,122	4,025	4,822
32,0	3,836	3,946	4,544
18,3	3,361	3,470	4,055
8,02	2,936	3,073	3,352
2,00	2,475	2,527	2,552

q kW/m ²	ΔT_T K	ΔT_S K	ΔT_B K
Structure A431, pressure p = 1,5 bar			
* 3,43	2,820	3,053	3,059
5,16	3,035	3,253	3,324
8,08	3,645	3,855	3,906
11,6	3,525	3,904	3,904
15,9	3,663	4,037	3,764
20,8	3,443	3,701	3,110
26,1	3,897	3,959	3,120
32,0	4,431	4,068	3,215
38,6	4,571	3,987	3,347
45,9	4,554	3,786	3,373
53,7	4,581	3,787	3,471
62,3	4,46	3,644	3,515
49,8	4,097	3,684	3,357
31,8	3,237	3,163	3,200
17,8	2,347	2,511	2,805
8,00	1,587	1,842	2,173
2,02	1,154	1,362	1,47

q kW/m ²	ΔT_T K	ΔT_S K	ΔT_B K
Structure A431, pressure p = 1,0 bar			
* 2,94	9,233	9,837	8,835
5,37	3,799	3,827	3,935
8,08	4,354	4,273	4,395
11,8	3,974	3,665	3,683
15,9	3,801	3,228	3,169
20,6	4,384	3,544	3,243
25,9	4,827	3,840	3,199
32,0	4,851	3,913	3,323
38,7	4,765	3,947	3,412
45,8	4,552	3,65	3,524
54,2	4,473	3,632	3,675
62,5	4,410	3,580	3,740
50,2	4,102	3,547	3,644
32,2	3,141	2,886	3,127
18,1	2,129	2,126	2,502
8,00	1,590	1,740	2,066
2,02	1,183	1,331	1,404

q kW/m ²	ΔT_T K	ΔT_S K	ΔT_B K
Structure A432, pressure p = 0,5 bar			
2,95	15,72	14,762	10,385
* 5,18	22,91	21,99	15,158
8,05	5,776	5,665	3,940
11,6	5,235	5,120	3,389
15,8	4,622	4,556	2,981
20,6	4,322	4,289	2,503
26,0	4,402	4,426	2,381
32,2	4,641	4,789	2,479
39,0	4,987	5,094	2,536
46,3	5,359	5,690	2,641
53,9	5,474	6,177	2,820
62,2	5,652	6,247	3,011
49,8	5,231	5,545	2,678
32,1	4,706	4,702	2,462
18,0	4,091	3,995	2,266
8,20	3,517	3,313	2,090
2,01	2,844	2,803	1,905

q kW/m ²	ΔT_T K	ΔT_S K	ΔT_B K
Structure A432, pressure p = 0,5 bar			
* 2,90	16,34	15,319	11,068
5,189	10,42	15,714	13,391
8,15	3,892	4,095	3,750
11,6	4,722	4,866	3,641
15,8	4,157	4,185	2,714
20,7	3,936	3,725	1,735
26,0	4,057	4,044	1,732
32,2	4,452	4,452	1,882
39,0	4,912	4,901	1,818
45,7	5,269	5,201	1,899
54,0	4,022	5,451	1,891
62,0	4,072	5,731	1,952
49,9	3,797	4,844	1,618
32,2	3,206	3,854	1,453
18,0	2,541	3,048	1,285
8,04	1,935	2,202	1,056
2,01	1,324	1,439	0,878

q kW/m ²	ΔT_T K	ΔT_S K	ΔT_B K
Structure A432, pressure p = 0,5 bar			
* 2,97	10,16	10,112	7,134
5,13	4,564	4,539	3,818
7,99	4,525	4,575	3,188
11,7	4,313	4,278	2,507
15,8	4,545	4,408	2,237
20,6	4,634	4,199	1,963
26,1	4,932	4,517	1,910
31,8	5,445	4,910	1,979
38,8	5,404	5,352	1,966
45,5	4,377	5,561	2,051
54,0	4,499	5,869	2,120
62,2	4,526	5,756	2,258
49,8	4,238	4,943	1,891
31,6	3,587	4,039	1,815
18,0	2,925	3,222	1,509
7,99	2,35	2,459	1,249
2,05	1,692	1,728	1,003

q kW/m ²	ΔT_T K	ΔT_S K	ΔT_B K
Structure A425, pressure p = 0,5 bar			
* 2,874	3,144	3,032	2,882
5,245	3,965	3,704	3,255
8,017	5,224	4,796	4,054
11,804	6,865	6,262	5,329
15,809	8,171	7,286	5,944
20,763	9,009	7,965	6,354
26,179	9,819	8,61	6,661
31,961	10,23	8,49	6,933
38,881	10,49	8,578	7,043
45,911	10,16	8,474	7,21
53,758	10,19	8,533	7,442
62,049	10,52	8,685	7,722
50,126	9,168	8,066	7,302
32,055	7,375	6,573	6,227
17,977	5,7	5,256	5,129
8,074	4,253	4,003	3,736
2,01	3,072	2,961	2,798

q kW/m ²	ΔT_T K	ΔT_S K	ΔT_B K
Structure A425, pressure p = 1,5 bar			
* 2,98	10,69	11,557	10,542
5,18	3,084	2,836	2,345
8,06	4,033	3,603	2,844
11,5	4,249	3,529	2,538
15,7	5,086	4,178	2,577
20,6	5,767	4,707	2,770
26,0	6,492	5,259	3,023
31,9	6,898	5,422	3,111
38,6	7,339	5,417	3,150
45,7	7,470	5,486	3,254
53,8	7,649	5,368	3,325
62,4	7,618	5,407	3,380
49,7	6,539	5,035	3,052
31,9	5,264	4,156	2,739
18,0	3,846	3,135	2,354
8,03	2,240	1,897	1,607
2,09	0,599	0,631	0,528

q kW/m ²	ΔT_T K	ΔT_S K	ΔT_B K
Structure A425, pressure p = 1,0 bar			
* 2,92	3,279	3,199	2,941
5,18	4,028	3,834	3,339
8,11	4,752	4,389	3,602
11,7	5,752	5,083	4,000
15,8	6,754	5,763	4,219
20,5	7,496	6,479	4,483
25,9	8,246	7,019	4,712
32,0	8,660	7,299	4,917
38,7	9,073	7,277	5,007
46,0	9,269	7,327	5,246
54,1	9,370	7,319	5,399
62,0	9,432	7,485	5,674
49,8	7,934	6,940	5,073
31,6	6,667	5,834	4,543
18,0	5,216	4,680	3,953
8,23	3,704	3,435	3,111
2,01	2,012	1,999	1,859

q kW/m ²	ΔT_T K	ΔT_S K	ΔT_B K
Structure A426, pressure p = 0,5 bar			
* 2,92	12,11	11,262	12,435
5,24	4,331	4,124	4,220
8,02	5,223	4,797	5,103
11,6	6,254	5,689	6,206
15,7	7,424	6,787	7,282
20,7	8,809	7,948	8,296
25,9	10,06	8,899	8,884
31,9	11,01	9,627	9,299
38,8	11,31	10,076	9,453
46,1	11,59	10,467	9,721
53,8	11,83	10,724	9,856
62,8	11,90	11,196	9,981
71,1	11,83	11,140	10,217
49,7	10,21	9,429	9,385
32,0	8,381	7,921	8,376
18,0	6,574	6,144	6,877
8,01	4,838	4,455	5,027

q kW/m ²	ΔT_T K	ΔT_S K	ΔT_B K
Structure A426, pressure p = 1,5 bar			
* 2,91	12,61	13,013	13,223
5,11	4,691	5,740	4,370
8,11	5,700	5,174	5,195
11,7	5,988	5,212	5,197
15,7	6,567	5,594	5,339
20,5	7,137	6,026	5,465
26,0	7,859	6,595	5,807
32,0	8,557	7,157	6,020
38,7	9,073	7,565	6,233
46,4	9,490	8,008	6,540
53,6	9,756	8,208	6,727
62,6	9,997	8,540	6,836
71,3	10,05	8,7580	6,861
49,7	8,890	7,630	6,436
31,8	7,063	6,291	5,844
17,8	5,205	4,719	4,920
8,00	3,611	3,304	3,725

q kW/m ²	ΔT_T K	ΔT_S K	ΔT_B K
Structure A426, pressure p = 1,0 bar			
* 2,92	16,91	15,679	17,299
5,34	5,003	4,869	4,747
8,90	6,363	5,752	5,875
11,5	5,954	5,191	5,213
15,8	6,986	5,954	5,735
20,5	7,908	6,679	6,140
26,0	8,666	7,305	6,462
32,0	9,295	7,873	6,683
38,5	9,858	8,391	7,054
46,2	10,22	8,752	7,208
54,0	10,55	9,060	7,354
62,3	10,80	9,416	7,655
71,3	10,56	9,720	7,756
49,7	9,217	8,341	7,206
31,6	7,344	6,839	6,555
18,0	5,695	5,360	5,540
7,97	4,194	3,904	4,321

q kW/m ²	ΔT_T K	ΔT_S K	ΔT_B K
Structure A427, pressure p = 0,5 bar			
* 2.86	4.192	3.661	4.224
5.16	4.184	3.226	3.866
7.96	5.495	3.662	4.650
11.3	6.959	4.380	5.931
15.3	8.209	5.015	7.066
20.2	9.026	5.716	7.683
25.5	9.497	6.315	8.063
31.5	9.431	6.843	8.393
38,0	9.235	7.264	8.620
45.3	9.194	7.295	8.829
52.8	9.046	7.537	9.040
61.3	8.427	7.339	9.139
70.0	8.272	7.323	9.383

Pressure driven experiments

p bar	ΔT_T K	ΔT_S K	ΔT_B K
Structure A419 Heat flux $q = 7,6 \text{ kW/m}^2$			
5,0	4,413	3,609	2,957
5,5	4,563	3,78	3,306
6,0	4,678	3,891	3,246
6,5	4,553	3,761	3,205
7,0	4,432	3,645	3,050
7,5	4,313	3,516	2,920
8,0	4,256	3,491	2,877
8,5	4,257	3,488	2,867
9,0	4,497	3,612	2,922

p bar	ΔT_T K	ΔT_S K	ΔT_B K
Structure A419 Heat flux $q = 67 \text{ kW/m}^2$			
5,0	9,680	6,750	4,581
5,5	9,233	6,360	4,539
6,0	8,840	6,082	4,411
6,5	8,509	5,809	4,282
7,0	8,273	5,635	4,214
7,5	7,998	5,428	3,893
8,0	7,772	5,258	3,762
8,5	7,670	5,220	3,760
9,0	7,355	5,002	3,479

p bar	ΔT_T K	ΔT_S K	ΔT_B K
Structure A419 Heat flux $q = 30 \text{ kW/m}^2$			
5,0	8,018	5,100	4,227
5,5	7,654	4,828	4,072
6,0	7,385	4,638	4,027
6,5	7,247	4,501	3,879
7,0	7,072	4,346	3,673
7,5	6,908	4,187	3,604
8,0	6,720	4,058	3,505
8,5	6,609	3,997	3,45
9,0	6,421	3,854	3,300

p bar	ΔT_T K	ΔT_S K	ΔT_B K
Structure A419 Heat flux $q = 120 \text{ kW/m}^2$			
5,0	8,970	6,567	5,047
5,5	8,619	6,408	4,883
6,0	8,259	6,141	4,778
6,5	7,986	5,883	4,544
7,0	7,776	5,659	4,329
7,5	7,561	5,405	4,057
8,0	7,431	5,275	3,895
8,5	7,365	5,215	3,829
9,0	7,191	5,040	3,654

p bar	ΔT_T K	ΔT_S K	ΔT_B K
Structure A4 01 Heat flux $q = 8,1 \text{ kW/m}^2$			
5,0	3,263	2,961	2,988
5,5	3,230	2,886	2,811
6,0	3,096	2,544	2,669
6,5	3,041	2,181	2,630
7,0	2,942	1,186	2,559
7,5	2,795	0,936	2,422
8,0	2,440	0,627	2,176
8,5	2,375	0,704	2,159
9,0	2,309	0,697	2,079

p bar	ΔT_T K	ΔT_S K	ΔT_B K
Structure A4 01 Heat flux $q = 72 \text{ kW/m}^2$			
5,0	5,883	4,135	3,800
5,5	5,606	3,963	3,573
6,0	5,428	3,812	3,432
6,5	5,113	3,658	3,322
7,0	4,862	3,503	3,083
7,5	4,675	3,392	2,993
8,0	4,454	3,216	2,821
8,5	4,259	3,088	2,680
9,0	4,066	2,937	2,542

p bar	ΔT_T K	ΔT_S K	ΔT_B K
Structure A4 01 Heat flux $q = 32 \text{ kW/m}^2$			
5,0	5,205	4,099	3,401
5,5	4,959	3,948	3,337
6,0	4,806	3,756	3,246
6,5	4,449	3,468	2,987
7,0	4,326	3,337	2,913
7,5	4,040	3,163	2,799
8,0	3,888	3,029	2,719
8,5	3,775	2,897	2,643
9,0	3,566	2,712	2,511

p bar	ΔT_T K	ΔT_S K	ΔT_B K
Structure A4 01 Heat flux $q = 120 \text{ kW/m}^2$			
5,0	5,575	4,518	3,923
5,5	5,466	4,388	3,904
6,0	5,271	4,212	3,538
6,5	5,129	4,060	3,422
7,0	4,993	3,929	3,290
7,5	4,838	3,749	3,172
8,0	4,497	3,562	2,862
8,5	4,384	3,472	2,808
9,0	4,288	3,411	2,775

Tandem tube experiments
Refrigerant R134a

Tandem A428+A425, p=5bar.

$q_{\text{test_tube}}$	$q_{\text{LT}} = 125 \text{ kW/m}^2$			$q_{\text{LT}} = 50 \text{ kW/m}^2$		
* 5,11	0,837	0,414	0,383	1,113	0,652	0,694
11,6	1,716	0,671	0,656	1,674	0,711	0,845
20,6	3,839	1,965	1,137	2,407	0,760	0,954
32,0	5,379	2,821	1,177	3,915	1,423	1,724
46,0	5,807	3,131	1,333	5,077	2,155	1,893
62,5	5,692	3,173	1,563	5,305	2,425	1,745
81,3	5,450	3,113	1,695	4,917	2,685	1,772
102	5,312	3,183	1,761	4,54	2,839	2,030
126	4,905	3,179	1,974	4,435	3,050	2,151
71,6	3,846	2,296	1,591	3,441	2,031	1,643
32,0	2,509	1,144	1,059	2,049	0,823	0,920
8,07	0,951	0,485	0,465	0,768	0,403	0,421
$q_{\text{test_tube}}$	$q_{\text{LT}} = 8 \text{ kW/m}^2$			$q_{\text{LT}} = q_{\text{test_tube}}$		
* 5,11	0,523	0,366	0,346	0,540	0,381	0,437
11,6	0,811	0,464	0,472	0,822	0,480	0,502
20,6	1,204	0,555	0,634	1,223	0,585	0,627
32,0	1,837	0,662	0,900	1,686	0,667	0,730
46,0	3,159	0,928	1,639	2,442	0,827	0,947
62,5	3,660	1,662	2,048	2,544	0,944	1,189
81,3	3,665	2,300	2,184	2,795	1,100	1,377
102	3,458	2,546	2,225	2,883	1,303	1,556
126	3,491	2,815	2,313	2,741	1,540	1,773
71,6	2,876	1,805	1,780	1,656	0,929	1,083
32,0	1,861	0,788	0,965	0,773	0,540	0,595
8,07	0,724	0,396	0,425	0,354	0,316	0,322

Tandem A428+A425, p=7,5bar.

$Q_{\text{test_tube}}$	$q_{\text{LT}} = 125 \text{ kW/m}^2$			$q_{\text{LT}} = 50 \text{ kW/m}^2$		
* 5,10	0,639	0,395	0,337	0,431	0,276	0,199
11,5	1,005	0,450	0,427	0,704	0,338	0,283
20,6	1,752	0,518	0,542	1,071	0,404	0,388
31,8	4,482	1,690	1,169	1,546	0,470	0,561
46,0	5,219	2,426	1,241	2,331	0,554	0,985
62,3	5,726	2,990	1,388	4,051	1,047	1,386
81,2	5,642	3,124	1,541	4,752	2,220	1,620
103	5,696	3,124	1,645	4,789	2,717	1,859
126	5,200	3,025	1,824	4,762	2,963	1,889
71,3	3,982	1,889	1,369	3,449	1,324	1,367
32,2	2,073	0,556	0,596	1,704	0,496	0,571
8,06	0,656	0,319	0,235	0,605	0,303	0,237
$Q_{\text{test_tube}}$	$q_{\text{LT}} = 8 \text{ kW/m}^2$			$q_{\text{LT}} = Q_{\text{test_tube}}$		
* 5,10	0,666	0,472	0,415	0,788	0,444	0,380
11,5	0,842	0,434	0,398	1,318	0,587	0,553
20,6	1,261	0,461	0,471	2,100	0,603	0,589
31,8	2,183	0,520	0,700	4,152	1,001	0,919
46,0	3,960	0,746	2,041	5,401	2,037	1,498
62,3	4,981	2,061	2,109	5,749	2,863	1,638
81,2	4,844	2,413	2,108	5,928	3,104	1,683
103	4,071	2,580	1,923	5,937	3,063	1,821
126	4,047	2,829	2,068	5,917	3,109	2,121
71,3	2,945	0,917	1,402	4,754	1,956	1,487
32,2	1,607	0,500	0,540	2,808	0,662	0,597
8,06	0,584	0,317	0,253	0,856	0,324	0,254

Tandem A428+A425, p=9bar.

$Q_{\text{test_tube}}$	$q_{\text{LT}} = 125 \text{ kW/m}^2$			$q_{\text{LT}} = 50 \text{ kW/m}^2$		
* 5,10	0,765	0,598	0,510	0,640	0,430	0,336
11,5	1,026	0,614	0,551	0,950	0,473	0,397
20,6	1,454	0,626	0,598	1,554	0,544	0,512
31,8	2,724	0,625	0,705	2,809	0,656	0,727
46,0	4,047	0,916	1,942	4,474	1,362	1,712
62,3	4,635	2,162	2,306	5,039	2,478	1,671
81,2	4,682	2,513	1,914	5,260	2,969	1,718
103	4,670	2,741	1,973	5,177	3,166	1,790
126	4,689	2,959	2,061	5,151	3,270	2,019
71,3	3,580	1,158	1,405	4,026	1,831	1,456
32,2	1,786	0,561	0,588	2,062	0,594	0,608
8,06	0,655	0,403	0,316	0,704	0,405	0,318
$Q_{\text{test_tube}}$	$q_{\text{LT}} = 8 \text{ kW/m}^2$			$q_{\text{LT}} = Q_{\text{test_tube}}$		
* 5,10	6,624	6,387	6,329	0,917	0,667	0,604
11,5	1,586	1,123	1,079	1,264	0,709	0,659
20,6	1,915	0,879	0,895	1,828	0,613	0,609
31,8	4,190	1,499	1,311	4,107	1,196	1,202
46,0	5,014	2,424	1,373	5,046	2,582	1,643
62,3	5,410	2,976	1,544	5,164	2,984	1,768
81,2	5,382	3,281	1,666	5,104	3,097	1,896
103	5,285	3,301	1,719	4,549	3,074	1,880
126	5,223	3,187	1,891	4,238	3,134	2,171
71,3	4,138	2,058	1,451	3,419	1,957	1,668
32,2	2,242	0,667	0,664	1,833	0,628	0,713
8,06	0,724	0,412	0,334	0,677	0,415	0,340

Tandem A437+A425, p=5bar.

$Q_{\text{test_tube}}$	$q_{\text{LT}} = 125 \text{ kW/m}^2$			$q_{\text{LT}} = 50 \text{ kW/m}^2$		
* 5,10	0,541	0,374	0,331	0,472	0,326	0,338
11,5	0,902	0,546	0,497	0,695	0,424	0,429
20,6	1,180	0,601	0,597	1,047	0,550	0,568
31,8	1,511	0,696	0,707	1,424	0,656	0,696
46,0	1,738	0,808	0,890	1,754	0,770	0,835
62,3	2,144	0,954	1,127	2,223	0,922	1,069
81,2	2,569	1,101	1,239	2,586	1,072	1,348
103	2,792	1,303	1,333	2,535	1,268	1,571
126	3,107	1,642	1,555	2,798	1,561	1,784
71,3	2,013	0,995	1,116	1,721	0,937	1,058
32,2	0,919	0,580	0,653	0,803	0,553	0,612
8,06	0,385	0,321	0,33	0,359	0,323	0,325
$Q_{\text{test_tube}}$	$q_{\text{LT}} = 8 \text{ kW/m}^2$			$q_{\text{LT}} = Q_{\text{test_tube}}$		
* 5,10	0,476	0,339	0,367	0,540	0,381	0,437
11,5	0,791	0,433	0,466	0,822	0,480	0,502
20,6	1,168	0,516	0,557	1,223	0,585	0,627
31,8	1,791	0,649	0,708	1,686	0,667	0,730
46,0	2,791	0,889	0,997	2,442	0,827	0,947
62,3	3,269	1,083	1,240	2,544	0,944	1,189
81,2	3,015	1,191	1,446	2,795	1,100	1,377
103	3,171	1,400	1,586	2,883	1,303	1,556
126	2,940	1,651	1,778	2,741	1,540	1,773
71,3	1,876	0,960	1,120	1,656	0,929	1,083
32,2	0,856	0,538	0,623	0,773	0,540	0,595
8,06	0,364	0,316	0,324	0,354	0,316	0,322

Tandem A437+A425, p=7,5bar.

$q_{\text{test_tube}}$	$q_{\text{LT}} = 125 \text{ kW/m}^2$			$q_{\text{LT}} = 50 \text{ kW/m}^2$		
* 5,17	0,555	0,397	0,331	0,474	0,324	0,248
11,7	0,660	0,366	0,302	0,692	0,378	0,325
20,6	0,972	0,431	0,384	0,947	0,442	0,411
32,0	1,474	0,520	0,504	1,523	0,534	0,625
45,9	2,319	0,647	0,697	2,887	0,793	0,844
62,5	3,260	0,879	0,943	3,912	1,204	1,005
81,6	3,249	0,985	1,063	3,621	1,434	1,110
102	3,091	1,193	1,226	3,558	1,791	1,196
126	3,152	1,589	1,433	3,532	2,221	1,367
71,5	1,669	0,751	0,861	1,895	0,877	1,002
32,0	0,622	0,419	0,396	0,715	0,447	0,452
7,88	0,259	0,230	0,160	0,276	0,237	0,181
$q_{\text{test_tube}}$	$q_{\text{LT}} = 8 \text{ kW/m}^2$			$q_{\text{LT}} = q_{\text{test_tube}}$		
* 5,17	0,592	0,441	0,382	0,281	0,261	0,204
11,7	0,533	0,386	0,321	0,628	0,334	0,281
20,6	0,729	0,408	0,370	1,027	0,425	0,412
32,0	1,092	0,460	0,455	2,454	0,634	0,739
45,9	2,131	0,563	0,749	3,708	1,023	0,907
62,5	3,223	0,789	1,009	3,778	1,234	1,085
81,6	2,906	0,897	1,132	3,649	1,501	1,223
102	3,240	1,305	1,341	3,266	1,755	1,409
126	3,277	1,591	1,452	2,894	2,044	1,594
71,5	3,247	1,911	1,613	1,525	0,849	1,063
32,0	1,664	0,815	1,011	0,613	0,444	0,478
7,88	0,647	0,426	0,469	0,281	0,261	0,204

Tandem A437+A425, p=9bar.

$q_{\text{test_tube}}$	$q_{\text{LT}} = 125 \text{ kW/m}^2$			$q_{\text{LT}} = 50 \text{ kW/m}^2$		
* 5,12	0,283	0,266	0,170	0,750	0,409	0,336
11,6	0,362	0,315	0,243	1,175	0,454	0,425
20,5	0,478	0,375	0,336	2,355	0,609	0,748
32,0	0,679	0,473	0,541	3,358	0,832	0,830
45,8	1,089	0,619	0,865	3,606	1,212	0,998
62,4	1,928	0,932	1,061	3,684	1,669	1,160
81,1	2,916	1,726	1,180	3,494	2,010	1,280
102	3,292	2,166	1,301	3,497	2,423	1,406
126	3,511	2,551	1,406	1,873	0,924	0,976
71,4	2,343	1,424	1,070	0,649	0,433	0,431
31,9	0,763	0,472	0,487	0,289	0,256	0,168
$q_{\text{test_tube}}$	$q_{\text{LT}} = 8 \text{ kW/m}^2$			$q_{\text{LT}} = q_{\text{test_tube}}$		
* 5,12	0,622	0,356	0,284	0,653	0,364	0,278
11,6	0,861	0,396	0,336	1,039	0,447	0,379
20,5	1,194	0,446	0,429	1,760	0,513	0,527
31,9	2,111	0,576	0,710	3,068	0,729	0,749
45,8	2,702	0,769	0,945	3,398	0,986	0,950
62,4	2,652	1,022	1,120	3,177	1,285	1,106
81,1	2,556	1,300	1,256	2,801	1,570	1,243
102	2,791	1,708	1,450	2,871	1,944	1,449
126	1,371	0,769	0,827	1,375	0,794	0,928
71,4	0,527	0,401	0,373	0,568	0,436	0,413
31,9	0,257	0,231	0,150	0,282	0,269	0,177

Electronic fluid FC-3284

Tandem A428+A425, p=0,5bar

Q _{test_tube}	q _{LT} = 8 kW/m ²			q _{LT} = 50 kW/m ²			q _{LT} = Q _{test_tube}		
* 5,14	4,062	3,600	3,171	3,159	2,975	2,897	4,958	4,433	3,848
11,6	5,958	5,235	3,879	4,639	4,565	4,597	5,996	5,421	4,154
20,5	5,868	4,883	3,981	5,266	5,120	5,009	5,609	5,678	4,262
32,0	5,966	5,139	4,104	5,083	5,284	4,743	5,567	5,987	4,388
45,9	5,204	5,152	4,255	4,759	5,323	4,820	4,990	5,654	4,537
62,3	4,560	4,984	4,406	4,825	5,306	4,968	4,672	5,259	4,804
32,2	4,195	4,349	4,056	4,371	4,602	4,413	4,355	4,590	4,355
8,03	3,403	3,272	3,195	3,404	3,342	3,420	3,436	3,330	3,329

Tandem A428+A425, p=1,0bar

Q _{test_tube}	q _{LT} = 8 kW/m ²			q _{LT} = 50 kW/m ²			q _{LT} = Q _{test_tube}		
* 5,21	3,173	2,984	2,726	2,716	2,538	2,184	2,332	2,176	2,016
11,5	3,804	3,454	2,958	4,378	4,044	2,980	2,860	2,601	2,313
20,5	4,497	3,892	2,909	5,180	5,245	3,416	3,608	3,199	2,743
31,9	5,280	4,508	3,067	5,395	4,885	3,628	4,441	3,945	3,268
45,8	5,557	4,559	3,135	5,391	4,605	3,594	4,752	4,360	3,579
61,7	5,118	4,455	3,406	4,908	4,383	3,598	4,559	4,627	3,794
31,9	4,070	3,543	2,849	3,906	3,460	2,997	3,662	3,601	3,096
8,02	2,526	2,336	2,168	2,443	2,268	2,145	2,406	2,299	2,167

Tandem A428+A425, p=1,5bar

q _{test_tube}	q _{LT} = 8 kW/m ²			q _{LT} = 50 kW/m ²			q _{LT} = q _{test_tube}		
* 5,12	3,232	2,725	1,928	3,572	3,268	3,051	2,451	2,371	2,153
11,5	5,179	4,108	2,273	5,035	4,330	3,650	2,853	2,730	2,334
20,6	5,440	4,379	2,435	5,277	4,090	3,178	3,199	3,037	2,404
31,9	5,466	4,132	2,506	5,013	4,079	2,981	3,851	3,753	2,669
45,7	5,380	3,928	2,602	4,290	4,291	2,989	4,241	4,360	2,985
62,1	4,805	3,959	2,762	4,240	4,187	3,058	4,207	4,544	3,175
31,9	3,741	3,049	2,358	3,390	3,198	2,521	3,368	3,427	2,610
8,00	2,120	1,870	1,671	1,994	1,884	1,703	2,033	1,986	1,765

Tandem A437+A425, p=0,5bar

q _{test_tube}	q _{LT} = 8 kW/m ²			q _{LT} = 50 kW/m ²			q _{LT} = q _{test_tube}		
* 5,16	1,709	1,838	1,258	1,333	1,509	1,365	3,271	3,509	2,92
11,6	2,909	3,194	1,621	2,167	2,502	2,425	4,505	4,683	3,444
20,5	3,172	2,874	1,682	2,684	3,191	2,341	4,615	4,638	3,683
32,0	3,254	2,699	1,767	2,849	3,218	2,330	4,873	4,481	3,839
45,9	2,867	2,486	1,895	2,919	3,022	2,394	4,333	4,537	3,918
62,3	2,600	2,063	1,828	2,705	2,916	2,328	4,166	4,526	3,941
31,9	1,761	1,663	1,535	1,984	2,283	2,096	3,574	3,909	3,691
8,04	0,954	0,987	0,878	1,268	1,569	1,454	2,904	3,024	2,935

Tandem A437+A425, p=1,5bar

q _{test_tube}	q _{LT} = 8 kW/m ²			q _{LT} = 50 kW/m ²			q _{LT} = q _{test_tube}		
* 5,12	1,389	1,498	1,262	1,466	1,572	1,345	2,47	2,433	1,784
11,5	1,614	1,773	1,427	1,713	1,863	1,505	3,055	3,209	1,709
20,4	1,943	2,147	1,681	2,007	2,225	1,714	3,589	4,087	1,867
31,9	2,344	2,597	1,865	2,433	2,714	1,919	3,677	3,846	1,952
45,8	2,845	3,085	1,974	2,926	3,145	2,09	3,654	3,313	1,970
62,1	3,291	3,236	2,043	3,246	3,278	2,097	3,581	3,178	2,074
31,8	2,286	2,487	1,779	2,240	2,453	1,744	2,480	2,449	1,780
8,01	1,464	1,597	1,315	1,434	1,572	1,301	1,494	1,579	1,288

Reverse experiments with tandem tubes
Refrigerant R134a

Tandem A428+A425, p=5bar.

q_{LT} kW/m ²	ΔT_T K	ΔT_S K	ΔT_B K
$q_{\text{Test tube}} = 8 \text{ kW/m}^2$			
5,20	3,048	2,196	1,104
11,7	2,784	1,931	1,101
20,5	2,213	1,223	0,889
32,0	1,339	0,570	0,575
46,0	1,161	0,527	0,556
62,5	1,087	0,522	0,551
81,4	1,015	0,522	0,560
102	0,981	0,510	0,559
126	0,949	0,509	0,571
71,5	0,971	0,523	0,567
32,0	1,008	0,526	0,566
8,05	1,054	0,545	0,579

q_{LT} kW/m ²	ΔT_T K	ΔT_S K	ΔT_B K
$q_{\text{Test tube}} = 125 \text{ kW/m}^2$			
5,20	4,408	2,949	2,017
11,7	4,304	2,92	2,007
20,5	4,192	2,880	2,069
32,0	4,102	2,84	2,108
46,0	4,033	2,823	2,162
62,5	3,925	2,813	2,142
81,4	3,809	2,806	2,177
102	3,526	2,786	2,212
126	3,288	2,662	2,212
71,5	3,285	2,644	2,202
32,0	3,302	2,657	2,147
8,05	3,314	2,650	2,046

q_{LT} kW/m ²	ΔT_T K	ΔT_S K	ΔT_B K
$q_{\text{Test tube}} = 32 \text{ kW/m}^2$			
5,20	5,501	3,332	1,354
11,7	5,163	3,101	1,354
20,5	4,925	2,951	1,363
32,0	4,749	2,810	1,413
45,9	4,470	2,659	1,461
62,5	4,245	2,532	1,489
81,4	4,067	2,435	1,538
102	3,963	2,371	1,559
126	3,841	2,287	1,603
71,5	3,831	2,267	1,617
32,0	3,858	2,281	1,619
8,05	3,940	2,378	1,538

Tandem A428+A425, p=7,5bar.

q_{LT} kW/m ²	ΔT_T K	ΔT_S K	ΔT_B K
$q_{\text{Test tube}} = 8 \text{ kW/m}^2$			
5,20	0,924	0,444	0,389
11,7	0,766	0,373	0,320
20,5	0,747	0,365	0,306
32,0	0,723	0,349	0,291
45,9	0,713	0,354	0,291
62,5	0,686	0,339	0,276
81,4	0,653	0,335	0,276
102	0,636	0,333	0,271
126	0,607	0,320	0,264
71,5	0,616	0,328	0,268
32,0	0,632	0,333	0,272
8,05	0,634	0,338	0,283

q_{LT} kW/m ²	ΔT_T K	ΔT_S K	ΔT_B K
$q_{\text{Test tube}} = 125 \text{ kW/m}^2$			
5,20	4,795	2,900	1,993
11,7	4,720	2,856	2,018
20,5	4,664	2,820	1,971
32,0	4,590	2,828	2,029
45,9	4,521	2,810	2,083
62,5	4,428	2,805	2,067
81,4	4,363	2,799	2,142
102	4,094	2,749	2,153
126	3,999	2,699	2,172
71,5	4,005	2,701	2,158
32,0	4,020	2,714	2,178
8,05	4,041	2,723	1,969

q_{LT} kW/m ²	ΔT_T K	ΔT_S K	ΔT_B K
$q_{\text{Test tube}} = 32 \text{ kW/m}^2$			
5,20	5,319	3,191	1,417
11,7	5,206	3,047	1,372
20,5	5,057	2,879	1,320
32,0	4,958	2,796	1,403
45,9	4,848	2,695	1,409
62,5	4,716	2,588	1,432
81,4	4,571	2,496	1,463
102	4,390	2,378	1,497
126	4,246	2,268	1,535
71,5	4,244	2,203	1,505
32,0	4,343	2,293	1,432
8,05	4,454	2,384	1,380

Tandem A428+A425, p=9bar.

q_{LT} kW/m ²	ΔT_T K	ΔT_S K	ΔT_B K
$q_{\text{Test tube}} = 8 \text{ kW/m}^2$			
5,20	1,488	1,086	1,040
11,7	1,250	0,893	0,831
20,5	1,107	0,770	0,697
32,0	0,862	0,526	0,447
45,9	0,855	0,538	0,461
62,5	0,794	0,492	0,413
81,4	0,754	0,470	0,390
102	0,713	0,452	0,371
126	0,704	0,452	0,373
71,5	0,703	0,450	0,369
32,0	0,711	0,452	0,370
8,05	0,696	0,437	0,358

q_{LT} kW/m ²	ΔT_T K	ΔT_S K	ΔT_B K
$q_{\text{Test tube}} = 125 \text{ kW/m}^2$			
5,20	5,384	3,501	2,227
11,7	5,356	3,502	2,271
20,5	5,168	3,360	2,201
32,0	4,992	3,222	2,134
45,9	4,908	3,201	2,110
62,5	4,798	3,154	2,191
81,4	4,697	3,116	2,238
102	4,544	3,076	2,227
126	4,409	2,939	2,195
71,5	4,466	2,960	2,073
32,0	4,489	2,956	2,162
8,05	4,508	2,988	2,003

q_{LT} kW/m ²	ΔT_T K	ΔT_S K	ΔT_B K
$q_{\text{Test tube}} = 32 \text{ kW/m}^2$			
5,20	5,790	3,907	2,304
11,7	5,240	3,276	1,754
20,5	4,830	2,773	1,399
32,0	4,618	2,404	1,270
45,9	4,439	1,897	1,145
62,5	4,298	1,634	1,074
81,4	4,146	1,343	0,993
102	4,012	1,165	0,902
126	3,969	1,152	0,908
71,5	3,971	1,126	0,902
32,0	4,067	1,243	0,915
8,05	4,220	1,510	1,012

Electronic fluid FC-3284A428+A425, $q_{\text{Test tube}} = 32 \text{ kW/m}^2$.

q_{LT} kW/m^2	ΔT_{T} K	ΔT_{S} K	ΔT_{B} K
p = 0,5 bar			
5,10	4,339	4,683	4,186
11,6	4,444	4,723	4,264
20,5	4,407	4,718	4,317
32,0	4,443	4,759	4,361
45,9	4,445	4,770	4,401
62,3	4,423	4,775	4,451
32,2	4,480	4,839	4,485
8,03	4,487	4,836	4,288
q_{LT} kW/m^2	ΔT_{T} K	ΔT_{S} K	ΔT_{B} K
p = 1,0 bar			
5,10	5,627	4,287	2,859
11,6	5,592	4,262	2,906
20,5	5,450	4,323	3,039
32,0	5,364	4,275	3,075
45,9	5,125	4,204	3,104
62,3	5,085	4,164	3,144
32,2	5,146	4,196	3,100
8,03	5,251	4,289	3,033
q_{LT} kW/m^2	ΔT_{T} K	ΔT_{S} K	ΔT_{B} K
p = 1,5 bar			
5,10	3,629	3,611	2,360
11,6	3,642	3,617	2,495
20,5	3,616	3,587	2,517
32,0	3,580	3,589	2,566
45,9	3,566	3,568	2,625
62,3	3,538	3,554	2,647
32,2	3,579	3,587	2,590
8,03	3,657	3,622	2,340

A437+A425, $q_{\text{Test tube}} = 32 \text{ kW/m}^2$.

q_{LT} kW/m^2	ΔT_{T} K	ΔT_{S} K	ΔT_{B} K
p = 0,5 bar			
5,10	3,627	3,974	3,529
11,6	3,620	3,980	3,566
20,5	3,630	3,990	3,633
32,0	3,695	4,064	3,775
45,9	3,675	4,049	3,828
62,3	3,684	4,076	3,962
32,2	3,704	4,110	3,800
8,03	3,734	4,125	3,620
q_{LT} kW/m^2	ΔT_{T} K	ΔT_{S} K	ΔT_{B} K
p = 1,5 bar			
5,10	1,880	2,063	0,963
11,6	1,731	1,918	0,890
20,5	1,719	1,908	0,897
32,0	1,624	1,821	0,823
45,9	1,534	1,738	0,755
62,3	1,493	1,693	0,733
32,2	1,484	1,685	0,707
8,03	1,503	1,706	0,638